



## ***ACKNOWLEDGEMENTS***

### **CHAPTER 1 - INTRODUCTION**

1.1 RESEARCH SIGNIFICANCE	2
1.2 OUTLINE OF THE THESIS	4

### **CHAPTER 2 - LITERATURE REVIEW**

2.1 AN OVERVIEW OF THE FRP PROPERTIES	6
2.2 FRP FLEXURAL STRENGTHENING TECHNIQUES FOR CONCRETE MEMBERS	10
2.2.1 External Bonded Reinforcement (EBR)	11
2.2.2 Near Surface Mounted system (NSM)	14
2.2.3 Comparison between strengthening techniques	22
2.3 FRP BEHAVIOUR AT HIGH TEMPERATURE	23
2.3.1 Influence of high temperature on bond properties	26
2.3.1.1 Influence of high temperature on bond properties of EBR FRP	26
2.3.1.2 Influence of high temperature on bond properties of NSM FRP	27
2.3.2 Flexural tests at high temperature of FRP strengthened RC members	28

### **CHAPTER 3 - THERMO-MECHANICAL PROPERTIES OF MATERIALS**

3.1 THERMAL PROPERTIES OF STRENGTHENING MATERIALS	32
3.1.1 Dynamic Mechanic Analysis	33
3.1.1.1 DMA of a commercial CFRP bar	35
3.1.1.2 Specimens' preparation and analyzer's arrangement	35
3.1.1.3 Evaluation of the glass transition temperature	39

3.1.2 Thermogravimetric Analysis (TGA)	44
3.1.2.1 TGA of a commercial CFRP bar	46
3.1.2.2 Specimens' preparation and tests' settings	47
3.1.2.3 Evaluation of the decomposition temperature	48
3.1.3 Differential Scanning Calorimetry (DSC)	52
3.1.3.1 Evaluation of the specific heat of a commercial CFRP bar	53
3.1.4 CFRP's Thermal conductivity	54
3.1.4.1 Evaluation of the thermal conductivity of a commercial CFRP bar	55
3.1.4.2 Specimens' preparation and tests' settings	57
3.1.4.3 Test results and discussion	58
3.1.5 Thermal conductivity tests of cementitious mortar	59
3.2 MECHANICAL PROPERTIES OF MATERIALS	61
3.2.1 Concrete tests at ambient temperature	61
3.2.1.1 Tests at 28 days	62
3.2.1.2 Tests at 76 days	64
3.2.2 Steel tensile tests at ambient temperature	65
3.2.3 Compression test of Cementitious grout at ambient temperature	67
3.2.4 FRP tensile tests at ambient temperature	69
<b>CHAPTER 4 - BOND TESTS AT AMBIENT TEMPERATURE</b>	
4.1 EXPERIMENTAL PROGRAM	73
4.1.1 Fabrication and concrete	76
4.1.2 Instrumentation	79
4.1.3 Test setup	81
4.2 RESULTS AND DISCUSSION	82

## **CHAPTER 5 - EXPERIMENTAL TESTS OF NSM FRP STRENGTHENED RC BEAMS**

5.1 EXPERIMENTAL PROGRAM	92
5.1.1 Design	94
5.1.2 RC beams' manufacturing and NSM strengthening	102
5.2 FLEXURAL TEST SETUP	105
5.2.1 Innovative instrumentation: Digital Image Correlation	111
5.3 RESULTS	112
5.3.1 Ambient temperature tests of un-strengthened beams	112
5.3.2 Ambient temperature tests of strengthened beams	117
5.3.3 High temperature tests	127
5.3.3.1 Global heating configuration	127
5.3.3.2 Localised heating configuration	132
5.3.4 Residual tests	141
5.4 SUMMARY OF THE EXPERIMENTAL RESULTS AND CONCLUSION	143

## **CHAPTER 6 - NUMERICAL ANALYSES**

6.1 THERMAL ANALYSES OF THE TESTED BEAMS	148
6.1.1 The SAFIR thermal model	148
6.1.2 Thermal properties of materials	149
6.1.3 Finite element thermal models	150
6.1.4 Analyses results and numerical – experimental comparison	152
6.2 THERMO-MECHANICAL ANALYSIS OF A FULL-SCALE BEAM	155
6.2.1 Description of the case study	156

6.2.2 Thermo-mechanical properties of materials at high temperature	156
6.2.3 The thermal finite element model and analysis results	157
6.2.4 Mechanical analysis	158
<b>CONCLUSIONS</b>	<b>161</b>
<b>REFERENCES</b>	<b>R.1</b>
<b>ANNEX I - PROCESSING OF DMA AND TGA DATA</b>	<b>A-I.1</b>

## LIST OF FIGURES

- Figure 2. 1 – Unidirectional composite: Fibres embedded in matrix
- Figure 2. 2 – Multidirectional fibres
- Figure 2. 3 – Fibre comparison (no matrix): Stress-Strain (Kodur et al, 2005)
- Figure 2. 4 – Young modulus of structural materials (Buyukozturk et al, 2004)
- Figure 2. 5 – Failure modes of FRP flexurally strengthened members (Buyukozturk et al, 2004)
- Figure 2. 6 – Debonding and delamination of externally bonded FRP systems: a,b,c) ACI 440.2R-08; d) Buyukozturk et al, 2004
- Figure 2. 7 - Main stages of the NSM strengthening: a) Grooving; b) Adhesive and FRP placement; c) Strengthened member
- Figure 2. 8 – A/C interface failure (De Lorenzis et al, 2002)
- Figure 2. 9 – Longitudinal Splitting of the resin (De Lorenzis et al, 2002)
- Figure 2. 10 – Splitting of the cementitious adhesive (De Lorenzis et al, 2002)
- Figure 2. 11 – Minimum dimension of grooves (Parretti & Nanni, 2004)
- Figure 2. 12 – Typical failures of NSM specimens with varying degrees of concrete damage (Round Robin tests - Bilotta et al, 2015)
- Figure 2. 13 – Splitting-related (top) and pull-out (bottom) failures in NSM specimens (Robin Round Tests – Bilotta et al, 2015)
- Figure 3. 1 - Possible test arrangements of a dynamic mechanic analyser (Ehrenstein et al, 2004)
- Figure 3. 2 - Triton Technology Dynamic Mechanical Analyzer (TTDMA)
- Figure 3. 3 – FireStrong CFRP bar
- Figure 3. 4 - Specimens for DMA tests in single cantilever configuration
- Figure 3. 5 - Specimens' preparation: a) bar's chopping; b) central part's extraction; c) outer surface's peeling off.
- Figure 3. 6 - Dynamic mechanic analyzer in single cantilever configuration
- Figure 3. 7 - Specimens for DMA tests in three-point bending moment configuration
- Figure 3. 8 - Dynamic mechanic analyzer in 3 point bending moment configuration
- Figure 3. 9 - SC CFRP-1-15: storage modulus  $E'$ , loss modulus  $E''$  loss factor  $\tan \delta$  vs temperature
- Figure 3. 10 - TPB CFRP-1-40: storage modulus  $E'$ , loss modulus  $E''$  loss factor  $\tan \delta$  vs temperature
- Figure 3. 11. Normalized storage modulus versus Temperature. Comparison between SC and TPB
- Figure 3. 12 - SC CFRP-1-15: Normalized storage modulus vs Temperature. Definition of  $T_g$  offset
- Figure 3. 13 - TPB CFRP-1-40: Normalized storage modulus vs Temperature. Definition of  $T_g$  offset
- Figure 3. 14 - SC CFRP-1-15: Normalized storage modulus vs Temperature. Definition of  $T_g$  onset
- Figure 3. 15 - TPB CFRP-1-40: Normalized storage modulus vs Temperature. Definition of  $T_g$  onset
- Figure 3. 16 - SC CFRP-1-15: Normalized storage modulus vs Temperature and First derivative of  $E/E_{(70^\circ\text{C})}$  vs Temperature. Definition of  $T_g$  midpoint
- Figure 3. 17 - TPB CFRP-1-40: First derivative of  $E/E_{(70^\circ\text{C})}$  vs Temperature. Definition of  $T_g$  midpoint

Figure 3. 18 - Thermobalance designs (Gabbott, 2008)

Figure 3. 19 - METTLER TOLEDO Thermogravimetric analyzer

Figure 3. 20 - Specimens placed in the aluminium crucibles (70 $\mu$ l)

Figure 3. 21 - Weight loss vs Temperature (TGA curves)

Figure 3. 22 - First derivative of weight loss vs Temperature (DTG curves)

Figure 3. 23 - CFRP-N2-A: Weight loss vs Temperature. Definition of  $T_d$  offset

Figure 3. 24 - CFRP-N2-A: Weight loss vs Temperature. Definition of  $T_d$  onset

Figure 3. 25 - CFRP-N2-A: TGA curve and DTG curve. Definition of  $T_d$  midpoint

Figure 3. 26 - CFRP-Air-A: DTG curve. Definition of  $T_d$  midpoint

Figure 3. 27 – CFRP Specific heat capacity versus Temperature. Comparison between experimental results and the value provided in literature for a similar product

Figure 3. 28 - Holometrix Model TCHM-LT C-Matic

Figure 3. 29 - Scheme of C-Matic (Netzsch Instruments, Inc)

Figure 3. 30 - CFRP samples

Figure 3. 31 - Insulation cylinder

Figure 3. 32 - Specimens for thermal conductivity tests (L=longitudinal; T=transversal)

Figure 3. 33 - Specimen covered by the heat sink compound

Figure 3. 34 - CFRP Longitudinal thermal conductivity vs Temperature

Figure 3. 35 - CFRP Transverse thermal conductivity vs Temperature

Figure 3. 36 – Specimens of cementitious mortar for thermal conductivity tests

Figure 3. 37 – Cementitious mortar’s thermal conductivity vs Temperature

Figure 3. 38 - Avery 7104 Compression and tension testing machine

Figure 3. 39 - Scheme of apparatus for splitting cylinders (IS:1999 5816-1970)

Figure 3. 40 - Apparatus for splitting cylinder test

Figure 3. 41 - Instron 600 LX Compression and tension testing machine

Figure 3. 42 - INSTRON 600 LX set for tensile test

Figure 3. 43 - Camera’s position during tensile tests: a) isometric view; b) front view

Figure 3. 44 - Patches monitored through DIC (Steel tensile test)

Figure 3. 45 - Steel constitutive law

Figure 3. 46 - Elastic branch of the constitutive law

Figure 3. 47 - Mixing procedure (Contractor Training Manual)

Figure 3. 48 - Specimen for compression test of the cementitious grout

Figure 3. 49 - 810 Material Testing Machine (MTS)

Figure 3. 50 - 810 Failure mode of the tested specimen

Figure 3. 51 - Specimens’ preparation: CFRP bars embedded in gripping steel tubes

Figure 3. 52 - MTS set for tensile test

Figure 3. 53 - Bar instrumented with strain gauge and painted for DIC

Figure 3. 54 - Patches monitored through DIC (CFRP tensile test)

Figure 3. 55 - Failure mode of the tested specimens

Figure 3. 56 - Stress-strain relationships of CFRP

Figure 3. 57 - Interpolation of CFRP stress-strain relationships

Figure 4. 1 – Scheme of a specimen for pull-out test (isometric view):

Figure 4. 2 – Scheme of a specimen for pull-out test (cross section): a)  $b_g16$ -TOP; b)  $b_g16$ -CENTRE; c)  $b_g20$ -TOP

Figure 4. 3 – Steel formworks for casting of concrete prisms

Figure 4. 4 –Casting of concrete: a) concrete prisms; b) concrete cylinders

Figure 4. 5 – Placement of CFRP bars into the grooves

Figure 4. 6 – Casting of cementitious mortar in the groove

Figure 4. 7 – Placement of thixotropic resin in the groove

Figure 4. 8 – Strain gauges on CFRP bars

Figure 4. 9 – Strain gauges' spacing on CFRP bar: a)  $L_b$  300 mm;  $L_b$  400 mm

Figure 4. 10 – Installation of steel pipes at the end of the CFRP bars

Figure 4. 11 – Single shear test setup

Figure 4. 12 – Specimens after pull-out test: a)  $L_b300-b_g16-T-CM$ ; b)  $L_b300-b_g16-T-R$ ; c)  $L_b300-b_g20-T-CM$ ; d)  $L_b300-b_g20-T-R$

Figure 4. 13 – Load versus crosshead displacement ( $L_b300-T-R$ )

Figure 4. 14 – Load versus crosshead displacement ( $L_b300-T-CM$ )

Figure 4. 15 – Failure at A/C interface after the main failure at B/A interface

Figure 4. 16 – Load versus total slip ( $L_b300-T-R$ )

Figure 4. 17 – Load versus total slip ( $L_b300-T-R$ )

Figure 4. 18 – Load versus total slip ( $L_b300-T-CM$  vs  $L_b300-T-R$ )

Figure 4. 19 – Strain profiles  $\varepsilon(z, P)$ : a)  $L_b300-b_g16-T-CM-02$ ; b)  $L_b300-b_g20-T-CM-01$

Figure 4. 20 – Strain profiles  $\varepsilon(z, P)$ : a)  $L_b300-b_g16-T-R-01$ ; b)  $L_b300-b_g20-T-R-02$

Figure 4. 21 – Strain profiles  $\varepsilon(z, P = 6kN)$ : a)  $L_b300-T-CM$ ; b)  $L_b300-T-R$

Figure 4. 22 – Strain profiles  $\varepsilon(z, P = 18kN)$ : a)  $L_b300-T-CM$ ; b)  $L_b300-T-R$

Figure 4. 23 – Shear stress versus slip ( $\tau - s$ ):  $L_b300-T-R$

Figure 4. 24 – Shear stress versus slip ( $\tau - s$ ):  $L_b300-T-CM$

Figure 5. 1 - RC beam

Figure 5. 2 - NSM FRP strengthened RC beam

Figure 5. 3 - Discretization of cross-sections

Figure 5. 4 - Moment curvature diagram of the RC beam

Figure 5. 5 – Actual Curvature  $\chi(z, F)$  and Moment  $M(z, F)$  – un-confined concrete (EN1992-1-2)

Figure 5. 6 - Virtual Moment distribution on the beam

Figure 5. 7 - Load-Deflection curve of RC beam (EN1992-1-2)

Figure 5. 8 - Load-Deflection curve of RC beam (Full Mander model)

Figure 5. 9 - Load-Deflection curve of NSM FRP strengthened RC beam



Figure 5. 10 - Stages of the fabrication: a) preparation of the steel reinforcing cages; b) placement of the reinforcing cages in the formworks; c) concrete cast.

Figure 5. 11 - Stages of the strengthening: a) cutting of parallel vertical slots; b) remaining fin removing; c-d) groove smoothing and cleaning; e) bar placement; f) bar grouting in cementitious mortar

Figure 5. 12 - Main stages of the strengthening in real buildings: a) cutting of parallel vertical slots; b) bar hanged in the slot; c) application of the tape formwork; d) gout's pumping (Zeiler, 2013)

Figure 5. 13 - Scheme of the flexural test setup

Figure 5. 14 - Flexural test setup at ambient temperature: a) main components of the setup; b) LP100; c) LP25-LHS; d) strain gauge at the md-length of the CFRP bar

Figure 5. 15 - Flexural test setup at high temperature: a) main components of the setup; b) Loading jack and LPs; c) Pressure transducer line and Instron actuator

Figure 5. 16 - Radiant panel's dimension and location in LocH configuration

Figure 5. 17 - Radiant panels' dimension in GloH configuration

Figure 5. 18 - Thermocouples' location: a) cross-section; b-c) along the CFRP bar

Figure 5. 19 - Un-strengthened beams: Load vs Displacement curves.

Figure 5. 20 - UN-S\_1: Load vs Displacement curves. Comparison between LP100 and DIC

Figure 5. 21 - UN-S\_2: Load vs Displacement curves. Comparison between LP100 and DIC

Figure 5. 22 - Specimen UN-S\_1 after failure

Figure 5. 23 - Patches monitored in DIC (UN-S\_2 beam)

Figure 5. 24 - Generic step of DIC (UN-S\_2 beam)

Figure 5. 25 - Load and strain vs Logging Time

Figure 5. 26 - Strain distribution along the height of the UN-S\_2 beam for different load values

Figure 5. 27 - Un-strengthened beams: Load vs Displacement curves. Comparison between experimental and predicted results.

Figure 5. 28 - Load vs Displacement curves. Comparison between un-strengthened and strengthened beams.

Figure 5. 29 - S-1: Load vs Displacement curves. Comparison between LP100 and DIC

Figure 5. 30 - S-1: Load vs Slip curves

Figure 5. 31 - S-1: Load vs bar's Slip and bar's Strain

Figure 5. 32 - Specimen S-1 after failure

Figure 5. 33 - S-2: Load vs Displacement curves. Comparison between LP100 and DIC

Figure 5. 34 - S-2: Load vs Slip curves

Figure 5. 35 - S-2: Load, bar's Slip and bar's Strain vs Logging Time

Figure 5. 36 - Patches monitored through DIC (S-2 beam)

Figure 5. 37 - Generic step of DIC (S-2 beam)

Figure 5. 38 - Patches monitored through DIC. Failure stage (S-2 beam)

Figure 5. 39 - Final step of DIC (S-2 beam in failure stage)

Figure 5. 40 - S-2: Load and Strain vs Logging Time

Figure 5. 41 - S-2: Strain distribution along the height of the beam

Figure 5. 42 - S-2: Load vs Slip curves. Comparison between S-1 and S-2

Figure 5. 43 - S-2: Load vs CFRP bar's strain. Comparison between S-1 and S-2

Figure 5. 44 - S-3: Load vs Displacement curves. Comparison between LP100 and DIC

Figure 5. 45 - Strengthened beams: Load vs Displacement curves. Comparison between experimental and predicted results.

Figure 5. 46 – GloH-SL-1: Temperature versus Time curves

Figure 5. 47 – GloH-SL-1 after 90 min of heating exposure: a) front side; b) Bottom side

Figure 5. 48 – GloH-SL-1: Midspan deflection versus time

Figure 5. 49 – Deflection of GloH-SL-1 after 90 min of heating exposure: a) Front side; b) Isometric view

Figure 5. 50 – Temperature vs time of fire exposure curves. Comparison between GloH-SL-1 and GloH-SL-2

Figure 5. 51 – Midspan displacement vs time of fire exposure curves. Comparison between GloH-SL and UN-S\_GloH-SL

Figure 5. 52 – Loch-SL-1: Temperature versus Time curves

Figure 5. 53 – Loch-SL-1: Midspan displacement vs Time curves

Figure 5. 54 – Loch-SL-1. Bar's Slip: a) RHS and LHS Slip vs Time curves; b) RHS Slip vs Temperature

Figure 5. 55 – Loch-SL-1. Load, CFRP strain, Slip versus Time

Figure 5. 56 – Temperature vs time curves. Comparison between Loch-SL-1 and Loch-SL-2

Figure 5. 57 – Slip versus Temperature. Comparison between Loch-SL-1 and Loch-SL-2.

Figure 5. 58 – Midspan deflection versus Temperature. Comparison between Loch-SL-1 and Loch-SL-2.

Figure 5. 59 –Loch-SL-1 after 90 min of heating

Figure 5. 60 –Loch-SL-2 after 90 min of heating

Figure 5. 61 – Loch-HL-1. Slip versus Temperature curves

Figure 5. 62 – Loch-HL-1 after failure: a) Bottom side of the beam; b) Front side of the beam

Figure 5. 63 –Slip versus Temperature curves. Loch-HL-1 vs Loch-HL-2

Figure 5. 64 – Load versus Midspan displacement. Comparison between UN-S\_GloH-SL\_residual and UN-S\_i.

Figure 5. 65 – Load versus Midspan displacement. Comparison between GloH-SL-i\_residual and UN-S\_i.

Figure 5. 66 – GloH-SL-1\_residual after the residual test: a) Front side; b) Bottom side

Figure 5. 67 – Load versus Midspan displacement. Comparison between Loch-SL-1\_residual and S-i.

Figure 5. 68 – Loch-SL-1\_residual after the residual test

Figure 5. 69 – Midspan displacement versus Time of heating curves. Comparison between high temperature tests.

Figure 6. 1 – CFRP's Specific heat and Specific weight versus temperature

Figure 6. 2 – 2D FEM of NSM FRP strengthened RC beam subjected to the experimental soffit temperature: a) cross-sectional FEM; b) FEM of the longitudinal section

Figure 6. 3 – 2D cross-sectional FEM of NSM FRP strengthened RC beam subjected to ISO834 at beam's soffit

Figure 6. 4 – 2D FEM of NSM FRP strengthened RC beam: location of the monitored nodes

Figure 6. 5 – Temperature vs time curves. Numerical-experimental comparison

Figure 6. 6 – Thermocouples' position along the CFRP bar

Figure 6. 7 – Temperature vs time curves. Numerical prediction of heat transfer from exposed to unexposed zone

Figure 6. 8 – Temperature vs time curves. Numerical prediction (ISO834)

Figure 6. 9 – CFRP tensile strength reduction curve (Bisby et al, 2005)

Figure 6. 10 – 2D cross-sectional FEM of NSM FRP strengthened 300x500 RC beam subjected to ISO834

Figure 6. 11 – Temperature vs time curves. Numerical prediction in case of ISO834 standard fire exposure (NSM FRP strengthened 300x500 RC beam)

Figure 6. 12 – Bending moment resistance versus time of standard fire exposure

Figure 6. 13 – Bending moment resistance versus time of standard fire exposure (un-strengthened beam)

Figure I. 1 - SC CFRP-1-15: storage modulus  $E'$ , loss modulus  $E''$  loss factor  $\tan \delta$  vs temperature

Figure I. 2 - SC CFRP-2-15: storage modulus  $E'$ , loss modulus  $E''$  loss factor  $\tan \delta$  vs temperature

Figure I. 3 - SC CFRP-3-15: storage modulus  $E'$ , loss modulus  $E''$  loss factor  $\tan \delta$  vs temperature

Figure I. 4 - TPB CFRP-1-40: storage modulus  $E'$ , loss modulus  $E''$  loss factor  $\tan \delta$  vs temperature

Figure I. 5 - TPB CFRP-2-40: storage modulus  $E'$ , loss modulus  $E''$  loss factor  $\tan \delta$  vs temperature

Figure I. 6 - TPB CFRP-3-40: storage modulus  $E'$ , loss modulus  $E''$  loss factor  $\tan \delta$  vs temperature

Figure I. 7 - SC CFRP-1-15: Normalized storage modulus vs Temperature. Definition of  $T_g$  offset

Figure I. 8 - SC CFRP-2-15: Normalized storage modulus vs Temperature. Definition of  $T_g$  offset

Figure I. 9 - SC CFRP-3-15: Normalized storage modulus vs Temperature. Definition of  $T_g$  offset

Figure I. 10 - TPB CFRP-1-40: Normalized storage modulus vs Temperature. Definition of  $T_g$  offset

Figure I. 11 - TPB CFRP-2-40: Normalized storage modulus vs Temperature. Definition of  $T_g$  offset

Figure I. 12 - TPB CFRP-3-40: Normalized storage modulus vs Temperature. Definition of  $T_g$  offset

Figure I. 13 - SC CFRP-1-15: Normalized storage modulus vs Temperature. Definition of  $T_g$  onset

Figure I. 14 - SC CFRP-2-15: Normalized storage modulus vs Temperature. Definition of  $T_g$  onset

Figure I. 15 - SC CFRP-3-15: Normalized storage modulus vs Temperature. Definition of  $T_g$  onset

Figure I. 16 - TPB CFRP-1-40: Normalized storage modulus vs Temperature. Definition of  $T_g$  onset

Figure I. 17 - TPB CFRP-2-40: Normalized storage modulus vs Temperature. Definition of  $T_g$  onset

Figure I. 18 - TPB CFRP-3-40: Normalized storage modulus vs Temperature. Definition of  $T_g$  onset

Figure I. 19 - SC CFRP-1-15: First derivative of  $E/E(70^\circ\text{C})$  vs Temperature. Definition of  $T_g$  midpoint

Figure I. 20 - SC CFRP-2-15: First derivative of  $E/E(70^\circ\text{C})$  vs Temperature. Definition of  $T_g$  midpoint

Figure I. 21 - SC CFRP-3-15: First derivative of  $E/E(70^\circ\text{C})$  vs Temperature. Definition of  $T_g$  midpoint

Figure I. 22 - TPB CFRP-1-40: First derivative of  $E/E(70^\circ\text{C})$  vs Temperature. Definition of  $T_g$  midpoint

Figure I. 23 - TPB CFRP-2-40: First derivative of  $E/E(70^\circ\text{C})$  vs Temperature. Definition of  $T_g$  midpoint

Figure I. 24 - TPB CFRP-3-40: First derivative of  $E/E(70^\circ\text{C})$  vs Temperature. Definition of  $T_g$  midpoint

Figure I. 25 - CFRP-N2-A: Weight loss vs Temperature. Definition of  $T_d$  offset

Figure I. 26 - CFRP-N2-B: Weight loss vs Temperature. Definition of  $T_d$  offset

Figure I. 27 - CFRP-N2-C: Weight loss vs Temperature. Definition of  $T_d$  offset  
Figure I. 28 - CFRP-Air-A: Weight loss vs Temperature. Definition of  $T_d$  offset  
Figure I. 29 - CFRP-Air-B: Weight loss vs Temperature. Definition of  $T_d$  offset  
Figure I. 30 - CFRP-Air-C: Weight loss vs Temperature. Definition of  $T_d$  offset  
Figure I. 31 - CFRP-N2-A: Weight loss vs Temperature. Definition of  $T_d$  onset  
Figure I. 32 - CFRP-N2-B: Weight loss vs Temperature. Definition of  $T_d$  onset  
Figure I. 33 - CFRP-N2-C: Weight loss vs Temperature. Definition of  $T_d$  onset  
Figure I. 34 - CFRP-Air-A: Weight loss vs Temperature. Definition of  $T_d$  onset  
Figure I. 35 - CFRP-Air-B: Weight loss vs Temperature. Definition of  $T_d$  onset  
Figure I. 36 - CFRP-Air-C: Weight loss vs Temperature. Definition of  $T_d$  onset  
Figure I. 37 - CFRP-N2-A: DTG curve. Definition of  $T_d$  midpoint  
Figure I. 38 - CFRP-N2-B: DTG curve. Definition of  $T_d$  midpoint  
Figure I. 39 - CFRP-N2-C: DTG curve. Definition of  $T_d$  midpoint  
Figure I. 40 - CFRP-Air-A: DTG curve. Definition of  $T_d$  midpoint  
Figure I. 41 - CFRP-Air-B: DTG curve. Definition of  $T_d$  midpoint  
Figure I. 42 - CFRP-Air-C: DTG curve. Definition of  $T_d$  midpoint

## LIST OF TABLES

- Table 2. 1 – Thermal behaviour of cement pastes and mortar (Chung, 2001)
- Table 2. 2 – Mechanics of Resins (ISIS Canada, 2005-2014)
- Table 2. 3 – Mechanics of Fibres (ISIS Canada, 2005-2014)
- Table 3. 1 - Specimens' geometry (SC)
- Table 3. 2 - Specimens' geometry (TPB)
- Table 3. 3 -  $T_g$  (max tan  $\delta$ ). Average ( $\mu$ ) and standard deviation ( $\sigma$ ).
- Table 3. 4 -  $T_g$  offset. Average ( $\mu$ ) and standard deviation ( $\sigma$ ) of test results
- Table 3. 5 -  $T_g$  onset. Average ( $\mu$ ) and standard deviation ( $\sigma$ ) of test results
- Table 3. 6 -  $T_g$ \_midpoint. Average ( $\mu$ ) and standard deviation ( $\sigma$ ) of test results
- Table 3. 7 - Specimens' initial weight and tests' settings TGA
- Table 3. 8.  $T_d$  offset. Average ( $\mu$ ) and standard deviation ( $\sigma$ ) of test results
- Table 3. 9 -  $T_d$  onset. Average ( $\mu$ ) and standard deviation ( $\sigma$ ) of test results
- Table 3. 10 -  $T_d$  midpoint. Average ( $\mu$ ) and standard deviation ( $\sigma$ ) of test results
- Table 3. 11 - CFRP Thermal conductivity. Test results
- Table 3. 12 - Concrete batch
- Table 3. 13 - Compression test results (28 days)
- Table 3. 14 - Tension test results (28 days)
- Table 3. 15 - Compression test results (76 days)
- Table 4. 1 – Pull-out experimental program
- Table 4. 2 – Geometrical and mechanical properties of the NSM strengthening system
- Table 4. 3 - Concrete batch for prisms manufacturing
- Table 4. 4 - Compression test results (28 days, 63 days)
- Table 4. 5 – Summary of the main experimental results
- Table 5. 1 - Experimental program
- Table 5. 2 - Materials' mechanical properties
- Table 5. 3 - Summary of the ambient temperature test results
- Table 6. 1 – Thermal properties of cementitious mortar
- Table 6. 2 – Transversal and Longitudinal thermal conductivities of CFRP
- Table 6. 3 – Mechanical properties of materials at ambient temperature
- Table I. 1 -  $T_g$  (max tan $\delta$ ). Average ( $\mu$ ) and standard deviation ( $\sigma$ ) of test results
- Table I. 2 -  $T_g$  offset. Average ( $\mu$ ) and standard deviation ( $\sigma$ ) of test results
- Table I. 3 -  $T_g$  onset. Average ( $\mu$ ) and standard deviation ( $\sigma$ ) of test results
- Table I. 4 -  $T_g$  midpoint. Average ( $\mu$ ) and standard deviation ( $\sigma$ ) of test results
- Table I. 5 -  $T_d$  offset. Average ( $\mu$ ) and standard deviation ( $\sigma$ ) of test results
- Table I. 6 -  $T_d$  onset. Average ( $\mu$ ) and standard deviation ( $\sigma$ ) of test results
- Table I. 7 -  $T_d$  midpoint. Average ( $\mu$ ) and standard deviation ( $\sigma$ ) of test results

## **ACKNOWLEDGEMENTS**

I would never thought to do a PhD and now I'm going to say THANKS to Professor E. Nigro, who realized that this path could be the right direction for me. I don't know if I have been a good researcher, but I'm sure to have done all my best to satisfy his expectations. On my way, I met many people, very good colleagues, who became good friends. Dr. A. Bilotta, Antonio for friends :-), was one of them, who gave me always useful advices for my research and for practical things of life. I will never forget it.

I have to say THANKS also for several opportunities that I had during the last three years, which led me around the world for conferences and meeting, where my supervisor let me speak to important audiences.

The most fruitful travel, led me in Edinburgh, where I met Professor L. Bisby. He has been another important reference for my academic path and enabled to develop a part of my research program at Edinburgh University.

Thanks to Prof. T. Stratford, manager of the Engineering Structures Lab of Edinburgh University, and to all the technicians, who helped me during experimental tests. Many thanks to all the members of the Fire Group of Edinburgh University that welcomed me in their wonderful family.

I am very thankful for the helping received by Prof. Andrea Prota, manager of Materials and Structures Lab “Adriano Galli” of University of Naples, and by all the technicians. A special acknowledgement to Engg. E. Scaiella and G. Campanella.

Many thanks to *Milliken & Company* and *MAPEI* for providing materials.

At the end of this experience, I realized that, wherever I will be in the future, I will never forget my room-mates, those crazy guys. Antonio B., Marco G. d’A., Stefano, Paolino, Andrea, Ciro, Antonio S., Costantino, Fernando, Marco M., thank you so much for the laughs and the special moments spent together. Thanks for having tolerated me. Thanks God for giving me the patience to tolerate them!!!

Many thanks to my historical colleagues, Anna, Mimmo, Giuseppe, Romeo, for the successful job done together.

I cannot conclude my acknowledgements, without thanking my parents, especially my mother and my grandmother, who always tolerated my nervousness in stressful periods (very frequent in the last three years).

Many many thanks to my best friends, Annamaria, Clelia, Fiorella, for the prayers and encouragements, when I thought that I would fail.

At the end, I would like to spend few words to say thanks to the man, who gave important meaning to my life. Angelo, thank you so much, for tolerating those weekends (so many) that I spent working or abroad. You know how it is hard for me saying “I Love you”, but today I don’t want to feel embarrassment and I would like that everyone knows: *Hope to live this dream forever.*

*Iolanda Del Prete*

## **RINGRAZIAMENTI**

Non avrei mai pensato di fare un Dottorato di Ricerca e oggi mi ritrovo a dire GRAZIE al Prof. E. Nigro, il quale si è accorto che questo percorso potesse essere per me la giusta direzione. Non so se sono stata una buona ricercatrice, ma sono sicura di aver fatto il mio meglio per soddisfare le sue aspettative.

Lungo il mio percorso ho incontrato molte persone, ottimi colleghi, che sono diventati buoni amici. Il Dr. A. Bilotta, Antonio per gli amici, è uno di quelli che mi ha sempre dato ottimi consigli per la mia ricerca e per le cose pratiche della vita. Non lo dimenticherò mai.

Devo dire grazie anche per le molteplici opportunità che mi sono state date negli ultimi 3 anni, che mi hanno condotto in giro per il mondo per conferenze e meeting, dove il mio tutor mi ha concesso di parlare a un pubblico importante. Uno dei viaggi più significativi mi ha portato a Edimburgo, dove ho conosciuto il Prof. L. Bisby. Lui è stato un altro importante punto di riferimento per il mio percorso accademico e mi ha permesso di sviluppare parte della mia ricerca all'Università di Edimburgo. Grazie al Prof. T. Stratford, manager del laboratorio di Ingegneria Strutturale dell'Università di Edimburgo, e a tutti i tecnici, che mi hanno aiutato durante la sperimentazione.

Grazie mille a tutti i membri del Fire Group dell'Università di Edimburgo, che mi hanno accolto nella loro meravigliosa famiglia.

Sono davvero riconoscente per l'aiuto datomi dal Prof. Prof. Andrea Prota, manager del laboratorio di Materiali e Strutture "Adriano Galli" dell'Università di Napoli, e da tutti i tecnici. Uno speciale ringraziamento va agli ingg. E. Scaiella e G. Campanella.

Grazie mille a *Milliken & Company* e *MAPEI* che hanno fornito i materiali.

Alla fine di questa esperienza, mi sono accorta che, dovunque sarò nel mio future, non dimenticherò mai i miei compagni di stanza, quei pazzi ragazzi. Antonio B., Marco G., Stefano, Paolino, Andrea, Ciro, Antonio S., Costantino, Fernando, Marco M., grazie mille per le risate e gli splendidi momenti trascorsi insieme. Grazie per avermi sopportato. Grazie Dio per avermi dato la pazienza di sopportare loro!!!

Grazie mille ai miei storici colleghi, Anna, Mimmo, Giuseppe, Romeo, per i risultati raggiunti insieme.

Non posso concludere senza ringraziare la mia famiglia, specialmente mia madre e mia nonna per aver sopportato il mio nervosismo nei momenti più stressanti (molto frequenti negli ultimi tre anni).

Mille mille grazie alle mie migliori amiche, Annamaria, Clelia, Fiorella, per le preghiere e gli incoraggiamenti, quando pensavo che avrei fallito.

Alla fine, vorrei spendere un paio di parole per dire grazie all'uomo, che ha dato un importante significato alla mia vita. Angelo, grazie mille, per aver tollerato quei weekend (troppi) in cui ho lavorato o sono stata all'estero. Tu sai quanto sia difficile per me dire "Ti Amo", ma oggi non voglio sentirmi imbarazzata e voglio che tutti sappiano: *Spero di vivere questo sogno per sempre.*

*Iolanda Del Prete*

*Acknowledgements*

To my nephews:  
Today my dream came true.  
I wish you courage to pursue your dreams

Ai miei nipoti:  
Oggi il mio sogno si è avverato.  
Vi auguro il coraggio di perseguire i vostri.



## ***Chapter 1 - Introduction***

The aging of the built heritage and infrastructures throughout the civil and industrialized world, as well as their deterioration due to environmental effects, and/or changing in service demand, lead to increasing interest in novel techniques aimed to design, maintain and rehabilitate concrete structures.

Among the available strengthening techniques for improving the performance of concrete structures, the strengthening with Fibre Reinforced Polymers (FRP) gained huge and fast popularity during the last twenty years in the field of civil engineering. Their increasing popularity is mainly related to their attractive properties, such as: light-weight; excellent durability properties; electro-magnetic permeability; corrosion resistance; high versatility since a wide range of product's shapes and dimension is available; ease and speed of application. Therefore, these materials experienced a recognition as effective and efficient materials, even if the composite products are relatively expensive, in comparison with the traditional materials for structural strengthening, such as concrete and steel. Actually, the spread of FRPs for civil infrastructure applications led to a decrease of the FRP costs.

The FRP products widely used to repair/strengthen structures are bars, plates, sheets and wraps. They are obtained combining two materials, usually high strength fibres and polymeric or cementitious matrix, forming a new useful product with enhanced properties, which are usually superior to those of the individual constituents. The high strength fibres sustain loads while the matrix transfers the loads to the fibres, also protecting them from environmental and mechanical damage. Similarly, in the FRP strengthened RC members, the strengthening system is made of an FRP product and a bonding agent, which transfers the load from the RC member to the strengthening material. In civil engineering application the most commonly used bonding agents are polymeric resins, even if cementitious adhesive are experiencing widely spread in this field,

since their lower costs and their better behaviour in not ordinary condition, such as in fire, in comparison with resins.

In the field of external strengthening of RC members using bonded FRP sheets or strips with an adhesive, the most popular technique is the Externally Bonded Reinforcement (EBR) that have several practical limitations both in ordinary and not ordinary conditions. Based on several experimental studies, EBR is often unable to provide the full tensile strength of the FRP product due to the failure in the bond region, which occurs prior to the designed or predicted capacity of the strengthened member. Moreover, being applied at the outer surface of RC members, EBR is directly exposed to environmental effects, fire, and vandalism. EBR may also result uneconomical due to limiting values of strain, imposed by several design procedures.

The alternative strengthening technique that experienced a widespread in the recent years is the Near Surface Mounted (NSM) strengthening system, in which the FRP is placed into the groove, cut into the surface of structural members, and bonded through an adhesive (epoxy resin or cement mortar). Several studies demonstrated that NSM with epoxy adhesive exhibits a better bond behaviour than EBR. Moreover, NSM is less prone to external attack, since the FRP is completely embedded in the adhesive. Despite that, the effectiveness of epoxy adhesive may be affected by high temperature, whereas cementitious adhesive may offer better performance than epoxies, keeping low the temperature in the FRP.

Objectively, the available literature about the behaviour of NSM FRP strengthened RC members is still limited, if compared to that available for EBR strengthening technique. Even worse is the knowledge about NSM with cementitious adhesive in not ordinary condition (fire). For this reason, very limited indications are available in the current codes for designing and predicting the capacity of the NSM strengthened members.

## 1.1 RESEARCH SIGNIFICANCE

At date, the performance of NSM strengthened RC members with cementitious adhesive both at ambient and at high temperature has not yet been significantly studied through research, aside from a limited number of available studies (see also Chapter 2). NSM FRP strengthening is potentially less prone to damage due to fire exposure than EBR FRP, also without costly insulation systems, provided that: (a) an FRP strengthening material with high glass transition temperature ( $T_g$ ) and decomposition temperature ( $T_d$ ); and (b) a

bonding agent with low thermal conductivity and good thermal stability, are used. FRP-NSM systems with cementitious adhesives may perform better at high temperatures because: (a) cementitious grout is not as severely affected as typical epoxies by elevated temperature; (b) the cementitious grout can provide additional thermal protection to the FRP bars; and (c) the resin of the FRP bar, when the bar is manufactured by pultrusion, typically has a  $T_g$  higher than common in-situ cured epoxy resins used in wet lay-up FRP strengthening applications.

Keeping that in mind, the thesis shows a research project undertaken on a high  $T_g$  FRP strengthening system bonded in a groove (NSM) with cementitious matrix, aimed to define its response at ambient and at elevated temperature.

Dynamic Mechanic Analysis (DMA) and Thermogravimetric Analysis (TGA) on the novel, high  $T_g$  commercial CFRP were conducted. Thermal conductivity tests were also performed on the CFRP and on the cementitious grout, to verify their thermal conductivities ( $\lambda$ ).

In order to investigate the behaviour of the CFRP NSM strengthening system bonded in cementitious agent, a series of bond tests were performed. The performance of this strengthening system were compared with those obtained with epoxy bonding agent. All the tests were carried out with the same CFRP bar, by varying the following parameters: the bonding length; the dimension of the square groove; the position of the bar inside the groove; the bonding agent.

The results of the tests mentioned above were very useful to interpretate the results of a series of tests on small-scale NSM FRP strengthened reinforced concrete beams, which were performed at both ambient and elevated temperature, considering two heating configurations (local and global heating). The thermo-structural response was investigated under sustained loads typical of maximum permissible service strain conditions in the FRP. Internal temperatures, beam displacements and slip of the FRP strengthening were measured, and strain gauges were applied for measuring the FRP bar strains; Digital Image Correlation (DIC) was also used to study strain distributions and beam displacements. All the results were correlated with DMA and TGA tests results in order to better explain the failure modes of the strengthened beams.

The main objectives of these tests are listed below:

- evaluation of the flexural resistance of un-strengthened beams at ambient temperature (reference specimens);
- evaluation of the flexural resistance of the strengthened beams at ambient temperature, in order to define the gain in flexural resistance obtained through the strengthening system;

- evaluation of the effectiveness of the strengthening system at elevated temperature with different heating configurations (local and global heating).

Note that the tests comprising this experimental program were executed using propane-fired radiant panels to heat the beams, rather than a standard fire-testing furnace. The radiant panels are very useful to simulate localised fire event, but they are also able to simulate global heating configurations, if an array of radiant panels is used. Obviously, the results of non-standard experimental tests cannot be used to define a standard time of fire resistance of the structural members, since the heating history can be significantly different to that provided by standard fire curve (e.g., ISO834) in terms of speed of temperature increasing, maximum temperature, duration of the heating stage. Therefore, in order to generalize the experimental results obtained through non-standard fire tests, and provide a reliable time of standard fire exposure that may be critical for the NSM FRP strengthened RC beams, thermal numerical analyses were conducted. A two dimension (2D) Finite Element Model (FEM) of the strengthened beam, subjected to the heating history recorded during the tests, was analysed and the results were compared with the temperatures recorded during the tests, in order to assess the reliability of the FEM simulating the experimental results. Thereafter, the 2D FEM was analysed in case of standard fire exposure to define a standard time, which may be critical for the effectiveness of the strengthening both in case of local and global heating.

Finally, a thermo-mechanical analysis of a full-scale NSM FRP strengthened RC beam was conducted in order to determine useful fire safety design criteria for this investigated structural typology.

## 1.2 OUTLINE OF THE THESIS

Chapter 2 presents a review of available literature on the behaviour of both NSM and EBR flexural strengthening applications for reinforced concrete members. Firstly, an overview of the main thermal and mechanical properties of the commercial FRPs and adhesives is shown. Then, the most recent experimental activities conducted on EBR and NSM, both at ambient and high temperature are summarized. Finally, the available international and national codes and guidelines are cited.

Chapter 3 provides information about the techniques commonly used to assess the main thermal and mechanical properties of structural materials. Particularly, the section 3.1 summarizes the most common techniques for measuring the thermal properties, such as  $T_g$  and  $T_d$  of polymeric materials. Moreover, the

results of the tests, e.g., Dynamic Mechanic Analysis (DMA), Thermogravimetric Analysis (TGA) and Differential Scanning Calorimetry (DSC), conducted on a novel commercial CFRP bar are shown. In addition, the results of thermal conductivity tests of CFRP and cementitious grout are discussed. The section 3.2 summarizes the results of the tests conducted for defining the mechanical properties of the concrete, the steel bars, the cementitious grout and the CFRP bar, used to manufacture the above-mentioned beams.

The Chapter 4 summarizes the results of the bond pull-out tests conducted on the new commercial cementitious-bonded CFRP NSM strengthening system, by varying the bond affecting parameters. Moreover, a comparison between the performances of this strengthening system and the performances of a resin-bonded CFRP NSM strengthening system is also shown.

The Chapter 5 shows the design of the un-strengthened and strengthened beams with a prediction of their flexural capacity by means of cross sectional analyses. Moreover, a photographic report of the manufacturing and strengthening stages, the test setup and of the instrumentation of the beams is also shown. Particular attention is dedicated to the Digital Image Correlation (DIC), nowadays considered as innovative and powerful technique for displacements and strains measuring. Finally, the results of the tests of NSM FRP strengthened reinforced concrete beams, performed at both ambient and elevated temperature, by varying also the heating configuration, are discussed.

The Chapter 6 shows a detailed description of the finite element models implemented in SAFIR 2011 for the thermal analysis of the tested NSM FRP strengthened RC beams, subjected to both the non-standard heating history recorded during the experimental tests and to the standard fire curve ISO834. The results of the thermal analyses, compared with the experimental results, are also provided and discussed. Finally, useful fire safety design criteria of NSM FRP strengthened RC beams are provided, based on the results of thermo-mechanical analysis, conducted on this structural typology.

## ***Chapter 2 - Literature review***

Fiber Reinforced Polymers (FRP) are nowadays widely applied at the outer surface of a broad range of reinforced concrete (RC) structural members, such as beam, columns, slabs, to repair or strengthen structures. The widespread of these materials inspired the researchers all around the world to study the own physical nature of the materials constituent FRP, and particular issues deriving from the combination of different materials, as occurs when a reinforced concrete (RC) member is strengthened with FRPs.

This chapter provides, firstly, an overview of the main thermal and mechanical properties of the FRPs, then, the two most common flexural strengthening techniques for RC members, such as Near Surface Mounted (NSM) and External Bonded Reinforcement (EBR), are presented, highlighting advantages and the disadvantages by means of the conducted literature review. It also enabled to assess the most likely failure modes of both NSM and EBR FRP strengthened RC members, both in ordinary condition and at high temperature. As widely known, in fact, high temperature represent a very critical issue for FRPs, especially if they are directly exposed to fire or other environmental conditions, which lead to thermal states different from the normal, as may occur in EBR FRP strengthened RC members.

### **2.1 AN OVERVIEW OF THE FRP PROPERTIES**

FRPs are obtained combining two materials, usually high strength fibres and matrix, chemically and thermally compatible, forming a new useful product with enhanced properties, which are usually superior to those of the individual constituents.

The matrices have several critical functions, such as: bind the fibres together and wet-out the fibres; protect the fibres from physical (environment) and

mechanical (abrasion) attacks; separate the fibres in the composite; transfer the force between the fibres. The mechanical properties of the matrix are definitely lower than those of the fibres, but as previously said, their combination provide a very efficient material, in terms of strength and durability.

The matrices can be polymeric or cementitious. The latter was more recently introduced in the field of composite materials than the polymeric one. The inorganic cementitious matrix is made of an hydraulic binder pozzolanas based and admixtures, which provide the enhancement of physical and mechanical properties different from those typical of organic polymeric matrix. The Table 2. 1 provides useful data about the thermal behaviour of cement pastes and mortars (Chung, 2001). Cement paste and mortar strength can be affected by several factors, such as: water-cement ratio, cement-fine aggregate ratio, type and grading of fine aggregate, manner of mixing and molding specimens, curing conditions, size and shape of specimen, moisture content at time of test, loading conditions and age (Mindess and Young, 1981).

Chung, 2001 also stats that the cement-matrix composites are not only thermally attractive, but they enhance high structural performance by carbon fibres addition. They increase the tensile strength, the tensile ductility, the impact resistance; moreover, they reduce the drying shrinkage and improve freeze-thaw durability. The tensile and flexural strength decrease with increasing specimen size and this effect is larger as the fibres length increases.

Table 2. 1 – Thermal behaviour of cement pastes and mortar (Chung, 2001)

<b>Material</b>	<b>Specific weight (<math>kg/m^3</math>)</b>	<b>Specific heat (J/gK)</b>	<b>Thermal diffusivity (<math>mm^2/s</math>)</b>	<b>Thermal conductivity (<math>W/mK</math>)</b>
Cement paste without silica flume	2010	0.736	0.36	0.53
Cement paste with silica flume	1730	0.788	0.24	0.33
Mortar without silica flume	2040	0.642	0.44	0.58
Mortar with silica flume	2200	0.705	0.58	0.54

The polymeric matrices are organic compounds comprised of long-chain molecules, which consists of smaller repeated units called monomers. These matrices can be made of thermoplastics (polyethylene, polyamide) or thermo-setting polymers (epoxy, vinylester, polyester). The most commonly used matrix in structural applications is the epoxy resin, which irreversible cures through heat induction. The Table 2. 2 summarizes the main physical and mechanical properties of the commonly used resins, collected by ISIS Canada (2005-2014).

Table 2. 2 highlights that all the polymers have a specific weight significantly lower than cementitious pastes and mortars. Moreover, their Coefficient of Thermal Expansion (CTE) is significantly higher than that of hardened cement pastes, which typical values are about  $15\text{-}20 \cdot 10^{-6}/^{\circ}\text{C}$  (Shui et al, 2010), and of mortars, which typical values are about  $8\text{-}13 \cdot 10^{-6}/^{\circ}\text{C}$  (Lamond & Pielert, 2006).

Table 2. 2 – Mechanics of Resins (ISIS Canada, 2005-2014)

Material	Specific weight ( $\text{kg}/\text{m}^3$ )	Ultimate strength (MPa)	Modulus of Elasticity (GPa)	CTE ( $10^{-6}/^{\circ}\text{C}$ )
Polyester	1280	45-90	2.5-4.0	100-110
Vinylester	1070	90	4.0	80
Epoxy	1030	90-110	3.5-7.0	45-65
Phenolic	1500-1750	45-59	5.5-8.3	30-45

The resins are good insulators, as well as cement pastes and mortars, since their thermal conductivity is very low, but all polymers are not very stable materials, since they soften and/or decompose at high temperature. Particularly, for thermosetting polymers, the softening occurs at the achievement of the Glass Transition Temperature ( $T_g$ ), whereas the decomposition occurs at the achievement of the Decomposition Temperature ( $T_d$ ), which is usually greater than  $T_g$  (see section 3.1).

The fibres have the critical function of providing the strength and the stiffness of FRP. A high length to diameter ratio usually characterizes the fibres ( $\frac{l}{d} > 1000$ ). The long fibres are usually aligned and wet-out of resin, in order to form bars, plates and sheets. Short fibres are also available and they are randomly inserted in composite products.

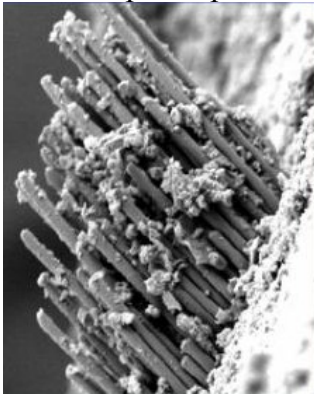
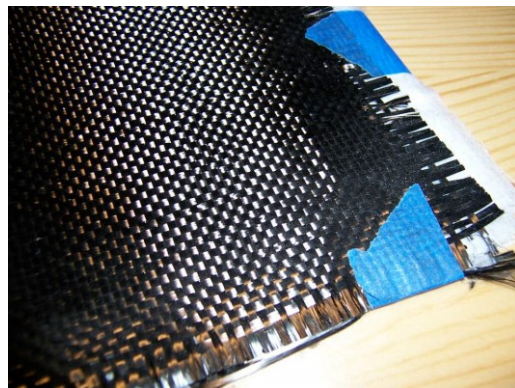
Figure 2. 1 – Unidirectional composite:  
Fibres embedded in matrix

Figure 2. 2 – Multidirectional fibres



The most commonly used fibres in civil applications are: glass, carbon, aramid and basalt. Glass fibres are the cheapest one and, thus, they are the most widely used. Carbon fibres are also very common, since they exhibit the best mechanical performance and durability. Table 2. 3 summarizes the main mechanical properties and Figure 2. 3 shows a comparison between the stress-strain relationships of of the most common commercial fibres used in composite materials. Composites with unidirectional fibres (Figure 2. 1) are very versatile and they are characterized by high values of stiffness and strength, rather than the multi-directional composites (Figure 2. 2), which can be affected by local failure due to manufacturing defects.

Table 2. 3 – Mechanics of Fibres (ISIS Canada, 2005-2014)

<b>Material</b>	<b>Fibre</b>	<b>Ultimate strength (MPa)</b>	<b>Modulus of Elasticity (GPa)</b>	<b>Ultimate strain %</b>
Glass	E	2400	72.4	3.5
	AR	3030	72.4	3.5
	S	4600	88.0	5.7
Aramid	49	2760	125	2.4
	29	2750	83	4.0
Carbon	IM	5200	300	1.73
	HM	3500	400	0.88
	HS	5020	260	2.00

Actually, the most important parameter for FRP products is not the tensile strength, since their maximum strength is very hard to achieve under the usual service loads, whereas as higher is the elastic modulus as effective is the strengthening intervention. Therefore, in the strengthening applications, the strengthening material should have similar or higher stiffness than the strengthened member. Figure 2. 4 provides the Young Modulus of the most common structural materials, showing that the stiffness of most FRP composite systems are considerably less than that of structural steel, but similar or higher than concrete. This makes FRP strengthened RC members mechanically advantageous.

FRPs are anisotropic materials, which properties depend on mechanical properties of the matrix, the mechanical properties of fibres, the fibre volume fraction, the fibre cross sectional area, the fibre orientation in the matrix, fibre/matrix interaction, the manufacturing method. The anisotropy of the FRPs mainly affects the shear strength of this product and their bond performance.

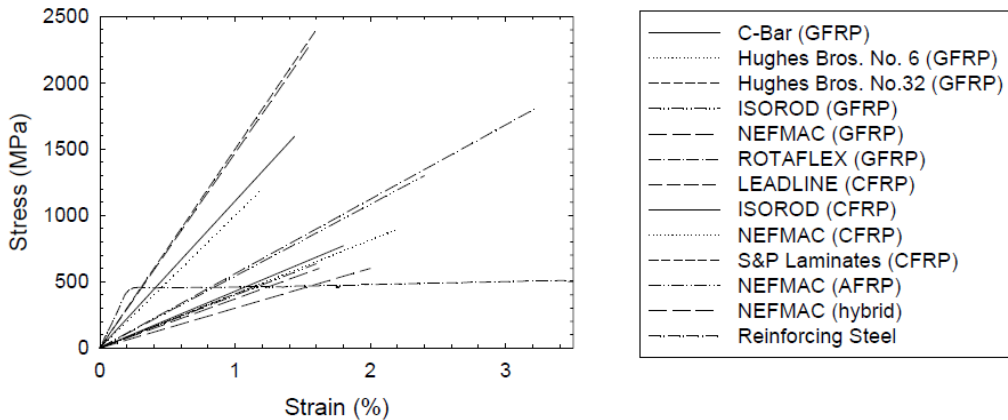


Figure 2. 3 – Fibre comparison (no matrix): Stress-Strain (Kodur at al, 2005)

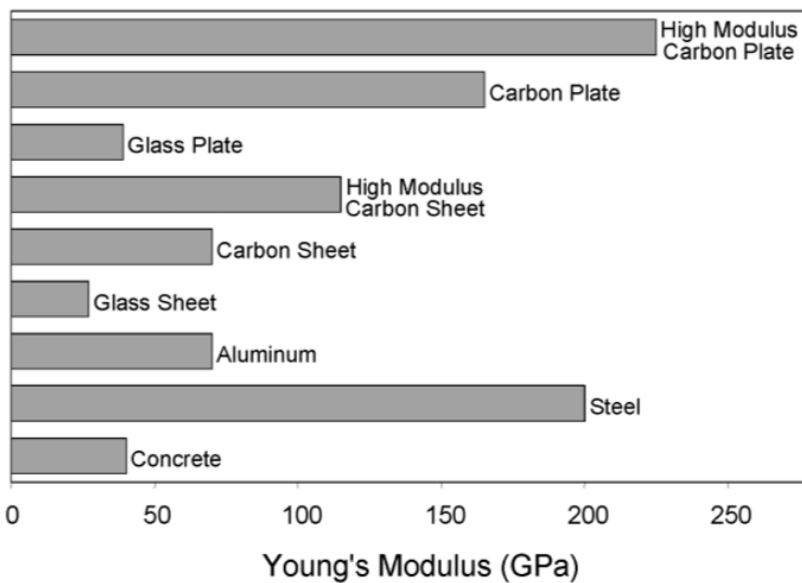


Figure 2. 4 – Young modulus of structural materials (Buyukozturk et al, 2004)

## 2.2 FRP FLEXURAL STRENGTHENING TECHNIQUES FOR CONCRETE MEMBERS

In the last 20 years, FRPs have experienced an increasing interest in the field of RC strengthening techniques, alternatively to that traditionally realized with concrete and steel. The great potential of FRPs in strengthening/repairing RC members is exploited through two main techniques: Externally Bonded Reinforcement - FRP (FRP EBR); Near Surface Mounted - FRP (FRP NSM).

The EBR FRP consists of an FRP product, usually a strip, bonded to the rough concrete surface by means of a structural adhesive that is generally an epoxy resin, which ensure the transfer of forces between concrete and FRP.

The NSM FRP is an emerging technique, which consists of a bar/rod/strip, applied in a groove, cut into the concrete cover of a RC member and bonded in place by filling the groove with a proper bonding agent. Epoxy resins are usually used as bonding agent, even though recently some researchers show their interest in finding out the behaviour of cementitious pastes/mortars bonded NSM FRP (El-Gamal et al, 2012; Petri et al, 2013). Although NSM is still considered an emerging technique, NSM system has been used in Europe for strengthening of RC structures since early fifties, by using steel rebars (Asplund, 1949) instead of FRP.

The rapid increase in the use of FRPs as structural material over the last 20 years, led to the need of design guidelines. Several national and international design guidelines have become available for the design and application of FRP for strengthening or reinforcing concrete structures. The international guidelines currently available are the Japanese JCI\_TC952, the American standard ACI 440.2R-08, the European Model Code 2010 (MC2010). The Italian reference for design of EBR-FRP strengthened structures is the CNR DT-200 R1/2013.

The following sections provide more information about these two strengthening techniques, highlighting the weakest and the strongest points of both.

### ***2.2.1 External Bonded Reinforcement (EBR)***

Externally bonded FRP sheets and strips are currently the most commonly used techniques for flexural strengthening of concrete members.

For EBR FRP systems, as well as for the NSM system, the bond between the FRP and the substrate is the most important property that enables to transfer the stress. The bond of EBR FRP strengthening systems is particularly affected by the substrate status, which should always be taken into account as mandatory and preliminary stage of the FRP placement, since the condition of the original concrete and the concrete substrate can compromise the integrity of the FRP system. Several codes (ACI 440.2R-08, CNR-DT 200 R1/2013) provided useful and general guidelines about the procedures for installing FRP systems. Basically, the check of the substrate status need to be conducted, in order to place the FRP on homogeneous concrete, avoiding the peeling and/or the detachment of the concrete cover. Moreover, the concrete should not have a strength lower

than 15 MPa (CNR-DT 200 R1/2013) and it should not have suffered the carbonation and the steel corrosion. Substrates with cracks wider than 0.3 mm should be pressure injected with epoxy before FRP installation in accordance with ACI 224.1R. Smaller cracks exposed to aggressive environments may require resin injection or sealing to prevent corrosion of existing steel reinforcement. The bond-critical application (flexural and shear strengthening) require a bond adhesive between FRP and concrete. Sandblasting shall provide a roughness degree of at least 0.3 mm, measured using suitable instruments, e.g., a laser profilometer or an optical profile-measuring device (CNR-DT 200 R1/2013). Poor concrete surfaces that do not require remedial work before FRP application, should be treated with a consolidating agent before *primer* application takes place. Cleaning of the concrete surface shall remove any dust, laitance, oil, surface lubricants, foreign particles, or any other bond-inhibiting material.

Based on the experimental results obtained by GangaRao & Vijay (1998), in ACI 440.2R-08, the failure modes of EBR FRP strengthened RC members are classified as in the following (see also Figure 2. 5, Figure 2. 6): concrete crushing before yielding of the reinforcing steel; steel yielding followed by FRP rupture; steel yielding followed by concrete crushing; shear failure if the shear capacity of the beam cannot accommodate the increase in the flexural capacity (Buyukozturk et al, 2004); cover delamination; FRP debonding.

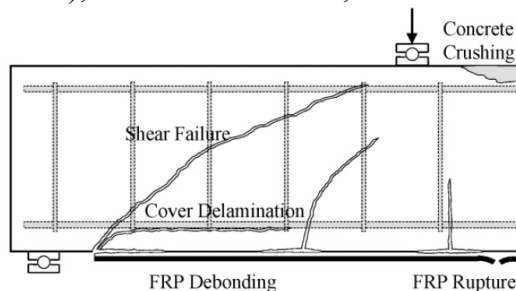


Figure 2. 5 – Failure modes of FRP flexurally strengthened members (Buyukozturk et al, 2004)

Particularly, as shown in fib Bulletin n°14, the debonding process may start from different point, such as: peeling-off in the anchorage zone as a result of bond shear fracture through the concrete; peeling-off caused at flexural cracks; peeling-off caused at shear cracks; peeling-off caused by the unevenness of the concrete surface.

Obviously, the prescription and the statements of the above-mentioned codes are the product of several researches, conducted in many years about the behaviour of EBR FRP flexural strengthened members (Spadea et al, 1998; Chen & Teng 2001; El-Hacha & Rizkalla 2004; Toutanji et al 2006; Enochsson et al,

2007; Castro et al, 2007; Chickh et al, 2013). In the following the conclusions of some studies are summarized.

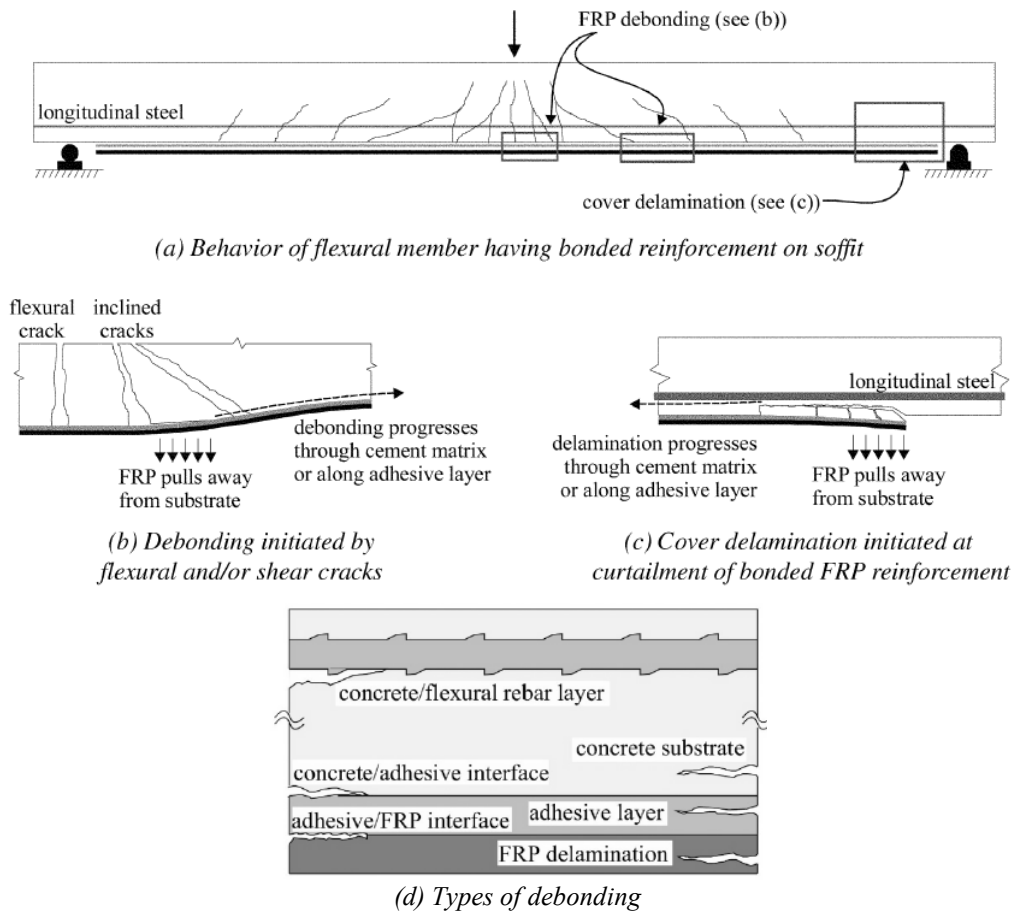


Figure 2. 6 –Debonding and delamination of externally bonded FRP systems: a,b,c) ACI 440.2R-08; d) Buyukozturk et al, 2004

Spadea et al (1998) conducted experimental tests of RC beams strengthened with EBR CFRP sheets, demonstrating that bonding FRP as external reinforcement without consideration about the end-anchorage may result in significant brittle failures due to explosive debonding, which unable to make use of the full potential of the FRP.

Similarly, Chen & Teng (2001), based on existing test data observed that the main failure mode of FRP plates bonded to concrete is concrete failure under shear, which occurs generally at a few millimetres from the concrete-to-adhesive surface. Therefore, the bond strength depends strongly on the concrete strength. Moreover, an effective bond length exists and an extension of this length cannot increase the bond strength.

El-Hacha & Rizkalla (2004) observed that the failure of members strengthened with EBR FRP sheets and strips could be brittle due to debonding and/or peeling of the FRP reinforcements, especially in the zones of high flexural and shear stresses.

Toutanji et al (2006) showed that FRP EBR multi-layer sheets with an epoxy resin is an effective technique for strengthening and repairing reinforced concrete (RC) beams under flexural loads, even if the bond between FRP and concrete may not be strong enough to ensure the rupture of the composite. They observed that due to the flexural cracks formed in the constant moment region as the load increased, the bond between FRP and concrete started to fracture at a certain load level and the failure propagated towards the shear span until most parts of FRP composites detached from the concrete beams.

Since the bond is the most important property for EBR FRP strengthening systems, several meaningful studies were conducted. The most recent experimental researches about this topic were conducted by Bilotta et al (2014), Chickh et al (2013), Martinelli et al (2011), Bilotta et al (2011), Aiello & Leone (2008).

Furthermore, degradation of mechanical properties of EBR FRP (strength, stiffness and bond) due to high temperature (Dai et al., 2013; Nigro et al. 2012), moisture absorption (Jia et. al, 2005), cycling loads (Nigro et al., 2011c; Dai et al., 2005), ultraviolet rays (ACI Committee 440 1996) is a key aspect for a durable efficiency of composite materials. In some cases, insufficient protection against these factors may reduce the service life of the structure (El-Hacha & Rizkalla, 2004).

### ***2.2.2 Near Surface Mounted system (NSM)***

The NSM technique has been widely used in pioneer countries, such as USA and Canada. This technique is nowadays recognized as promising method for increasing flexural strength of RC members, more convenient than using EBR FRP laminates. In fact, NSM FRP strengthening does not require any surface preparation, except the grooving, which can be easily done in one step using suitable tools (see section 5.1.2). Obviously, the choice of high-viscosity bonding agent, such as thixotropic resins, may be helpful during the groove's filling stage, but also fluid products, such as cementitious pastes and mortars, can easily grout the FRP product even for strengthening members in positive moments. The section 5.1.2 provides useful advices for using a fluid mortar like bonding agent for the strengthening of RC beams in positive moment region.



a)



b)



c)

Figure 2. 7 - Main stages of the NSM strengthening: a) Grooving; b) Adhesive and FRP placement; c) Strengthened member

Figure 2. 7 shows the main stages of the NSM strengthening technique. Particularly, Figure 2. 7 a) shows an un-strengthened bridge slab after the grooving; Figure 2. 7 b) depicts the grooves filled with the bonding agent and a technician, who easily places the strip into the groove; Figure 2. 7 c) shows the bridge slab after the strengthening.

In negative moment region ( $M^-$ ), the NSM technique is even more attractive than in positive moment region ( $M^+$ ), because in  $M^-$  NSM does not require any additional protective cover, usually needed by external reinforcement in order to avoid mechanical and environmental damage. Furthermore, the FRP product, placed in the member to be strengthened, can be easily anchored into adjacent members, increasing the effectiveness of the system.

As previously said, the NSM system has been used in Europe for strengthening of RC structures since early fifties, by using steel rebars (Asplund, 1949) instead of FRP. Actually, the advantages of using FRP instead of steel are multiple. Since the FRPs are usually characterized by high tensile strength, FRP rods with smaller diameters than steel rebars can be used for a given required tensile force, reducing the groove size. Moreover, the better corrosion resistance of FRPs rather than steel enables a further reduction in groove's depth. Note that an un-appropriate groove's dimension might induce possible bond failures due to the splitting of the bonding agent, which is a very common phenomenon when adhesives with medium tensile strength are used. Actually, De Lorenzis et al (2002) stated that it is very likely that, for a given cover, rebars with stiffer surface deformations like steel display a greater tendency to induce splitting than FRP rods, the latter having soft surface deformations made of polymer resin.

Szabó & Balázs (2007) differentiated the possible failure modes of the NSM system in four groups: interfacial failure mode; cover splitting; edge splitting; FRP tensile rupture.

The interfacial failure modes may occur at adhesive-to-concrete (A/C) interface and at reinforcement-to-adhesive (R/A) interface.

The pure interfacial failure at R/A interface is recognizable for the absence of adhesive at the FRP surface after failure, whereas adhesive is usually found both at the FRP and at the concrete surface in case of cohesive shear failure in the adhesive. R/A interfacial failure usually occurs when a smooth or lightly sand-blasted FRP products are used. In these cases, in fact, the bond relies on adhesion instead of mechanical interlock between reinforcement and adhesive.

The interfacial A/C failure occurs when the groove's surface is too smooth (Figure 2. 8). This is typical of precast grooves.



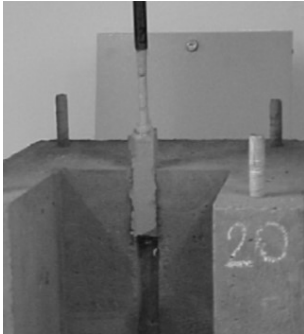


Figure 2. 8 – A/C interface failure (De Lorenzis et al, 2002)

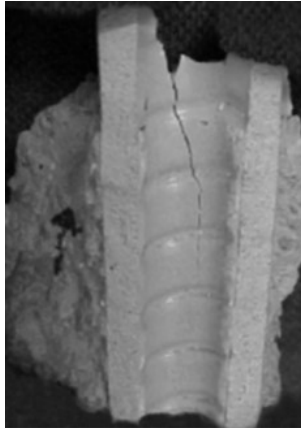


Figure 2. 9 – Longitudinal Splitting of the resin (De Lorenzis et al, 2002)

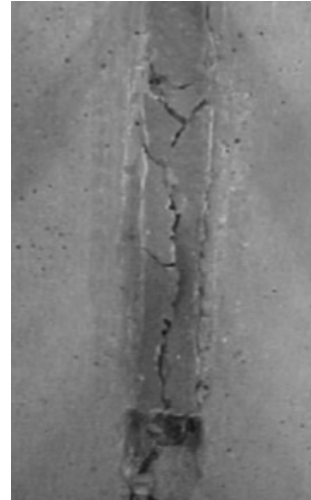


Figure 2. 10 – Splitting of the cementitious adhesive (De Lorenzis et al, 2002)

The cover splitting is caused by the radial component of the bond stress and it is a phenomenon very similar to the splitting bond failure of steel deformed bars. As stated also by De Lorenzis et al (2002), this failure mode is typical of strengthening systems where adhesives with medium tensile strength have been used, but it is very unlikely. The Figure 2. 9 and Figure 2. 10 show two cases of splitting failure respectively in resin and cementitious mortar.

The edge splitting failure occurs in members where the grooves' width is too small and, thus, the FRP product is too close to the edge of the concrete member. Several studies (Blaschko, 2003, Parretti & Nanni, 2004) provided useful design indications, including the minimum dimension of the grooves, which may be limited by the depth of the concrete cover (Figure 2. 11).

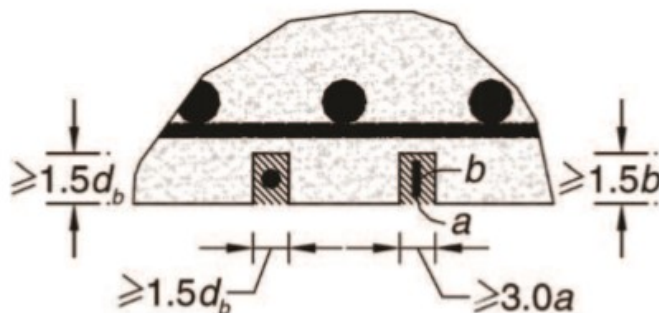


Figure 2. 11 – Minimum dimension of grooves (Parretti & Nanni, 2004)

Finally, the tensile failure of the FRP, which actually have been very rarely observed, is a very explosive failure mode that should be avoided.

The available literature on NSM FRP is relatively limited, especially on cementitious-bonded NSM FRP.

The aim of the main available studies is the assessment of the load bearing capacity of NSM FRP strengthened RC members. Wu et al (2013), Burke et al (2008), Foret & Limam (2008), Castro et al (2007), Teng et al (2006), El-Hacha & Rizkalla (2004), De Lorenzis et al (2000), conducted the most recent researches in this field. Other studies were conducted in the late 90's (see De Lorenzis et al, 2000). Note that most of the cited studies refer to NSM FRP systems manufactured using mainly resins like bonding agent.

These studies showed that NSM FRP systems significantly improve the flexural performance of RC members, increasing the load carrying capacity and, in some cases, the flexural stiffness, limiting the deflection and the cracks width.

In the following, some details of the cited researches are summarized.

Particularly, Wu et al (2013) investigated the effects of the number of FRP bars, 40% prestressing in the NSM-FRP bar, and different types of end treatments. The prestressing was not analysed for the aim of this literature review, while high attention was given to the other two parameters. The strengthening materials used in this study included CFRP bars, epoxy adhesive, and epoxy cement mortar cast at the beams' bottom side. The authors tested two non prestressed beams, where the CFRP bars were directly placed into the groove, and a non prestressed beam, where the CFRP bars were anchored to U-shaped steel-plate hoops, installed on both ends. The authors concluded that the NSM technique was effective, since it increased the flexural capacity of RC beams, but the ductility of the strengthened specimens was lower than the control beam. The ductility was even lower for the beams strengthened with two NSM-CFRP bars. Moreover, they found that the mechanical U-shaped steel-plate hoops were very effective, since most of the beams failed due to concrete crushing.

Burke et al (2008) investigated the relative performance of both epoxy and cementitious adhesives for NSM FRP applications for RC members at room and low temperatures. Moreover, they investigated the effects of groove width on the performance of NSM FRP strengthening systems. One of the aim of this study was the reduction of the costs of these systems by reducing the required volume of adhesives and by using low-cost adhesives. This research activity showed that epoxy adhesives provide superior performance as compared with cementitious grout adhesives for NSM FRP strengthening systems for RC members, although grout adhesives can be used effectively. The failure occurred due to debonding

at adhesive/concrete interface when epoxy was used, while the failure was due to debonding at adhesive/FRP interface when cementitious grout adhesives were used. Moreover, they observed that there is no considerable impact of groove width on the performance of epoxy adhesive strengthened members, and that there are no significant negative effects of low temperature on the performance of NSM FRP strengthened RC slabs using either epoxy or cementitious grout adhesives.

El-Hacha & Rizkalla (2004) tested NSM FRP (CFRP bars/strips, GFRP strips) strengthened T-shape RC beams. They observed a full composite action between NSM CFRP strip and concrete, in fact the tests mainly provided the FRP tensile rupture as failure mode, whereas FRP-epoxy-split failure was the dominant failure mode for beams strengthened with NSM CFRP reinforcing bars, as a result of high tensile stresses at the CFRP reinforcing bar-epoxy interface. Moreover, they observed a concrete split failure as governing mode of failure for beams strengthened with NSM GFRP thermoplastic strips. They concluded that NSM CFRP bars provided a considerably less increase of the load-carrying capacity than that provided by NSM CFRP strips with the same axial stiffness. It might be due to possible early debonding failure that occurred at the CFRP reinforcing bar-epoxy interface and to the smaller bonding surface of the NSM CFRP reinforcing bars compared to the NSM CFRP strips.

The tests conducted by De Lorenzis et al (2000) on NSM CFRP and GFRP rods strengthened T-shape RC beams showed an increase in capacity ranging between 25.7% and 44.3% over the control beam. A remarkable increase in stiffness was also obtained. However, the bond appeared to be very critical for the effectiveness of the NSM technique in some cases. In fact, when bond controlled the failure, the increasing of the amount of the NSM reinforcement did not produce any significant gain in capacity.

Accordingly to that stated by other researchers, Foret & Limam (2008), testing NSM CFRP strengthened RC two-way slabs, observed a significant increase of the flexural strength (about 67%). The failure occurred due to the debonding of the strengthening system.

Based on that summarized above, the NSM system is considerably affected by the bond behaviour, which efficiency depends on several parameters, such as: the materials' mechanical properties; the dimension and surface treatment of the grooves; the geometry of the FRP product; the position of the FRP reinforcement in the groove; the type of bonding agent; the shape of the FRP product and its superficial treatment. The most recent researches about the bond behaviour of NSM strengthening systems by varying the above-mentioned influencing

parameters were conducted by Bilotta et al (2014-2015), Chickh et al (2013), Ceroni et al (2013); Seo et al (2013), Palmieri et al (2012), El-Gamal (2012), Costa & Barros (2011), Bilotta et al (2011).

Some of the cited experimental researches were recently carried out within the framework of the European funded Marie Curie Research Training Network, EN-CORE, with the support of Task Group 9.3 of the International Federation for Structural Concrete (fib). Ten laboratories participated in this research activity: University of Sheffield, University of Sannio, Ghent University, Laboratory EMPA, University of Naples, University of Budapest, University of Bologna, University of Minho, University of Lulea, and University of Latvia (Bilotta et al, 2015). Both single shear tests and double shear tests were conducted. The main result of this activity is that the debonding at the concrete-epoxy interface was the most observed type of failure. It occurred with varying degrees of concrete damage (Figure 2. 12). However, other types of failure, such as, debonding at the FRP-epoxy interface, longitudinal splitting of the epoxy, splitting of the concrete specimens, bar/strip pull-out, as well as tensile failure of the FRP reinforcement were also observed (Figure 2. 13). Moreover, despite the differences in the bond behaviour of specimens tested according to single or double setup (ranging between 10% and 25%), they concluded that the single shear setup is preferable as standard test method for characterizing the bond behaviour and strength of FRP NSM systems.

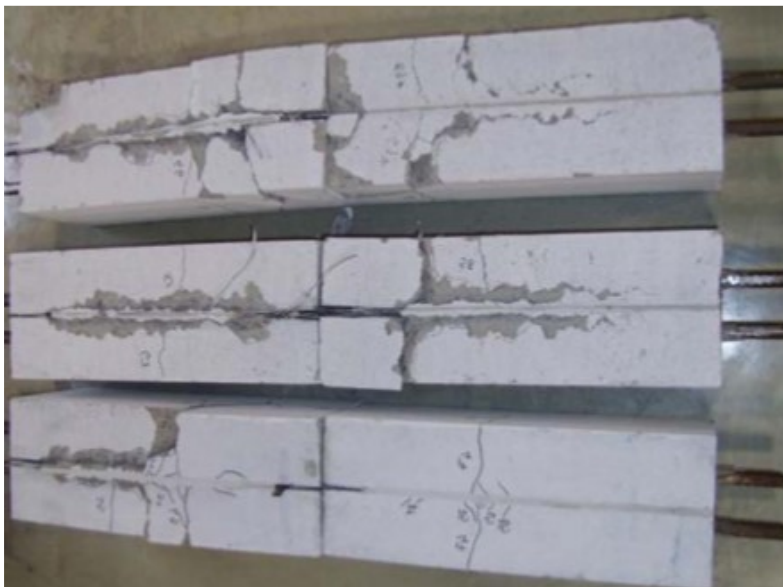


Figure 2. 12 – Typical failures of NSM specimens with varying degrees of concrete damage (Round Robin tests - Bilotta et al, 2015)



Figure 2. 13 – Splitting-related (top) and pull-out (bottom) failures in NSM specimens (Robin Round Tests – Bilotta et al, 2015)

As previously stated, Chickh et al (2013) conducted other meaningful tests, investigating the influences of the concrete strength, the type of the reinforcement (smooth carbon rod and smooth carbon plate) and its configuration (plate fully or partially inserted in the groove), and the embedded length on the bond behavior between the three materials (concrete, epoxy adhesive and CFRP). A pull-out bending test configuration was used. The authors concluded that a better performance was achieved by carbon plates compared to carbon rods and that the pull-out force increases almost linearly with the bond length. Moreover, as expected, they observed that the resistance to pull-out improves with increasing concrete strength and this influence especially effects the smaller bond lengths.

El-Gamal et al (2012) presented the results of pull-out tests conducted on NSM-GFRP bars strengthened C-shaped concrete blocks, aimed to investigate the effect on the bond performance of the following parameters: adhesive (cement and epoxy-based adhesives), groove size (approximately 1.5 and 2.0 times the actual bar diameter), bonded length (16, 24, and 32 times the actual bar diameter), environmental condition, and concrete strength. The authors observed

the splitting of the epoxy after the concrete cracking in almost cases, when the epoxy was used like adhesive, conversely mortar splitting accompanied by concrete cracking or mortar-concrete interface failure mode were observed depending on the type of mortar. Moreover, they noticed that the performance of the specimens with epoxy-filled grooves was almost similar and provided higher pull-out loads compared to the specimens with cement mortar adhesives. They also observed that the pull-out loads increased as the groove size increased. The tests conducted on the specimens manufactured with high-strength concrete showed that the failure of the specimens with epoxy-filled grooves was due to the splitting of the epoxy after the concrete cracking and it was mainly governed by concrete strength, while the groove-filling material mainly governed the failure of the specimens with cement mortar-filled grooves. The investigation of the effect of the bond length clearly showed that as the bonded length increased as the corresponding free end slip values decreased. Finally, they stated that the use of epoxy adhesives is more efficient with shorter bonded lengths (16 and 24 times the actual bar diameter) than that with longer bonded lengths (32 times the actual bar diameter).

### ***2.2.3 Comparison between strengthening techniques***

The previous sections summarize the main results of the experimental tests recently conducted by several researchers on NSM and EBR strengthening systems. Based on the conducted literature review, this section provides a comparison between the two strengthening systems, which will enable the designers to choose the most suitable strengthening system for their projects.

El-Hacha & Rizkalla (2004) stated that NSM technique has many advantages vs EBR, such as: larger bond surface that induces better anchorage capacity, providing higher resistance against peeling-off, so a higher percentage of the tensile strength can be mobilized; no preparation work is needed other than grooving; FRP reinforcement protected by the surrounding concrete against mechanical influences; improved protection against freeze/thaw cycles, elevated temperatures, fire, ultraviolet rays and vandalism; improved ductility; ultimate load develop more independent from concrete surface tensile strength. Moreover, they observed brittle debonding failures of EBR FRP strips that occurred at load levels significantly lower than that measured for beams strengthened with NSM CFRP reinforcing bars or strips and NSM GFRP thermoplastic strips. The authors did not observe any slip for the different NSM FRP reinforcing bars and strips strengthening techniques up to ultimate load-carrying capacity.

Similarly, Foret & Limam (2008), who tested both EBR and NSM CFRP strengthened RC two-way slabs, observed a more pseudo-ductile behaviour comparing NSM to EBR. The debonding occurred in both cases, more sudden in EBR than in NSM. Since a higher amount of carbon was used in EBR for almost the same average bearing capacity, the authors considered NSM more economic than EBR.

Bilotta et al (2011) conducted experimental tests on concrete blocks strengthened with different types of EBR and NSM FRP systems and they observed that the tensile strength of the FRP materials is better exploited by the NSM technique with much higher utilization factors (36–100%) than those attained in EBR systems (approximately 15%). They also stated that NSM technique also allows higher efficiency factors to be attained against lower axial stiffness, especially if the reinforcement surface is ribbed. Moreover, since a low concrete strength (approximately 19 MPa) was used in the experimental program, they observed a concrete-adhesive interface failure in most specimens strengthened with both FRP systems.

In summary, the NSM FRP strengthening technique could be considered as a valid, attractive and efficient alternative to an EBR FRP strengthening system, since NSM enhances the stiffness and the flexural strength of deficiently reinforced concrete members, keeping relatively low the costs.

### **2.3 FRP BEHAVIOUR AT HIGH TEMPERATURE**

As concerns the effect of high temperature on FRP products, a critical condition occurs when the glass transition temperature,  $T_g$ , of the polymer matrix is achieved, due to the softening of the resin, which reduces the capacity of stress transfer between the fibers. The precise definition of the  $T_g$  is still under discussion in the scientific community, because the progressive nature of the softening process makes difficult to identify a precise temperature limit. Nevertheless, the safety check often is conservatively performed, in the temperature domain, with reference to the value of  $T_g$  properly reduced (ACI 440.2R-08, 2008).

FRPs, which polymerize in ordinary conditions, typical of in situ applications, are characterized by very low  $T_g$  (between 45°C and 80°C for normal and heat resistant resins, respectively). For preformed FRPs, used as internal reinforcement, is easily possible to obtain reinforcements with  $T_g$  above 100°C.

Curing processes carried out at temperatures and pressures different from ordinary ones, allow to further increase the  $T_g$ .

Although overcoming the  $T_g$  implies a reduction in strength of the reinforcement, the drastic degradation of the resistance is reached at temperatures close to melting of the resin (temperature of decomposition,  $T_d > T_g$ ) or even higher. The reduction of stiffness, instead, depends on the type of fibre reinforcement and it is generally negligible compared to the reduction of resistance. Therefore, the real capacity of the concrete members reinforced with FRP, at high temperatures, can be considerably high (Nigro et al. 2011a, 2001b, 2013). Bisby et al (2005 a, b) conducted an extended literature review, collecting data about the fibres and FRPs' reduction of strength and stiffness at high temperature. This study suggests that carbon fibres themselves are relatively insensitive to elevated temperatures, while glass and aramid fibres experience significant deterioration of strength at high temperature. Conversely, CFRPs, GFRPs and AFRPs suffer a reduction of strength and stiffness properties with increasing temperature, although there is a great deal of scatter in the results, due the wide range of possible matrix formulations, fibre orientations, and fibre volume fractions considered. Another experimental and numerical research about this topic was conducted by McIntyre et al (2014), who performed direct tensile tests on FRP bars at different steady-state temperatures varying from 20°C to temperatures at which decomposition of the resin occurs. These results were used to calibrate a novel predictive model for the reduction in tensile strength of FRP materials at high temperature.

Note that the softening of the resin, which begins when the  $T_g$  is achieved, involves also a drastic reduction of the adhesion properties (Foster and Bisby, 2008). Hence, the efficiency of the strengthening system for existing structures, which mainly depends on the effectiveness of the bond between FRP and concrete, is strongly affected by the temperature. Some experimental tests (Deuring, 1994) showed similar problem when conventional steel strengthening is used without mechanical anchoring. The comparison between steel and EBR FRP strengthening systems showed that FRP, in particular sheets, without protection behave better than steel plates because of the lower heat conductivity and their smaller weight. Clearly, FRP externally strengthened RC beams or slabs need the protection with additional insulation in order to avoid the debonding between FRP sheets or laminates and concrete support. Obviously, if the FRP strengthening is not directly heated by fire or other sources of heat, the performances may be better. Hence, FRPs can be successfully used to strengthen infrastructure, such as bridges, where fire is not a primary action to be considered



during design (Bisby et al 2005a). Nevertheless, should be noted that other thermal action, not necessarily due to fire, such as bituminous paving casting on a bridge deck, can easily lead to high temperature (e.g. 200°C).

For this reasons, Del Prete et al (2015) conducted a numerical study aimed to investigate the thermo-mechanical behaviour of RC bridge decks strengthened with externally bonded FRP plates, by considering two possible environmental conditions, which lead to thermal states different from the normal ones: (a) fire exposure over the bridge deck due to an accident involving camions; (b) bituminous paving casting on a bridge deck at high temperature. In this study, the influence of different types of adhesive resins (normal  $T_g$  or elevated  $T_g$ ) and the thickness of the protective layer was also investigated. The philosophy of this study was to check the structure for ultimate and damage limit states (ULS and DLS). The ULS checks were conducted comparing the design values of the relevant effects of actions in the fire situation at time  $t$ ,  $E_{fi,d,t}$ , with the corresponding design value of the resistance of the member in the fire situation at same time  $t$ ,  $R_{fi,d,t}$  (EN1991 1-2, 2002; NTC2008, 2008). The ULS checks were always satisfied, mainly because the flexural capacity provided by FRP can be neglected during fire or maintenance activity. By contrast, the DLS checks, performed to assess damages of the FRP strengthening system during these events, show that constructive details and type of resin play a key role.

Another important and not secondary issue to take into account when FRPs are used for strengthening structures, where the probability of occurrence of a fire is high, is the smoke generation and toxicity of FRP matrices and adhesives. Kodur & Beingo (1998) and Bisby et al (2005) collected useful data from literature about toxicity of FRPs in fire. They stated that combustion gases from burning FRPs create a toxicity hazard for humans, and can be highly corrosive to equipment and electronics. In fact, thermoset resins commonly used in structural FRPs generate unacceptable quantities of smoke that have relatively poor flame spread characteristics, and that burning resins generated varying quantities of carbon monoxide, hydrogen fluoride, hydrogen chloride, hydrogen sulfide, and hydrogen cyanide, all of which are potentially harmful compounds. Actually, various resin additives can enhance the ability of polymer materials to resist ignition, flame spread, and smoke generation. However, these additives tend to diminish mechanical properties, discouraging their use in structural applications. Obviously, composites with cementitious matrices or FRPs installed with cementitious adhesive does not create significantly hazard for humans, if involved in fire.

### 2.3.1 Influence of high temperature on bond properties

Since the bond between the FRP and concrete is significantly influenced by high temperature, studies aimed to increase the knowledge about the decrease of the properties of the FRP-concrete interface at elevated temperatures need to be conducted. In fact, the literature currently available about this topic is very limited. In the following sections, the research conducted in the recent past about the variation of the bond properties of both NSM and EBR FRP strengthened RC elements has been summarized.

#### 2.3.1.1 Influence of high temperature on bond properties of EBR FRP

The maximum force transmitted by the FRP-to-concrete interface in normal temperature condition is related to the so called “specific fracture energy”  $\Gamma_f$  of the interface bond law, which can be expressed as (Bilotta et al., 2012; (2. 1)).

$$F_{deb} = b_f \sqrt{2 E_f t_f \Gamma_f} \quad (2. 1)$$

where  $F_{deb}$  is the maximum load before the debonding, and  $b_f$ ,  $t_f$ ,  $E_f$  are the width, the thickness and the Young’s Modulus of the FRP plate.

The conducted literature review led to 77 bond tests, performed in the recent past, on CFRP plates and sheets by several researchers (Blontrock, 2003; Wu et al, 2004; Cai, 2008; Klamer, 2009; Leone et al, 2009). The examined experimental programs include tests at ambient temperature (i.e. 20-30°C) and tests at high temperatures, ranging between 50°C and 300°C, which enabled to define the degradation of the fracture energy at high temperature. Del Prete et al (2015) highlighted for each specimen the type of bond test (single shear test, SST, or double shear test, DST), the main geometrical and mechanical properties, the  $T_g$  of the adhesive, the temperature T at which each test was performed and the maximum load,  $P_{max}$ , recorded during each test. Then, the fracture energy for each specimen was calculated through the following relationship:

$$\Gamma_f = \frac{P_{max}^2}{2 b_f^2 E_f t_f} \quad (2. 2)$$

Therefore, the experimental tests were used to calibrate a relationship to predict the decrease of bond strength versus the temperature. Particularly, the temperature-dependent reduction curve has the following general relationship:

$$\frac{\Gamma_f(T)}{\Gamma_0} = b_1 \tanh \left( b_2 \left( \frac{T}{T_g} + b_3 \right) \right) + b_4 \quad (2.3)$$

where:  $\Gamma_0$  is the fracture energy at ambient temperature;  $b_1$ ,  $b_2$ ,  $b_3$ ,  $b_4$  are coefficients, obtained by best fitting of the experimental results.

Finally, the reduction of the maximum strain for intermediate debonding due to high temperature was correlated to the specific fracture energy  $\Gamma_f(T)$ .

### 2.3.1.2 Influence of high temperature on bond properties of NSM FRP

Although recent researches (Palmieri et al, 2011 a; Burke et al, 2013; Kodur et al, 2013; Petri & Rizkalla, 2013) showed the performance in fire of NSM FRP strengthened RC members (insulated or not insulated), the variation of the bond properties of this strengthening system is not yet well investigated.

At the moment, a very limited literature is available.

Palmieri et al (2011 b) conducted a study about the influence of temperature on the bond capacity of NSM FRP. A series of 18 double shear tests at different temperatures (20, 50, 65, 80, 100=1.5 $T_g$ ) were performed. They investigated the influence of FRP reinforcement shape (rods versus strips), the type of fibres, as well as the type of surface treatment (sand coated and ribbed bars). The material used were CFRPs and GFRPs embedded in epoxy resin. They found that the failure load first increases with elevated temperature and only decrease for temperature equal to or beyond the glass transition temperature. However, the decrease of the failure load at glass transition temperature was only 10%-18%, depending on the type of strengthening system, with respect to the failure load at room temperature. They did not observe the complete degradation of bond strength and they found different failure modes with increasing test temperature. Particularly, at 50 °C, the failure mode was characterized by debonding with splitting of the resin, whereas increasing the temperature, a debonding at the FRP/resin interface with pull out of the bars/strips occurred. Moreover, increasing the temperature, the strains along the bonded length become more uniform distributed and the transfer length increases.

Another meaningful research was conducted by Yu & Kodur (2014). Their experimental program consisted of 36 pull-out tests on NSM FRP specimens at temperatures ranging between 20-400°C. The NSM FRP specimens were made with two cross sectional shapes of CFRP, strip and rod, embedded in two types of adhesives epoxy resins. The authors concluded that at room temperature, type of epoxy and cross sectional shape of reinforcement affect bond strength and

bond failure modes of NSM FRP system. Type of epoxy has higher influence on bond strength than type of reinforcement. At high temperatures, the failure mode of NSM CFRP system was through pull-out of CFRP strips or rods, whereas at room temperature failure mode was through detachment of concrete layer or pull-out, depending on the type of used adhesive. They observed that the bond strength and modulus of NSM CFRP system decrease by about 80% of their original values at 200°C, and becomes negligible at 400°C. With this study, the researchers were able to define temperature dependant relations for degradation of bond strength and bond modulus of NSM CFRP system, which can be used to gauge the effect of temperature on bond performance of NSM CFRP reinforcement. However, specific values of bond strength and slip may vary for epoxy types other than the ones used in this study.

At date, studies about the bond performance of NSM FRP strengthening systems with cementitious adhesive have not yet been conducted.

### ***2.3.2 Flexural tests at high temperature of FRP strengthened RC members***

As previously stated, the available literature about the fire resistance of concrete members strengthened with FRP reinforcement is very limited.

The available studies regarding the fire performance of EBR FRP strengthened RC members highlighted the need to protect the members using passive fire protection systems. These researches were devoted to evaluate the minimum requirements to obtain satisfactory performances in fire (Blontrock et al. 2001, Bisby et al, 2005a, Williams et al 2008, Palmieri et al 2010, Firmo et al 2012).

Firmo et al (2012) conducted one of the most recent experimental study on EBR FRP strengthened RC members in fire.

They observed that the fire resistance of the unprotected beams is compromised by the susceptibility of EBR FRP strengthening systems when exposed to high temperatures. Although the oven walls in a length of 0.20 m thermally insulated the anchorage zones of the laminate, the CFRP laminate debonded after only 23 min of fire exposure. This results pointed out the need to thermally insulate the strengthening system not only in the anchorage zones but also along the span. Anyway, they measured an average temperature at the CFRP-concrete interface (midspan section) of 414 °C, when the strengthening system of beam CFRP debonded. This temperature was considerably higher than the  $T_g$  of the adhesive (about 55 °C). It was possible since the anchorage zones were thermally insulated. Another interesting observation was that the heated length

of the FRP laminate transformed into a “cable” fixed at the anchorage zones, where the CFRP-concrete bond remained relatively undamaged.

The most recent studies regarding the fire performance of NSM FRP strengthened RC members are summarized in the following.

Palmieri et al (2011a, 2013) tested RC beams strengthened with several NSM FRP configurations, insulated and not insulated, to evaluate fire performance. Epoxy and cementitious grout were used on different beams to study the influence of the adhesive on the behavior of NSM FRP system at both ambient and elevated temperatures. Despite the high service load of the strengthened beams, and the partial failure of the fire protection of some beams, all the beams were able to sustained the applied load without failure for the 2 h of ISO 834 standard fire exposure, even after the adhesive temperature exceed its glass transition temperature. Moreover they found that U-shaped fire protection (extending to the sides of the beam) is more efficient than that of a flat protection at the bottom surface of the beam only. Residual strength tests on fire-tested beams demonstrated also that, if the insulation is able to maintain the adhesive temperature below 200 °C the FRP is able to retain bond strength to the concrete and the beam is still able to retain part of the flexural capacity of the FRP strengthened beam at ambient condition.

Burke et al (2013) presented tests of reinforced concrete slabs strengthened in flexure with a single strip of NSM FRP tape under elevated temperature (up to 200°C). Epoxy and cementitious grout were used on different slabs. The test results showed that epoxy adhesive on NSM FRP reinforcement provides higher strength in comparison to cementitious grout at ambient temperature. This results, according to that found by Palmieri et al, were attributed to better bond behaviour of epoxy adhesive than cementitious adhesive. However, at elevated temperature, the slabs with cementitious grout yielded higher failure time than those with epoxy adhesive. They also stated that insulated NSM FRP strengthened slabs may provide required fire resistance for building applications.

Petri & Rizkalla (2013), tested RC slabs strengthened with NSM system through pultruded carbon fiber rods, embedded in high temperature inorganic grout, insulated with an ultra-high temperature insulation system consisting of gap filling ceramic fiber blanket and an inch thick ceramic fiber board. The tested FRP strengthening system demonstrated its capability to withstand temperatures greater than 200 °C. They obtained a satisfactory margin of safety, for over two and a half hours of an E119 fire under the maximum permissible load with no structural deficiencies.

Since there is only limited information about the fire performance of concrete members strengthened with NSM FRP reinforcement, Kodur & Yu (2013) developed a numerical model, which was able to predict the fire response of a reinforced concrete beam with NSM FRP. They observed that a concrete beam strengthened with NSM FRP reinforcement yields fire resistance (75 min) that is slightly lower than a conventional concrete beam (85 min) but higher than that of a similar concrete beam strengthened with externally bonded FRP laminate (65 min). Moreover, an NSM FRP-strengthened RC beam, under fire conditions, may experience failure through rupture of NSM reinforcement. This is in contrast to the ambient temperature failure mode, which is through the crushing of concrete. The location of FRP reinforcement has also an influence on the fire resistance of concrete beams strengthened with NSM FRP: NSM FRP at the middle of the beam soffit yields higher fire resistance (75 min) as compared to that when NSM FRP is located closer to the bottom corners of the beam (65 min). They also confirmed the results found by other researchers: an appropriate fire insulation can significantly enhance the fire response of RC beams strengthened with NSM FRP reinforcement, especially if U-shaped fire protections are used.

## ***Chapter 3 - Thermo-mechanical properties of materials***

This chapter shows the available techniques for characterizing the main physical and mechanical properties of structural materials.

Particularly, the section 3.1 summarizes the most common techniques for measuring the thermal properties, such as the glass transition and decomposition temperature ( $T_g$  and  $T_d$  respectively), of polymeric materials. Moreover, the results of the tests, e.g., Dynamic Mechanic Analysis (DMA), Thermogravimetric Analysis (TGA) and Differential Scanning Calorimetry (DSC), conducted on a novel commercial CFRP bar, in order to define its main thermal properties, are shown. The tested CFRP bar, manufactured by *Milliken*, is defined *FireStrong* bar, since its elevated nominal  $T_g$  and  $T_d$ . It is a spirally wound round rods, which can be used to strengthen reinforced concrete structures, through the Near Surface Mounted technique: the bar is applied in a groove cut into the concrete cover of a RC member and bonded in place by filling the groove with a proper bonding agent. The manufacturer advises the use of *FireStrong* bars with a cementitious mortar, denominated *FireStrong Grout*, which is characterized by a nominal low thermal conductivity. It should be clear that (a) FRP with high  $T_g$  and  $T_d$  and (b) bonding agent with low thermal conductivity enable to realize a NSM system, which is less prone to FRP damage due to fire exposure. Therefore, in addition to DMA, TGA and DSC tests on the CFRP bar, thermal conductivity tests were also performed on the CFRP bar and on the cementitious grout, to verify their thermal conductivities. Based on the test results, these materials were chosen to manufacture a series of NSM FRP strengthened reinforced concrete beams, tested at ambient and elevated temperature, as described in Chapter 5.

Obviously, the effectiveness of the strengthening system, both at ambient and at elevated temperature, depends even on the mechanical properties of the involved materials. Therefore, the section 3.2 summarizes the results of the tests

conducted for the definition of the mechanical properties of the concrete, the steel bars, the cementitious grout and the CFRP bar, used to manufacture the above-mentioned beams (see the experimental program in Chapter 5).

### 3.1 THERMAL PROPERTIES OF STRENGTHENING MATERIALS

Polymeric materials suffers undesirable changes of properties, when heated. It obviously influences the effectiveness of the strengthening system, in which the polymeric material is involved.

Thermal analyses should be conducted, in order to define the material physical properties, capable to influence the strengthening behaviour at high temperature. These analyses usually measure the material physical property as a function of the temperature, whilst that material is subjected to a controlled temperature programme.

As stated above, the  $T_g$  is a very important thermal property, which definition has been discussed for a long time in literature. Anyway, it can be defined as the temperature region where a material changes from a glassy phase to a rubbery phase upon heating, or vice versa if cooling (Rieger, 2001). Dynamic Mechanic Analysis (DMA) and Differential Scanning Calorimetry (DSC) are thermal analyses used to characterize the  $T_g$ . Basically, they provide the  $T_g$  based on changes of material property during the glass transition. Particularly, DMA measures the changes of mechanical strength and energy loss, while DSC evaluates the changes in material's heat capacity.

The  $T_d$ , according to ASTM E 176, is the temperature region where extensive chemical changes occur. In practice, the material begins to chemically decompose and lose weight due to the generation of gaseous fuel vapours, which can react with the air above the polymer and burn. It may lead to a loop in which the heat produced by the burning of the volatiles transfers back to the polymer, which continues the process. In addition to the chemical process, physical changes, such as melting and charring, occur (Beyler et al, 2001). The Thermogravimetric Analysis (TGA), is a useful technique to characterize the  $T_d$ . TGA measures the amount and rate of change in the mass of a sample as a function of temperature during a controlled temperature programme, in a controlled atmosphere. Moreover, TGA is used to determine the thermal and/or oxidative stabilities of materials as well as their compositional properties.

The thermal conductivity ( $\lambda$ ) is the property of materials to conduct heat. It is defined as the quantity of heat transmitted through a unit thickness of a material, in a direction normal to a surface of unit area, due to a unit temperature gradient



under steady state conditions. Thermal conductivity is measured in W/(mK). Several techniques are available in literature to measure this property. The most common machines usually measure the amount of heat provided to a solid material, placed between two plates controlled at different temperatures, and the overall temperature difference between the two surfaces in contact with the sample.

### 3.1.1 Dynamic Mechanic Analysis

Dynamic Mechanic Analysis (DMA) provides information about the mechanical properties of a specimen placed in sinusoidal oscillation, as a function of time (t) and temperature, by a small sinusoidal oscillating force. The applied stress (3. 1) determines a corresponding strain (3. 2), whose amplitude ( $\varepsilon_a$ ) and phase shift ( $\delta$ ) need to be determined, in order to define the complex modulus  $E^*$ , which is the stiffness of the material (ISO 6721-1, ASTM D4092).

$$\sigma = \sigma_a \sin(\omega t + \delta) \quad (3. 1)$$

$$\varepsilon = \varepsilon_a \sin(\omega t) \quad (3. 2)$$

$E^*$  is composed of the real part, the storage modulus  $E'$ , and the imaginary part, the loss modulus  $E''$ , as shown in (3. 3).

$$E^* = E' + i E'' \quad (3. 3)$$

The formula of complex modulus magnitude is shown in (3. 4)

$$|E^*| = \frac{\sigma_a}{\varepsilon_a} = \sqrt{[E'(\omega)]^2 + [E''(\omega)]^2} \quad (3. 4)$$

where:

$$E'(\omega) = |E^*| \cos \delta \quad (3. 5)$$

$$E''(\omega) = |E^*| \sin \delta \quad (3. 6)$$

$$\delta = \arctan \frac{E''(\omega)}{E'(\omega)} \quad (3. 7)$$

$\omega$  is the frequency of strain oscillation.

According to ISO 6721-1: the storage modulus  $E'$  represents the stiffness of a viscoelastic material and it is proportional to the energy stored during a loading cycle; the loss modulus  $E''$  represents the viscous portion and it is proportional to the energy dissipated, for example as heat, during one loading cycle. This means that a high loss factor  $\tan\delta$  is indicative of a material characterized by a high non-elastic strain component, and vice versa.

DMA measurement can be carried out in deformation control, applying a sinusoidal deformation to the specimen and measuring the stress, or vice versa in force control. The dynamic load can be achieved in free vibration or in forced vibration: in the first configuration, the specimen freely oscillates; in the second one, a variable frequency apparatus applies a constant amplitude of stress or deformation.

The analyzer can apply both torsional and axial stress/strain. The torsional analysers are commonly used for liquid materials, while the axial one for solid or semi-solid materials. Moreover, the analyser can be set in different arrangements, such as: three-point or four-point bending; single or dual cantilever; tensile; compressive; shear (Figure 3. 1).

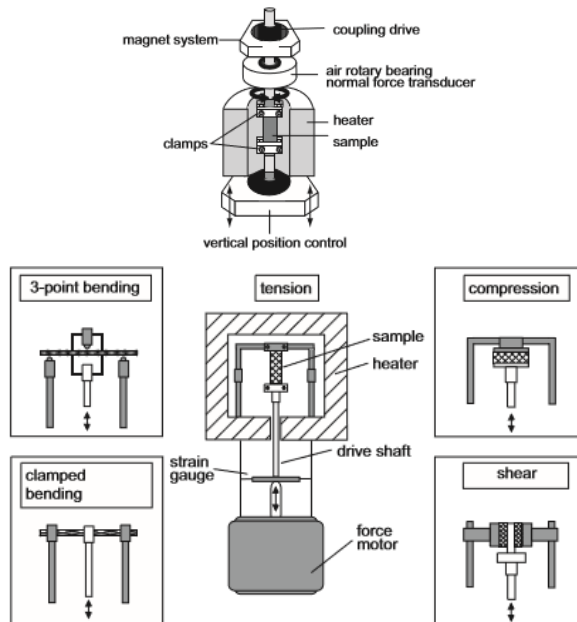


Figure 3. 1 - Possible test arrangements of a dynamic mechanic analyser (Ehrenstein et al, 2004)

### 3.1.1.1 DMA of a commercial CFRP bar

In order to define the glass transition temperature of the *FireStrong* bar, Dynamic Mechanic Analyses were carried out through the Triton Technology Dynamic Mechanical Analyzer (TTDMA), shown in Figure 3. 2. The sections 3.1.1.2 and 0 provide all the information about the performed tests, according to the suggestion of ISO 6721-1.

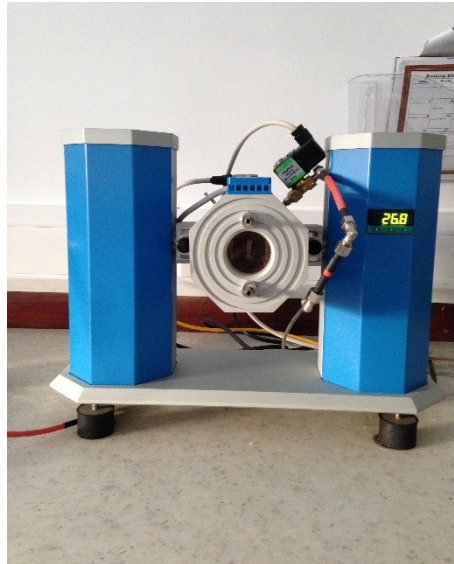


Figure 3. 2 - Triton Technology Dynamic Mechanical Analyzer (TTDMA)

### 3.1.1.2 Specimens' preparation and analyzer's arrangement

The experimental program is made of 6 tests: 3 tests in single cantilever (SC) configuration and 3 tests in three-point bending (TPB) configuration.



Figure 3. 3 – FireStrong CFRP bar



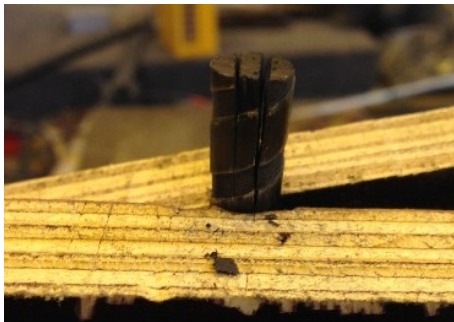
Figure 3. 4 - Specimens for DMA tests in single cantilever configuration

The Figure 3. 4 shows the specimens tested in single cantilever configuration. Those specimens are 15 mm long and have rectangular cross section, whose

dimensions are summarized in Table 3. 1. The CFRP bar (Figure 3. 3) was chopped in pieces 15 mm long (Figure 3. 5 a), and then the central part of each piece was extracted (Figure 3. 5 b). The outer surface, made essentially of resin, was peeled off (Figure 3. 5 c) and accurately made smooth and clean.



a)



b)



d)

Figure 3. 5 - Specimens' preparation: a) bar's chopping; b) central part's extraction; c) outer surface's peeling off.

Figure 3. 6 shows the analyser in single cantilever arrangement: the specimen is firmly clamped on one end and excited on the other end. This arrangement is

better than dual cantilever, where the specimen is clamped to both supports and excited at its midpoint. In fact, in the latter arrangement, specimens that expand considerably when heated may distort, falsifying the reading.

The tests were conducted in single frequency (1 Hz), with a temperature rate 2°C/min and by setting a displacement amplitude equal to 0.05 mm.

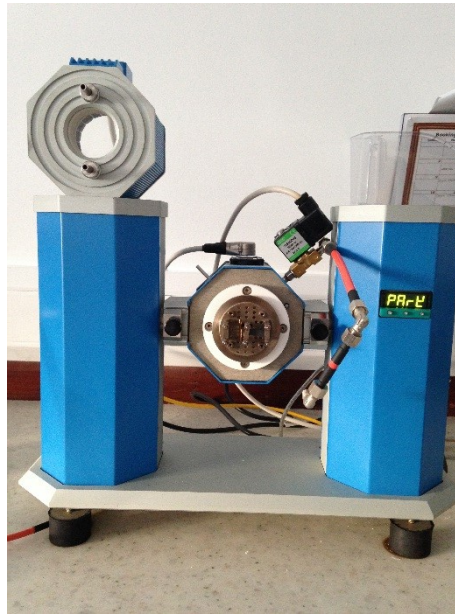


Figure 3. 6 - Dynamic mechanic analyzer in single cantilever configuration

Table 3. 1 - Specimens' geometry (SC)

Label	Dimension		
	Length L (mm)	Thickness t (mm)	Width w (mm)
CFRP-1-15	15.00	1.50	6.53
CFRP-2-15		1.52	7.19
CFRP-3-15		1.48	5.96

The Figure 3. 7 shows the specimens tested in three-point bending configuration. Those specimens are 40 mm long and have approximately square cross section, whose dimensions are summarized in Table 3. 2. Those specimens were prepared in the way described above.

The Figure 3. 8 shows the analyser in three-point bending arrangement: the ends are freely supported and the load is applied to the midpoint. The tests were

conducted in single frequency (1 Hz), with a temperature rate 2°C/min and by setting a displacement amplitude equal to 0.05 mm.

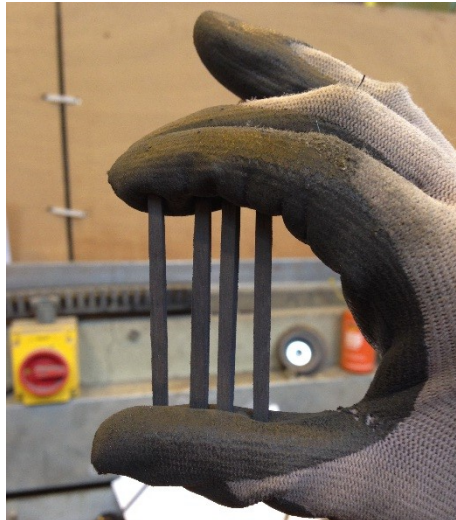


Figure 3. 7 - Specimens for DMA tests in three-point bending moment configuration

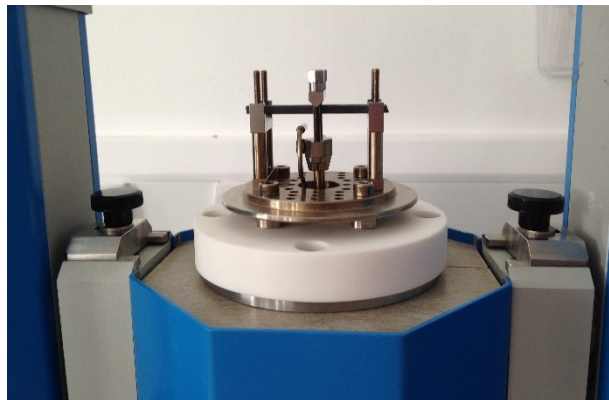


Figure 3. 8 - Dynamic mechanic analyzer in 3 point bending moment configuration

Table 3. 2 - Specimens' geometry (TPB)

Label	Dimension		
	Length L (mm)	Thickness t (mm)	Width w (mm)
CFRP-1-40	40.00	2.53	3.07
CFRP-2-40		2.80	3.47
CFRP-3-40		3.23	3.47

### 3.1.1.3 Evaluation of the glass transition temperature

Various standards (ISO/CD 6721 - 11:2008; DIN 65 583, 1999) and apparatus manufacturers provide several proposals for determining the glass transition temperature in practice.

The most common techniques are:

- evaluation of the peak of the loss factor  $\tan \delta$ ;
- evaluation of the peak of the loss modulus  $E''$ ;
- 2% offset method (start of glass transition);
- tangent method (start of glass transition);
- inflection point method.

The results of the performed tests were processed with these techniques, as shown in the following.

#### Evaluation of the peak of the loss factor $\tan \delta$

The glass transition temperature may be defined as the temperature corresponding to the maximum loss factor  $\tan \delta$ . This method provides the highest  $T_g$  value, compared to the values provided by the other methods.

The storage modulus  $E'$ , the loss modulus  $E''$  and the loss factor  $\tan \delta$  are depicted versus the temperature in Figure 3. 9 and Figure 3. 10, referring, for example, to two of the six performed tests. Those figures show that  $T_g(\max \tan \delta)$  is greater than  $200^\circ\text{C}$  and the values obtained in TPB (Figure 3. 10) arrangement are slightly greater than those obtained in SC (Figure 3. 9).

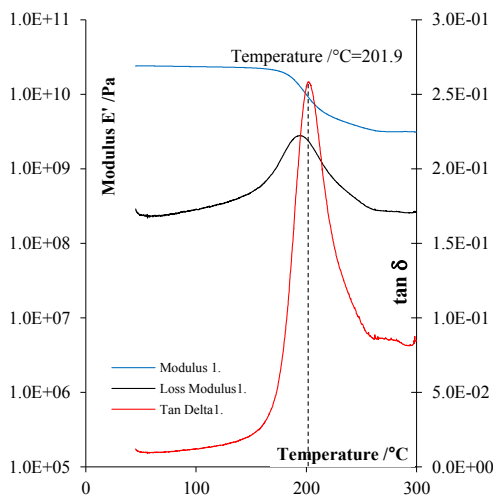


Figure 3. 9 - SC CFRP-1-15: storage modulus  $E'$ , loss modulus  $E''$  loss factor  $\tan \delta$  vs temperature

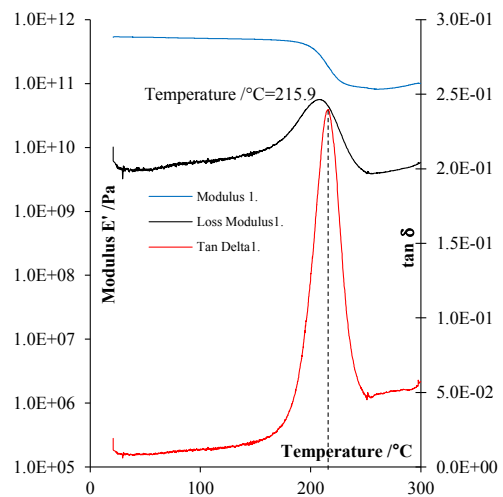


Figure 3. 10 - TPB CFRP-1-40: storage modulus  $E'$ , loss modulus  $E''$  loss factor  $\tan \delta$  vs temperature

Moreover those figure clearly show that  $T_g(\max \tan \delta)$  is greater than  $T_g(\max E'')$ , which is almost equal to the value obtained with the inflection point method ( $T_g$  midpoint)

The Table 3. 3 and the Annex I summarizes the test results of the overall experimental program. The Table 3. 3 shows the calculated values of average and standard deviation: TPB provided  $T_g$  values, characterized by a greater scatter than that had in SC.

Table 3. 3 -  $T_g(\max \tan \delta)$ . Average ( $\mu$ ) and standard deviation ( $\sigma$ ).

Analyzer arrangement	Label	$T_g$ (°C)	$\mu$	$\sigma$	$\mu$	$\sigma$
SC	CFRP-1-15	201.9	202.7	0.29	211.48	10.71
	CFRP-2-15	202.4				
	CFRP-3-15	201.9				
TPB	CFRP-1-40	215.9	220.9	4.52		
	CFRP-2-40	222.0				
	CFRP-3-40	224.7				

Evaluation of  $T_g$  offset

The 2% offset method provides the starting temperature of glass transition ( $T_g$  offset).

In practice, a line is drawn parallel and 2% below the tangent to the linear portion of the curve, that represents the storage modulus versus temperature; the intersection of the parallel line with the curve  $E'$ -T defines the  $T_g$  offset

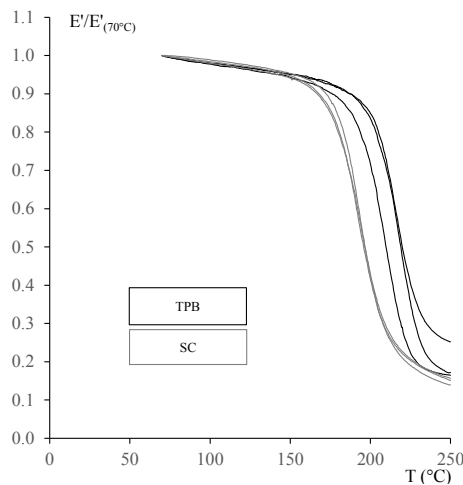


Figure 3. 11. Normalized storage modulus versus Temperature. Comparison between SC and TPB



The  $T_g$  offset has been evaluated referring to the normalized storage modulus  $E'$ , namely the non-dimensional ratio of storage modulus  $E'$  to the storage modulus at temperature  $T=70^\circ\text{C}$  ( $E'_{70^\circ\text{C}}$ ), represented versus the temperature.

It has to be noted that the non-dimensional ratio  $E'/E'_{70^\circ\text{C}}$  enables a reasonable comparison between the results of the tests, performed in SC and TPB configuration. This comparison is shown in Figure 3. 11.

The Figure 3. 12 and Figure 3. 13 show the application of the 2% offset method, referring, for example, to two of the six performed tests. The results of the overall experimental program are summarized in Table 3. 4 and in Annex I.

As stated about the  $T_g$  ( $\max \tan \delta$ ), the TPB arrangement provided  $T_g$  offset values slightly greater than that obtained in SC arrangement, but characterized by a negligible scatter.

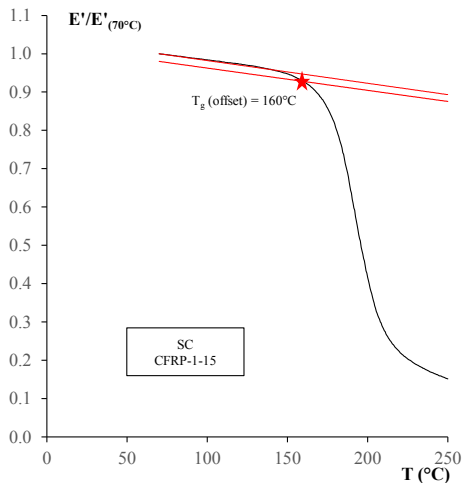


Figure 3. 12 - SC CFRP-1-15: Normalized storage modulus vs Temperature. Definition of  $T_g$  offset

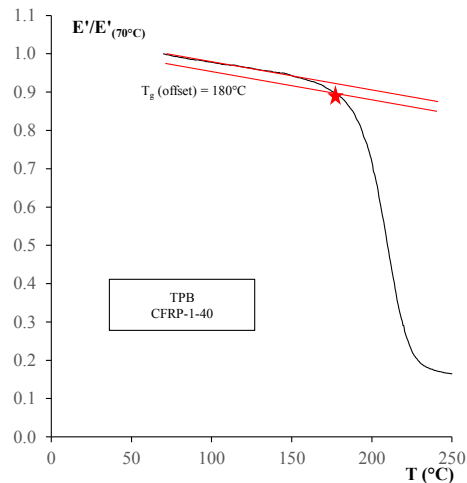


Figure 3. 13 - TPB CFRP-1-40: Normalized storage modulus vs Temperature. Definition of  $T_g$  offset

Table 3. 4 -  $T_g$  offset. Average ( $\mu$ ) and standard deviation ( $\sigma$ ) of test results

Analyzer arrangement	Label	$T_g$ ( $^\circ\text{C}$ )	$\mu$	$\sigma$	$\mu$	$\sigma$
SC	CFRP-1-15	160.0	161.0	3.61	170.75	10.94
	CFRP-2-15	165.0				
	CFRP-3-15	158.0				
TPB	CFRP-1-40	180.0	180.5	0.87		
	CFRP-2-40	181.5				
	CFRP-3-40	180.0				

Evaluation of  $T_g$  onset

The  $T_g$  onset is the glass transition temperature provided by the tangent method. It is defined as the temperature at the intersection between the tangents to the linear portion of the curve of storage modulus versus temperature and to the inflection point of the same curve.

The Figure 3. 14 and Figure 3. 15 show the application of the tangent method, referring to the curves of the normalized storage modulus versus temperature, obtained through two of the six performed tests. The Table 3. 5 and Annex I summarizes the results of the application of the tangent method on the overall experimental program, showing that  $T_g$  onset values are slightly greater than  $T_g$  offset and, as expected, less than  $T_g$ (max tan  $\delta$ ).

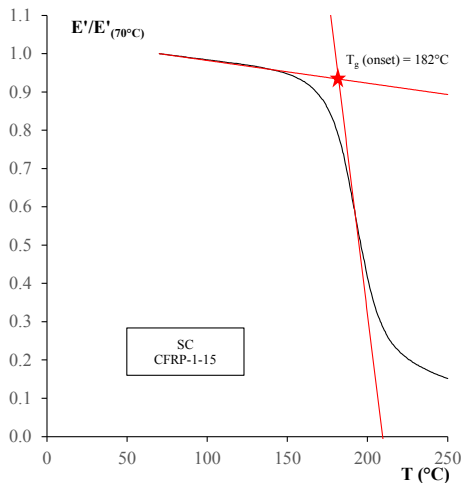


Figure 3. 14 - SC CFRP-1-15: Normalized storage modulus vs Temperature. Definition of  $T_g$  onset

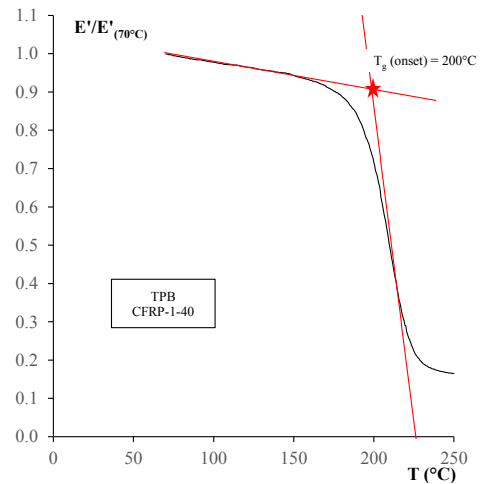


Figure 3. 15 - TPB CFRP-1-40: Normalized storage modulus vs Temperature. Definition of  $T_g$  onset

Table 3. 5 -  $T_g$  onset. Average ( $\mu$ ) and standard deviation ( $\sigma$ ) of test results

Analyzer arrangement	Label	$T_g$ (°C)	$\mu$	$\sigma$	$\mu$	$\sigma$
SC	CFRP-1-15	182.0	181.67	0.58	192.42	11.92
	CFRP-2-15	181.0				
	CFRP-3-15	182.0				
TPB	CFRP-1-40	200.0	203.17	2.84		
	CFRP-2-40	204.0				
	CFRP-3-40	205.5				

### Evaluation of $T_g$ midpoint

The  $T_g$  midpoint is the glass transition temperature provided by the inflection point method.

The  $T_g$  midpoint, in practice, is defined as the temperature corresponding to the inflection point of the curve of the storage modulus versus temperature. Therefore, it can be calculated as the maximum of the first derivative of the storage modulus versus temperature curve (Figure 3. 16).

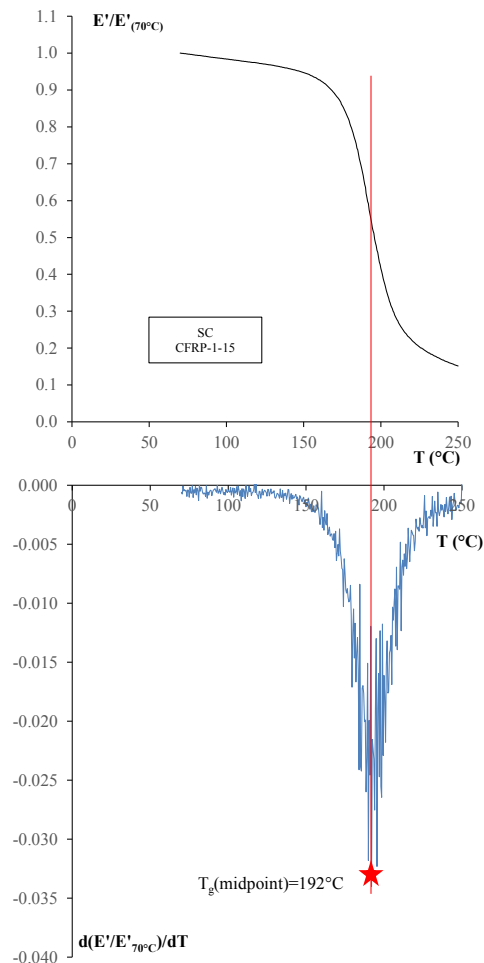


Figure 3. 16 - SC CFRP-1-15: Normalized storage modulus vs Temperature and First derivative of  $E'/E'(70^{\circ}\text{C})$  vs Temperature. Definition of  $T_g$  midpoint

The Figure 3. 16 and Figure 3. 17 show the curves of the first derivative of the normalized storage modulus versus temperature, obtained through two of the six performed tests. The application of the inflection point method on the overall set

of curves, obtained through the performed experimental program, provided  $T_g$  midpoint values, which are summarized in Table 3. 6 and in Annex I.

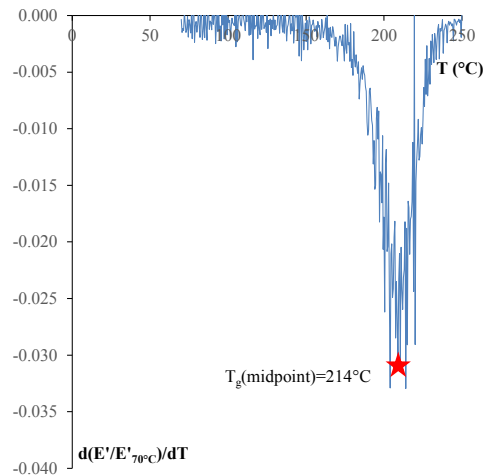


Figure 3. 17 - TPB CFRP-1-40: First derivative of  $E/E_{(70^{\circ}\text{C})}$  vs Temperature. Definition of  $T_g$  midpoint

Table 3. 6 -  $T_{g\_midpoint}$ . Average ( $\mu$ ) and standard deviation ( $\sigma$ ) of test results

Analyzer arrangement	Label	$T_g$ (°C)	$\mu$	$\sigma$	$\mu$	$\sigma$
SC	CFRP-1-15	192.0	194.17	2.02	205.83	12.99
	CFRP-2-15	194.5				
	CFRP-3-15	196.0				
TPB	CFRP-1-40	214.0	217.50	3.04		
	CFRP-2-40	219.0				
	CFRP-3-40	219.5				

### 3.1.2 Thermogravimetric Analysis (TGA)

Thermogravimetric analysis (TGA) is an experimental technique, which provides the weight or the mass of a sample, measured as a function of temperature or time in isothermal experiments.

The thermogravimetric analyzer is the instrument used to perform TGA analysis. It is a thermobalance, through which a purge gas, e.g., nitrogen or oxygen, flows creating an atmosphere that can be respectively inert or oxidizing.

Several different arrangements of the balance and furnace are possible:

- the sample holder may hang down from the balance into the furnace (bottom-loading or suspension design);

- the sample holder is rigidly attached to the top of the balance arm (top-loading design);
- the sample holder is rigidly attached to the end of the balance arm in horizontal configuration (side-loading design).

The modern and commercial systems have furnace able to cool as low as -160°C and heat up to 1600 °C, with a user defined rate.

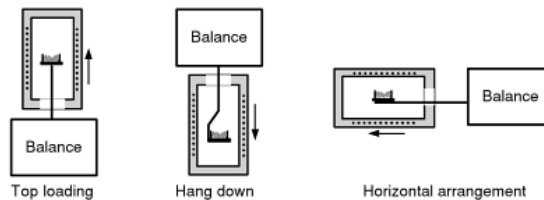


Figure 3. 18 - Thermobalance designs (Gabbott, 2008)

The TGA measurements are commonly depicted as a TGA curve, in which the mass is plotted versus temperature or time. In addition, a Differential Thermogravimetric (DTG) curve, which is the first derivative of TGA curve, provides the rate of mass changes versus temperature or time.

The steps in TGA curve and peaks in DTG curve represent the mass loss, due to several effects, such as: loss of water of crystallisation; evaporation of volatile substances; chemical thermal decomposition in an inert atmosphere with generation of gaseous products; oxidative decomposition of organic substances in air or oxygen; other chemical reactions (Gabbott, 2008)

Several studies (Haines, 2002; Menczel & Prime, 2008; Gabbott, 2008) provided useful information about the main factors that may affect the TGA measurement.

The buoyancy is one of the disturbing factors in TGA measurement, defined as the upward force on the sample (equation (3. 8) ), produced by the surrounding atmosphere (atmosphere effect). The buoyancy effect occurs as the density  $\rho$  of the gas in the balance decreases with increasing temperature, affecting the apparent mass of the sample. The buoyancy effect is not constant, since the gas density is temperature dependent, as shown in (3. 9) , where:  $\rho_0$  is the value of the gas density at the reference temperature  $T_0$  (25°C);  $T$  is the temperature in a generic instant of time during the test. Therefore, even if any change of mass occurs, the decrease of the buoyancy force with increasing temperature leads to an increase of the apparent mass. For this reason, the TGA measurements need to be corrected through a “blank measurement” (baseline): a “blank experiment” is carried out with the same temperature program and crucible used for the

experiment, but without sample; the obtained blank curve is then subtracted to the TGA measurements.

$$F = V \cdot \rho \cdot g \quad (3.8)$$

$$\rho = \rho_0 \frac{T_0}{T} \quad (3.9)$$

Other factors, associated to the increase of temperature, may affect TGA measurements, e.g., the thermal expansion of the thermobalance components, the presence of thermal convection currents.

Many disturbing effects may be reduced or eliminated through an accurate sample preparation, by setting suitable parameters (heating rate, atmosphere) and using appropriate crucibles.

The sample should be homogeneous and have an appropriate size and morphology, in order to achieve the required test's precision and not affect the heat transfer process. Moreover, the sample preparation process should be reproducible and it should not contaminate the sample.

The real sample temperature may be slightly different to that measured, which is heating rate dependent. This effect may be reduced through a temperature calibration by using pure metals with a good thermal conductivity. Obviously polymers may exhibit different thermal conductivity behaviour, therefore their measured temperature may be still slightly influenced by the heating rate. The influence of the heating rate is more important for those samples, which undergo chemical reaction during the test.

Regarding the crucibles, it should be clear that their material must not influence the reaction of the sample. The crucible usually employed in TGA measurements are made of alumina, sapphire or platinum: the alumina crucibles can be heated up to 1600°C; the sapphire crucibles are suitably employed for measuring metals that partially dissolve and penetrate ordinary alumina crucibles; the platinum crucibles have a good thermal conductivity.

### 3.1.2.1 TGA of a commercial CFRP bar

In order to define the decomposition temperature of the *FireStrong* CFRP bar, Thermogravimetric Analyses were carried out through the METTLER TOLEDO Thermogravimetric Analyzer (MTTGA), shown in Figure 3. 19. The MTTGA is a thermobalance with horizontal arrangement. The sections 3.1.2.2 and 3.1.2.3 provide all the information about the performed tests.



Figure 3. 19 - METTLER TOLEDO Thermogravimetric analyzer

### 3.1.2.2 Specimens' preparation and tests' settings

The experimental program is made of 6 tests: 3 tests in Nitrogen ( $N_2$ ) atmosphere (50  $\mu$ l/min) and 3 tests in air.

The tested specimens were extracted by the core of the CFRP bar, through a procedure similar to that explained in section 3.1.1.2. They were placed in the 70  $\mu$ l alumina crucibles, which were set in the sample holder, shown in Figure 3. 20.

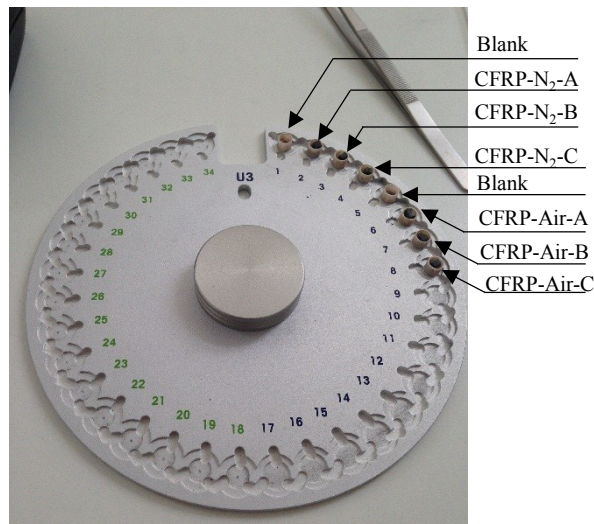


Figure 3. 20 - Specimens placed in the aluminium crucibles (70 $\mu$ l)

The Table 3. 7 summarizes the specimens' initial weight and the tests' settings in terms of temperature rate and range.

Table 3. 7 - Specimens' initial weight and tests' settings TGA

Label	Initial weight (mg)	Rate (°C/min)	Temperature range (°C)
CFRP-N <sub>2</sub> -A	51.6	10	25 - 800
CFRP-N <sub>2</sub> -B	42.5		
CFRP-N <sub>2</sub> -C	46.6		
CFRP-Air-A	47.7		
CFRP-Air-B	43.6		
CFRP-Air-C	50.2		

### 3.1.2.3 Evaluation of the decomposition temperature

The results of the performed tests are depicted as Weight loss versus Temperature curves (TGA curves) in Figure 3. 21 and First derivative of weight loss versus Temperature curves (DTG curves) in Figure 3. 22.

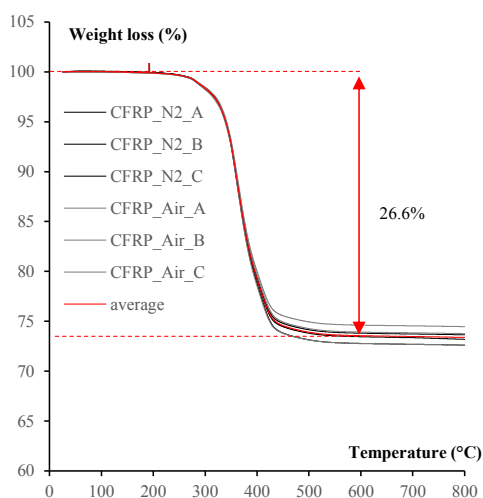


Figure 3. 21 - Weight loss vs Temperature (TGA curves)

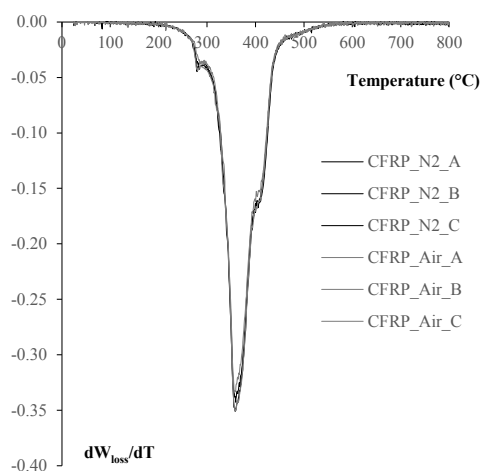


Figure 3. 22 - First derivative of weight loss vs Temperature (DTG curves)

Those figures highlight that the material is very stable, since the scatter between the TGA curves, and similarly between the DSC curves, is very negligible, especially referring to the tests conducted in N<sub>2</sub> environment. Moreover, when the decomposition occurred, the weight loss was about 27%. This means that the percentage in weight of fibres is about 73%.

Similarly to that explained in section 0, various standards and apparatus manufacturers provide several proposals for determining the decomposition temperature.



The most common techniques are:

- 2% offset method (start of decomposition);
- tangent method (start of decomposition);
- inflection point method.

These techniques were applied on the results of the performed tests, as shown in the following.

### Evaluation of $T_d$ offset

The 2% offset method provides the starting temperature of decomposition stage ( $T_d$  offset).

In practice, a line is drawn parallel and 2% below the tangent to the linear portion of the curve, that represents the weight loss versus temperature; the intersection of the parallel line with the curve (Weight loss – T) defines the  $T_d$  offset.

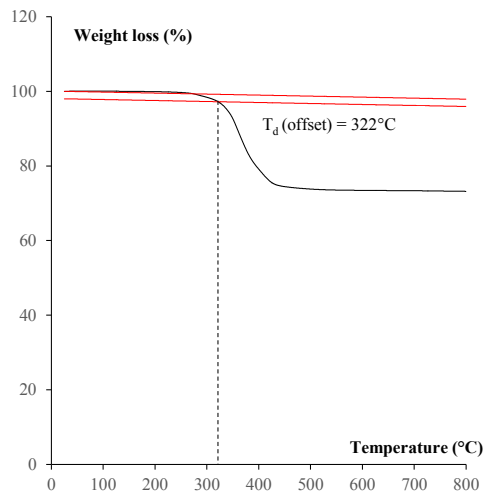


Figure 3. 23 - CFRP-N<sub>2</sub>-A: Weight loss vs Temperature. Definition of  $T_d$  offset

Figure 3. 23 shows the application of the 2% offset method on the experimental curve obtained testing, for example, the specimens CFRP-N<sub>2</sub>-A. The results of the overall experimental program are summarized in Table 3. 5 and in Annex I, showing that  $T_d$  offset ranges between 314°C (average of  $T_d$  values in air) and 322°C (average of  $T_d$  values in N<sub>2</sub>). Therefore the mean  $T_d$  offset ( $\mu$ ), considering the overall experimental program, is about 318°C corresponding to a standard deviation ( $\sigma$ ) equal to 4.4. Clearly, the  $\sigma$  values, calculated referring respectively to the results of the tests in N<sub>2</sub> and in air, are significantly lower than 4.4.

Table 3. 8.  $T_d$  offset. Average ( $\mu$ ) and standard deviation ( $\sigma$ ) of test results

Label	$T_d$ (°C)	$\mu$	$\sigma$	$\mu$	$\sigma$
CFRP- N <sub>2</sub> -A	322.0	321.50	2.50	317.92	4.43
CFRP- N <sub>2</sub> -B	324.0				
CFRP- N <sub>2</sub> -C	319.0				
CFRP-Air-A	315.0	314.33	2.08		
CFRP- Air -B	316.5				
CFRP- Air -C	312.0				

### Evaluation of $T_d$ onset

The  $T_d$  onset is the decomposition temperature provided by the tangent method. It is defined as the temperature at the intersection between the tangents to the linear portion of the weight loss versus temperature curve and to the inflection point of the same curve.

Figure 3. 24 shows the application of the tangent method on the experimental curves obtained testing, for example, the specimens CFRP- $N_2$ -A

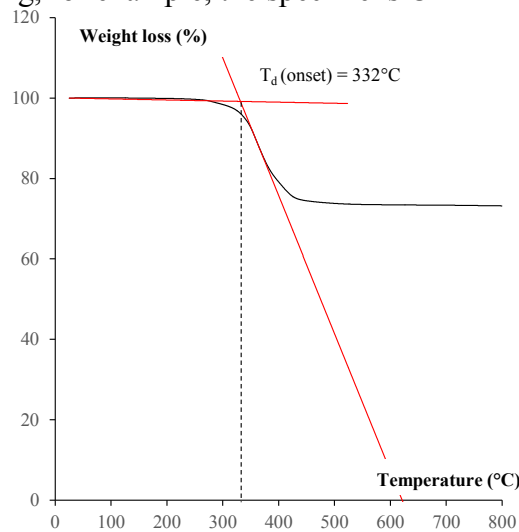
Figure 3. 24 - CFRP- $N_2$ -A: Weight loss vs Temperature. Definition of  $T_d$  onset

Table 3. 9 and Annex I summarize the results of the application of the tangent method on the overall experimental program, showing that the mean  $T_d$  onset is 331°C, corresponding to a standard deviation equal to about 0.5. Moreover, both the tests in  $N_2$  and in air provided results in very good agreement.

The application of the tangent method, as expected, provided a mean decomposition temperature higher than that obtained through the offset method.

Table 3. 9 -  $T_d$  onset. Average ( $\mu$ ) and standard deviation ( $\sigma$ ) of test results

Label	$T_d$ (°C)	$\mu$	$\sigma$	$\mu$	$\sigma$
CFRP- N <sub>2</sub> -A	332.0	331.00	0.50	330.92	0.49
CFRP- N <sub>2</sub> -B	331.0				
CFRP- N <sub>2</sub> -C	331.0				
CFRP-Air-A	332.0	330.83	0.58		
CFRP- Air -B	331.5				
CFRP- Air -C	331.0				

### Evaluation of $T_d$ midpoint

The  $T_d$  midpoint is the decomposition temperature provided by the inflection point method.

The  $T_d$  midpoint, in practice, is defined as the temperature corresponding to the inflection point of the TGA curve. Therefore, it can be calculated as the maximum of the DTG curve (e.g., Figure 3. 25).

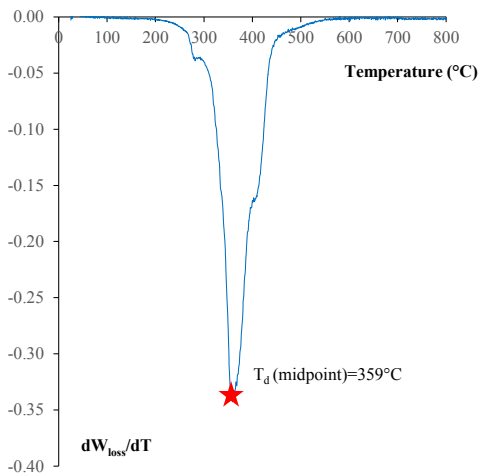


Figure 3. 25 - CFRP-N<sub>2</sub>-A: TGA curve and DTG curve. Definition of  $T_d$  midpoint

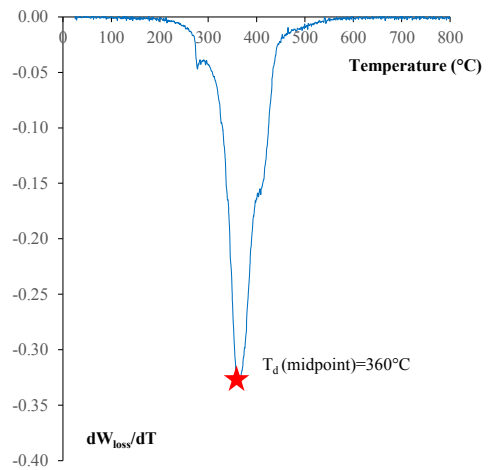


Figure 3. 26 - CFRP-Air-A: DTG curve. Definition of  $T_d$  midpoint

Table 3. 10 and Annex I summarize the results of the application of the midpoint method on the overall experimental program, showing that this method, compared to those summarized in the previous sections, provided the greatest  $T_d$  values. Their mean value is about 358°C, corresponding to a standard deviation equal to about 1.33.

Moreover, note that the tests conducted in Nitrogen provided exactly the same result.

Table 3. 10 -  $T_d$  midpoint. Average ( $\mu$ ) and standard deviation ( $\sigma$ ) of test results

Label	$T_d$ (°C)	$\mu$	$\sigma$	$\mu$	$\sigma$
CFRP- N <sub>2</sub> -A	359.0	359.00	0.00	358.33	1.33
CFRP- N <sub>2</sub> -B	359.0				
CFRP- N <sub>2</sub> -C	359.0				
CFRP-Air-A	360.0	357.70	1.76		
CFRP- Air-B	356.5				
CFRP- Air-C	358.0				

### 3.1.3 Differential Scanning Calorimetry (DSC)

The Differential Scanning Calorimetry (DSC) is a thermal analysis commonly conducted to detect the transition phases of the materials, based on the changes in its heat capacity. The specific heat capacity at a constant pressure ( $c_p$ ) is the required amount of heat per unit mass ( $m$ ) to raise the temperature by 1°C. It can be written as in (3. 10),

$$c_p = \frac{dQ}{dT} \frac{1}{m} = \frac{dH}{dT} \frac{1}{m} \quad (3. 10)$$

where:

$\frac{dQ}{dT}$  is the heat capacity, namely the amount of heat,  $dQ$ , necessary to raise the temperature  $dT$ ;

$\frac{dH}{dT}$  is the increase in the enthalpy, caused by the supplied amount of heat,  $dQ$ .

In practice, a DSC analysis tracks the changes in the heat flow ( $\Phi$ ) of a sample of known mass, which is heated or cooled, as a function of temperature.

Since the rate of change of enthalpy  $\frac{dH}{dt}$  is equal to the DSC heat flow, the specific heat capacity can be re-written as in (3. 11)

$$c_p = \frac{dH}{dT} \frac{1}{m} = \frac{dH/dt}{dT/dt} \frac{1}{m} = \frac{\Phi}{\beta_s m} \quad (3. 11)$$

where:  $\beta_s$  is the rate of change of temperature of the sample.

Several methods may be used to determine the glass transition temperature of a material, based on the DSC curve, the enthalpy curve or the heat capacity versus temperature diagram (Haines, 2002; Gabbot, 2008, ASTM D 3418).

The DSC analyses should be performed through a specifically designed instruments, which measure calorimetric data while scanning, even if several

Thermogravimetric analyser are able to conduct both TGA and DSC measurements.

### 3.1.3.1 Evaluation of the specific heat of a commercial CFRP bar

The METTLER TOLEDO Thermogravimetric Analyzer (MTTGA), shown in Figure 3. 19, is an instrument able to conduct both TGA and DSC measurements. Therefore, this machine was used to characterize the main thermal properties of the *FireStrong* CFRP bar. Particularly, the processing of TGA measurements, shown in section 3.1.2.3, provided the decomposition temperature of that CFRP bar, while the processing of DSC measurements, shown in this section, provided the specific heat capacity of that commercial product.

Figure 3. 27 depicts the specific heat capacity of the CFRP bar versus temperature, calculated according to the equation (3. 11), referring to the DSC measurements, conducted on three specimens.

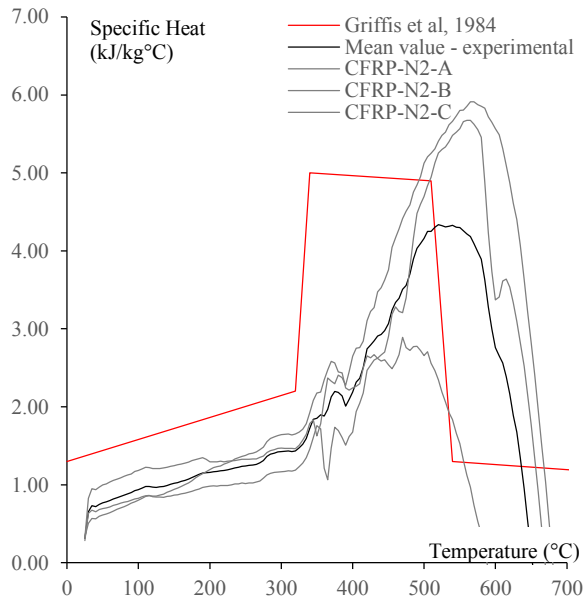


Figure 3. 27 – CFRP Specific heat capacity versus Temperature. Comparison between experimental results and the value provided in literature for a similar product

The mean value of  $c_p$  was also calculated and compared to that provided in literature for a similar carbon/epoxy product (Griffis et al, 1984). According to Griffis et al,  $c_p$  linearly increased in the temperature range 20-300°C, then the slope of the curve  $c_p - T$  increased significantly up to the achievement of the peak value. Referring to the mean experimental curve, after the achievement of

the maximum  $c_p$  at about 545°C, the specific heat capacity suddenly decreased. Similarly, the specific heat capacity obtained by Griffis et al suddenly decreased at 500°C, but the peak value was almost constant in the temperature range 340-500°C. Clearly, the perfect agreement between the experimental results and that found in literature is impossible to achieve, since the thermal properties of FRPs depend on the fibre/resin volume fraction, which can be significantly different in various products.

It should be noted that after the achievement of the decomposition temperature of the CFRP bar (360 °C based on the inflection point method), the DSC results are very scattered.

The DSC measurements were not processed to determine the glass transition temperature, because DMA results were considered sufficiently reliable.

### 3.1.4 CFRP's Thermal conductivity

The thermal conductivity of FRPs, used as NSM strengthening or internal reinforcement, does not significantly affect the heat transfer within the structural member, since its small cross-sectional area, compared to concrete section. Conversely, when FRP is used for external strengthening (e.g., wrap, plate), since its low transverse thermal conductivity, can provide a certain thermal protection to the concrete. Moreover, the charred FRP laminates, due to fire exposure, may act as insulation material for the concrete member.

The type of resin, the type and orientation of fibres, and the fibre volume fraction influence the thermal conductivity of FRPs. They are thermal anisotropic materials, characterized by different thermal conductivity values in various directions; in unidirectional composites, the longitudinal thermal conductivity ( $\lambda_l$ ) is fibre controlled while the transverse ( $\lambda_t$ ) is matrix controlled. For this reason, CFRPs are characterized by high longitudinal thermal conductivity, due to the high thermal conductivity of carbon fibres.

These statements are based on the available theories for predicting the thermal conductivity of unidirectional FRPs in the direction parallel and perpendicular to fibre axis. These theories provide the FRP thermal conductivity as a function of fibre and matrix properties and volume fractions (Springer and Tsai, 1967, )

$$\lambda_l = \lambda_{fibre}V_{fibre} + \lambda_{matrix}V_{matrix} \quad (3.12)$$

$$\frac{1}{\lambda_t} = \frac{V_{fibre}}{k_{fibre}} + \lambda_{matrix} \frac{V_{matrix}}{k_{matrix}} \quad (3.13)$$

Generally, the thermal conductivities of FRPs are low, if compared to that of other structural materials, such as steel and concrete.

The thermal conductivity, as well as other important thermal properties, such as specific heat and density, are temperature dependent, but very limited information are available, especially for temperatures above 400°C.

Bisby et al (2005b) collected typical values of thermal conductivities for various FRP materials at room temperature and the experimental works on the variation of the thermal properties available for FRPs in the literature. Griffis et al (1984) tested carbon/epoxy FRP by subjecting specimens to radiant heat by laser irradiation up to temperatures of 3000°C. The results of these studies showed an initial thermal conductivity of about 1.4 W/mK, decreasing to about 0.2 W/mK at 500°C; then the thermal conductivity was almost constant with increasing temperature. Scott and Beck (1992) found that the thermal conductivity of the tested FRP varied almost linearly from 0.77 W/m°C to 0.85 W/m°C between the temperatures of 30°C and 135°C.

Sweeting et al (2004) conducted other studies on a carbon/epoxy FRP laminate with 45% fibre volume fraction. They found that the “in-plane” thermal conductivity varied almost linearly from 2 W/m°C to 3 W/m°C between the temperatures of 20°C and 170°C, while the “through-thickness” conductivity changed from approximately 0.5 to 0.7 W/m K in the same temperature range. It has to be noted that the in-plane conductivity was approximately four times the through-thickness conductivity.

It is clear that, generalizations about the thermal conductivity, both at room and elevated temperature, are not possible and specific tests for thermal characterizing FRPs are needed.

Note that the thermal conductivity of FRP bars is very hard to determine using the available commercial machine, usually designed for testing specimens with cylindrical/prismatic shape or plates.

#### *3.1.4.1 Evaluation of the thermal conductivity of a commercial CFRP bar*

The experimental program, aimed to the evaluation of the thermal conductivity of the *FireStrong* CFRP bar (Figure 3. 3), was conducted through the available machine at University of Edinburgh, which is the Holometrix Model TCHM-LT C-Matic, shown in Figure 3. 28. The C-MATIC measures the thermal conductivity of solid materials through a guarded heat flow meter. The test sample is a cylinder, 50 mm diameter and maximum 20 mm thick. It is placed between two plates controlled at different temperatures, resulting in a heat flow from the hotter (lower) to the colder (upper) plate (Figure 3. 29). A thin heat flux

transducer, attached to the lower plate, measures the amount of heat. A cylindrical guard heater, maintained at or near the mean sample temperature, surrounds the sample, in order to minimize lateral heat transfer. Built-in thermocouples measure the overall temperature difference between the two surfaces in contact with the sample. A thin layer of a commercially available heat sink compound is usually applied to the sample, to reduce the thermal resistance of the interfaces between the sample and adjacent surfaces.



Figure 3. 28 - Holometrix Model TCHM-LT C-Matic

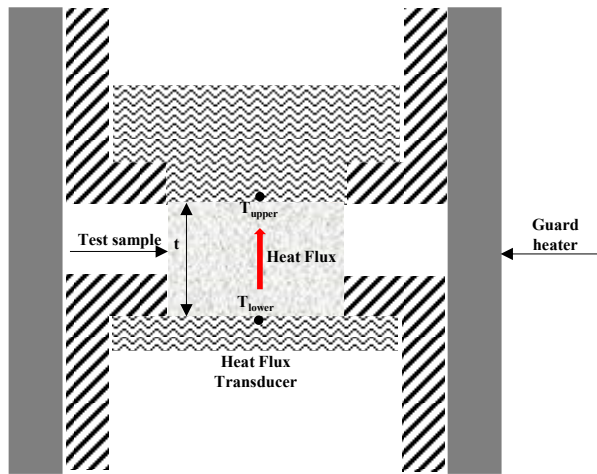


Figure 3. 29 - Scheme of C-Matic (Netzsch Instruments, Inc)

When the sample achieves the thermal equilibrium (steady state), the Fourier heat flow equation may be applied, providing the sample thermal resistance ( $R_s$ ), as shown in equation (3. 14),

$$R_s = N \frac{T_l - T_u}{Q} - R_0 \quad (3. 14)$$

where:

$N$  is a proportionality constant;

$T_l$  is the lower surface temperature,

$T_u$  is the upper surface temperature,

$Q$  is the heat flux transducer output,

$R_0$  is the contact thermal resistance.

Then, the thermal conductivity ( $\lambda$ ) may be calculated as shown in (3. 15)

$$\lambda = \frac{t}{R_s} \quad (3. 15)$$



where  $t$  is the sample thickness.

The C-MATIC machine needs a calibration at different temperature values, by testing samples with known thermal conductivity, in order to obtain the dependent parameters  $N$  and  $R_0$ .

The reference materials are the Vespel SP1, 12 mm thick, and the PYREX 7740 (6mm and 12 mm thick).

### 3.1.4.2 Specimens' preparation and tests' settings

Since the testing material is a CFRP bar of 8 mm diameter, the specimen's shape is not suitable in C-MATIC machine.

The idea was to test small CFRP samples (Figure 3. 30), extracted by the core of the bar, embedded in an insulation cylinder (Figure 3. 31) with known thermal conductivity ( $\lambda_{insulation}$ ). Measuring the thermal conductivity of the overall specimen (insulation plus CFRP,  $\lambda_{tot}$ ), the CFRP thermal conductivity ( $\lambda_{CFRP}$ ) may be determined through the generally valid equation (3. 16) .

$$\lambda_{tot} = \lambda_{CFRP} \frac{V_{CFRP}}{V_{tot}} + \lambda_{insulation} \frac{V_{insulation}}{V_{tot}} \quad (3. 16)$$

where:

$\frac{V_{CFRP}}{V_{tot}}$  is the CFRP volume fraction,

$\frac{V_{insulation}}{V_{tot}}$  is the insulation volume fraction.



Figure 3. 30 - CFRP samples

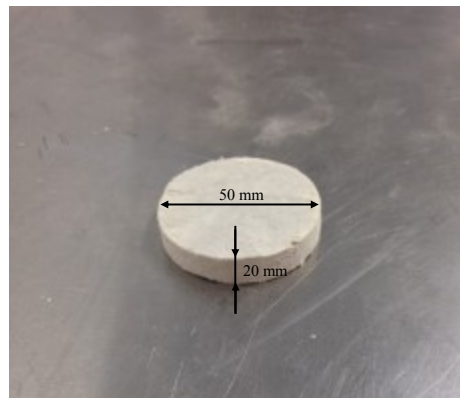


Figure 3. 31 - Insulation cylinder

The tests were conducted on six specimens, by varying the CFRP volume fraction and the fibre orientation. Particularly, three tests were performed

embedding CFRP samples in the insulation cylinder with fibres parallel to the direction of the heat flux (Figure 3. 32), in order to find the CFRP longitudinal thermal conductivity. Moreover, three tests were carried out embedding CFRP samples in the insulation cylinder with fibres perpendicular to the direction of the heat flux (Figure 3. 32), in order to find the CFRP transverse thermal conductivity.

Before testing, as recommended, the Dow Corning 340 heat sink compound was applied sparingly to both specimen surfaces (Figure 3. 33).

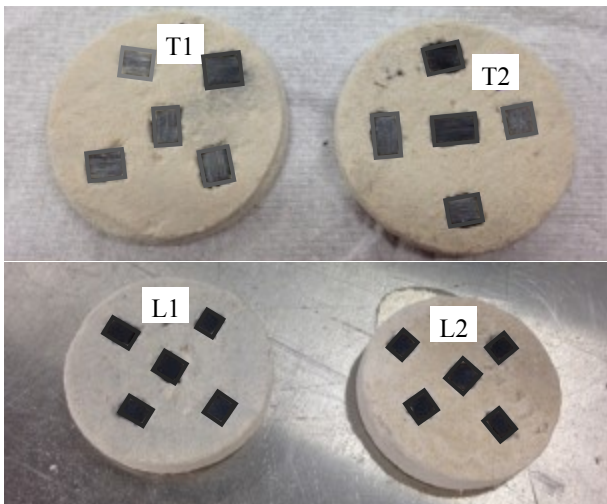


Figure 3. 32 - Specimens for thermal conductivity tests (L=longitudinal; T=transversal)



Figure 3. 33 - Specimen covered by the heat sink compound

The tests were conducted for four temperature values within the machine temperature range:  $T_1=50^{\circ}\text{C}$ ;  $T_2=100^{\circ}\text{C}$ ;  $T_3=150^{\circ}\text{C}$ ;  $T_4=200^{\circ}\text{C}$ .

### 3.1.4.3 Test results and discussion

Table 3. 11 summarizes the test results. As expected, the longitudinal thermal conductivity is significantly higher than the transverse one (about six times). Moreover, the thermal conductivities vary almost linearly in the analysed temperature range: the longitudinal thermal conductivity ranges between  $5.72\text{ W/m}^{\circ}\text{C}$  and  $7.54\text{ W/m}^{\circ}\text{C}$  in the temperature range  $50^{\circ}\text{C}$ - $200^{\circ}\text{C}$  (Figure 3. 34); the transverse conductivity varies from  $0.99\text{ W/m}^{\circ}\text{C}$  to  $1.29\text{ W/m}^{\circ}\text{C}$  in the same temperature range (Figure 3. 35).

Table 3. 11 - CFRP Thermal conductivity. Test results

Label(CFRP Volume fraction)	CFRP thermal conductivity (W/mk)			
	50°C	100°C	150°C	200°C
L1 <sub>(6.34)</sub>	5.14	5.86	6.27	6.87
L2 <sub>(7.58)</sub>	5.86	6.59	6.99	7.59
L3 <sub>(8.30)</sub>	6.17	7.01	7.49	8.15
$\mu_L$	<b>5.72</b>	<b>6.49</b>	<b>6.92</b>	<b>7.54</b>
$\sigma_L$	<b>0.52</b>	<b>0.47</b>	<b>0.50</b>	<b>0.52</b>
<b>Cov (<math>\sigma</math>)</b>	<b>0.09</b>	<b>0.07</b>	<b>0.07</b>	<b>0.07</b>
T1 <sub>(5.80)</sub>	0.77	0.81	0.81	0.88
T2 <sub>(9.39)</sub>	1.32	1.38	1.44	1.90
T3 <sub>(10.60)</sub>	0.91	0.98	0.99	1.08
$\mu_T$	<b>0.99</b>	<b>1.06</b>	<b>1.08</b>	<b>1.29</b>
$\sigma_T$	<b>0.28</b>	<b>0.29</b>	<b>0.32</b>	<b>0.54</b>
<b>Cov (<math>\sigma</math>)</b>	<b>0.29</b>	<b>0.28</b>	<b>0.30</b>	<b>0.42</b>
$\mu_L/\mu_T$	<b>5.73</b>	<b>6.11</b>	<b>6.40</b>	<b>5.86</b>

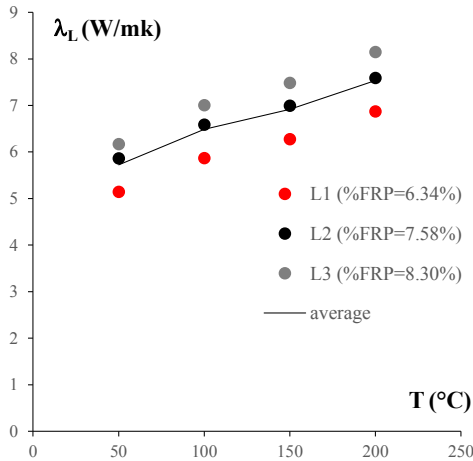


Figure 3. 34 - CFRP Longitudinal thermal conductivity vs Temperature

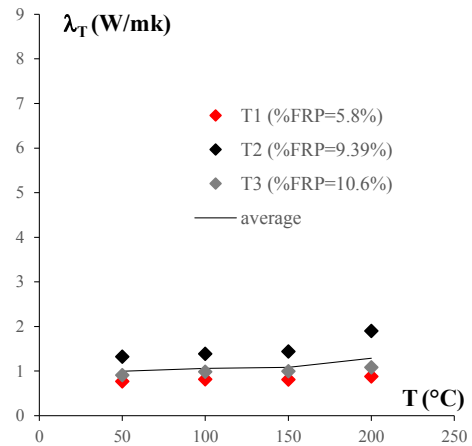


Figure 3. 35 - CFRP Transverse thermal conductivity vs Temperature

### 3.1.5 Thermal conductivity tests of cementitious mortar

This section summarizes the results of thermal conductivity tests, carried out on a cementitious grout, manufactured by *Milliken* and denominated *FireStrong Grout*. It is a pumpable grout, high flow, unsanded, especially formulated for the grouting of *FireStrong* bars (Figure 3. 3) in the typical groove of the NSM

strengthening system. The water/cement ratio of the mix was set equal to 0.23, according to the manufacturer technical data sheet.

The testing machine is Holometrix Model TCHM-LT C-Matic, presented in the previous section.

The thermal conductivity tests were conducted on the specimens shown in Figure 3. 36, which were cast and allowed to cure for 8 months. This is, actually, a period longer than that needed for the curing of this material (2-3 months).

The tests were conducted for four temperature values within the machine temperature range:  $T_1=50^\circ\text{C}$ ;  $T_2=100^\circ\text{C}$ ;  $T_3=150^\circ\text{C}$ ;  $T_4=175^\circ\text{C}$ .



Figure 3. 36 – Specimens of cementitious mortar for thermal conductivity tests

The Figure 3. 37 depicts the thermal conductivity ( $\lambda$ ) of this cementitious mortar versus temperature, showing that the thermal conductivity is almost constant in that temperature range and equal to about 0.55 W/(m K). It should be noted that  $\lambda$ , only at  $100^\circ\text{C}$ , assumed a value slightly higher than that obtained at  $50^\circ\text{C}$ ,  $150^\circ\text{C}$  and  $175^\circ\text{C}$ . This is clearly related to the water evaporation at  $100^\circ\text{C}$ , which led to a greater energy absorption than that needed to maintain a certain gradient of temperature in the sample, at other testing temperatures.

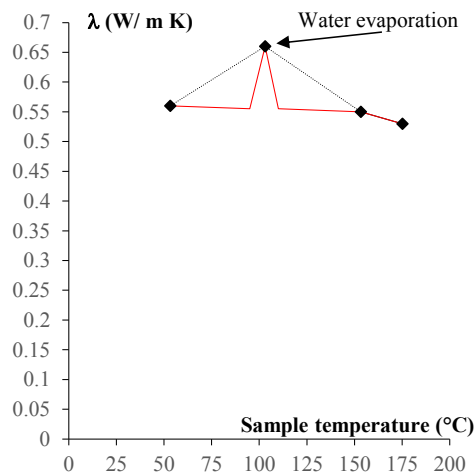


Figure 3. 37 – Cementitious mortar's thermal conductivity vs Temperature

Therefore, the bilinear branch depicted in Figure 3. 37 in the temperature range 50-150 °C is not representative of the variation of the thermal conductivity in the same range. Instead, it is very likely that  $\lambda$  is almost constant in the range 50-150 °C and equal to about 0.55 W/(m K), having a sudden increase from 0.55 W/(m K) to 0.66 W/(m K) in a small range around 100°C (red line).

Note that these values of thermal conductivity are also according to that provided by Chung (2001) for several cementitious mortars (see Table 2. 1).

## 3.2 MECHANICAL PROPERTIES OF MATERIALS

This section provides information about the techniques commonly applied to characterize the mechanical properties of the structural materials. Particularly the tests were conducted on the materials, which were used to manufacture the NSM FRP strengthened RC beams, tested at ambient and high temperature (Chapter 5).

### 3.2.1 Concrete tests at ambient temperature

The mix design of the concrete batch, used to manufacture the RC beams, is summarized in Table 3. 12.

Table 3. 12 - Concrete batch

COMPONENTS	QUANTITY	MOISTURE
Ordinary Portland Cement (OPC)	1002 kg	6.6
Ground Granulated Blast Furnace Slag (GGBFS)	669 kg	
Sand	1456 kg	
Aggregate 4/10 mm	3420 kg	
Additive Plastiment 180	5.04 kg	
Additive ViscoCrete 35RM	6720 ml	
Water	439 l	
W/C	0.44	

This concrete batch was characterized through compression and indirect tension tests of cylindrical specimens, 200 mm high and 100 mm diameter. After the concrete cast, the cylinders were stored in a room with controlled temperature and humidity.

The tests were conducted at 28 days and at 76 days (tests days of NSM FRP strengthened RC beams at ambient temperature).

### 3.2.1.1 Tests at 28 days

The tests at 28 days were performed through the AVERY 7104 Compression and Tension testing machine.

The compression tests were carried out in the loading range 1000 kN, with a loading rate equal to  $0.26 \text{ N}/(\text{mm}^2\text{s})$ , according to ASTM C39 and UNI-EN 12390-3.



Figure 3. 38 - Avery 7104 Compression and tension testing machine

Table 3. 13 summarizes the compression test results, showing that the mean value of compressive strength of this concrete batch at the age of 28 days is about 36 MPa. It should be noted that the blended cement of this concrete batch is 60% OPC (ordinary portland cement) and 40% GGBFS (ground granulated blast furnace slag). This is a very high GGBFS content, which may retard the strength gain of the mix, leading to higher strengths at later ages.

Table 3. 13 - Compression test results (28 days)

Label	Weight (g)	$P_{failure}$ (kN)	$f_c$ (MPa)	$f_{cm}$ (MPa)
C1	3920	278	35.4	35.6
C2	3949	264	33.6	
C3	3954	298	37.9	

The tensile strength of the concrete was evaluated through split-cylinder tests according to IS:1999 5816-1970.

The Figure 3. 39 depicts a scheme of the apparatus for splitting cylinders, while the Figure 3. 40 shows a cylinder placed in the apparatus, on the loading surface of the Avery. The compression load was applied diametrically and uniformly along the length of the cylinder until its failure, which was a splitting into halves. A strip of plywood was placed between the specimen and the loading

plates of the test machine, in order to allow a uniform distribution of stresses and to reduce the magnitude of compressive stresses near the points of application of this load.

The loading condition usually produces a high compressive stress, acting for about 1/6 specimen depth, and a tensile stress, due to Poisson effect, for the remaining 5/6, as estimated in literature.

Based on these assumptions and considering that the specimen behaves as an elastic body, the uniform lateral tensile stress  $f_{ct}$ , which causes the failure along the vertical plane, may be calculated as shown in (3. 17)

$$f_{ct} = \frac{2P_{failure}}{\pi Dh} \quad (3. 17)$$

where:

$P_{failure}$  is the compressive failure load;

$D$  is the diameter of the specimen;

$h$  is the height of the specimen.

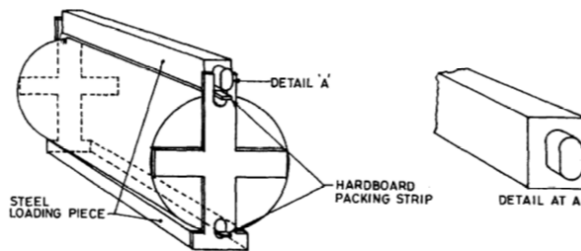


Figure 3. 39 - Scheme of apparatus for splitting cylinders (IS:1999 5816-1970)



Figure 3. 40 - Apparatus for splitting cylinder test

The Table 3. 14 summarizes the tension test results, showing that the mean value of tensile strength of this concrete batch at the age of 28 days is about 3.8

MPa. As expected, the “Splitting tensile strength” of this concrete batch ranges between  $(\frac{1}{8} \div \frac{1}{12})$  of the compressive strength.

Table 3. 14 - Tension test results (28 days)

Label	Weight (g)	Weight 1 <sup>st</sup> split half	Weight 2 <sup>nd</sup> split half	$P_{failure}$ (kN)	$f_{ct}$ (MPa)	$f_{ctm}$ (MPa)
T1	3911	1734	1984	130.5	4.15	3.83
T2	3963	1721	2085	120	3.82	
T3	3894	1939	1907	110	3.50	

### 3.2.1.2 Tests at 76 days

The tests at 76 days were performed through the INSTRON 600 LX, which have capacity 600 kN.

The compression tests were conducted with a loading rate equal to  $0.26 \text{ N}/(\text{mm}^2\text{s})$ , according to ASTM C39 and UNI-EN 12390-3.

Table 3. 15 summarizes the compression test results, showing that the mean value of compressive strength of this concrete batch at the age of 76 days is about 48 MPa.

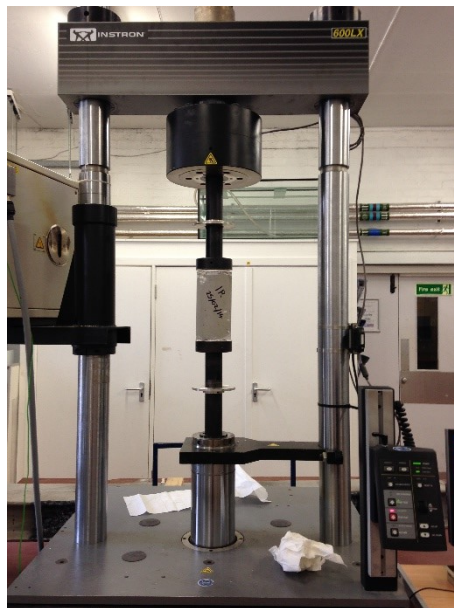


Figure 3. 41 - Instron 600 LX Compression and tension testing machine



Table 3. 15 - Compression test results (76 days)

Label	$P_{failure}$ (kN)	$f_c$ (MPa)	$f_{cm}$ (MPa)
C1	369	46.9	47.7
C2	381	48.5	

### 3.2.2 Steel tensile tests at ambient temperature

The longitudinal steel reinforcement of the testes RC beams consisted of 2 rebars, 10 mm diameter ( $d_0$ ), for use in tension, and 2 rebars, 6 mm diameter, placed in compression side (Figure 5. 2).

In order to define the constitutive law, the rebars used in tension, were tested through the INSTRON 600 LX (Figure 3. 42). A unidirectional tensile load was applied with a constant speed deformation equal to 2mm/min. The free length ( $L$ ) of the tested specimens was 460 mm, the grip's length ( $L_g$ ) was about 55 mm, therefore the total length ( $L_T$ ) of the specimen was 570 mm.

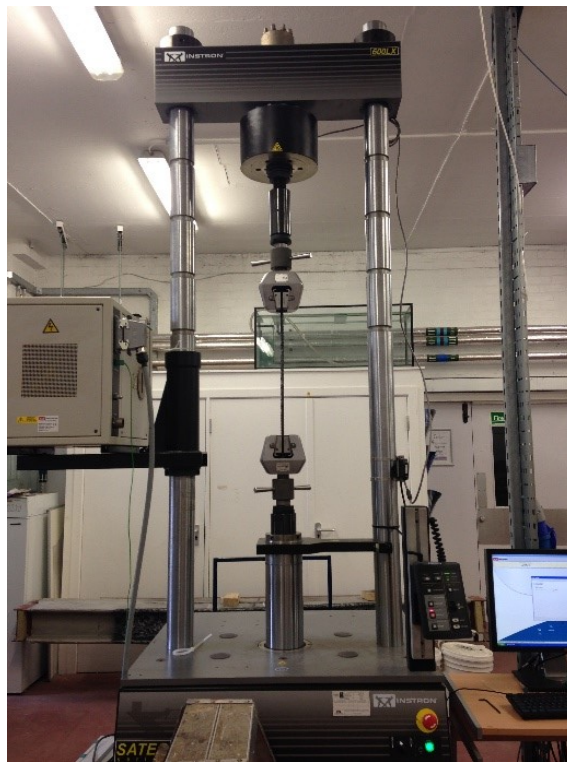


Figure 3. 42 - INSTRON 600 LX set for tensile test

A high resolution camera (CANON EOS 5D MARK II) was placed just in front of the testing machine (Figure 3. 43), and it was set for automatically taking pictures every 5 s. The specimen was painted with white random dot, in order to enable the pictures' processing through the Digital Image Correlation (DIC, see section 5.2.1). This technique revealed to be very useful for measuring displacement and strain, as shown in the following. The strain was calculated considering a gage length ( $L_0$ ) equal to  $5d_0$ , according to BS EN 10002-1:2001. The Figure 3. 44 shows the patches monitored through the DIC.

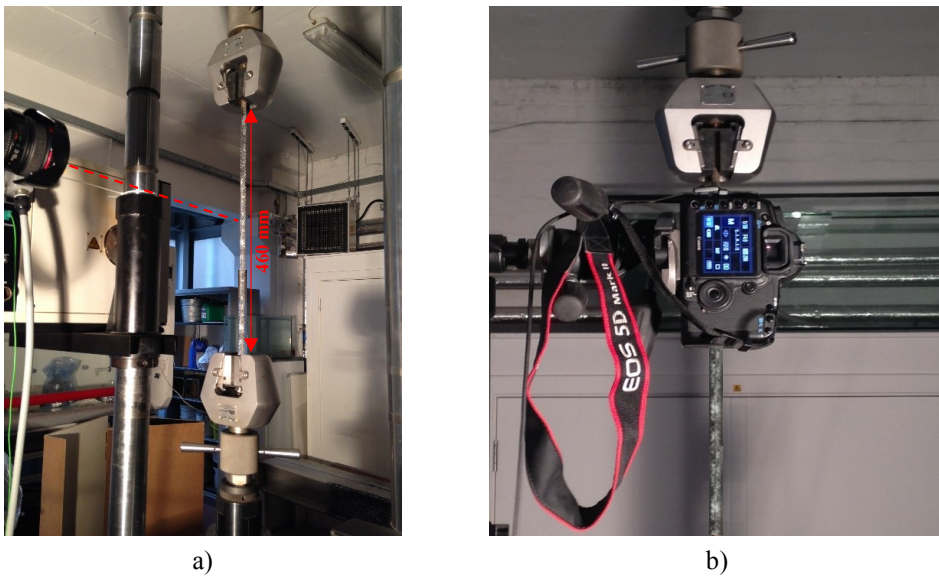


Figure 3. 43 - Camera's position during tensile tests: a) isometric view; b) front view

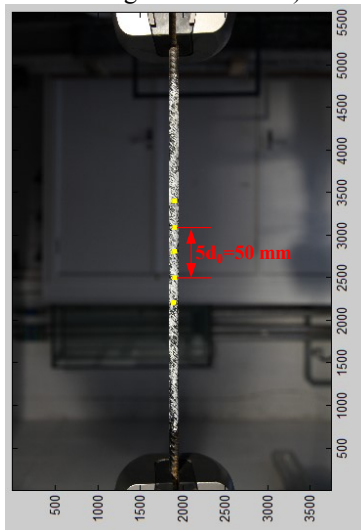


Figure 3. 44 - Patches monitored through DIC (Steel tensile test)

The tensile tests provided the steel constitutive law, shown in Figure 3. 45. This figure shows that the yielding strength is equal to about 525 MPa, corresponding to a strain equal to about 2.5%, since the elastic modulus is 210000 MPa (Figure 3. 46). In the hardening stage, which started with a strain value equal to 3%, the load increased up to the tensile strength equal to about 622 MPa.

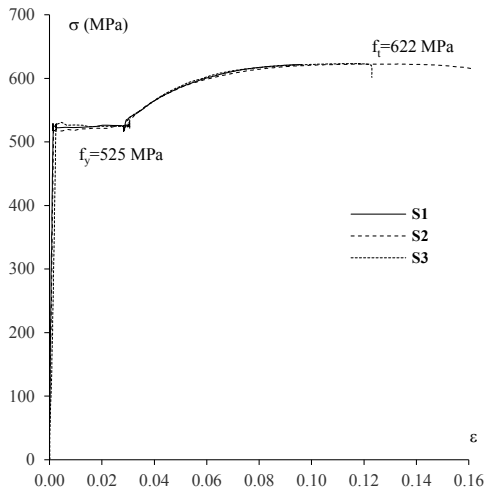


Figure 3. 45 - Steel constitutive law

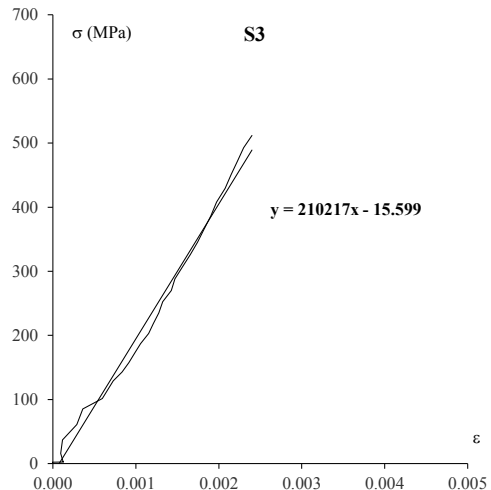


Figure 3. 46 - Elastic branch of the constitutive law

### 3.2.3 Compression test of Cementitious grout at ambient temperature

This section summarizes the results of a compression test, carried out on the *FireStrong Grout*. As already stated in section 3.1.5, it is a pumpable grout, high flow, unsanded, especially formulated for the grouting of *FireStrong* bars in the typical groove of the NSM strengthening system.



Figure 3. 47 - Mixing procedure (Contractor Training Manual)

The grout was mixed in a high-speed mixer with the prescribed volume of potable water, until a uniform consistency was achieved, according to the Contractor Training Manual (Figure 3. 47).

The water/cement ratio of the mix was set equal to 0.23, according to the manufacturer technical data sheet.

The tested specimen was a cylinder, 100 mm high and 50 mm diameter. (Figure 3. 48).

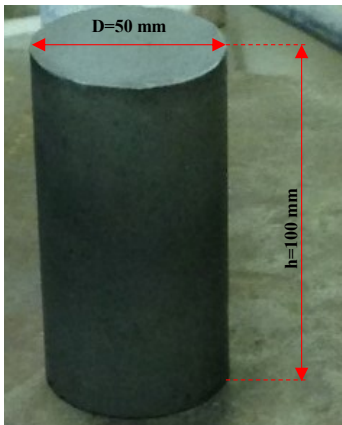


Figure 3. 48 - Specimen for compression test of the cementitious grout



Figure 3. 49 - 810 Material Testing Machine (MTS)

The compression test was carried out through the 810 Material Testing Machine (MTS), shown in Figure 3. 49, at the Material and Structures Laboratory of University of Naples.



Figure 3. 50 - 810 Failure mode of the tested specimen

The failure load of the tested specimen was 176 kN, therefore the ultimate strength of the grout is about 90 MPa, which is in accordance with the compressive strength at 28 days, provided by the manufacturer. The Figure 3. 50 shows the failure mode of the tested specimen.

### 3.2.4 FRP tensile tests at ambient temperature

The *FireStrong* CFRP bars, used to strengthen the RC beams through the NSM technique, were spirally wound round rods, 8 mm diameter.

In order to define the constitutive law, 3 tensile tests were conducted. The free length ( $L$ ) of the tested specimens was 300 mm ( $\sim 40d$ ), according to ACI 440R.3R-04, the grip's length ( $L_g$ ) was 350 mm, therefore the total length ( $L_T$ ) of the specimens was 1000 mm.

The ends of the bars were embedded in steel tubes using the two-component superfluid resin MAPEI EPOJET (Figure 3. 51).



Figure 3. 51 - Specimens' preparation: CFRP bars embedded in gripping steel tubes

The bar was loaded by gripping the steel tubes in the friction wedge of the Material Testing System (MTS), shown in Figure 3. 52. A unidirectional tensile load was applied with a constant speed deformation equal to 2mm/min. A high performance camera (NIKON D810) was placed just in front of the testing machine (Figure 3. 52), and it was set for automatically taking pictures every 1 s. The specimen was painted with white random dot (Figure 3. 53), in order to enable the pictures' processing through the Digital Image Correlation (DIC). This technique provided the bar's strain, which was calculated considering a gauge length ( $L_0$ ) equal to 50 mm, according to ASTM D 3039/D 3039M. The Figure 3. 54 shows the patches monitored through the DIC. The strain provided by the DIC was compared to that obtained through a traditional strain gauge, placed at

the mid-length of one of the tested bars (Figure 3. 53). It should be noted that, in order to enable the strain gauge placement, the bar was accurately made smooth in the area of strain gauge attachment.

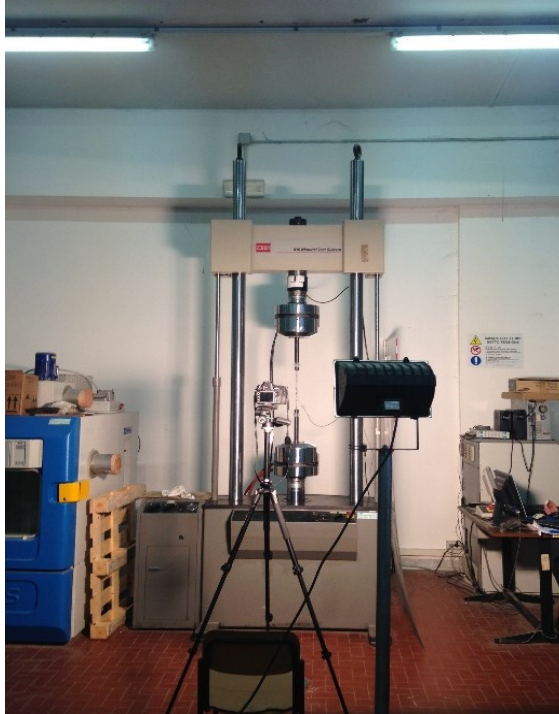


Figure 3. 52 - MTS set for tensile test

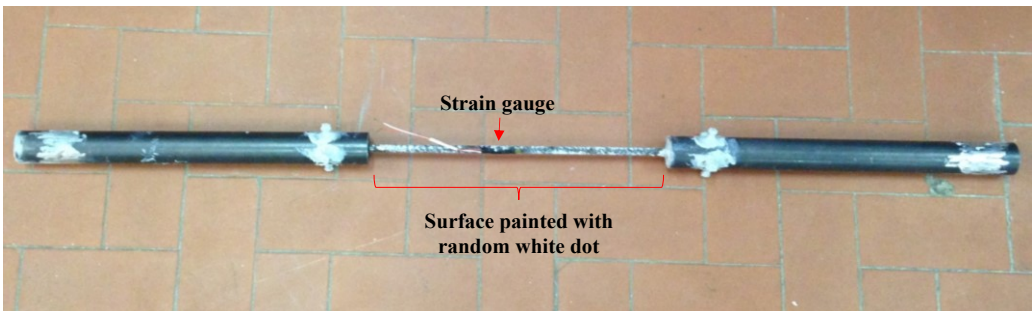


Figure 3. 53 - Bar instrumented with strain gauge and painted for DIC

The tested specimens failed with a typical tensile failure mode (Figure 3. 55), under the tensile load 88 kN, which corresponds to the ultimate stress 1750 MPa. The Figure 3. 56 shows the stress-strain relationships of the three tested CFRP specimens. It enabled the comparison between the strain obtained through the DIC and that read by the strain gauge.

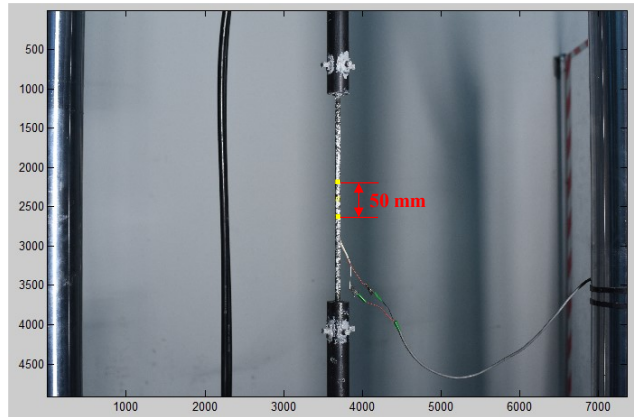


Figure 3. 54 - Patches monitored through DIC (CFRP tensile test)



Figure 3. 55 - Failure mode of the tested specimens

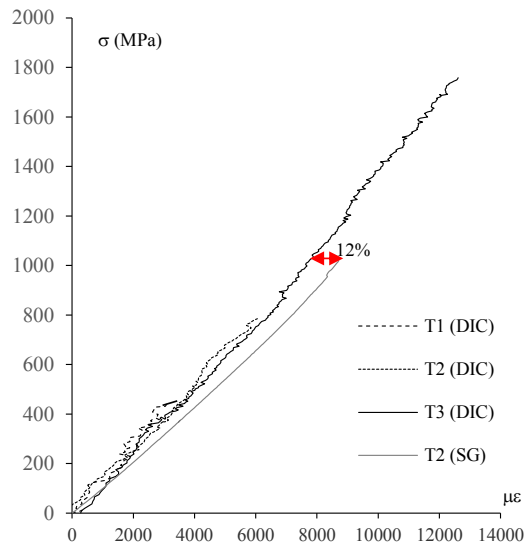


Figure 3. 56 - Stress-strain relationships of CFRP

The strain gauge provided strain values almost 12% higher than that provided by the DIC. Obviously, the strain obtained through the strain gauge may be

influenced by the treatment, made to get a smooth surface in the area of strain gauge attachment, and by the properties of the used glue. Moreover, the strain gauge detached when the stress in the bar reached about 1000 MPa. Conversely, the DIC provided strain values of the tested specimens with a very good agreement but, due to an acquisition mistake, some data were lost during the final stage of two tests. Actually, the collected data might be sufficient for the calculation of the elastic modulus, which is usually determined in the loading range equal to 25%-50% of the ultimate load, according to CAN/CSA-S806-02 and ASTM D 3039/D 3039M. Based on the interpolation of the experimental data, shown in Figure 3. 57, the mean value of the elastic modulus is 136 GPa, the coefficient of variation is about 4% and, finally, the ultimate strain is 1.28%.

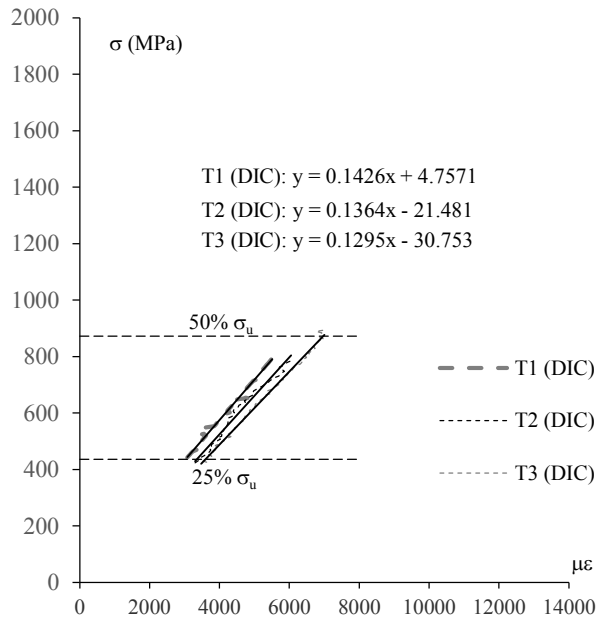


Figure 3. 57 - Interpolation of CFRP stress-strain relationships



## ***Chapter 4 - Bond tests at ambient temperature***

The efficiency of the Near Surface Mounted (NSM) fibre-reinforced polymer (FRP) technique depends on several parameters, namely: the materials' mechanical properties, the dimension and surface treatment of the grooves, the geometry of the FRP product, the position of the FRP reinforcement in the groove, the type of bonding agent.

Several studies have presented experimental bond tests and have shown that the bond between concrete and FRP is particularly efficient if epoxy adhesive is used (see Chapter 2), whereas relatively few tests are available using cementitious grout. However, FRP-NSM systems with cementitious adhesives may perform better at high temperatures because: (a) cementitious grout is not as severely affected as typical epoxies by elevated temperature; (b) the cementitious grout can provide additional thermal protection to the FRP bars; and (c) the resin of the FRP bar, which is manufactured by pultrusion, typically has a glass transition temperature  $T_g$  higher than common in-situ cured epoxy resins used in wet pay-up FRP strengthening applications.

This chapter summarizes all the meaningful data of the experimental program, conducted at University of Naples, aimed to analyze the bond-slip behaviour of NSM FRP strengthened RC elements. Particularly, a series of bond pull-out tests were performed on concrete specimens strengthened with a specific carbon (CFRP) NSM system, which has been developed specifically to address the performance of FRP strengthening systems at elevated temperatures, to investigate the bond between FRP and concrete for different bonding agents and positions of the bar in the groove.

### **4.1 EXPERIMENTAL PROGRAM**

The experimental program consisted of 14 bond tests on NSM system. The specimens were prismatic concrete blocks, strengthened with a specific CFRP

NSM system. The prismatic concrete blocks were cast in the same batch (see section 4.1.1) and they had the following dimension: width,  $b_c$ , equal to 160 mm; depth,  $d_c$ , equal to 200 mm; length,  $L_c$ , equal to  $L_b + 2 L_{free}$ , where  $L_{free}$  is the unbonded length of the bar, set equal to 50 mm (Figure 4. 1 and Figure 4. 2).

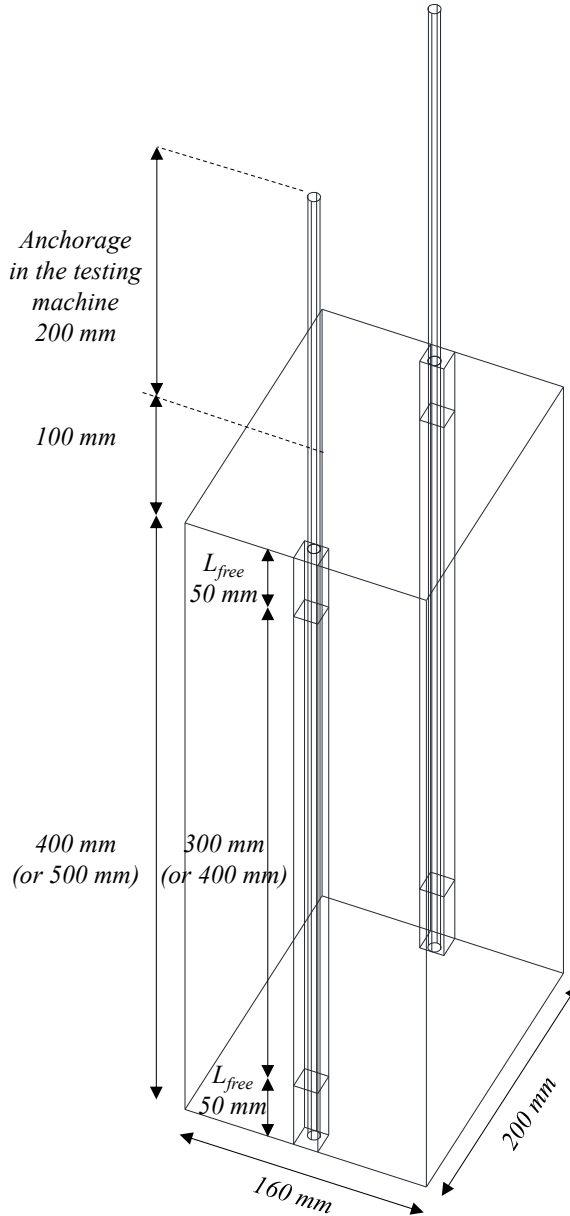


Figure 4. 1 – Scheme of a specimen for pull-out test (isometric view):

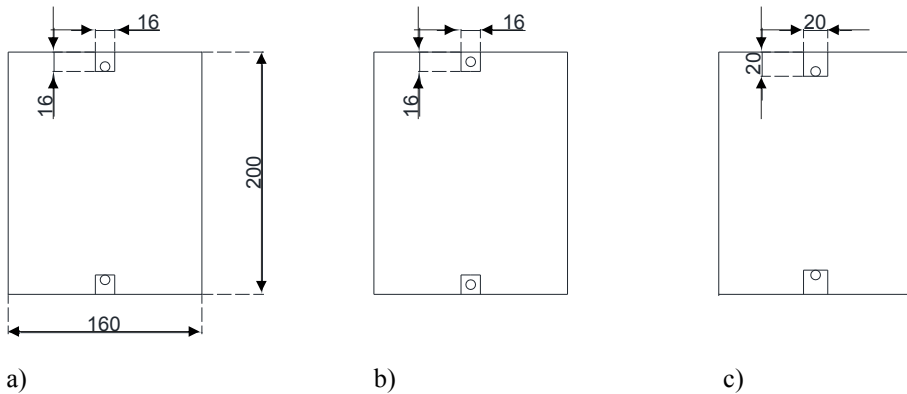


Figure 4. 2 – Scheme of a specimen for pull-out test (cross section): a)  $b_g$ 16-TOP; b)  $b_g$ 16-CENTRE; c)  $b_g$ 20-TOP

The mechanical properties of the concrete batch are summarised in section 4.1.1.

All the tests were conducted using the same FRP product that is the *FireStrong* CFRP bar, which properties are summarized in Chapter 3.

The Table 4. 1 summarizes the overall experimental program, made of two bond tests for each investigated parameter. Particularly, the tests were conducted varying the following parameters:

- the bonding length,  $L_b$ , (300 mm; 400 mm);
- the dimension of the square groove,  $b_g \times b_g$ , ( $16 \times 16 \text{ mm}^2$ ;  $20 \times 20 \text{ mm}^2$ );
- the position of the bar inside the groove (Top surface of the groove; Centre of the groove);
- the bonding agent (cementitious mortar; resin).

Table 4. 1 – Pull-out experimental program

Label	n	$L_b$ (mm)	$L_c$ (mm)	$b_g$ (mm)	Bar's position	Bonding agent
$L_b300-b_g16-T-CM$	2	300	400	16	TOP	Cementitious mortar
$L_b300-b_g16-C-CM$	2	300	400	16	CENTRE	Cementitious mortar
$L_b300-b_g16-T-R$	2	300	400	16	TOP	Resin
$L_b300-b_g16-C-R$	2	300	400	16	CENTRE	Resin
$L_b300-b_g20-T-CM$	2	300	400	20	TOP	Cementitious mortar
$L_b300-b_g20-T-R$	2	300	400	20	TOP	Resin
$L_b400-b_g16-T-CM$	2	400	500	16	TOP	Cementitious mortar

The cementitious mortar, used like bonding agent, is the *FireStrong Grout*, which was also used to manufacture the NSM-FRP strengthened RC beams that

were tested at ambient and at high temperature, as shown in Chapter 5. The properties of this material are summarized in Chapter 3.

The resin, used like bonding agent, is the commercial thixotropic ADESILEX PG1 epoxy resin, manufactured by MAPEI.

The Table 4. 2 lists important geometrical and mechanical parameters of the NSM strengthening, such as: the axial stiffness of the bar,  $E_f A_f$ , diameter of the bar,  $d$ ; the perimeter,  $p_g$ , of the groove; the perimeter of the NSM strengthening,  $p_{NSM}$ ; the shape ratio  $k$ , which is defined as  $\frac{b_g}{d}$  (De Lorenzis & Teng, 2007).

Table 4. 2 – Geometrical and mechanical properties of the NSM strengthening system

Label	$d$ (mm)	$E_f$ (GPa)	$E_f A_f$ (kN)	$p_g$ (mm)	$p_{NSM}$ (mm)	$k$
$L_b300-b_g16-T-CM$	8	136	6832	64	25.1	2
$L_b300-b_g16-C-CM$				64	25.1	2
$L_b300-b_g16-T-R$				64	25.1	2
$L_b300-b_g16-C-R$				64	25.1	2
$L_b300-b_g20-T-CM$				80	25.1	2.5
$L_b300-b_g20-T-R$				80	25.1	2.5
$L_b400-b_g16-T-CM$				64	25.1	2

It should be noted that the two investigated groove's dimensions ( $16 \times 16 \text{ mm}^2$ ;  $20 \times 20 \text{ mm}^2$ ) were chosen also considering that the shape ratio  $k$  needs to be greater than 1.5, in order to avoid the splitting failure of the epoxy (De Lorenzis & Teng, 2007; Ceroni et al, 2012)

#### 4.1.1 Fabrication and concrete properties definition

The concrete prisms were cast in the same batch, which mix design is summarized in Table 4. 3.

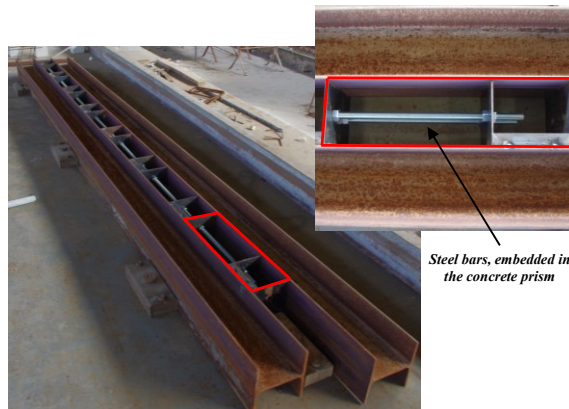


Figure 4. 3 – Steel formworks for casting of concrete prisms



a)



b)

Figure 4. 4 –Casting of concrete: a) concrete prisms; b) concrete cylinders

The casting was made using steel formworks, shown in Figure 4. 3. The Figure 4. 4 a and b depict respectively the casting of concrete prisms and cylindrical specimens. The latter were tested in compression, in order to define the compressive strength of this concrete batch.

Table 4. 3 - Concrete batch for prisms manufacturing

COMPONENTS	QUANTITY (per 1m <sup>3</sup> )
Cement (CEM_II_42.5_R)	380 kg
Sand	1456 kg
Aggregate 4/10 mm	825 kg
Superfluid (Chryso Premia 180)	4800 ml
Water	175 l
Water/Cement	0.46

Compression tests of cylindrical specimens, 200 mm high and 100 mm of diameter, were conducted at 28 days and at 63 days (bond tests days), through the Universal Testing Machine Mohr & Federhaff, which have capacity 400 kN.

Table 4. 4 summarizes the compression test results, showing that the mean value of compressive strength of this concrete batch at the age of 28 days was about 46 MPa, and it did not change significantly at 63 days, since it was 48 MPa.

Table 4. 4 - Compression test results (28 days, 63 days)

Age	Label	Weight (g)	$P_{failure}$ (kN)	$f_c$ (MPa)	$f_{cm}$ (MPa)
28 days	C1	3683	278	44.91	46.24
	C2	3704	264	47.33	
	C3	3710	298	46.48	
63 days	C1	3703	385	49.06	48.29
	C2	3699	381	48.54	
	C3	3712	371	47.27	

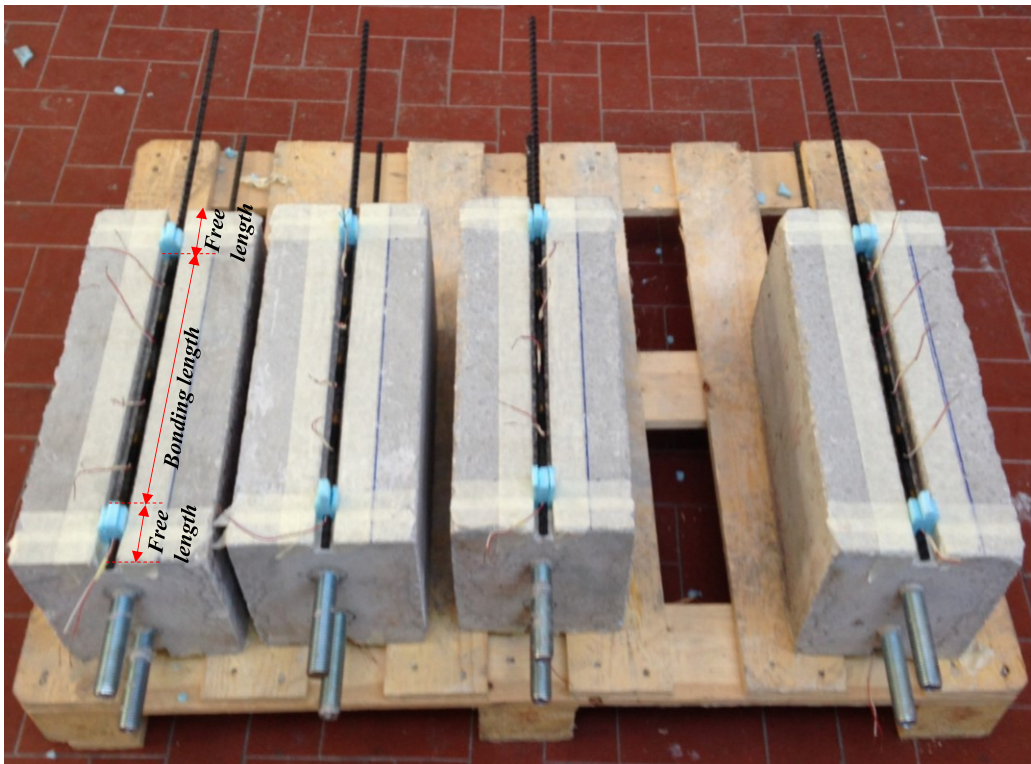


Figure 4. 5 – Placement of CFRP bars into the grooves

After concrete hardening, the bars were placed into the grooves, cut in the cover of the prisms (Figure 4. 5), and grouted through cementitious mortar (Figure 4. 6) or resin (Figure 4. 7). It should be noted that the strengthening was realized after the accurate cleaning of the grooves' surface; moreover, in case of

bonding through the resin, the grooves' surface was also treated through a primer (MAPEWRAP primer), as recommended by the manufacturer.

The Figure 4. 5, Figure 4. 6 and Figure 4. 7 show also that an unbonded length at both ends of the groove ( $L_{free}=50$  mm) was considered.



Figure 4. 6 – Casting of cementitious mortar in the groove



Figure 4. 7 – Placement of thixotropic resin in the groove

#### 4.1.2 Instrumentation

The local measurement of the strain along the bonded length of the bars was conducted by gluing strain gauges in five location on the CFRP bars before their placement and grouting inside the grooves (Figure 4. 8).



Figure 4. 8 – Strain gauges on CFRP bars

The spacing between the strain gauges was set equal to 70 mm and 90 mm respectively for the cases characterized by  $L_b$  equal to 300 mm (Figure 4. 9 a) and 400 mm (Figure 4. 9 b). This spacing should not influence the bond mechanism and enabled the local measurement of the bond shear stress. Note that several researchers tried to find a solution to the problem related to the attachment of strain gauges on the bonding length of the FRP. For instance, Seracino et al (2007), who tested FRP strip bonded in a NSM system, glued strain gauges to the strip every 50 mm on alternating sides so as not to compromise the bond on one side of the block.

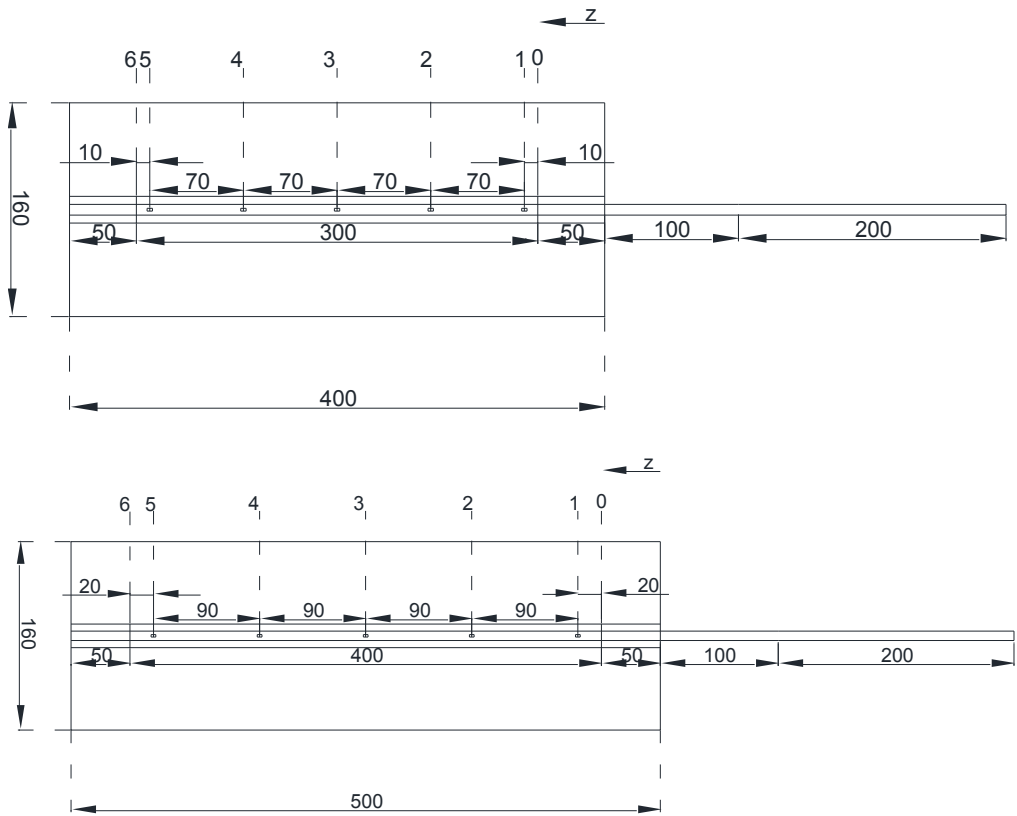


Figure 4. 9 – Strain gauges' spacing on CFRP bar: a)  $L_b$  300 mm;  $L_b$  400 mm



Figure 4. 10 – Installation of steel pipes at the end of the CFRP bars



Finally, steel pipes were installed at the end of the FRP bars and filled with MAPEI EPOJET epoxy resin (Figure 4. 10), in order to ensure adequate clamping in the grips of the testing machine.

### 4.1.3 Test setup

Researchers have used different test setup over the time to characterize the bond behaviour, since any standard procedure has yet been defined, even if it is well known that the testing procedure may influence the failure load (Aiello & Leone, 2008, Novidis and Pantazopoulos 2008, Yao et al. 2005;). The test setup, used for this experimental program, is a Single Shear Pulling test (definition given in Chen et al, 2001), which was adopted for other pull-out tests, conducted at University of Naples and Sannio (Bilotta et al, 2012; Ceroni et al, 2012), since it is considered reliable and not particularly affecting both the bond-slip relationship and the debonding load. Moreover, the single shear tests (SST) is a commonly used test (Costa & Barros, 2011; Savoia et al. 2009; Aiello & Leone, 2008; Ferracuti et al. 2008; Yao et al. 2005; Dai et al. 2005; Wu et al. 2001). Round Robin Tests initiative, also led to conclude that the SST setup is preferable as standard test method for characterizing the bond behaviour and strength of NSM FRP system. The higher simplicity of specimens preparation and of testing procedure cause a lower influence of detailing on the overall behaviour and lead to higher bond strength. Indeed, these main reasons justify the choice of such a set-up as standardized testing method (Bilotta et al, 2015).

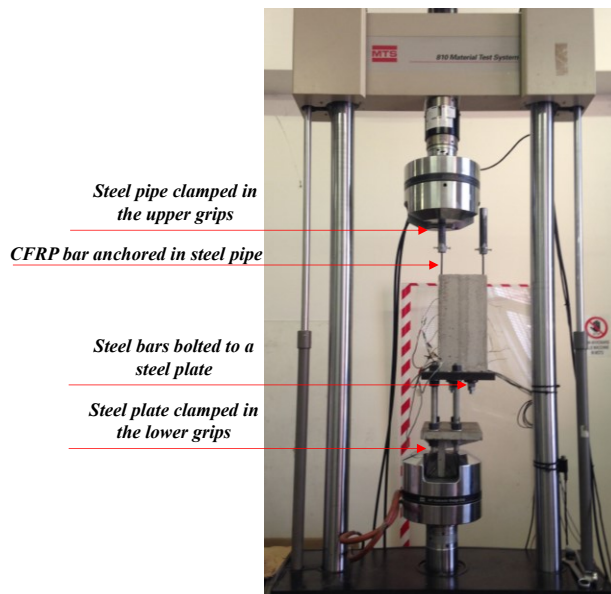


Figure 4. 11 – Single shear test setup

In practice, the single shear tests (SST) were conducted through the test setup shown in Figure 4. 11, which enabled to load the FRP bar in tension, whereas the concrete prism was blocked at the base of the Universal Material Testing Machine (MTS) by a couple of steel bars, 20mm diameter. The latter were embedded in the concrete prism (Figure 4. 3) and bolted to a steel plate, which was rigidly linked to a lower steel plate, clamped in the lower grips of the MTS.

The Figure 4. 11 clearly shows that two opposite sides of each concrete prism were strengthened, but each strengthened face was separately tested.

All tests were performed in displacement control with a speed of 0.015 mm/s.

## 4.2 RESULTS AND DISCUSSION

This section provide all the meaningful information about the results of the conducted tests.

The Figure 4. 12 (a to d) shows some specimens after the pull-out tests, highlighting that the failure occurred due to the debonding at bar/adhesive (B/A) interface, under the maximum load,  $P_{max}$ . Table 4. 5 summarizes the  $P_{max}$  values obtained for all the tested specimens. The peak values of the local shear stress,  $\tau_{max}$ , were evaluated based on the strains recorded by the strain gauges labelled as 1 and 2 (see Figure 4. 9), since between those the strain assumes fairly the maximum value. Generally, the shear stress of an FRP element between two following strain gauges (i and i+1) can be calculated based on the equilibrium equation

$$\tau_{i,i+1} = \frac{E_f A_f (\varepsilon_{i+1} - \varepsilon_i)}{p_f (z_{i+1} - z_i)} \quad (4. 1)$$

where:

$z_i$  and  $z_{i+1}$  define the location of the strain gauges i and i+1, with i ranging between 1 and 4;

$\varepsilon_i$  and  $\varepsilon_{i+1}$  are the local measurements of the strain respectively in  $z_i$  and  $z_{i+1}$ ;  
 $E_f A_f$  is the axial stiffness of the FRP (Table 4. 2);

$p_f$  is the perimeter of the bonded bar, assumed equal to  $p_{f,NSM}$  (Table 4. 2) since the failure occurred due to the debonding at bar/adhesive interface.

The measurement of the strains enabled also the calculation of the slip  $s_{i,i+1}$  corresponding to the shear stress  $\tau_{i,i+1}$ . The slip was practically calculated by integrating the strain from the un-loaded end, 6, to the opposite end, 0 (Figure 4. 9), where the theoretical strain,  $\varepsilon_0$ , assumes the following peak value:

$$\varepsilon_0 = \frac{P}{E_f A_f} \quad (4.2)$$

Thus, the slip  $s_{i,i+1}$  can be evaluated as in (4.3)

$$s_{i,i+1} = \sum_{k=i}^n (z_{k+1} - z_k) \left( \frac{\varepsilon_k + \varepsilon_{k+1}}{2} \right) \quad (4.3)$$

where  $n$  is the total number of strain gauges, which is 5 in this case.

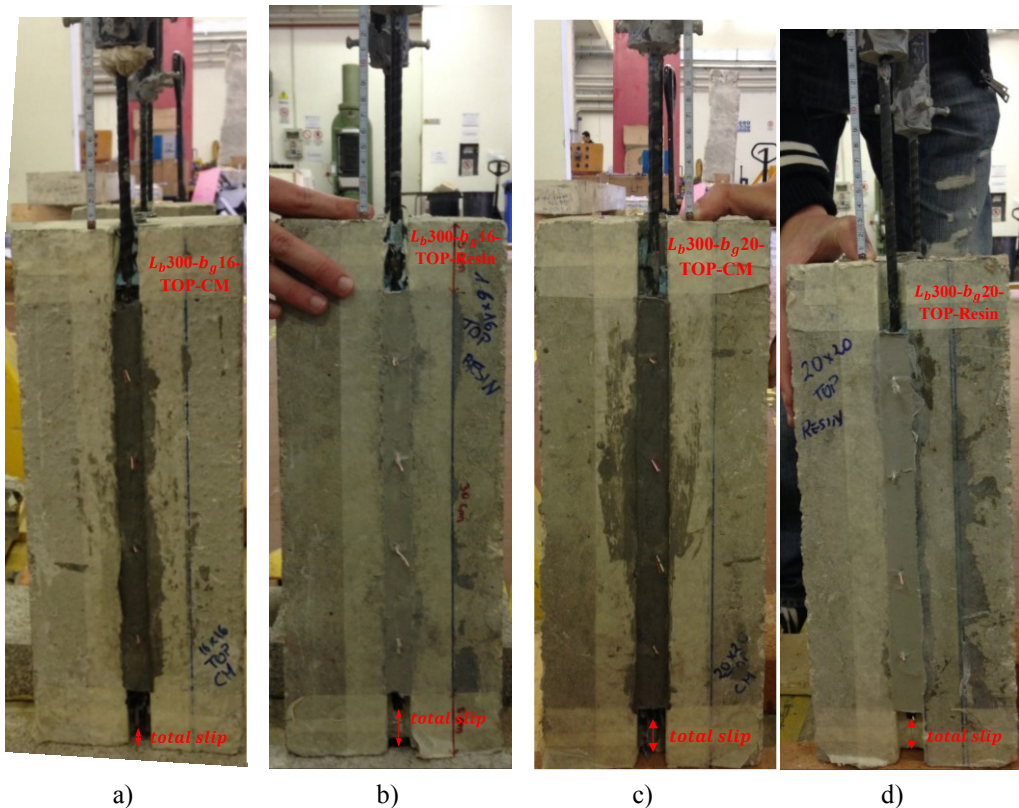


Figure 4. 12 – Specimens after pull-out test: a)  $L_b300-b_g16-T-CM$ ; b)  $L_b300-b_g16-T-R$ ; c)  $L_b300-b_g20-T-CM$ ; d)  $L_b300-b_g20-T-R$

In order to give information about the macroscopic bond behaviour of the tested specimens, the load ( $P$ ) was firstly plotted versus the crosshead displacement ( $\Delta$ ) of the testing machine, recorded during the tests. Referring to the specimens  $L_b300-b_g16-T-R$  and  $L_b300-b_g20-T-R$ , Figure 4. 13 shows that the maximum load recorded during the tests ( $P_{u,exp}$ ) was about 50 kN. After the achievement of  $P_{u,exp}$ , the curve  $P - \Delta$  shows subsequent peaks, ranging between 33-40 kN (66-80%  $P_{u,exp}$ ), representative of a sort of residual strength, based on

the interlocking mechanism between the adhesive resin and the ribbed bar. Referring to the specimens  $L_b300-b_g16-T-CM$  and  $L_b300-b_g20-T-CM$ , Figure 4. 14 shows that the maximum load was about 25 kN. In these cases, the specimens did not recover a significant residual strength, since it was only about 24% of  $P_{u,exp}$ . Note that, in order to evaluate the above mentioned residual strength, the specimens were tested until the achievement of very high slip values. It determined also the failure at adhesive/concrete (A/C) interface, after the main failure for debonding at B/A interface (Figure 4. 15). Figure 4. 13 and Figure 4. 14 show also that the dimension of the groove does not affect significantly the maximum load. Preliminarily, this seems to be in contrast to that shown by Bilotta et al (2014). They conducted a bond tests program using the same setup, specimens with the same shape and dimension, the same bonding length, a smooth CFRP bar with approximately the same elastic modulus, a different commercial resin as bonding agent and a very poor concrete, representative of the properties of existing structures. They stated that the efficiency of the NSM is also controlled by the groove dimension, which affects the maximum load. Moreover, the poor properties of the concrete they used affected the failure mode, which was at adhesive/concrete interface, whereas in the experimental program presented in this chapter the failure occurred always for debonding at B/A interface, since a high strength concrete was used. Therefore, it is very likely that the maximum load does not increase with the dimension of the groove when the failure for debonding at the B/A interface occurs.

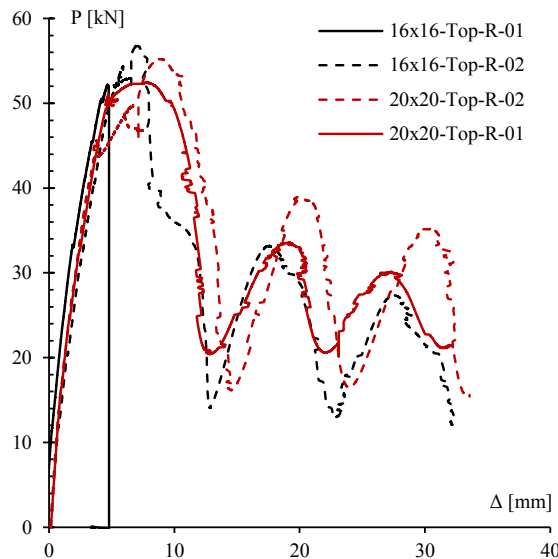


Figure 4. 13 – Load versus crosshead displacement ( $L_b300-T-R$ )

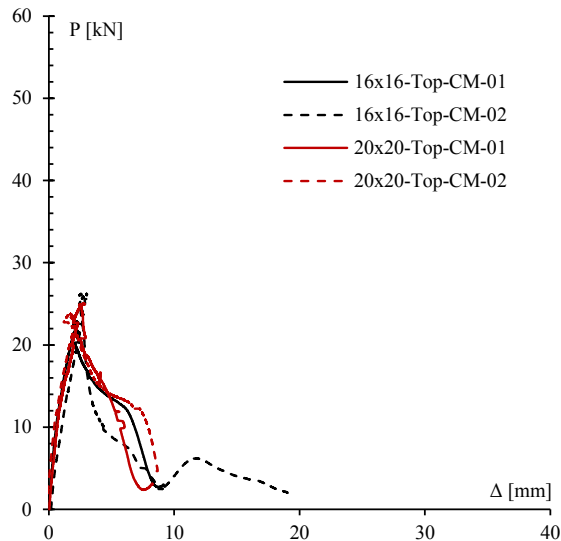


Figure 4. 14 – Load versus crosshead displacement ( $L_b300-T-CM$ )



Figure 4. 15 – Failure at A/C interface after the main failure at B/A interface

Obviously, the Figure 4. 13 and Figure 4. 14 cannot give any information about the stiffness of the strengthening system, since the crosshead displacement is not fully representative of the bond at B/A interface due to the slip between the anchorage and the grip as well as the elastic elongation of the FRP un-bonded length. Conversely,  $P$  versus  $s_0$  curve, where  $s_0$  is the total slip calculated at the loaded end according to (4. 3), enabled to define the stiffness of the strengthening system. Figure 4. 16 depicts  $P - s_0$  referring to the specimens  $L_b300-b_g16-TOP-R$  and  $L_b300-b_g20-T-R$ , showing that the dimension of the groove does not affect the stiffness of the strengthening, as well as the maximum load. A similar result was obtained referring to the specimens  $L_b300-b_g16-T-CM$  and  $L_b300-b_g20-T-CM$  (Figure 4. 17). These results confirmed the results shown in Bilotta et al (2014).

Figure 4. 18 shows the comparison between  $L_b300-b_g16-T-CM$  and  $L_b300-b_g16-T-R$ , highlighting that the strengthening with resin is stiffer than that with cementitious mortar.

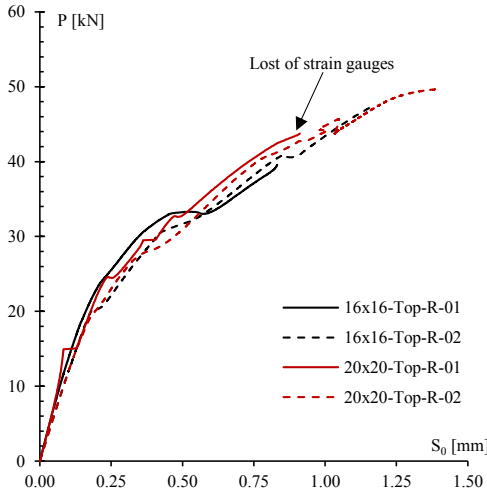


Figure 4. 16 – Load versus total slip ( $L_b300-T-R$ )

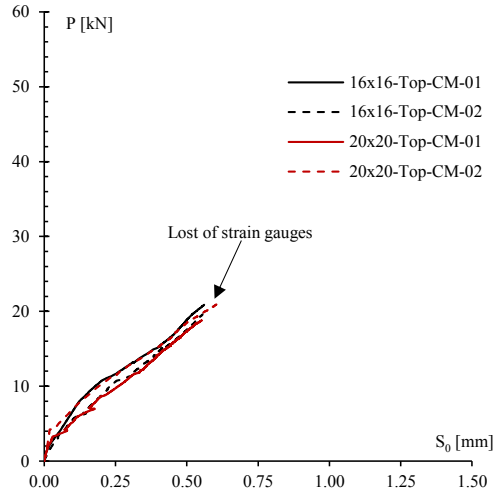


Figure 4. 17 – Load versus total slip ( $L_b300-T-CM$ )

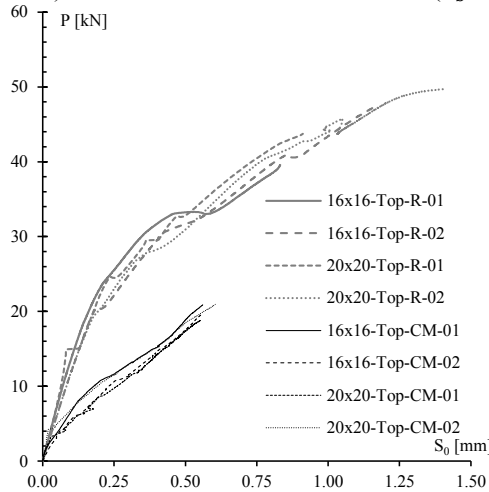


Figure 4. 18 – Load versus total slip ( $L_b300-T-CM$  vs  $L_b300-T-R$ )

In order to assess the effective bond length of the analysed strengthening systems, the strain measured by the strain gauges, placed as shown in Figure 4. 9 a, were represented versus the abscissas  $z$ , for different values of the load. The slope of these curves is representative of the capacity of the strengthening system to transfer the shear stress from the loaded end, 0 (where the theoretical strain,  $\epsilon_0$ , is assumed), to the un-loaded end, 6. Particularly, as higher is the slope as higher is the capacity to transfer the stress. Clearly, since the failure mode was

due to the debonding at B/A interface, over about the 70-80% of  $P_{u,exp}$ , the strain gauges did not properly work anymore, therefore the profile of strain along the bonded length could not be calculated in this load range. Anyway, comparing the strain profiles  $\varepsilon(z, P)$  obtained referring to  $L_b300-T-CM$  (Figure 4. 19 a-b) versus those obtained referring to  $L_b300-T-R$  (Figure 4. 20 a-b) is clear that when the cementitious adhesive is used a greater bonded length is needed. Comparing, for example,  $\varepsilon(z, P = 18 \text{ kN})$  of  $L_b300-b_g16-T-CM-02$  (Figure 4. 19 a) versus that of  $L_b300-b_g16-T-R-01$  (Figure 4. 20 a), it can be observed that when the cementitious adhesive is used a bonded length of 300 mm is needed, whereas 150 mm bonded length is more than enough when resin adhesive is used.

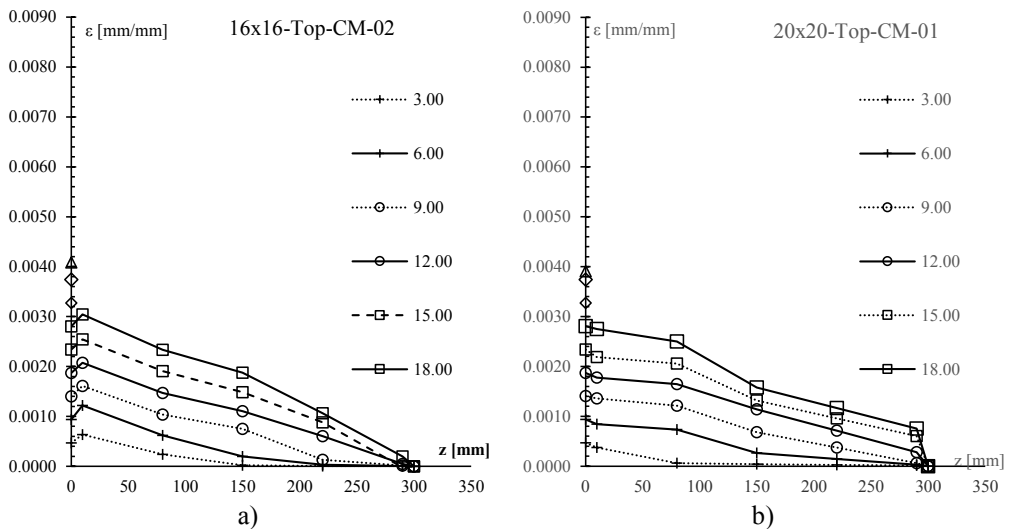


Figure 4. 19 – Strain profiles  $\varepsilon(z, P)$ : a)  $L_b300-b_g16-T-CM-02$ ; b)  $L_b300-b_g20-T-CM-01$

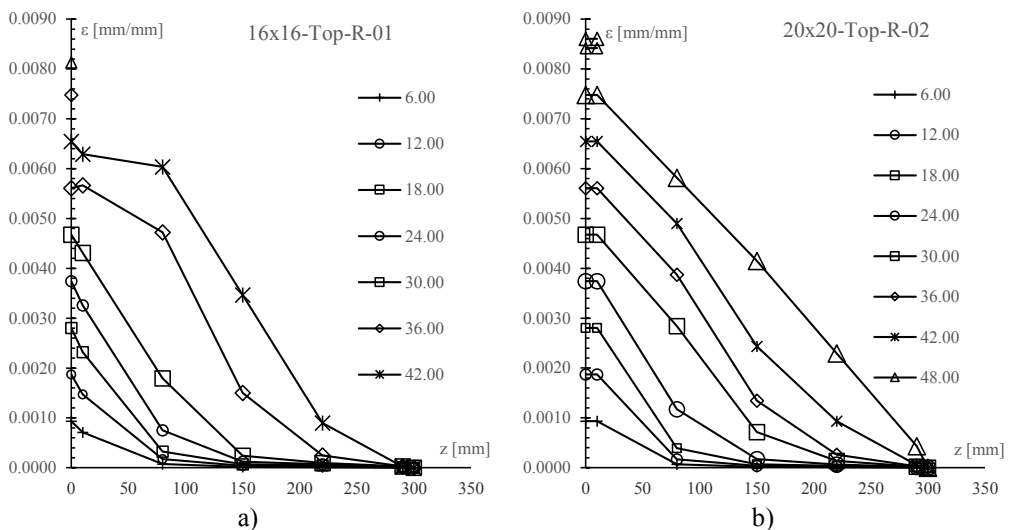


Figure 4. 20 – Strain profiles  $\varepsilon(z, P)$ : a)  $L_b300-b_g16-T-R-01$ ; b)  $L_b300-b_g20-T-R-02$

It should be noted that in some cases, such as  $L_b300-b_g16-T-CM$ ,  $\varepsilon(z = 10\text{mm})$  is greater than  $\varepsilon_0$  (Figure 4. 19 a). Clearly, it does not make any sense and it is just an experimental-theoretical incongruity.

Even though the groove dimension, as previously noticed, does not affect the global stiffness of the strengthening systems, the Figure 4. 21 a shows that, for low load level ( $P=6\text{kN}$ ), the local stiffness (at  $z=10\text{ mm}$ ) of  $L_b300-b_g16-TOP-CM$  is lower than  $L_b300-b_g20-TOP-CM$ . Moreover, this gap decreases when the load increases and micro-cracks occurs in cementitious adhesive (Figure 4. 22 a). It does not occur, when resin is used (Figure 4. 21 b and Figure 4. 22 b).

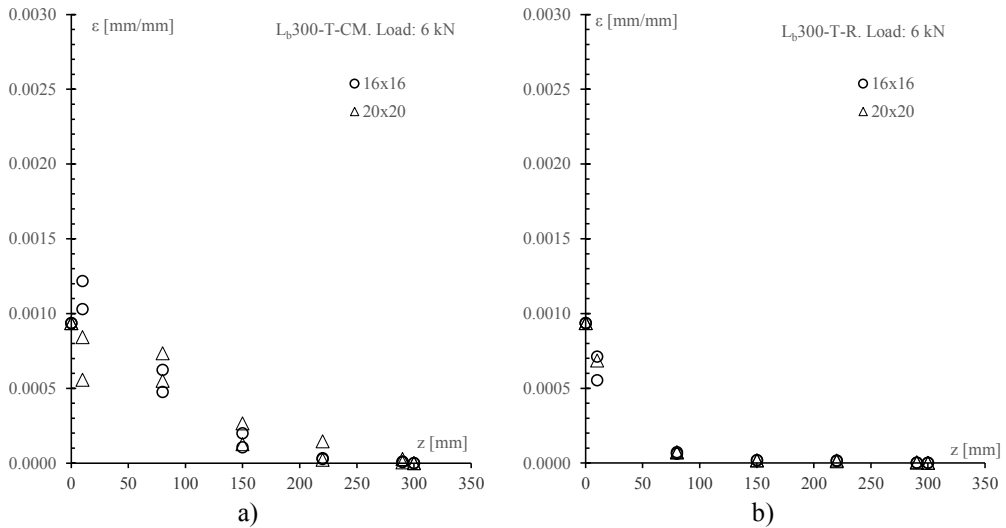


Figure 4. 21 – Strain profiles  $\varepsilon(z, P = 6\text{kN})$ : a)  $L_b300-T-CM$ ; b)  $L_b300-T-R$

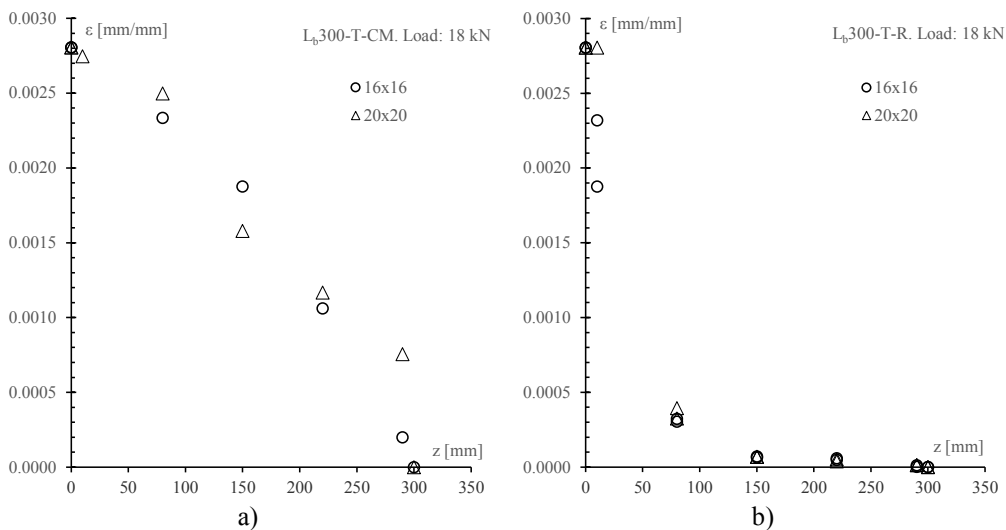


Figure 4. 22 – Strain profiles  $\varepsilon(z, P = 18\text{kN})$ : a)  $L_b300-T-CM$ ; b)  $L_b300-T-R$



Finally, the shear stress  $\tau_{1,2}$  was depicted versus the corresponding slip  $s_{1,2}$ . Particularly, the Figure 4. 23 shows that the shear stress of  $L_b300-b_g16-T-R$  is zero when the slip achieved about 0.8 mm, whereas the shear stress of  $L_b300-b_g20-T-R$ , after the achievement of the peak value, slightly decreased but it did not become zero. The  $\tau - s$  behaviour of  $L_b300-T-CM$  (Figure 4. 24) was significantly different from  $L_b300-T-R$ .

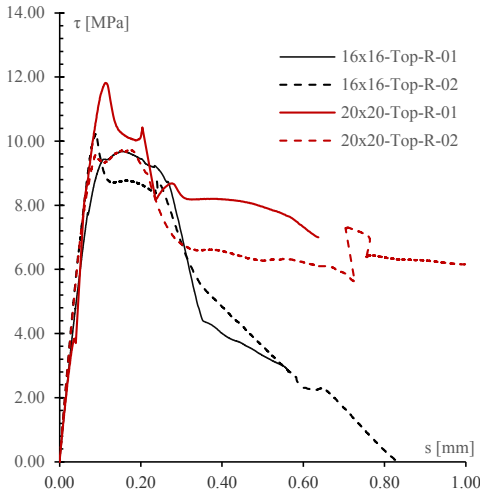


Figure 4. 23 – Shear stress versus slip  
( $\tau - s$ ):  $L_b300-T-R$

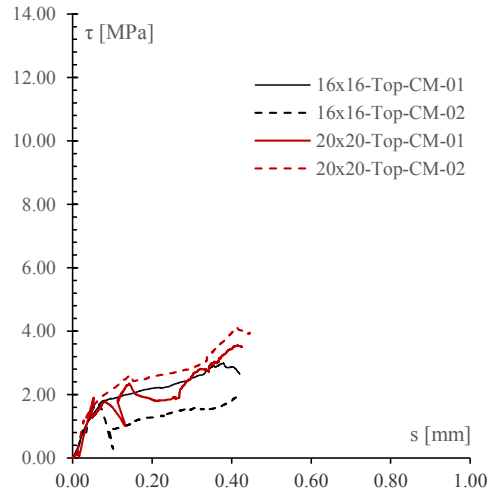


Figure 4. 24 – Shear stress versus slip  
( $\tau - s$ ):  $L_b300-T-CM$

Table 4. 5 – Summary of the main experimental results

Label	$P_{u,exp}$ (kN)	Failure mode
$L_b300-b_g16-T-CM-01$	22.85	B/A
$L_b300-b_g16-T-CM-02$	26.22	B/A
$L_b300-b_g16-C-CM-01$	20.86	B/A
$L_b300-b_g16-C-CM-02$	17.68	B/A
$L_b300-b_g16-T-R-01$	52.18	B/A
$L_b300-b_g16-T-R-02$	56.77	B/A
$L_b300-b_g16-C-R-01$	45.38	B/A
$L_b300-b_g16-C-R-02$	47.48	B/A
$L_b300-b_g20-T-CM-01$	25.05	B/A
$L_b300-b_g20-T-CM-02$	23.78	B/A
$L_b300-b_g20-T-R-01$	52.45	B/A
$L_b300-b_g20-T-R-02$	55.22	B/A
$L_b400-b_g16-T-CM-01$	24.47	B/A
$L_b400-b_g16-T-CM-02$	30.45	B/A

Moreover, the tests conducted on  $L_b300-b_g16-C-CM$  provided a maximum load 27% lower than that obtained testing  $L_b300-b_g16-T-CM$ . Similarly,  $L_b300-b_g16-C-R$  showed a strength 16% lower than  $L_b300-b_g16-T-R$ . It enabled to assess that the position of the bar in the groove has a not negligible influence.

Finally, the tests conducted on  $L_b400-b_g16-T-CM$  showed that a greater bonding length provides an increase of the maximum load equal to about 12%.

## ***Chapter 5 - Experimental tests of NSM FRP strengthened RC beams at ambient and elevated temperature***

With the NSM FRP strengthening technique, an FRP bar/rod/strip is applied in a groove cut into the concrete cover of a RC member and bonded in place by filling the groove with an epoxy or cementitious adhesive. Near surface mounted FRP strengthening is therefore potentially less prone to damage due to fire exposure than externally bonded FRP reinforcement (EBR), provided that: (a) an FRP strengthening material with high  $T_g$  and  $T_d$ ; and (b) a bonding agent with low thermal conductivity and good thermal stability, are used. This chapter presents a project undertaken on a specific high  $T_g$  and cementitious-bonded NSM FRP strengthening system.

Dynamic Mechanic Analysis (DMA) and Thermogravimetric Analysis (TGA) on the novel, high  $T_g$  commercial CFRP bar yielded a  $T_g$  value slightly higher than 200°C (based on Tan  $\Delta$  peak) and  $T_d$  of about 350°C (see section 3.1). Thermal conductivity tests were also performed on the cementitious grout, to verify its thermal conductivity ( $\lambda$ ), obtaining a value almost constant in the temperature range 20-175°C, equal to about 0.55 W/(m K) (see also section 3.1).

A series of tests on NSM FRP strengthened reinforced concrete beams were performed at both ambient and elevated temperature. The thermo-structural response was investigated under sustained loads typical of maximum permissible service strain conditions in the FRP. Internal temperatures, beam displacements and slip of the FRP strengthening were measured, and strain gauges were applied for measuring the FRP bar strains; Digital Image Correlation (DIC) was also used to study strain distributions and beam displacements. All the results were correlated with DMA and TGA tests results in order to better explain the failure modes of the strengthened beams.

The main objectives of this study are summarized below:

- evaluation of the flexural resistance of the un-strengthened beams at ambient temperature (reference specimens);
- evaluation of the flexural resistance of the strengthened beams at ambient temperature, in order to define the gain in flexural resistance obtained through the strengthening system;
- evaluation of the effectiveness of the strengthening system at elevated temperature, in different heating configurations.

The following sections provide (i) information about the design and the fabrication of the RC specimens, as well as the strengthening operations, (ii) the test setup and the instrumentation for temperature and displacements' monitoring, and, finally, (iii) discussion of the test results.

## 5.1 EXPERIMENTAL PROGRAM

The experimental program consisted of 12 four-point bending tests of RC beams and NSM FRP strengthened RC beams, 1450 mm long and 150 mm square in cross-section. The tests were performed at both ambient and elevated temperature. The tests at elevated temperature were executed using propane-fired radiant panels to heat the beams, rather than a standard fire-testing furnace. Two heating configurations were used, namely:

- (1) localised heating near midspan only;
- (2) global heating over the entire bonded length of the FRP system.

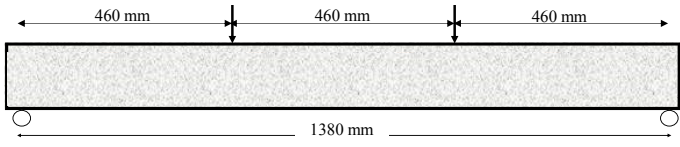
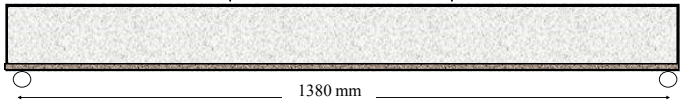


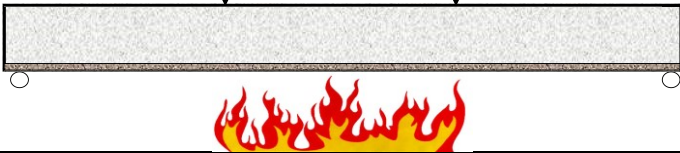
The thermo-structural response was investigated under sustained loads typical of maximum permissible service strain conditions in the FRP.

Table 5. 1 summarizes the experimental program, showing how the tested beams were labelled. It should be noted that:

- the label *UN-S* was associated to the **un**-strengthened beams;
- the label *S* was associated to the **strengthened** beams;
- the label *GloH* indicates that the beam was tested in **global heating** configuration;
- the label *LocH* indicates that the beam was tested in **local heating** configuration;
- the label *SL* indicates that the beam was tested under **service load**;
- the label *HL* indicates that the beam was tested under **high load**.

As shown in Table 5. 1, the beams were tested in four-point bending tests, by setting the distance between the supports (*L*) equal to 1380 mm and the distance between the forces equal to 460 mm (=1/3 *L*).

Table 5. 1 - Experimental program

Label	Scheme	Load
UN-S <sub>i</sub> i=1,2		2mm/min
Note:	2 tests at ambient temperature of un-strengthened beams	
S-i i=1,2,3_cut		2mm/min
Note:	3 tests at ambient temperature of strengthened beams	
UN-S_GloH_SL_1		SL=40 kN
Note:	1 test of un-strengthened beam in global heating configuration, under service load	
S_GloH_SL_i i=1,2		SL=40 kN
Note:	2 tests of strengthened beams in global heating configuration, under service load	
S_LocH_SL_i S_LocH_HL_i i=1,2		SL=40 kN HL=50 kN
Note:	- 2 tests of strengthened beams in localised heating configuration, under service load - 2 tests of strengthened beams in localised heating configuration, under high load	

The sustained loads (SL and HL), which were applied during the high temperature tests, were chosen based on the predicted strength of the RC beam (section 5.1.1) and based on its experimental failure load (section 5.3.1).

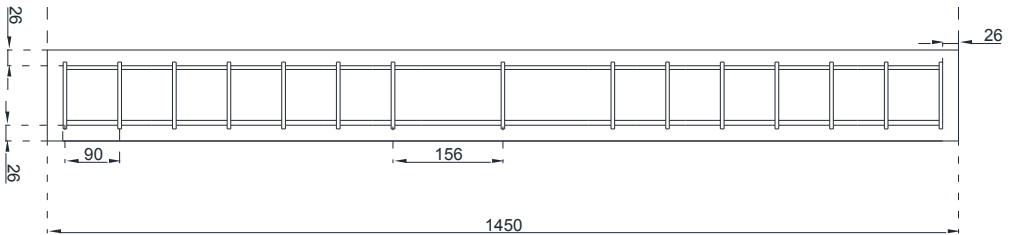
Residual tests were conducted on specimens that did not fail during the high temperature tests.

It should be noted that the ambient temperature tests were carried out after 76 days by the concrete casting, while the elevated temperature tests were conducted on beams 5 months old, to reduce problems of concrete spalling.

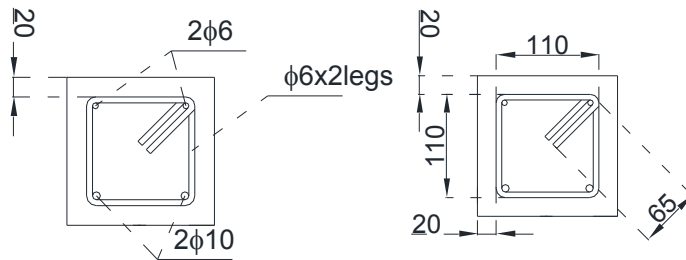
### 5.1.1 Design

The RC beams were 150 mm square in cross-section, 1450 mm in total long.

All the beams had a flexural reinforcement made of two steel rebars (nominal diameter  $\Phi$  10 mm) on the tension side and two rebars (nominal diameter 6 mm) in compression (Figure 5. 1 a and b).



a) Longitudinal section



b) Cross section

Figure 5. 1 - RC beam

Figure 5. 2 a and b depict respectively the longitudinal and the cross section of the NSM FRP strengthened RC beam. The designed strengthening system consisted of a CFRP bar (nominal diameter  $\Phi$  8 mm), grouted through a cementitious mortar in a groove 16 mm square in cross-section, cut into the concrete cover of the beam.

The shear reinforcement was designed in order to ensure that flexural failure would control the test. It consisted of steel stirrups (nominal diameter 6 mm) every 90 mm. The design was conducted according to EN1992-1 and ACI 318-08, but the stirrups' spacing provided by the European code was adopted.

The Table 5. 2 summarizes the mechanical properties of the materials, obtained through the tests (see also section 3.2).

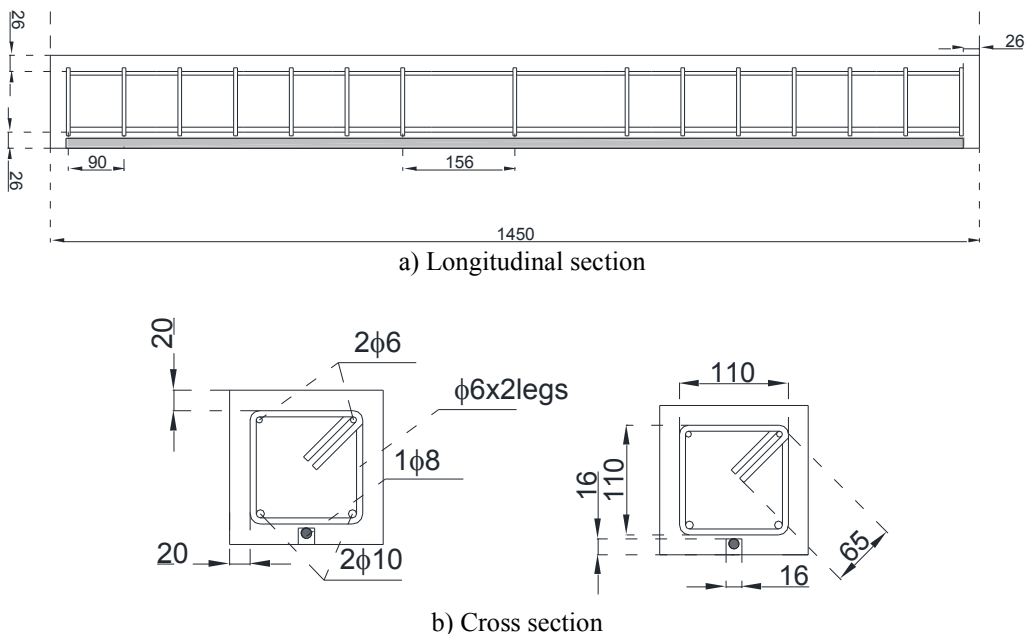


Figure 5. 2 - NSM FRP strengthened RC beam

Table 5. 2 - Materials' mechanical properties

Property	Symbol	Value (MPa)
Concrete compression strength (28 days)	$f_{cm,28}$	35.6
Concrete tensile strength (28 days)	$f_{ctm,28}$	3.83
Concrete compression strength (76 days)	$f_{cm,76}$	47.7
Steel yielding strength (rebars in tension side)	$f_{ym}$	525
Steel tensile strength (rebars in tension side)	$f_{tm}$	622
Steel yielding strength (rebars in compression side)	$f_{ym}$	700*
Cementitious Mortar compression strength (28 days)	$f_{ccm}$	90
CFRP tensile strength	$f_{ftm}$	1750
CFRP Young modulus	$E_f$	136000

\* specified by the manufacturer

A cross-sectional analysis (CSA) was conducted in order to predict the failure load of both the un-strengthened and the strengthened beam. The CSA was carried out through an incremental-iterative procedure, which provides the Moment-Curvature of the analysed section.

The cross-section of both the un-strengthened and the strengthened beam was discretized, as shown respectively in Figure 5. 3 a and b.

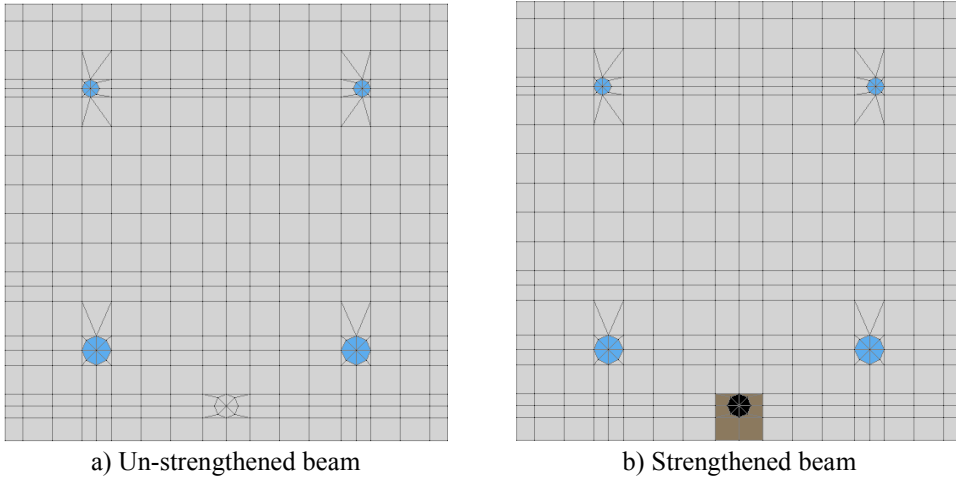


Figure 5.3 - Discretization of cross-sections

The Moment-Curvature diagrams of the cracked RC beam were calculated by considering both the concrete constitutive law according to EN1992-1-2 (unconfined concrete model) and Mander et al, 1988, which allows taking into account the concrete confinement provided by the shear reinforcement. Particularly, two CSAs were conducted according to Mander constitutive model: 1) by considering the unconfined concrete cover and the remaining confined concrete (full Mander model); 2) by considering unconfined concrete for the overall cross-section.

The curvature of the cracked section ( $\chi_2$ ) was interpolated with that of the uncracked section ( $\chi_1$ ), according to (5.1), in order to take into account the tension stiffening,

$$\chi = \chi_1(1 - \gamma) + \chi_2\gamma, \quad \text{if } M > M_{cr} \quad (5.1)$$

where:

$M_{cr}$  is the cracking moment;

$$\gamma = 1 - \beta \left( \frac{M_{cr}}{M} \right)^2;$$

$\beta$  is a coefficient dependent on the type of load, assumed equal to 1.

Therefore, the Moment-Curvature diagrams shown in Figure 5.4 were obtained. Based on the CSA's results, the yielding moment of the un-strengthened beam is 8.8 kNm. Regarding the failure moment, it is 9.7 kNm according to EN1992-1-2, otherwise it is about 11 kNm according to the unconfined Mander model, and 12.3 kNm according to the full Mander model for concrete. The latter provided a



significantly higher failure moment, since the ultimate concrete strain and strength of the confined concrete, is greater than that of un-confined concrete.

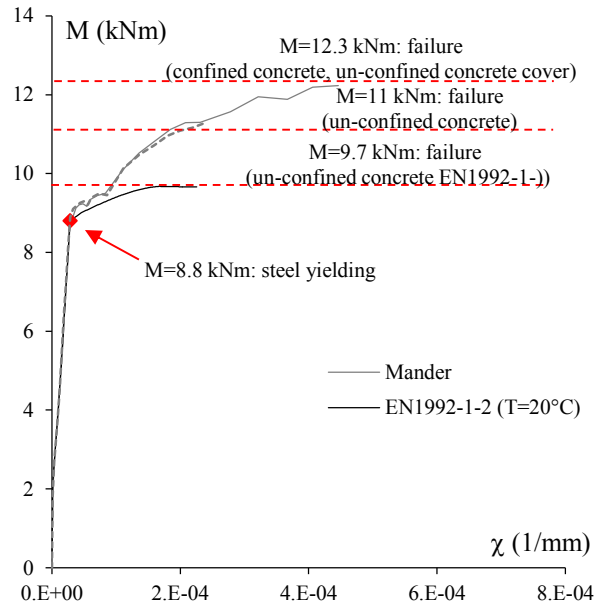


Figure 5. 4 - Moment curvature diagram of the RC beam

The Figure 5. 5 depicts the “actual” curvature  $\chi(z, F)$  and Moment distribution  $M(z, F)$  on the beam for different values of the load, according to EN1992-1-2 model. The calculation of the  $\chi(z, F)$  enabled the evaluation of the beam deflection ( $\delta$ ) in the beam’s midspan (Figure 5. 7), according to the principle of virtual work (5. 2):

$$L_e = 1 \cdot \delta = 2 \int_0^{\frac{L}{2}} M^{(1)}(z) \chi(z) dz = L_i \tag{5. 2}$$

where:

$L_e$  is the external virtual work, which is the product of a unit virtual force, applied at the beam’s midspan, and the actual displacement at the midspan (Figure 5. 6);

$M^{(1)}(z)$  is the virtual moment due to a unit virtual force, applied at the beam’s midspan (Figure 5. 6);

$L_i$  is the internal work.

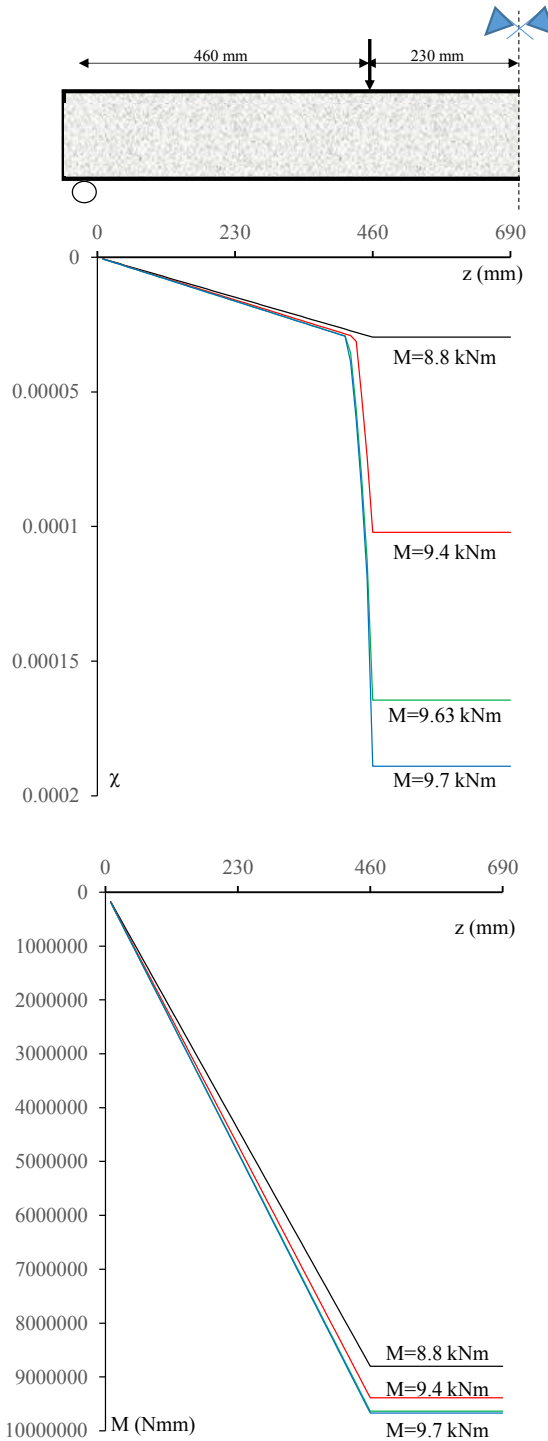


Figure 5. 5 – Actual Curvature  $\chi(z, F)$  and Moment  $M(z, F)$  – un-confined concrete (EN1992-1-2)

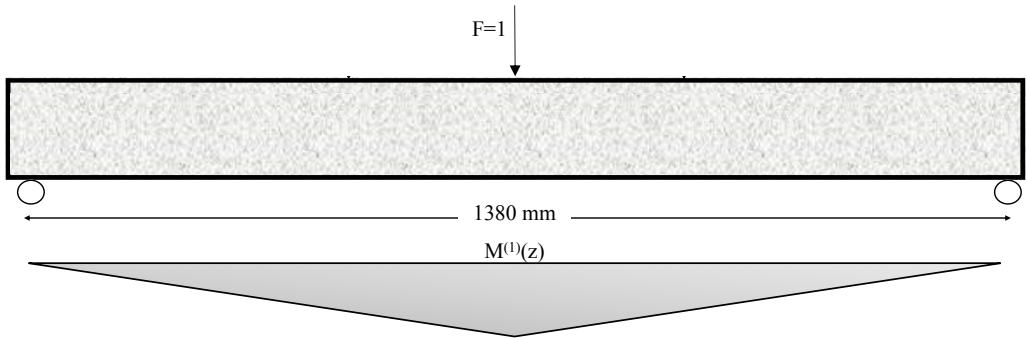


Figure 5. 6 - Virtual Moment distribution on the beam

The Figure 5. 7 shows that the cracking load is about 10 kN, the yielding load is 38 kN corresponding to a midspan deflection equal to 6mm, the failure load is 42 kN corresponding to a midspan deflection equal to 26mm.

The same calculation was conducted referring to the “Full Mander model” (Figure 5. 8), obtaining a failure load of about 53 kN corresponding to a midspan deflection equal to about 40 mm.

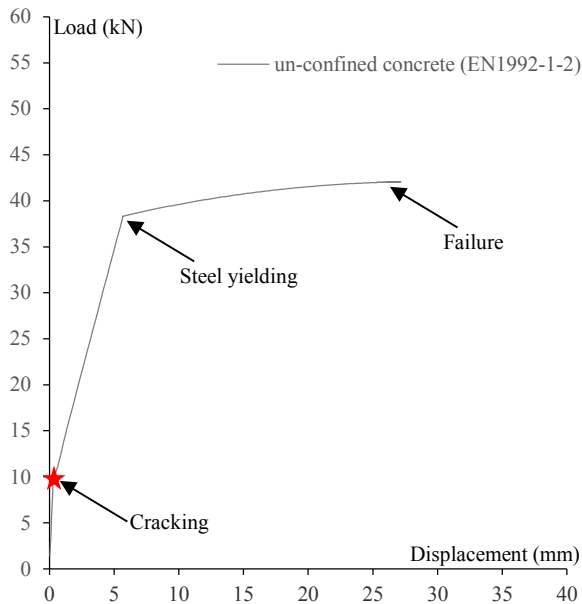


Figure 5. 7 - Load-Deflection curve of RC beam (EN1992-1-2)

Finally, the Figure 5. 9 shows the prediction of the Load-Deflection curve, calculated referring to the NSM FRP strengthened RC beam. The CSA was carried out by considering an end-debonding failure model (5. 3), proposed by Bilotta et al (2014),

$$\varepsilon_{end-deb} = 252 \frac{p_{f,NSM}^{0.66}}{(E_f A_f)^{0.823}} \quad (5.3)$$

where:

$p_{f,NSM}$  is the NSM FRP bar perimeter;

$E_f A_f$  is the axial stiffness of the NSM FRP bar.

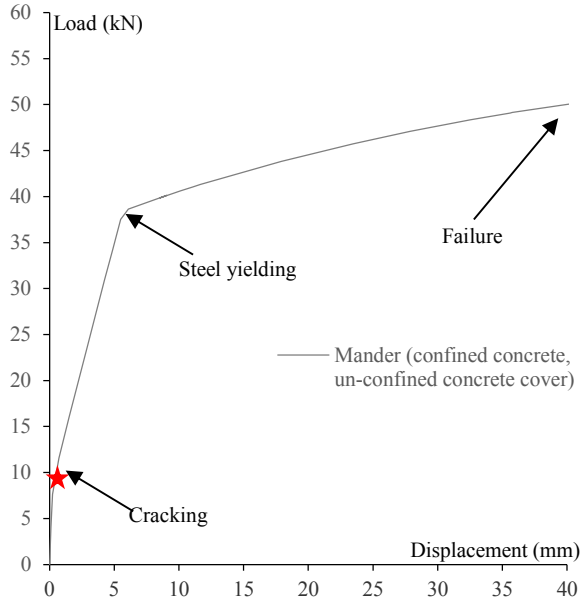


Figure 5. 8 - Load-Deflection curve of RC beam (Full Mander model)

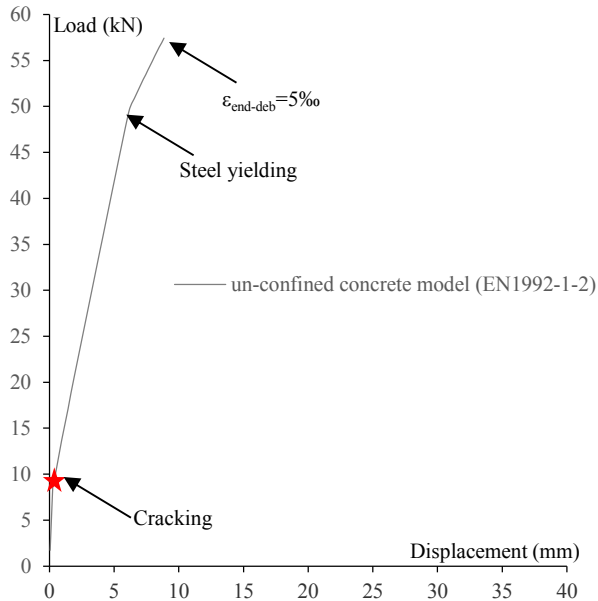


Figure 5. 9 - Load-Deflection curve of NSM FRP strengthened RC beam

Figure 5. 9 shows that the cracking load of the strengthened beam is about 10 kN (similar to that obtained analysing the un-strengthened beam, since the strengthening does not affect significantly the beam’s moment of inertia), the yielding load is 50 kN, the failure load is 59 kN.

The strength prediction of both the RC beam and the NSM FRP strengthened RC beam enabled the definition of the sustained loads to be applied on the beam during high temperature tests.

The “high sustained load” (HL) equal to 50 kN was chosen ensuring an allowable exploitation of the strengthening system. In fact, this load ensured that the CFRP strengthening system would experience a sustained midspan tensile strain levels lower than 55% of the ultimate strain, according to ACI 44.2R-08. Note that 50 kN sustained load is greater than the predicted failure load of the un-strengthened beam, ensuring that the failure should be related to the failure of the strengthening system during heating.

The “service sustained load” (SL) 40 kN was chosen based on the ACI 440.2R-08 design code, which recommends that the existing strength of the structure should be sufficient to resist under the load shown in (5. 4)

$$(\phi R_n)_{existing} \geq (1.1 S_{DL} + 0.7 S_{LL})_{new} \quad (5. 4)$$

where:  $(\phi R_n)_{existing}$  is the predicted factored strength of the existing member to be strengthened with FRP,  $S_{DL}$  is the strengthened service dead load and  $S_{LL}$  is the strengthened service live load. Assuming that the factored design load is 50% due to live load and 50% due to dead load and using the load factors 1.2 for dead load and 1.6 for live loads, the allowable strength of the strengthened member  $F_{max}$  was calculated through the equation (5. 5):

$$(\phi R_n)_{existing} = 37.8 \text{ kN} \geq \left( 1.1 \frac{0.5F_{max}}{1.2} + 0.7 \frac{0.5F_{max}}{1.6} \right) \quad (5. 5)$$

Therefore,  $F_{max} \leq 54.57 \text{ kN}^*$ .

Finally, the sustained load to be applied during the high temperature tests was calculated as shown in (5. 6)

$$S_{DL} + S_{LL} = \frac{0.5F_{max}}{1.2} + \frac{0.5F_{max}}{1.6} \cong 40 \text{ kN} = SL \quad (5. 6)$$

\* Note that  $(\phi R_n)_{existing}$  was predicted through the Moment-Curvature procedure, described above, referring to the un-confined concrete model provided by EN1992-1-2.

### 5.1.2 RC beams manufacturing and NSM strengthening

The RC beams were manufactured in the structures' lab of University of Edinburgh. The Figure 5. 10 shows all the stages of the RC beams' fabrication: a) preparation of the steel reinforcing cages; b) placement of the reinforcing cages in the formworks; c) concrete cast.

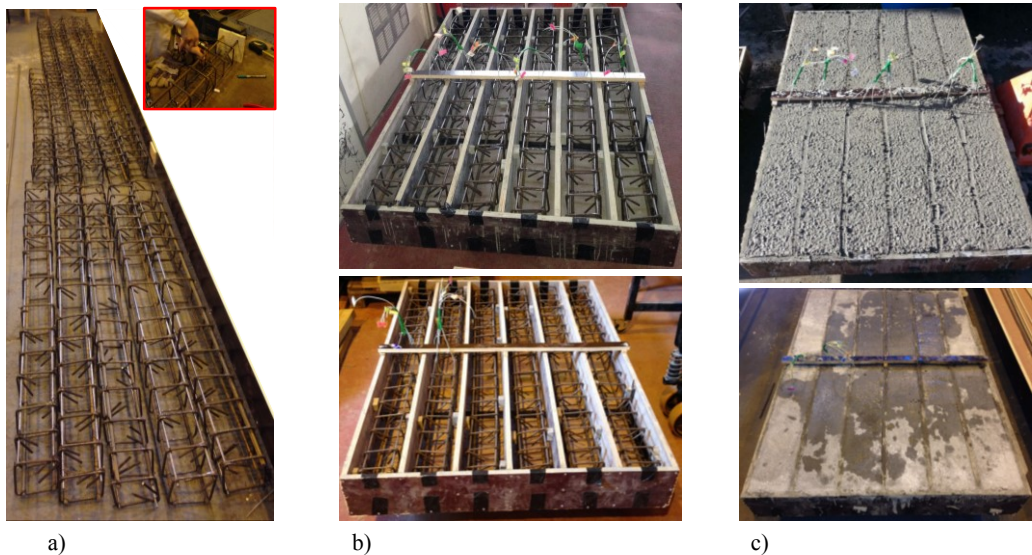
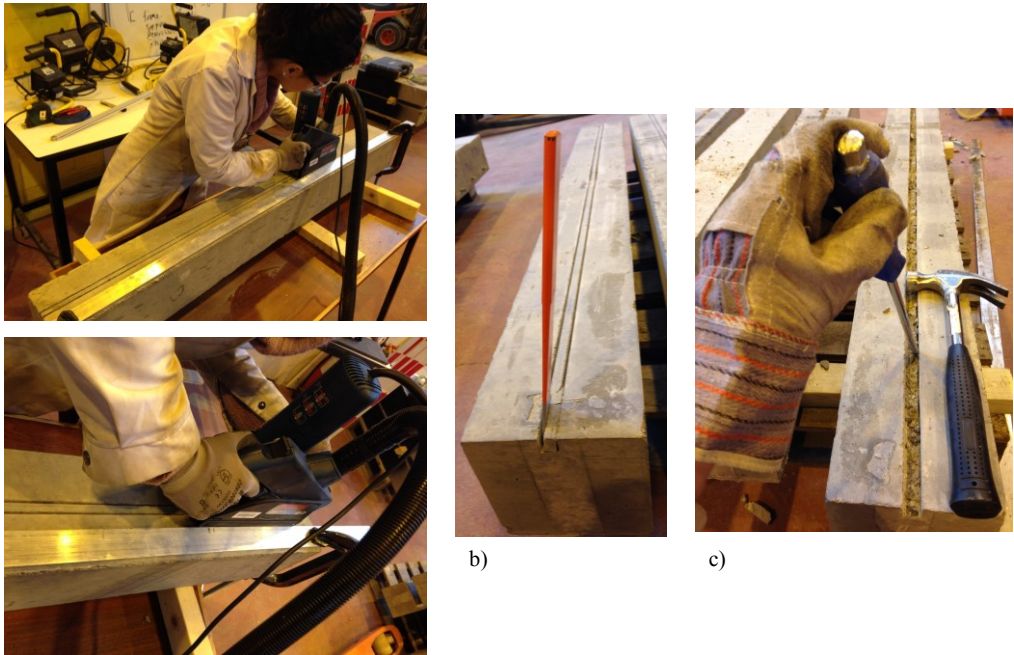
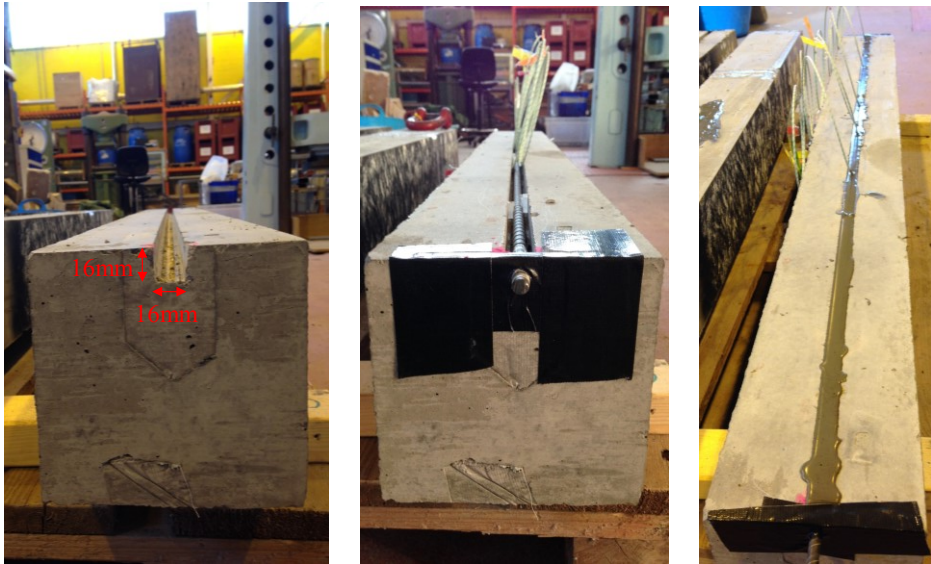


Figure 5. 10 - Stages of the fabrication: a) preparation of the steel reinforcing cages; b) placement of the reinforcing cages in the formworks; c) concrete cast.

After the concrete hardening, the NSM strengthening system was realized. Firstly, a machine with two parallel diamond cutting discs was used to cut the vertical slots in the bottom concrete cover of the beam (Figure 5. 11 a). After finishing the working procedure, the remaining fin of the material was removed with the break-out tool (Figure 5. 11 b). Then, the groove was accurately made smooth and clean (Figure 5. 11 c-d), as much as possible. Finally, the bar was placed in the groove (Figure 5. 11 e) and grouted inside through the cementitious mortar (Figure 5. 11 f).



a)



d)

e)

f)

Figure 5. 11 - Stages of the strengthening: a) cutting of parallel vertical slots; b) remaining fin removing; c-d) groove smoothing and cleaning; e) bar placement; f) bar grouting in cementitious mortar

As shown in Figure 5. 11 e-f, the CFRP bar was 40 mm longer than the RC specimen (1450 mm), in order to enable the measurement of the bar’s slip through a linear potentiometer (see 4.1.3). Therefore, the NSM bonding length was equal to the beam length. Since in the real buildings the effective bonding length is almost lower than the beam length, one test at ambient temperature was conducted on a specimen (labelled S3\_cut, see section 5.1), which NSM bonding length was 1350 mm instead of 1450. It enabled the evaluation of possible early failure, due to (i) lower bonding length (675 mm, namely  $\frac{1350}{2}$ , instead of 725 mm, namely  $\frac{1450}{2}$ , considering the beam’s symmetry) and (ii) no local confinement provided by the supports (see section 5.3.1).

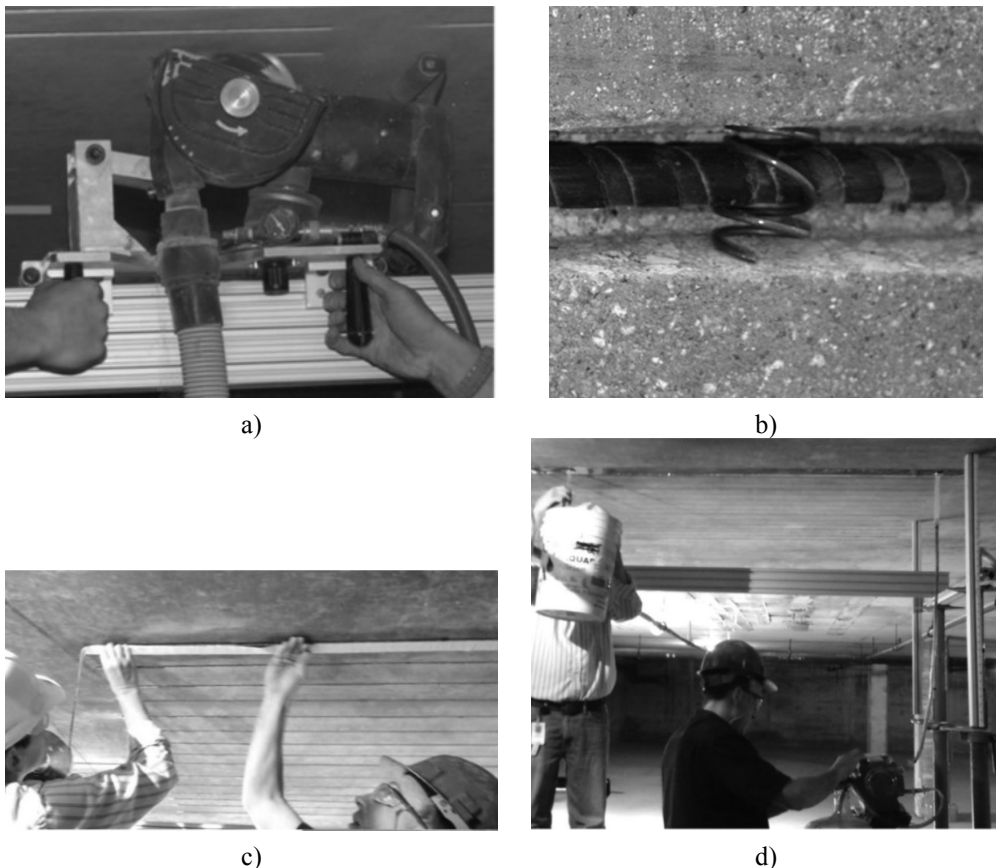


Figure 5. 12 - Main stages of the strengthening in real buildings: a) cutting of parallel vertical slots; b) bar hanged in the slot; c) application of the tape formwork; d) gout’s pumping (Zeiler, 2013)

Note that the strengthening system was easily realized placing the beam upside down. Actually, this strengthening technique is quite easy to realize also in real



buildings, according to the installation guide provided by Milliken (Zeiler, 2013, Figure 5. 11).

Basically, the NSM slots can be cut placing the saw, shown in Figure 5. 11, upside down, since this tool is very manageable and effective (Figure 5. 12 a). Then, the rod can be hanged in the slot, inserting the rod in the middle gap of a spring and placing them into NSM slot (Figure 5. 12 b). After the cleaning of the surface and the application of a primer, an adhesive formwork tape can be applied (Figure 5. 12 c) and finally the grout can be pumped in (Figure 5. 12 d).

## 5.2 FLEXURAL TEST SETUP

The Figure 5. 13 provides a scheme, which shows the flexural test setup that was used both for ambient and for high temperature tests.

During the ambient temperature tests, the load was applied through the INSTRON actuator installed within the Structures Testing Hall at the University of Edinburgh (Figure 5. 14a). Both the load and the crosshead displacement were recorded during the tests through a Data Analyzer (DA). A linear potentiometer with 100 mm of capacity (LP100) was used to measure the vertical displacement at the beam midspan (Figure 5. 14 a) and LPs with 25 mm of capacity (LP25) were used for measuring the bar's slip both at left hand side (LP25-LHS) and at right hand side (LP25-RHS) of the beams (Figure 5. 14 a,b). A traditional strain gauge was also attached at the mid length of the CFRP bar (Figure 5. 14 d), in order to evaluate the strain in the most stressed area.

In addition to the traditional instrumentation, a high-resolution camera (Figure 5. 14 a) was set for taking pictures every 5 seconds during the tests. It enabled a Digital Image Correlation (DIC) to monitor the vertical deflection and the flexural strains over the length of the beams. The section 5.2.1 provides more information about this technique.

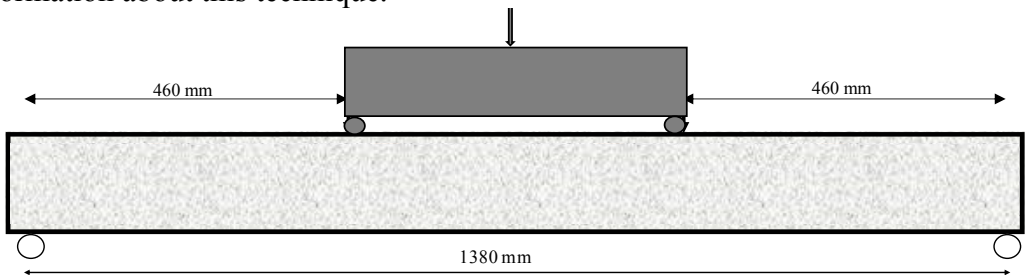


Figure 5. 13 - Scheme of the flexural test setup

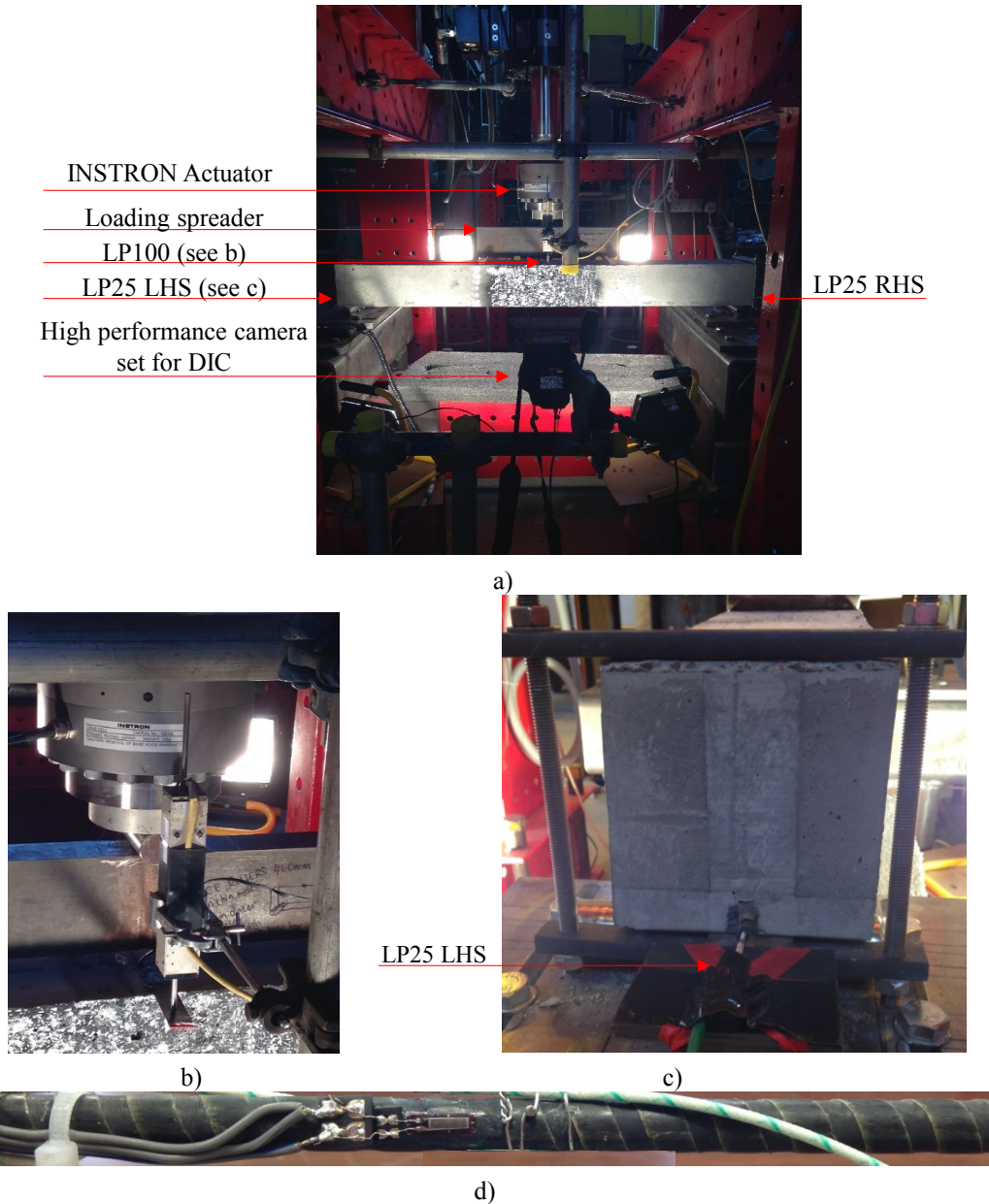
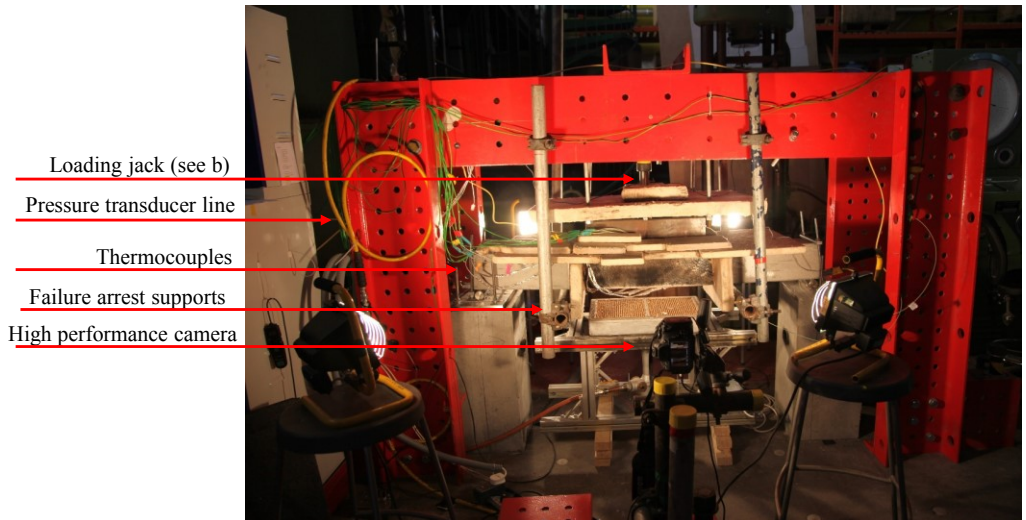


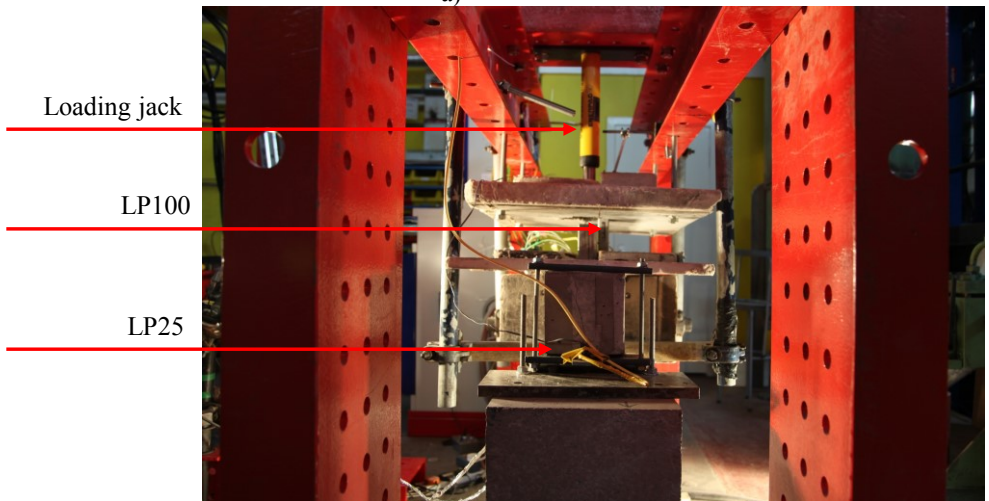
Figure 5. 14 - Flexural test setup at ambient temperature: a) main components of the setup; b) LP100; c) LP25-LHS; d) strain gauge at the md-length of the CFRP bar

The ambient temperature tests were conducted in displacement control at 2mm/min until the failure, in order to determine the load bearing capacity of the un-strengthened and strengthened beams, the FRP strain at failure and the failure mode.

The high temperature test setup was slightly different to that used for ambient temperature tests. The Figure 5. 15 a) shows the *ad hoc* designed testing frame: the load was applied through a loading jack (Figure 5. 15 b), connected to a pressure transducer line, linked to the INSTRON actuator (Figure 5. 15 c). As shown in Figure 5. 15, both traditional and innovative instrumentation for measuring displacement, slip and strain (LPs, DIC and strain gauges) were used.



a)



b)

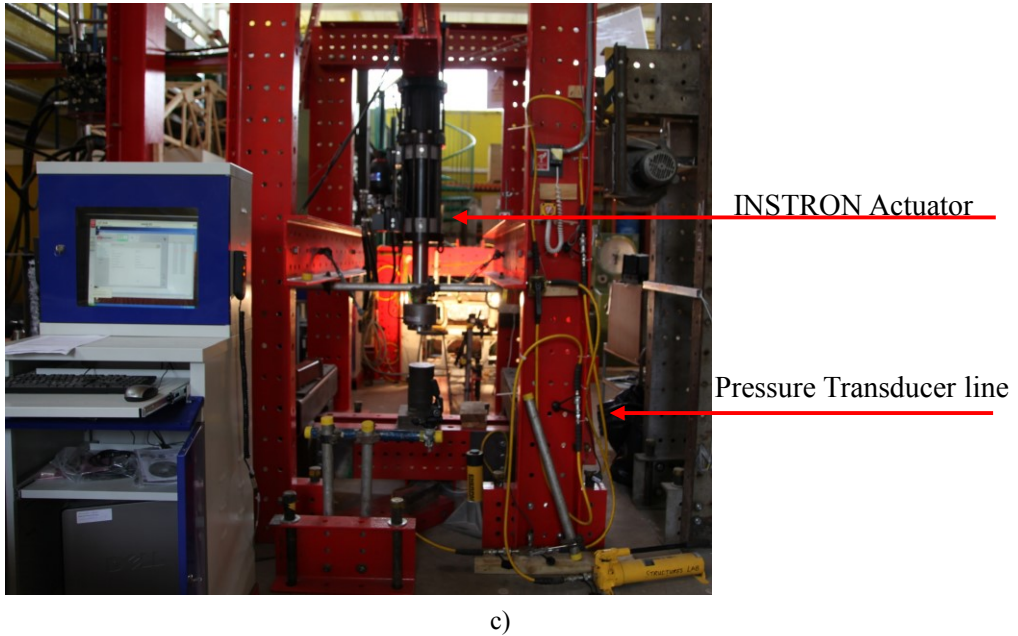


Figure 5. 15 - Flexural test setup at high temperature: a) main components of the setup; b) Loading jack and LPs; c) Pressure transducer line and Instron actuator

The high temperature tests were conducted under two different sustained loads (Table 5. 1), which were defined based on the strength prediction (at ambient temperature) of both the RC beam and the NSM FRP strengthened RC beam (see section 5.1.1.), quite according to the results of ambient temperature tests (see section 5.3.1). The beams were initially loaded at ambient temperature under displacement control at a rate of 2 mm/min and then, when the sustained load was achieved, the tests were switched in load control. After that, the heating stage started.

The tests in local heating configuration (LoCH) were carried out with a propane-fired radiant heating panel, which dimension was 485x330 mm, located at beams' midspan, 120 mm below the beams.

The tests in global heating configuration (GloH) were carried out with two radiant heating panels (Figure 5. 17), located 120 mm below the beams, as well as in LoCH. This setup ensured the heating over the entire bonded length of the FRP system, which was exactly 970 mm for the beams tested in this configuration. Note that the slip was not measured during those tests, because the LP25 could not be set, since the CFRP bar had a bonded length lower than the beam's length.

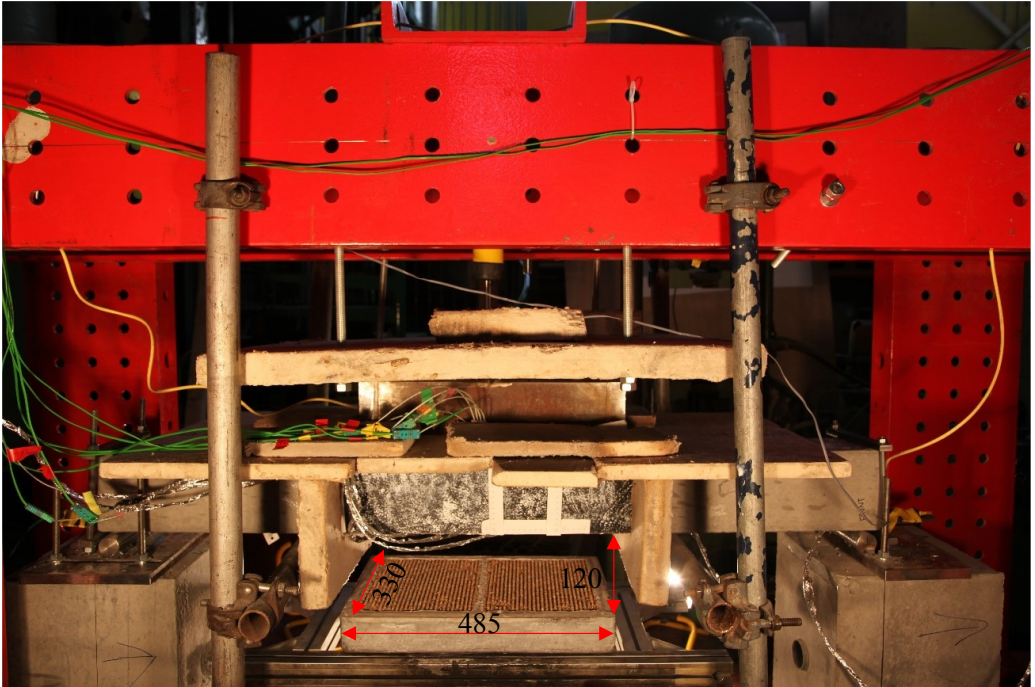


Figure 5. 16 - Radiant panel's dimension and location in Loch configuration

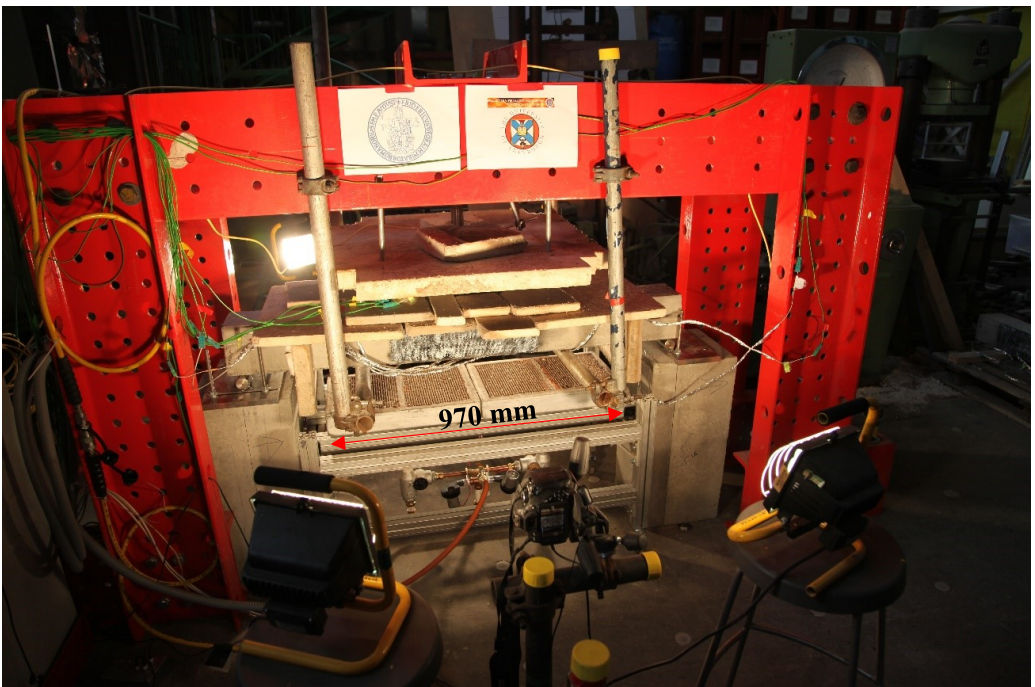


Figure 5. 17 - Radiant panels' dimension in GloH configuration

The radiant panel's heating method is significantly different from the traditional furnace tests, but it is a very reliable method, since it provides a uniform and repeatable heat flux (Bisby et al, 2013), as also shown by the test results (see section 5.3.3).

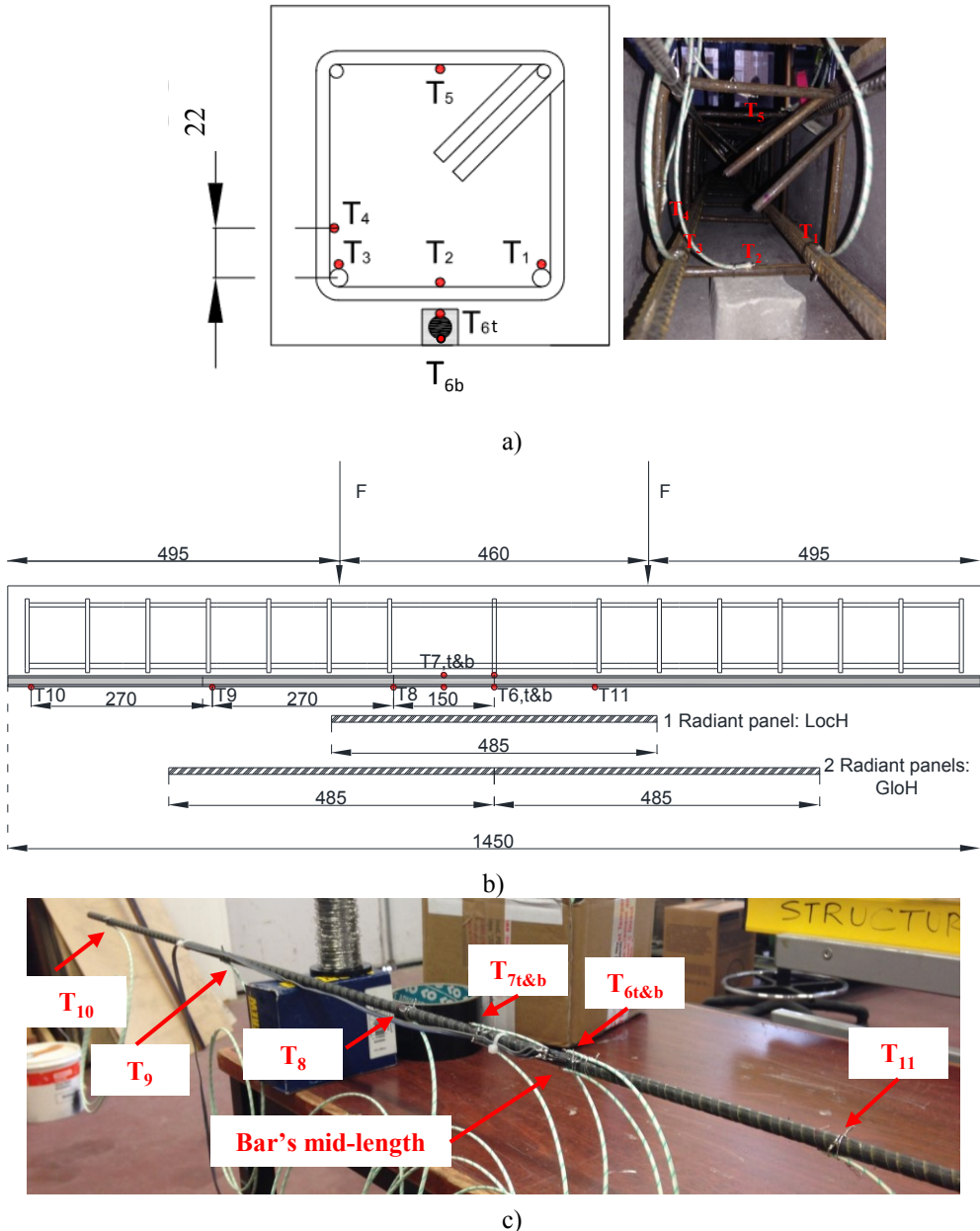


Figure 5. 18 - Thermocouples' location: a) cross-section; b-c) along the CFRP bar

The temperatures experienced during the high temperature tests were monitored by K-type thermocouples, located as shown in Figure 5. 18: a) five thermocouples were placed on the steel reinforcing cage and b) eight thermocouples were placed along the CFRP bar.

The beams that did not fail during the 90 mins of heating tests, were allowed to cool to ambient temperature over a period of 2 days, and then they were tested to failure using the method applied for ambient temperature tests (i.e. displacement control at 2 mm/min until failure).

### **5.2.1 Innovative instrumentation: Digital Image Correlation**

The Digital Image Correlation (DIC) or Particle Image Velocimetry (PIV) is an optical method, which can be used to find, through mathematical correlation, the movement of chosen targets in a series of digital images taken during the mechanical tests of a sample. This is a very powerful method, since the images, which have been recorded during an experiment, are post-processed providing information about displacements and strains. Therefore, it is an innovative or integrative solution, if compared to the traditional tools for directional measurements (Linear Potentiometers) and contact measurements (strain gauges). Obviously, the accuracy of this method is strictly related to the resolution of the digital cameras, which should be high, and the computing performance.

Practically, to apply this method, the surface of the specimen needs to be painted through random speckle pattern, creating an artificial texture.

The deformed images, obviously, will show a different random speckle pattern in comparison with the initial un-deformed reference image. These differences can be evaluated by correlating the patches (specified zones containing pixels), of the reference image and any deformed image, through a dedicated software. The software package, used for this study, is GeoPIV (White & Take, 2003), which algorithm searches for the maximum correlation between the patches of the un-deformed and the deformed images, providing the displacement vector of each patch. In order to achieve an accurate displacement measurement, the pixels comprising the chosen patch must contain enough information for them to be uniquely identifiable in a subsequent image. Moreover, for an accurate measurement other variables need to be taken into account, such as the distance between camera and specimen, the focal length of the lens and possible distortion effects, which can appear when the lens is zoomed and they need to be corrected.

This technique is nowadays considered very reliable, based on the results obtained by other researchers (Bisby et al, 2008; Dutton, 2012 ; Gales et al, 2012; Bewerse et al, 2013; McIntyre et al, 2014; Smith et al, 2014,).

In the frame of this work, DIC was used to measure beams' displacement and strain, which were compared with those obtained through directional and contact measurements (see section 5.3). Actually, this technique was also used to evaluate the steel and CFRP constitutive laws, based on the conducted steel and CFRP tensile tests (see section 3.2.2, 3.2.4).

### 5.3 RESULTS

The results of ambient temperature tests enabled to assess the strengthening system, define the FRP strain at failure and observe the failure mode. Moreover, the results were used to define the sustained loads on the specimens during the high temperature tests.

The high temperature tests provided useful information about the behaviour of the NSM FRP strengthened RC beams both in case of localised and global heating configuration.

#### 5.3.1 Ambient temperature tests of un-strengthened beams

In Figure 5. 19, the Load on the un-strengthened beams UN-S\_1 and UN-S\_2 is depicted versus the Midspan Displacement.

The beams cracked at a load equal to about 8 kN; then the load linearly increased up to the steel yielding load, equal to about 41 kN. The failure of UN\_S-1 occurred under a load equal to about 50 kN (22% greater than the yielding load), while the UN\_S-2 failed when the load achieved about 46 kN (12% greater than the yielding load).

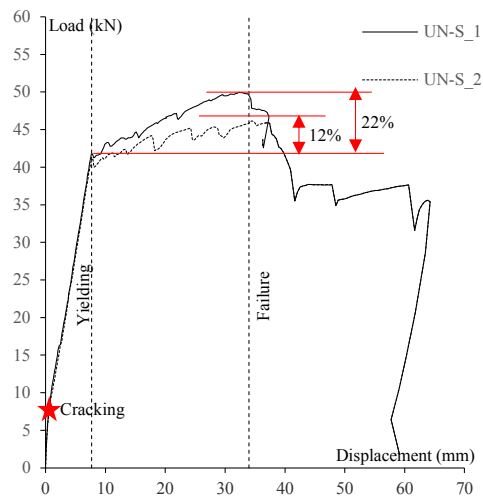


Figure 5. 19 - Un-strengthened beams: Load vs Displacement curves.



Figure 5. 20 depicts the Load versus the Midspan Deflection, measured through a Linear Potentiometer (LP100) and Digital Image Correlation (DIC), during the test of the UN-S\_1.

Both the LP100 and DIC provided almost the same midspan deflection, which was equal to about 8 mm, in the yielding stage, and about 35 mm under the failure load. Similar results are shown in Figure 5. 21, referring to the UN-S\_2.

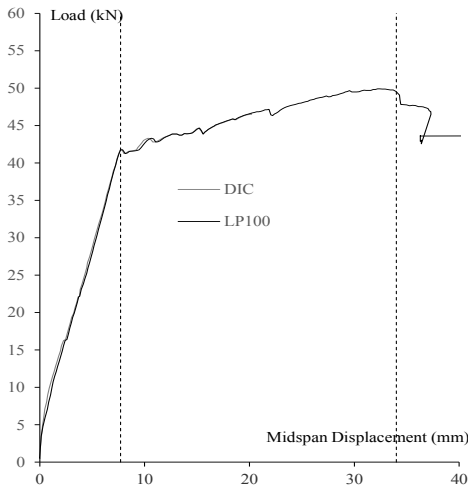


Figure 5. 20 - UN-S\_1: Load vs Displacement curves. Comparison between LP100 and DIC

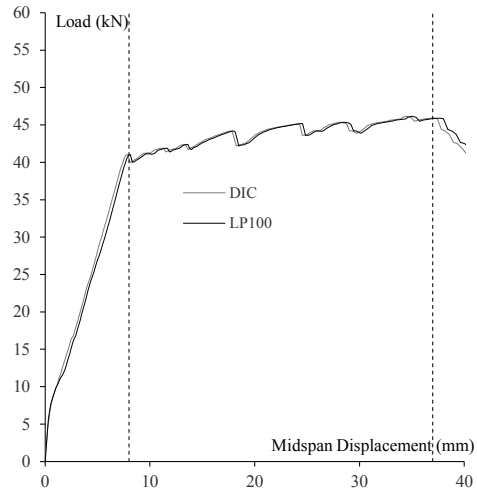
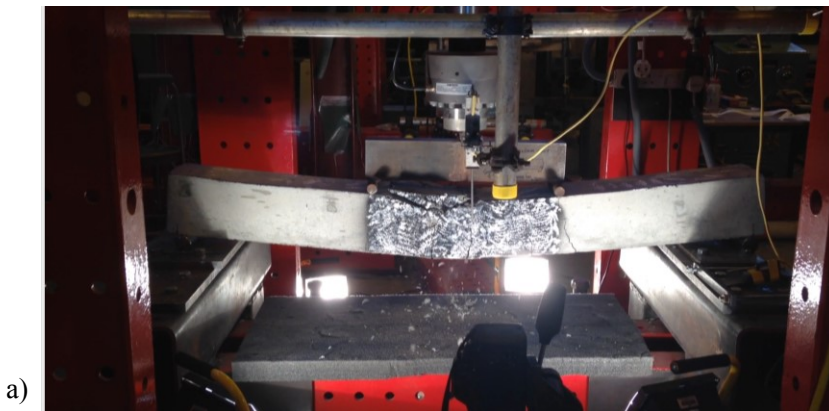


Figure 5. 21 - UN-S\_2: Load vs Displacement curves. Comparison between LP100 and DIC

Figure 5. 22 shows the UN-S\_1 beam during and after the failure. Those pictures clearly show that the beam failed due to the concrete crushing (Figure 5. 22 a), with buckled steel compressive reinforcement (Figure 5. 22 b) and extensive flexural cracks in tension side (Figure 5. 22 c, d).



a)

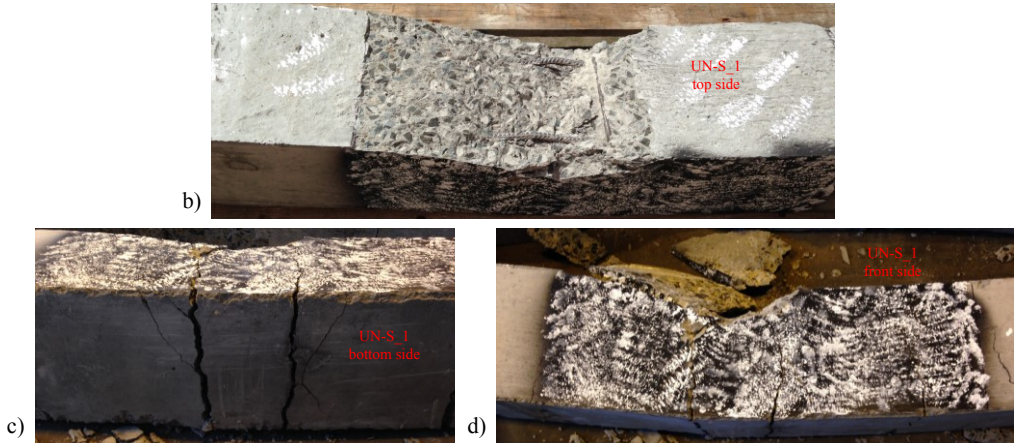


Figure 5. 22 - Specimen UN-S\_1 after failure

The strains of the beams were obtained through the DIC, in order to interpretate the beams' failure. Figure 5. 23 shows, for example, the 154 patches monitored through the DIC of UN-S\_2. Those patches were distributed within 220 mm, along the beam midspan ( $x$  axis), and within 130 mm, along the beam height ( $y$  axis). Figure 5. 24 shows, for example, the direction of patches' displacement in the early stage of the flexural test of UN-S\_2 beam, obtained through the DIC.

The longitudinal normal strain in  $x$  direction at the generic distance  $y$  from the beam bottom side (BBS) was calculated through the well-known expression (5. 7)

$$\varepsilon_x(y) = \frac{l(y) - l_0}{l_0} \quad (5. 7)$$

where:

$l(y)$  is the current distance between two patches, placed at height  $y$ ;

$l_0$  is the patches' initial distance.

Particularly, the strains were calculated at distance  $y$  from the BBS axis ranging between 10 mm and 140 mm. The horizontal distance between the patches was  $l_{0,1}=220$  mm,  $l_{0,2}=176$  mm,  $l_{0,3}=132$  mm and  $l_{0,4}=88$  mm (Figure 5. 23). Obviously, since the bending is pure and uniform between the two forces, the theoretical strain  $\varepsilon_x(y)$  is almost constant. In practice, since the beam is not a perfect continuous body, due to the concrete cracking, the strain along the beam midspan is not properly uniform. Therefore, the longitudinal normal strain  $\varepsilon_x(y)$  may exhibits a dependence on  $l_0$ . Note that the strain values  $\varepsilon_x(y = 30\text{mm}, l_{0,i})$  aroused particular interest, since the steel bars are located at  $y = 30\text{mm}$ . These values of strains are shown in Figure 5. 25, highlighting that the scattering

between the strain values  $\varepsilon_x(y = 30\text{mm}, l_{0,i})$  increases in the concrete crushing stage. Anyway, the average of those values can be considered representative of the longitudinal strain, at a distance  $y = 30\text{mm}$  from the BSB, in concrete as well as in the steel bars. Clearly, the latter statement is valid if the hypothesis of perfect bond between concrete and steel is accepted.

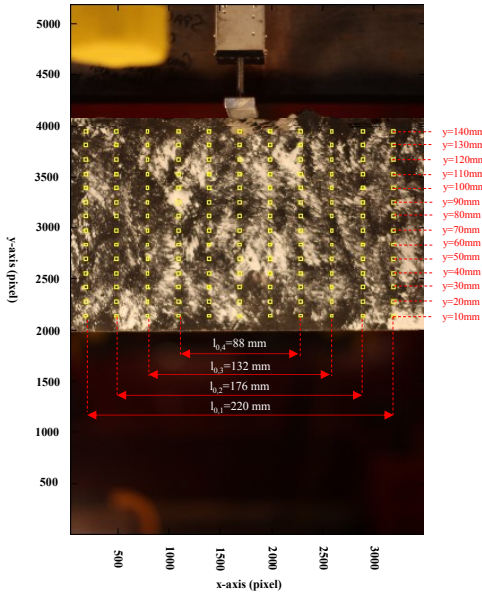


Figure 5. 23 - Patches monitored in DIC (UN-S\_2 beam)

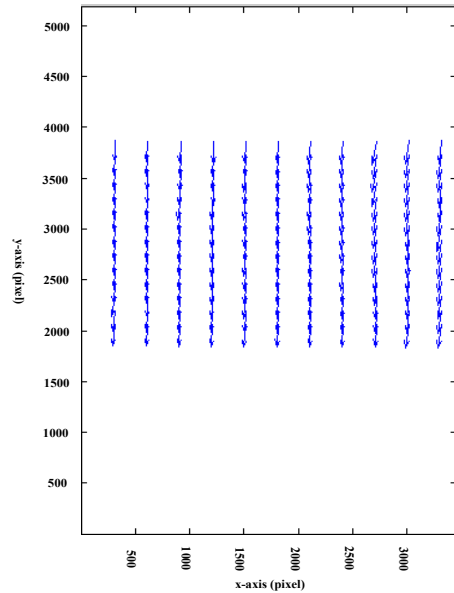


Figure 5. 24 - Generic step of DIC (UN-S\_2 beam)

In Figure 5. 25, the load and the strain  $\varepsilon_x(y = 30\text{mm}, l_{0,i})$  are depicted versus the logging time, even if the logging time is not a significant variable. It just enables to relate the load to the calculated strain values. When the load is about 41 kN,  $\varepsilon_x(y = 30\text{mm}, l_{0,i})$  ranges between 2.3‰ and 3.3‰, which is coherent with the steel yielding strain (2.5‰). Moreover, the load curve show a significant change in slope, representative of the stiffness reduction due to the steel yielding. Figure 5. 26 shows the strain distribution along the height of the beam for different load values, which is, as expected, linear. That figure enables to localize the neutral axis and to define the curvature depending on the value of the load. As expected, the depth of the neutral axis decreased up to 35 mm due to the concrete cracking ( $F=8$  kN), and decreased up to about 20 mm under higher loads. Then, in the failure stage, due to the concrete crushing ( $F \geq 46$  kN,  $\varepsilon_x(y = 150\text{mm}) > 4\text{‰}$ ), the depth of the neutral decreased again.

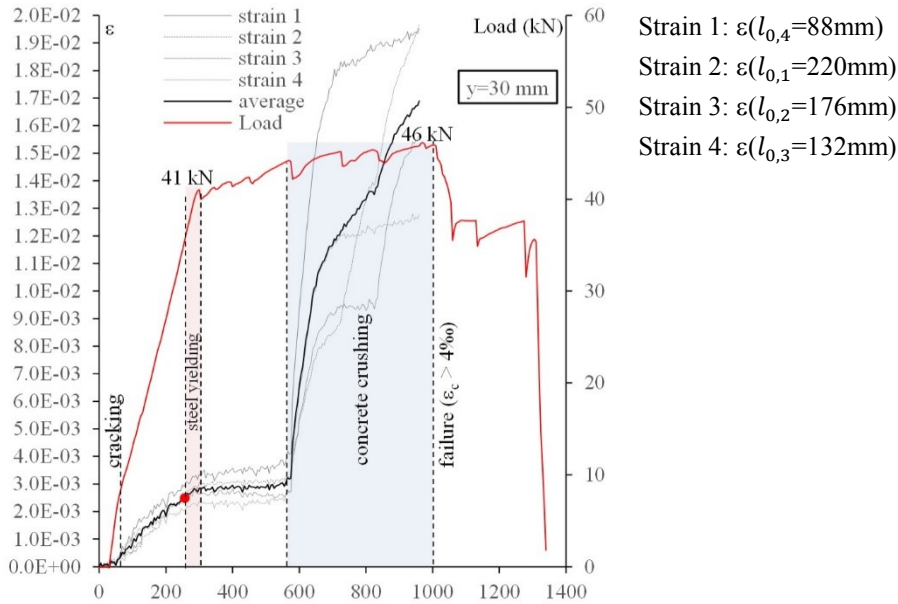


Figure 5. 25 - Load and strain vs Logging Time

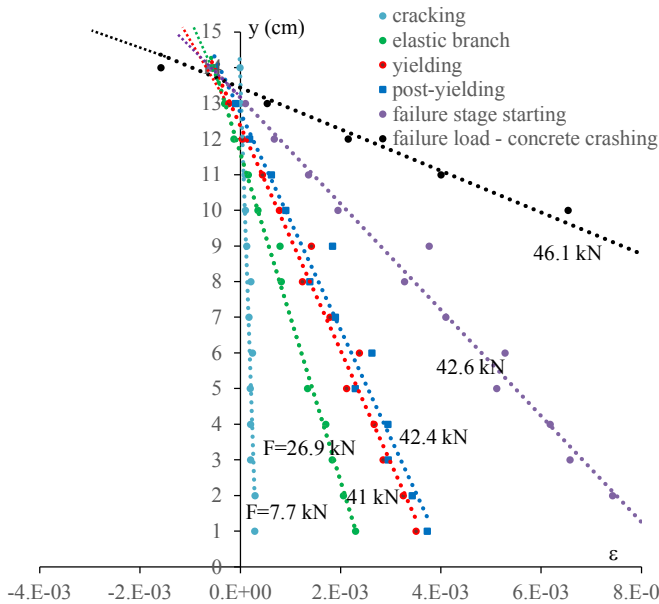


Figure 5. 26 - Strain distribution along the height of the UN-S\_2 beam for different load values

Finally, Figure 5. 27 shows a comparison between the experimental and the predicted results, discussed in section 5.1.1. The numerical models of the RC beam provided a behaviour more stiff than that experimentally observed. Moreover, the predicted yielding load was slightly lower than the experimental one. Nevertheless, the numerical model, which takes into account the concrete's confinement, was able to predict the failure load.

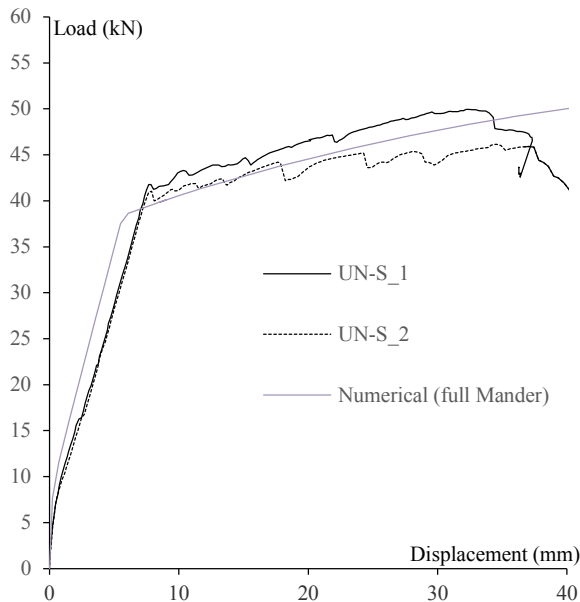


Figure 5. 27 - Un-strengthened beams: Load vs Displacement curves. Comparison between experimental and predicted results.

### 5.3.2 Ambient temperature tests of strengthened beams

The flexural test of the strengthened beam (S-1), showed that the beam cracked under about 8 kN, as well as observed for un-strengthened beams. This means that the strengthening, as expected, does not significantly affect the moment of inertia of the RC beam. Afterwards, the load linearly increased up to the yielding load, equal to about 56 kN (36% greater than the yielding load of the un-strengthened beams, Figure 5. 28), corresponding to the midspan deflection of about 9 mm (Figure 5. 29). After the steel yielding, the over-loading of the CFRP bar led to the slippage between FRP and bonding agent. Then, the load increased up to about 59 kN (19% greater than the failure load of UN-S\_1), with a significant increase of the midspan deflection, up to about 21 mm (Figure 5. 29), due to the complete debonding of the CFRP bar in the cementitious grout. Note that DIC revealed to be a very useful technique for measuring displacements, especially during this test. In fact, LP100 did not properly work for the overall duration of the test, whereas DIC provided deflection values, which are in very good agreement with those provided by the LP100, when the latter properly worked (see Figure 5. 29).

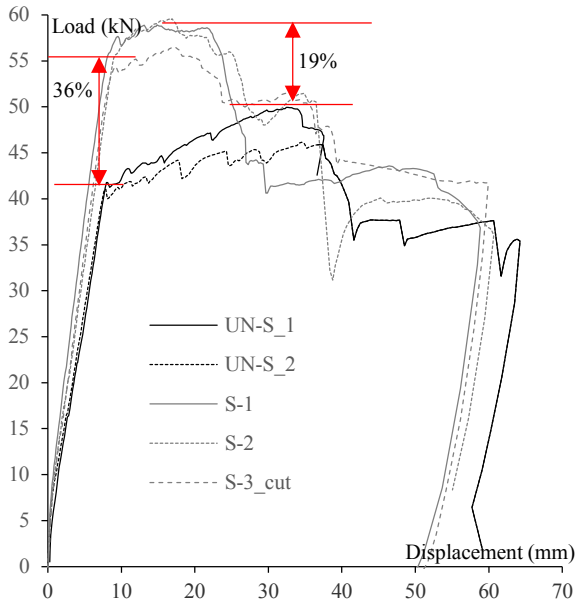


Figure 5. 28 - Load vs Displacement curves. Comparison between un-strengthened and strengthened beams.

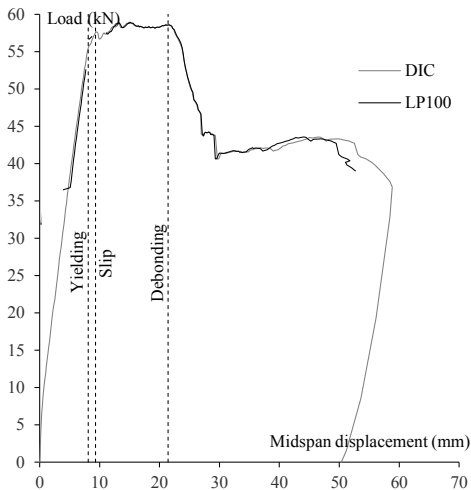


Figure 5. 29 - S-1: Load vs Displacement curves. Comparison between LP100 and DIC

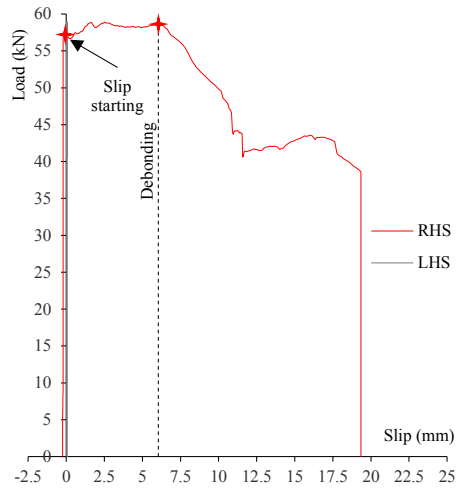


Figure 5. 30 - S-1: Load vs Slip curves

After the debonding of the strengthening system, occurred when the slip of the bar on the RHS achieved about 6 mm (Figure 5. 30), S-1 showed a behaviour similar to that exhibited by UN-S\_1 and UN-S\_2 (Figure 5. 28). In fact, the beam failure occurred due to the concrete crushing. The Figure 5. 31 supports the interpretation of the beam failure mode. That figure shows that the strain in the

CFRP bar, after the concrete cracking, linearly increased up to  $5170 \mu\epsilon$ , until the starting of the bar's slippage. Then, during the debonding stage, the strain in the bar increased up to about  $5850 \mu\epsilon$ , corresponding to a slight increase of the load. Finally, when the slip of the bar on RHS (Right Hand Side) achieved about 6 mm, the load and the strain decreased, due to the failure of the strengthening system. Note that the bar slipped only on RHS, being the slip on LHS (Left Hand Side), read by LP25, equal to zero (Figure 5. 30).

Figure 5. 32 shows the S-1 beam after the failure. Those pictures show that the beam failed due to the concrete crushing (Figure 5. 32 a), with extensive flexural cracks in tension side (Figure 5. 32 b,c). Clearly, the concrete crushing occurred after the end-debonding, when the bar's slip achieved about 20 mm (Figure 5. 32 d).

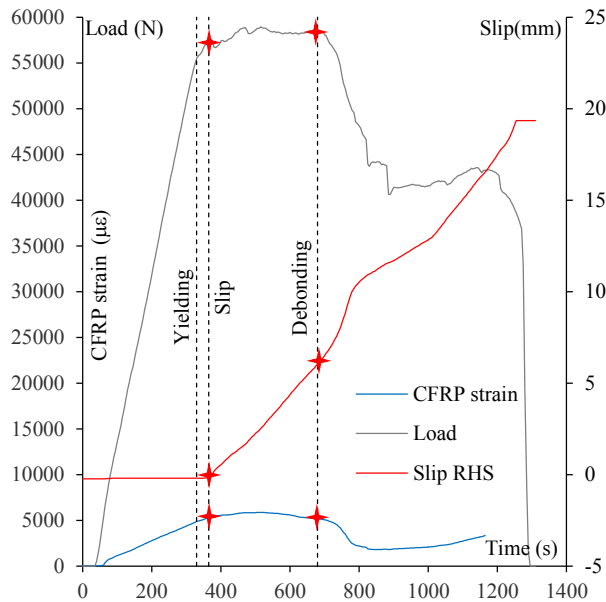


Figure 5. 31 - S-1: Load vs bar's Slip and bar's Strain

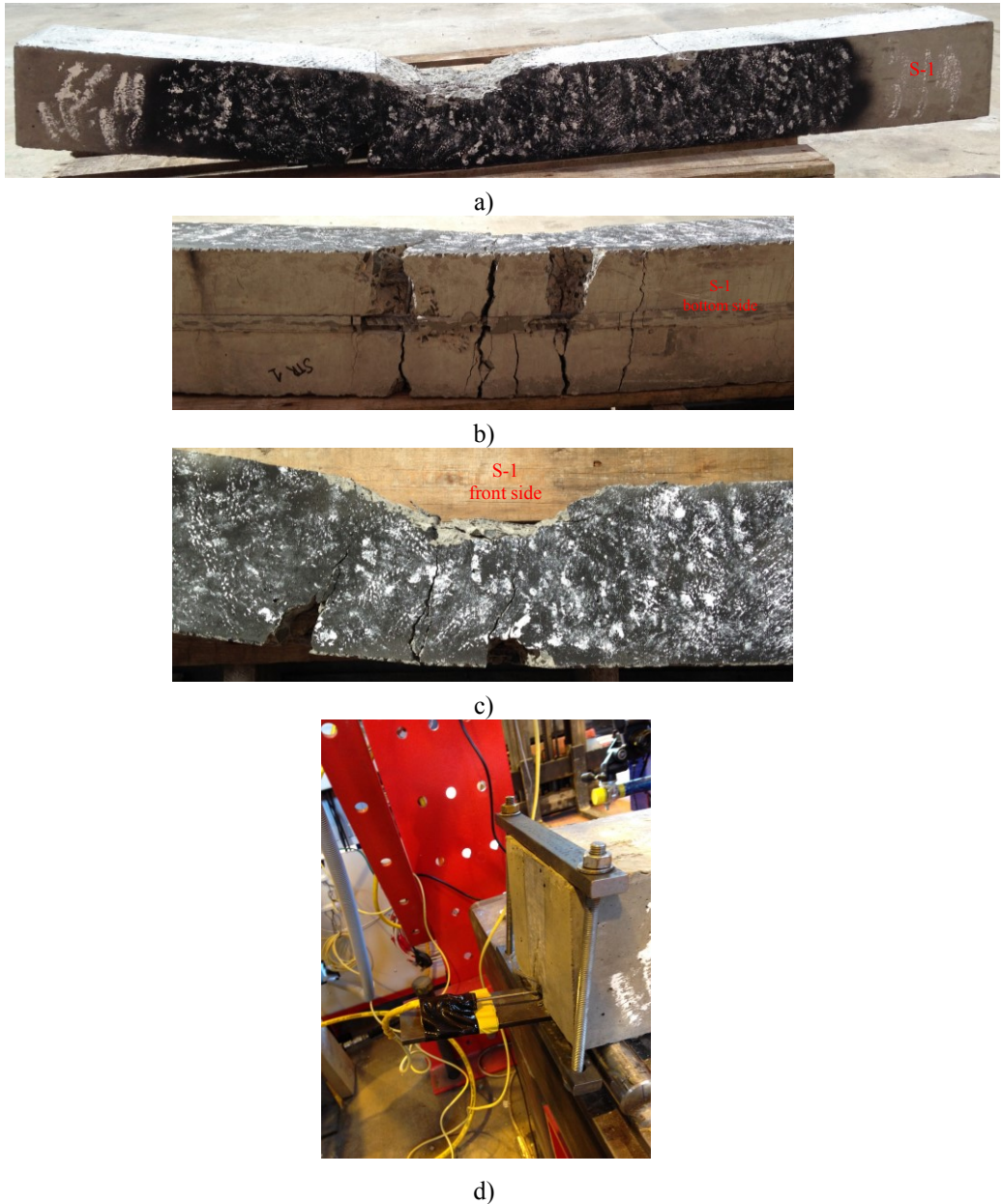


Figure 5. 32 - Specimen S-1 after failure

Similarly to S-1, the S-2 linearly achieved the yielding load equal to about 56 kN, corresponding to the midspan deflection of about 9 mm (Figure 5. 33), without any damage of the strengthening system. After the steel yielding, the over-loading of the CFRP bar led to the slippage between FRP and bonding agent. Then, the load increased up to about 60 kN, with a significant increase of the



midspan deflection, up to about 25 mm (Figure 5. 33), due to the complete debonding of the CFRP bar in the cementitious grout. After the debonding of the strengthening system, occurred when the slip of the bar on the RHS achieved about 7.5 mm (Figure 5. 34), S-2 showed a behaviour similar to that exhibited by UN-S\_1 and UN-S\_2 (Figure 5. 28).

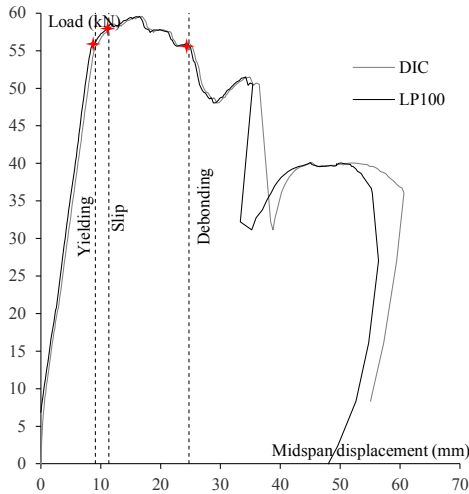


Figure 5. 33 - S-2: Load vs Displacement curves. Comparison between LP100 and DIC

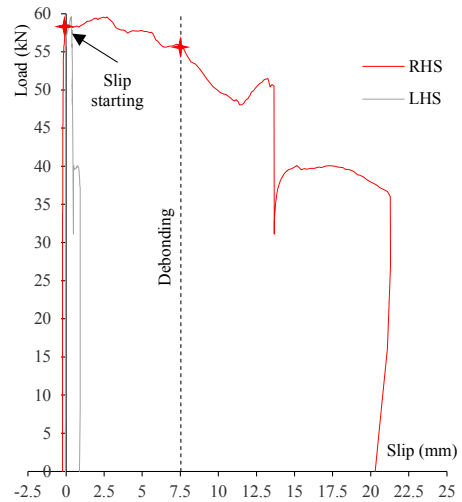


Figure 5. 34 - S-2: Load vs Slip curves

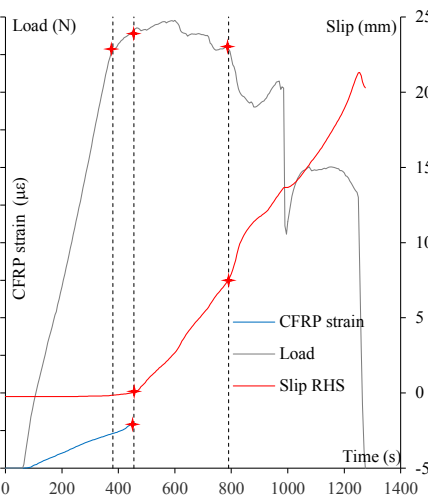


Figure 5. 35 - S-2: Load, bar's Slip and bar's Strain vs Logging Time

Moreover, Figure 5. 35 shows that the strain in the CFRP bar, after the concrete cracking, linearly increased up to 5300  $\mu\epsilon$ , until the bar started to slip. During the debonding stage, the strain gauge did not work anymore, but all the statements provided above for the S-1 test's results can be extended to S-2, since,

as shown in the following, a very good agreement was obtained between the results of those tests. Note that the bar, also in this case, slipped significantly only on RHS, being negligible the slip read by LP25 on LHS (Figure 5. 34).

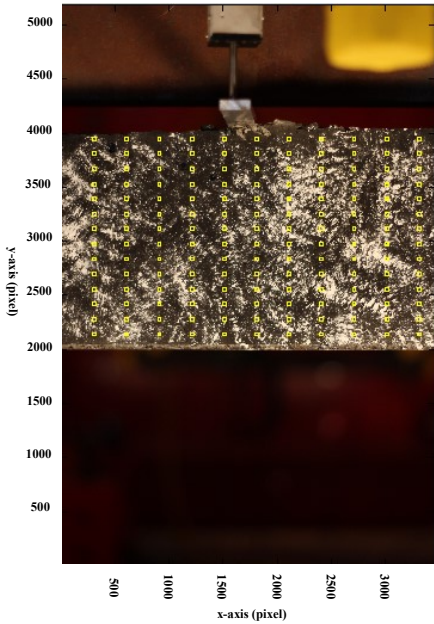


Figure 5. 36 - Patches monitored through DIC (S-2 beam)

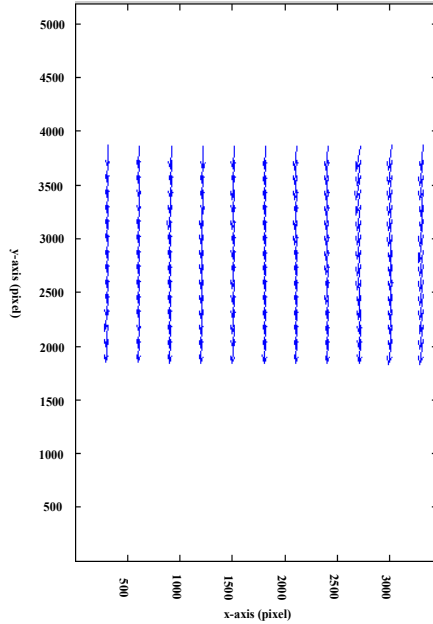


Figure 5. 37 - Generic step of DIC (S-2 beam)

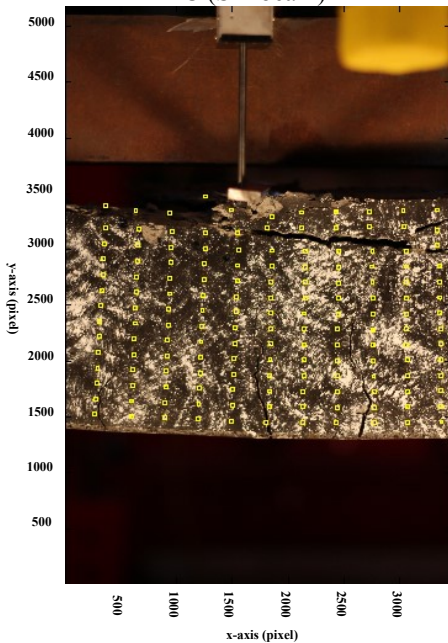


Figure 5. 38 - Patches monitored through DIC. Failure stage (S-2 beam)

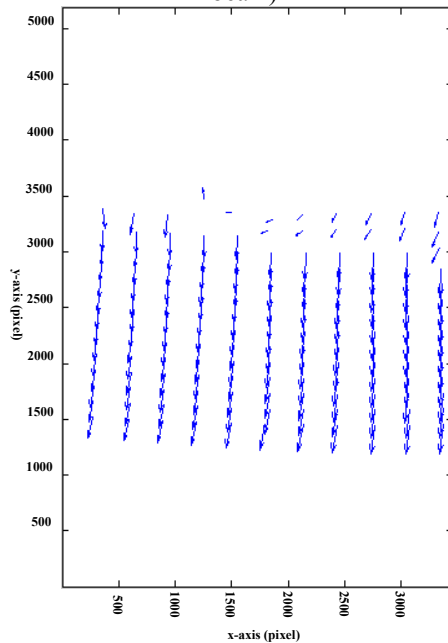


Figure 5. 39 - Final step of DIC (S-2 beam in failure stage)

The strain distribution on the tested beams was calculated through the DIC, as previously explained. The Figure 5. 36 shows, for example, the 154 patches monitored through the DIC of S-2. Those patches were placed within 220 mm, along the beam midspan ( $x$  axis), and within 130 mm, along the beam height ( $y$  axis). The Figure 5. 37 and the Figure 5. 39 show, for example, the direction of patches' displacement in the early and the failure stage of the flexural test of S-2 beam, obtained through the DIC.

The load, the CFRP strain, read by a strain gauge, and the strain  $\epsilon_x(y = 30mm, l_{0,i})$  are depicted versus the logging time in Figure 5. 40, even if the logging time is not a significant variable. As previously said, it just enables to relate the load to the calculated strain values. When the load achieves about 56 kN, the load curve shows a significant change in slope, representative of the stiffness reduction due to the steel yielding, while  $\epsilon_x(y = 30mm, l_{0,i})$  ranges between 2.5‰ and 3.5‰, which is slightly higher than the expected steel yielding strain (2.5‰). It may depend on the extensive concrete cracking, which led to the slight overestimation of the strain. Anyway, the proportionality between the average of  $\epsilon_x(y = 30mm, l_{0,i})$  and the CFRP strain may prove the reliability of the strain calculation.

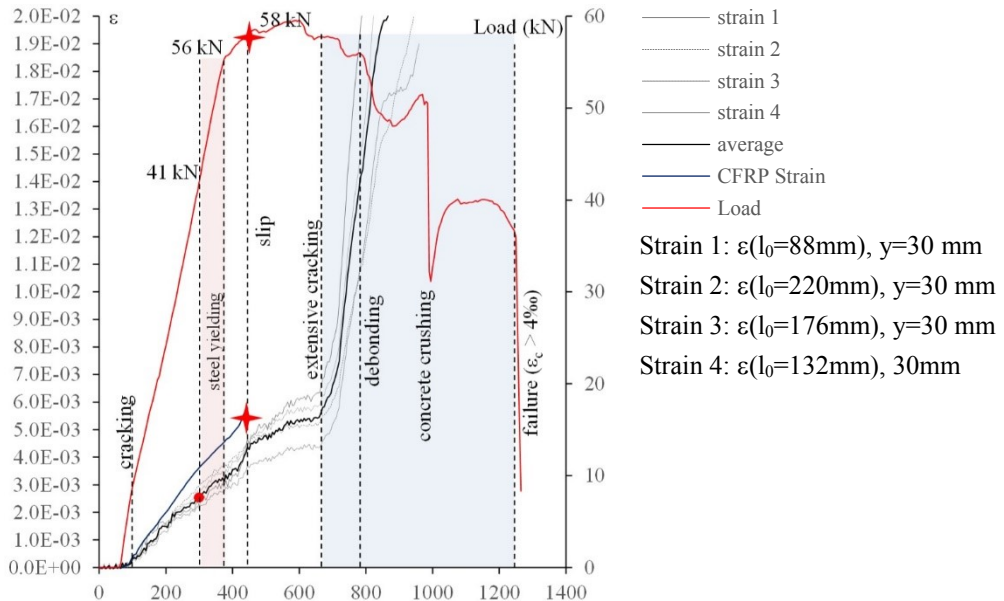


Figure 5. 40 - S-2: Load and Strain vs Logging Time

Figure 5. 41 shows the strain distribution on the beam for different load values, which is, as expected, linear. That figure enables, as previously said, the

localization of the neutral axis and the definition of the curvature depending on the value of the load.

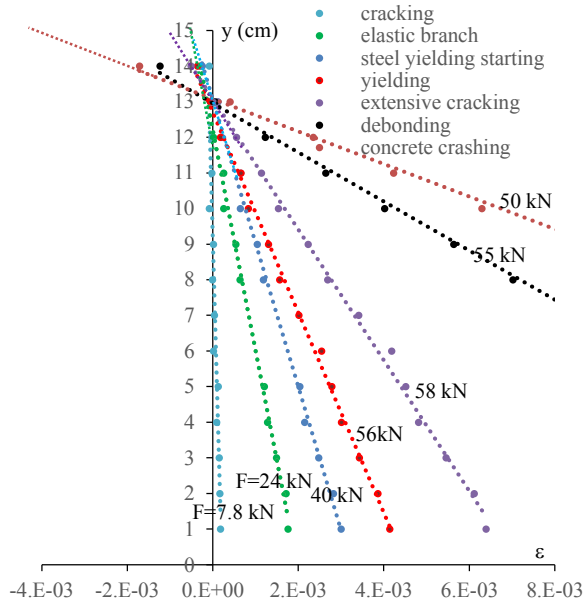


Figure 5.41 - S-2: Strain distribution along the height of the beam

Figure 5.42 and Figure 5.43 show a comparison between S-1 and S-2, highlighting that a very good agreement was obtained between these tests.

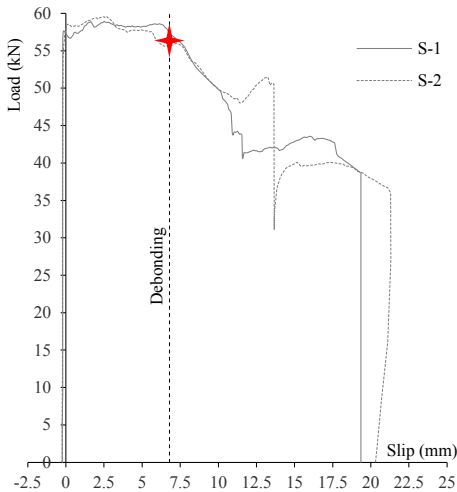


Figure 5.42 - S-2: Load vs Slip curves. Comparison between S-1 and S-2

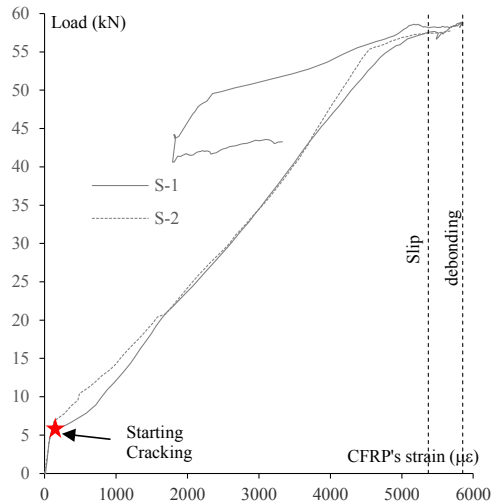


Figure 5.43 - S-2: Load vs CFRP bar's strain. Comparison between S-1 and S-2

Moreover, Figure 5. 43 worth clarify that stated above: the strain in the CFRP bar, after the concrete cracking, linearly increased up to about 5000  $\mu\epsilon$ , both in S-1 and S-2, until the starting of the bar’s slippage. Then, during the debonding stage, the strain in the bar increased of about 20%, corresponding to a slight increase of the load. Finally, when the slip of the bar increased significantly, the the strain decreased due to the failure of the strengthening system.

The performance of S-3\_cut was slightly worse than S-1 and S-2, due to the lower bonding length (625 mm instead of 725 mm) of the bar into the groove. Anyway S-3\_cut achieved the yielding load equal to about 54 kN (32% greater than the yielding load of the un-strengthened beams), corresponding to the midspan deflection of about 9 mm (Figure 5. 44), without any damage of the strengthening system. The slippage of the bar in the groove started under a load slightly higher than the yielding load and, finally, the debonding occurred leading to an elevated increase of the midspan deflection of about 24 mm. Therefore, a bonding length of 625 mm instead of 725 mm, as expected did not significantly change the behaviour of the strengthening. This means also that the local confinement provided by the supports did not worth anchor the bar at the end, when a greater bonding length was used.

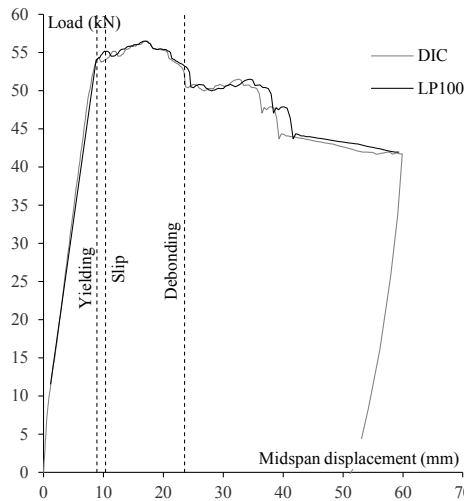


Figure 5. 44 - S-3: Load vs Displacement curves. Comparison between LP100 and DIC

Finally, Figure 5. 45 shows a comparison between the experimental and the predicted results, discussed in section 5.1.1. The numerical model of the NSM FRP strengthened RC beam was able to predict reasonably the stiffness of the strengthening system, whereas it slightly underestimated the yielding load. Nevertheless, the numerical model provided a reliable prediction of the

experimental failure load, corresponding to the achievement of the strain equal to about 5‰ in the CFRP bar. Note that the strain limit set in the numerical model at 5‰ was chosen considering an end-debonding failure model, proposed by Bilotta et al (2014). Obviously, a CSA is not able to predict the behaviour of beam during the debonding stage.

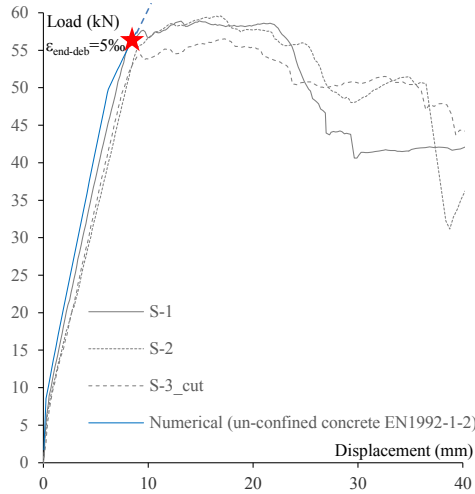


Figure 5. 45 - Strengthened beams: Load vs Displacement curves. Comparison between experimental and predicted results.

Table 5. 3 summarizes the test results, which were discussed above, highlighting that the strengthening provided a significant increase of the load bearing capacity, since the gain in yielding load ranges between 32-36% and the gain in failure load ranges between 17-25%. The strengthened beams failed due to concrete crushing after the FRP debonding that occurred with a strain in the CFRP equal to 5.8‰.

Table 5. 3 - Summary of the ambient temperature test results

Test ID	Yielding Load	Failure Load	Maximum CFRP strain	Failure mode
UN-S_1	40.8 kN,	50.7 kN	-	F
UN-S_2	40.8 kN,	45.5 kN	-	F
S-1	56.4 kN,	59.0 kN	5.8‰	D/F
S-2	56.4 kN,	59.6 kN	5.8‰	D/F
S-3_cut	54.1 kN,	56.6 kN	Not measured	D/F

\*F=Flexural; \*\*D/F=Debonding/Flexural

### 5.3.3 High temperature tests

The following sections summarize the results of the conducted high temperature tests, to investigate the behaviour of the NSM FRP strengthened RC beams both in case of global and local heating.

Note that the tests were conducted in global heating configuration (GloH) under a typical service load (SL) equal to 40 kN, whereas the tests in local heating configuration (LoCH) were carried out under both SL and a very high service load (HL) equal to 50 kN. These loads correspond to two different utilization factors of the member in fire,  $\eta_{fi}$ , namely the ratio between the relevant effects of actions in the fire situation at time  $t$ ,  $E_{d,fi,t}$ , and the design value of the resistance of the member in fire situation at beginning of thermal transient,  $R_{d,fi,0}$  (EN1991-1-2). Particularly, when the sustained load is 40 kN,  $\eta_{fi}$  of the beam is 0.7, whereas when the sustained load is 50 kN,  $\eta_{fi}$  is 0.8.

#### 5.3.3.1 Global heating configuration

Figure 5. 46 shows the Temperature recorded by the thermocouples in a NSM FRP strengthened RC beam, tested in global heating configuration, under 40 kN sustained load (GloH-SL-1). Figure 5. 46 shows that the temperature along the bonded length of the FRP bar (T6b – T7b – T8 – T11) is almost uniform and its maximum value, after 90 min of fire exposure, varies in the range 500-580°C. Note that the temperature in the heated zone of the bar was uniform until the opening of large cracks (after 50 min of fire exposure), and then a maximum scatter of 80°C was recorded after 90 min of exposure. Figure 5. 47 shows the the position of the above-mentioned cracks after 90 min of heating.

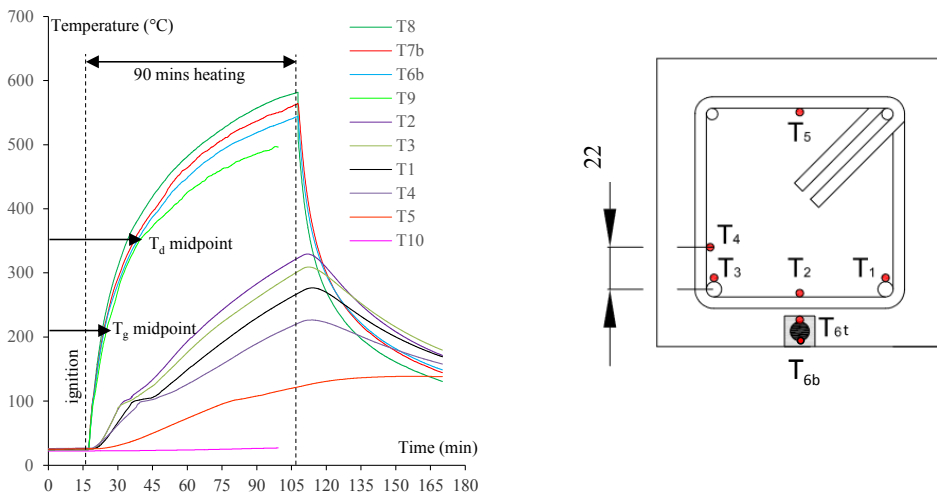


Figure 5. 46 – GloH-SL-1: Temperature versus Time curves

Figure 5. 46 shows also that the maximum temperature in the tensile steel reinforcement (T2) was about 300°C, while it was about 65°C in stirrup's top arm. This means that when the strengthening system completely lost its effectiveness, due to high temperature, the un-strengthened beam was able to sustain the load, since no reduction in stiffness and resistance of steel occurred. In fact, the beam did not fail after 90 min of heating.

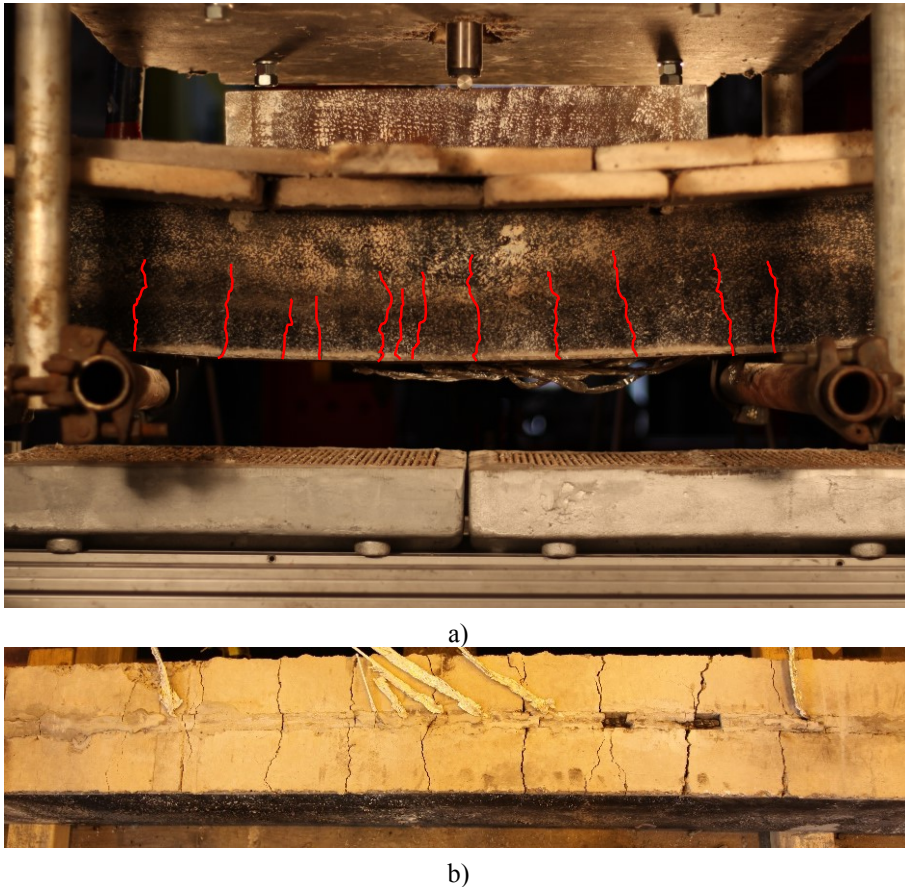


Figure 5. 47 – GloH-SL-1 after 90 min of heating exposure: a) front side; b) Bottom side

In Figure 5. 48 the midspan deflection is plotted versus time. The beam deflected of about 7 mm, when 40 kN sustained load was attained. Then, when the heating stage started, the deflection increased due to the thermal gradient over the beam, which induced a thermal curvature. Note that at the attainment of the  $T_g$  (max  $\tan\delta$ ) in the FRP bar, after about 10 min of heating (25 min by the beginning of the test), no particular changes in the deflection curve were observed. After about 25 min of heating (40 min by the beginning of the test) the



FRP bar achieved the decomposition temperature ( $T_d$  midpoint, see 3.1.2.1) and a change in the slope of the deflection vs time curve was recorded. Basically, this is representative of the transition between the strengthened beam and the un-strengthened one. Moreover, the temperature in the steel rebars, in the same time, attained 100°C, which is the temperature that induces a stiffness reduction. Therefore, the change in displacement slope, observed after about 25 min of heating is also related to the greater deformability of the un-strengthened beam in comparison to that at ambient temperature.

Figure 5. 48 shows also the comparison between the displacements read by the LP100 and that measured through the DIC, showing that a very good agreement was obtained, even if the LP did not work anymore after about 90 min by the beginning of the test, due to the overheating of the tool. It confirms that DIC is very useful, since the traditional tools might not work properly due to high temperature, as occurred during this test. Figure 5. 48 and Figure 5. 49 demonstrate that a very large deflection was recorded during the heating.

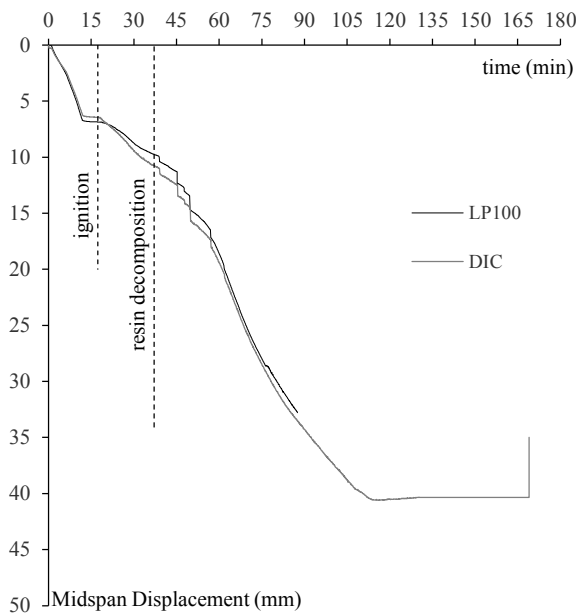
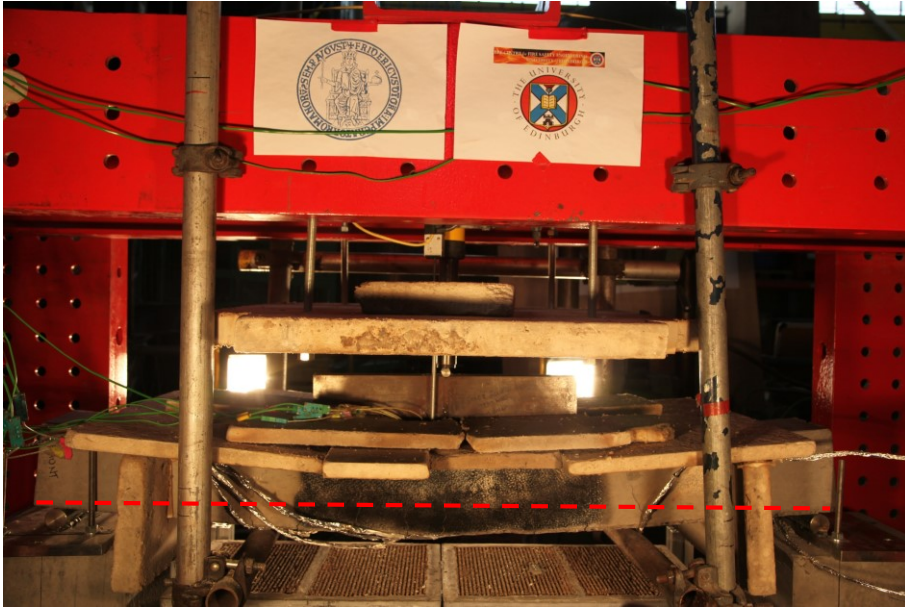
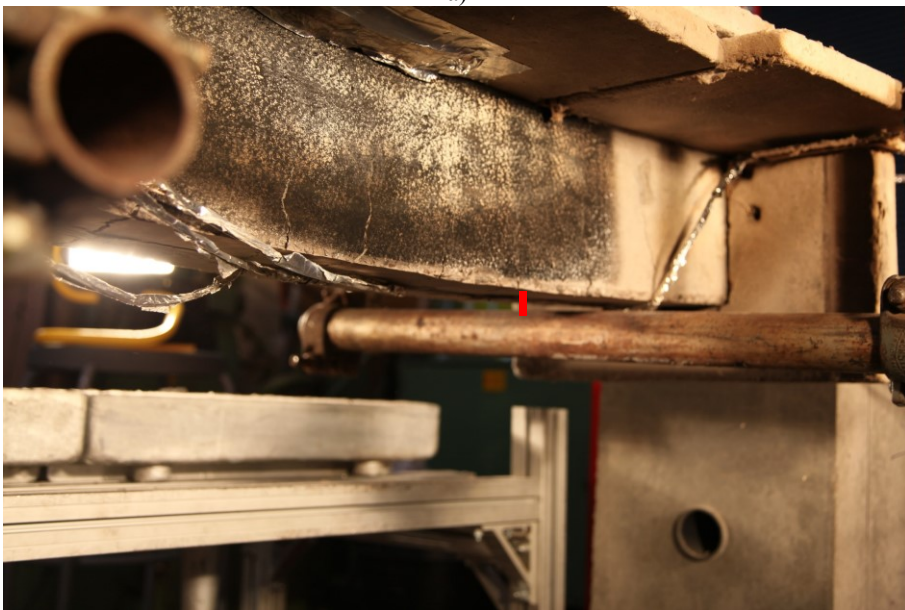


Figure 5. 48 – GloH-SL-1: Midspan deflection versus time

Note that the slip was not measured during this test, because the LP25 could not be set, since the CFRP bar had a bonded length lower than the beam's length. After the test, the grout was removed and the total slip of 21 mm was measured.



a)



b)

Figure 5. 49 – Deflection of GloH-SL-1 after 90 min of heating exposure: a) Front side; b) Isometric view

The chosen heating method can be considered highly reliable, since it provided a repeatable heat flux, as shown in Figure 5. 50, where the temperature

read by thermocouples during the test GloH-SL-1 are compared with those read during the test GloH-SL-2.

Figure 5. 51 shows a comparison between the tests conducted on strengthened beams (GloH-SL-1 and GloH-SL-2) and that carried out on the un-strengthened beam (UN-S\_GloH-SL-1), in terms of midspan displacement versus time of heating. This comparison confirms that the achievement of the decomposition temperature of the bar along the overall bonded length determined the failure of the strengthening system, leading to a change in the slop of these curves.

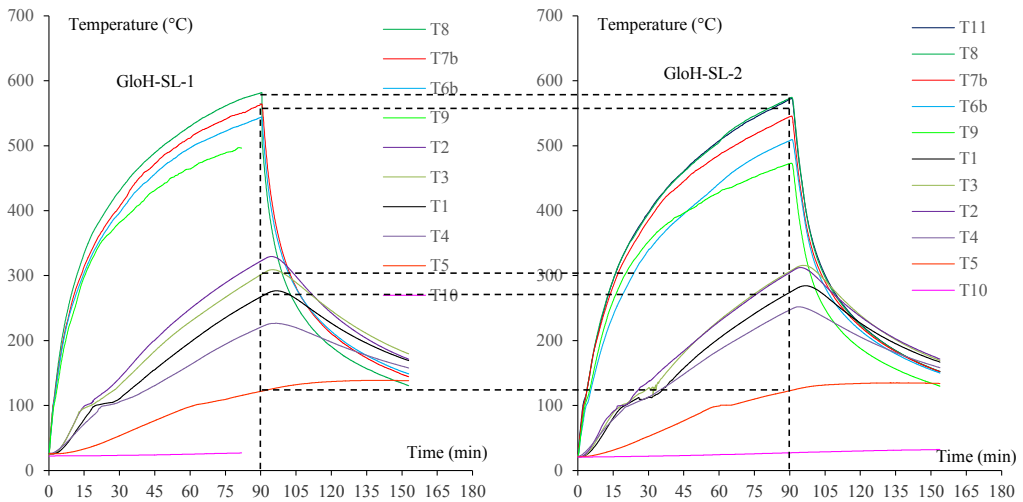


Figure 5. 50 – Temperature vs time of fire exposure curves. Comparison between GloH-SL-1 and GloH-SL-2

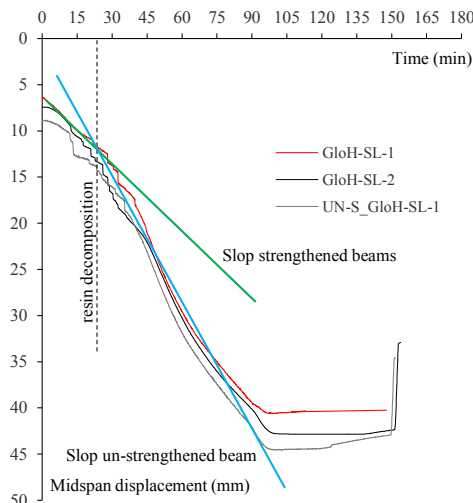


Figure 5. 51 – Midspan displacement vs time of fire exposure curves. Comparison between GloH-SL and UN-S\_GloH-SL

Anyway, the beams did not fail at high temperature, since the RC beams alone were still able to sustain the load, therefore they were allowed to cool for two days and then residual tests were conducted (see 5.3.4).

### 5.3.3.2 Localised heating configuration

Figure 5. 52 shows the temperature recorded by the thermocouples placed in a NSM FRP strengthened RC beam (Figure 5. 18), tested in local heating configuration, with  $\eta_{fi}$  equal to 0.7 (LocH-SL-1). Figure 5. 52 shows that the temperature along the bonded length of the bar is significantly not uniform: its maximum value, after 90 min of fire exposure, varies in the range 580-630°C near the exposed midspan, while it is about 30-50 °C near the supports. As already shown in the previous section, the temperature in the steel reinforcement was lower than that able to reduce the steel strength.

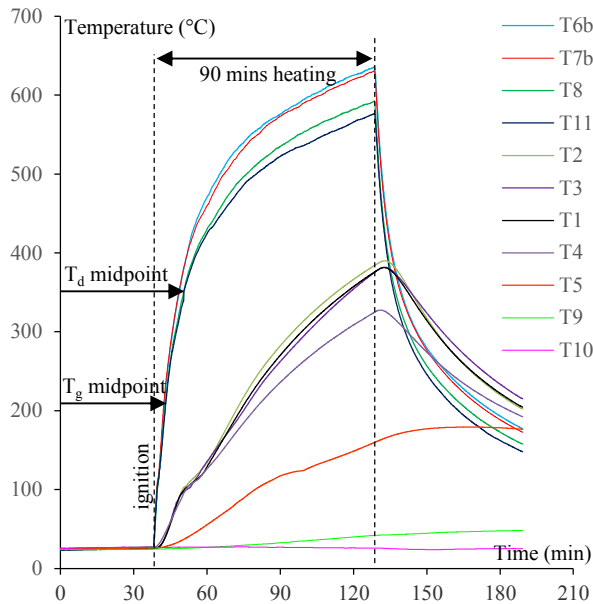


Figure 5. 52 – LocH-SL-1: Temperature versus Time curves

Figure 5. 53 shows the comparison between the displacements read by the LP100 and those measured through the DIC, confirming the good agreement for the entire duration of the test. This figure shows also that when  $\eta_{fi}$  was 0.7, the beam deflected of about 7 mm, Then, the midspan deflection increased up to about 16 mm, due to 90 min of heating exposure, which determined a thermal curvature associated to the thermal gradient over the beam.

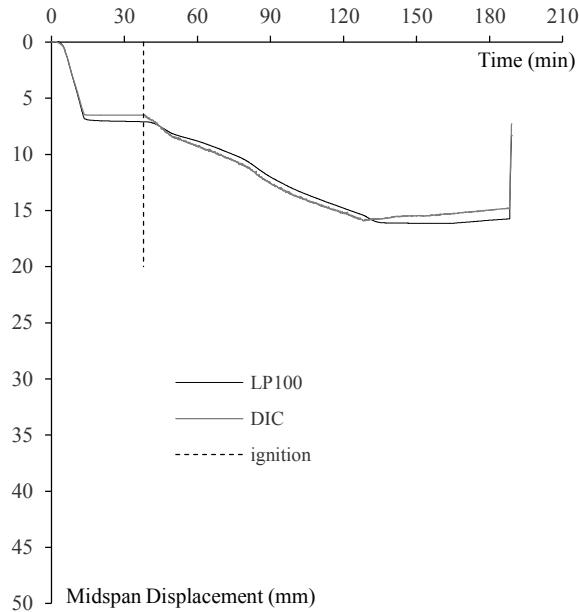


Figure 5. 53 – LocH-SL-1: Midspan displacement vs Time curves

Figure 5. 54a shows the comparison between the slip read by the LPs on RHS and LHS, depicted versus the time, highlighting that the slip was in practice negligible, but slightly higher on RHS. The RHS slip was also plotted versus the maximum temperature read by the thermocouples near the midspan (Figure 5. 54b), showing that the achievement of the glass transition temperature, first, and of the decomposition temperature, later, did not determine any damage of the strengthening system, since the end-anchorage was practically cold. The bar started to slip when its temperature in the midspan achieved about 600°C, whereas near the supports was still cold. It is very likely that a part of the end-anchorage in the unexposed zone, close to that exposed, entered in the glass transition stage, reducing the effective end-anchorage length and leading to the slippage of the bar. Anyway, the strengthening system did not fail, as the residual tests showed (see section 5.3.4), since the effective end-anchorage was able to sustain the stress transferred from the midspan when the CFRP in the heated zone completely decomposed. Unfortunately, the effective cold end-anchorage length could not be experimentally determined since no thermocouples were placed on the CFRP bar, in the unexposed zone, close to that exposed. Anyway an estimation of the minimum needed effective end-anchorage, based on the results of bond tests at ambient temperature (Chapter 4) and on the CFRP strain attained in the midspan of the beam (Figure 5. 55) can be provided.

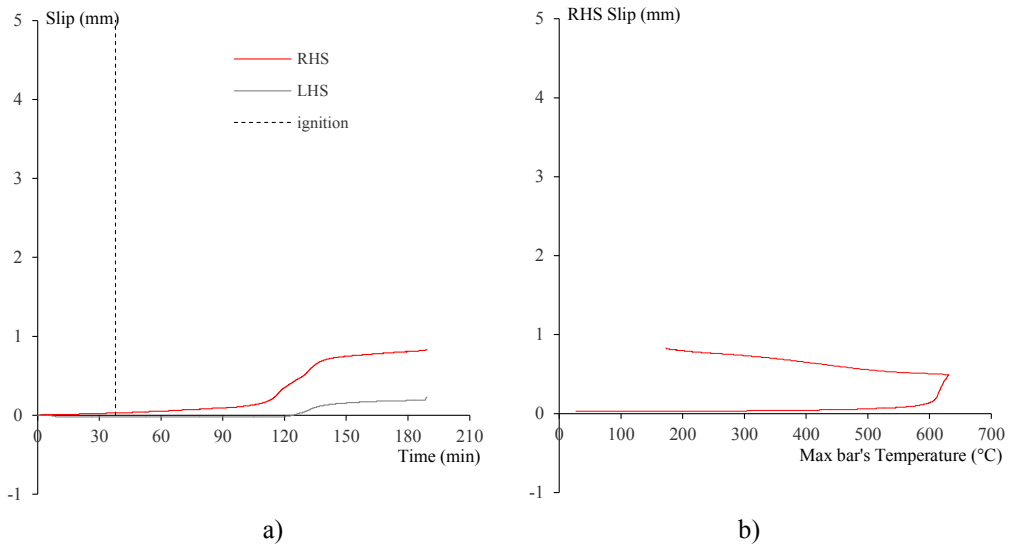


Figure 5. 54 – LocH-SL-1. Bar's Slip: a) RHS and LHS Slip vs Time curves; b) RHS Slip vs Temperature

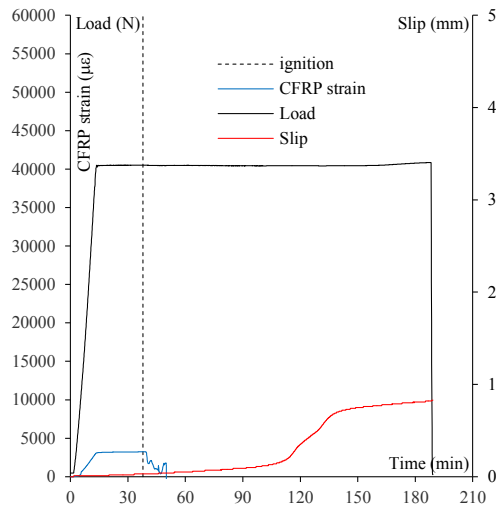


Figure 5. 55 – LocH-SL-1. Load, CFRP strain, Slip versus Time

The bond tests showed that, when the bonding length is 300 mm, the failure occurs for debonding at bar/adhesive interface under about 25 kN pull-out load ( $F_{deb}$ ). The latter determines a strain in the CFRP bar ( $\epsilon_{deb}$ ) equal to about 3.6‰. Figure 5. 55 shows that CFRP strain at midspan attained about 3.5‰ during flexural tests. This means that the strengthening system would be effective with a minimum cold end-anchorage length of 300 mm. Anyway, the portion of end-

anchorage effectively entered in the glass transition stage was evaluated through a thermal numerical analysis, which results are shown in section 6.1.

Also in localised heating configuration, the chosen heating mode was able to provide a repeatable heat flux. Figure 5. 56 shows, for example, the temperatures recorded by thermocouples during the test LocH-SL-1, which are compared with those read during the test LocH-SL-2.

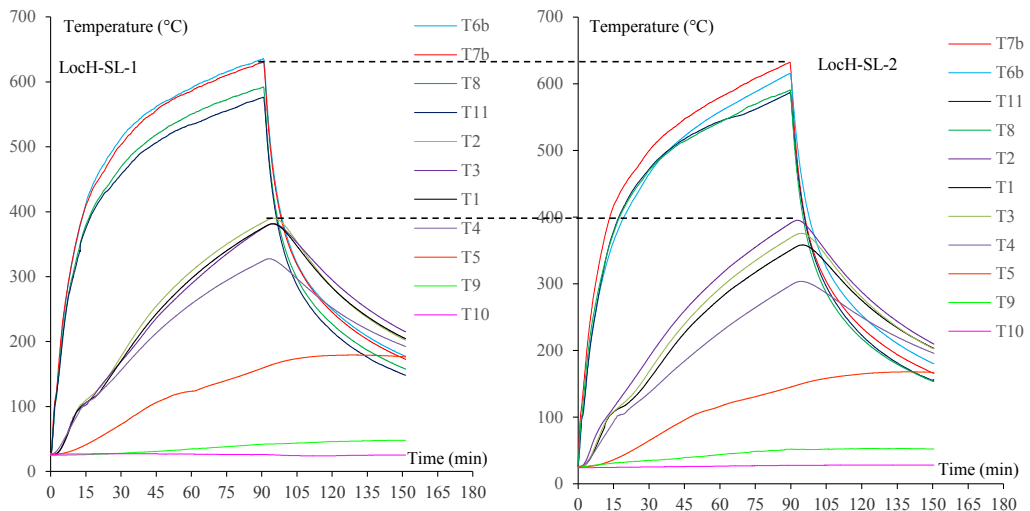


Figure 5. 56 – Temperature vs time curves. Comparison between LocH-SL-1 and LocH-SL-2

The test LocH-SL-2 confirmed that the bar started to slip when its maximum temperature, near the midspan, was about 600°C, whereas near the supports was practically cold (Figure 5. 57). Unfortunately the amount of slip occurred in LocH-SL-2 was significantly higher than that occurred in LocH-SL-1, which may be related to a manufacturing defect of the strengthening system.

Also the comparison, shown in Figure 5. 58, in terms of midspan deflection versus time demonstrated that the two beams behaved similarly until the bar started to slip. Later on, the midspan deflection of LocH-SL-2 significantly increased, due to the completely loss of the strengthening system. This interpretation was verified through the residual tests, conducted after two days, when the beams were completely cooled.

Finally, Figure 5. 59 and Figure 5. 60 show respectively the LocH-SL-1 and LocH-SL-2 at the end of the tests, highlighting the position of the largest cracks.

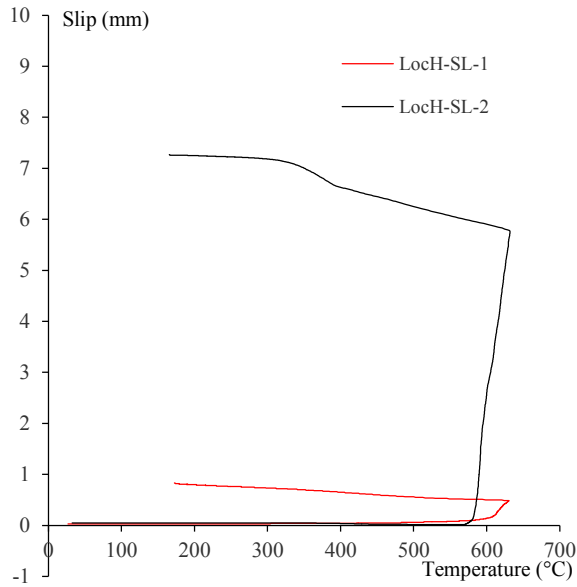


Figure 5. 57 – Slip versus Temperature. Comparison between LocH-SL-1 and LocH-SL-2.

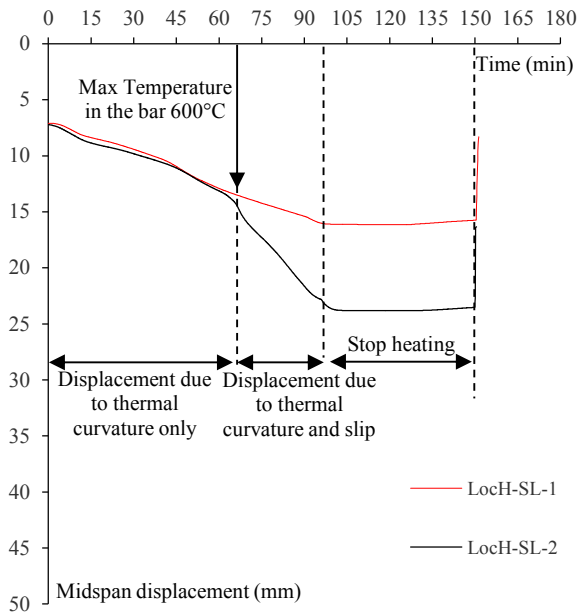


Figure 5. 58 – Midspan deflection versus Temperature. Comparison between LocH-SL-1 and LocH-SL-2.





Figure 5. 59 –LochH-SL-1 after 90 min of heating



Figure 5. 60 –LochH-SL-2 after 90 min of heating

The last two strengthened beams, manufactured for this experimental program, were tested in local heating configuration, under a quite high sustained load equal to 50 kN ( $\eta_{fi}$  equal to 0.8). During the loading stage of LocH-HL-1, the strain in the CFRP bar, near the midspan, attained about 4.5%. Thereafter, the heating stage started and the strain gauge did not work anymore, due to the overheating. Figure 5. 61 shows that the failure occurred when the temperature in the bar, near the heated midspan, ranged between 470÷530°C, whereas the temperature near the supports was practically that at ambient.

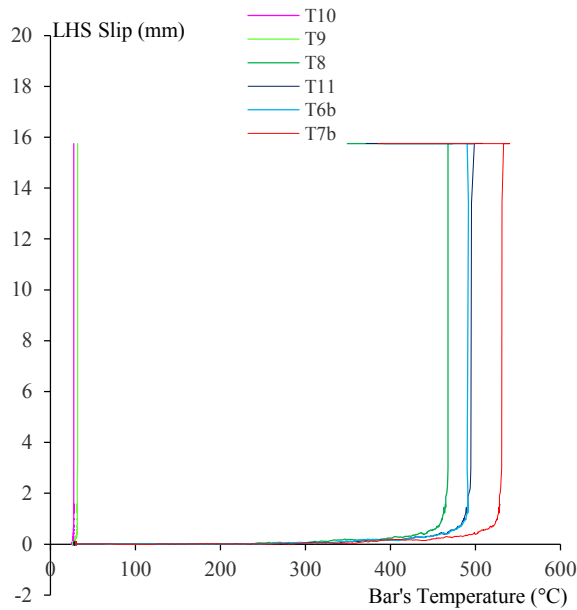
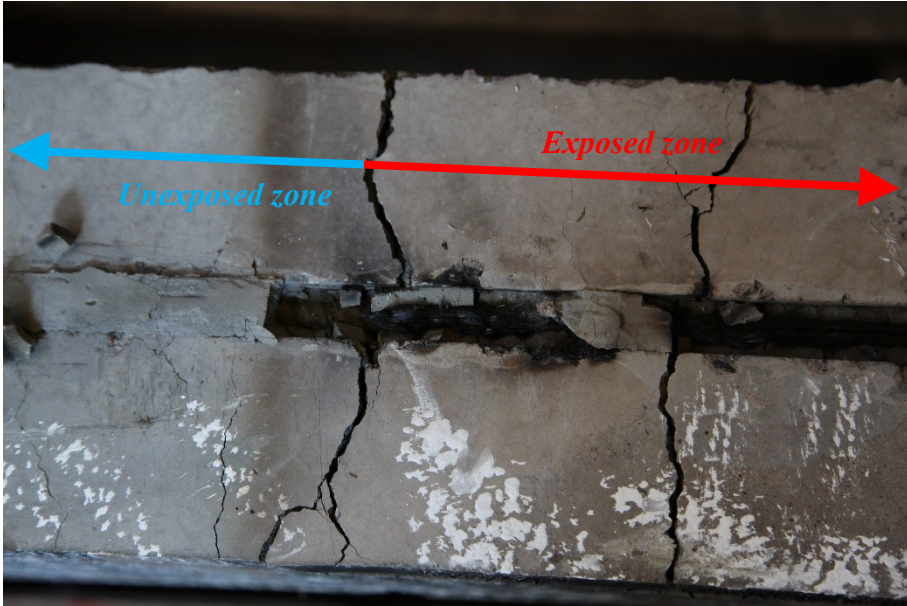


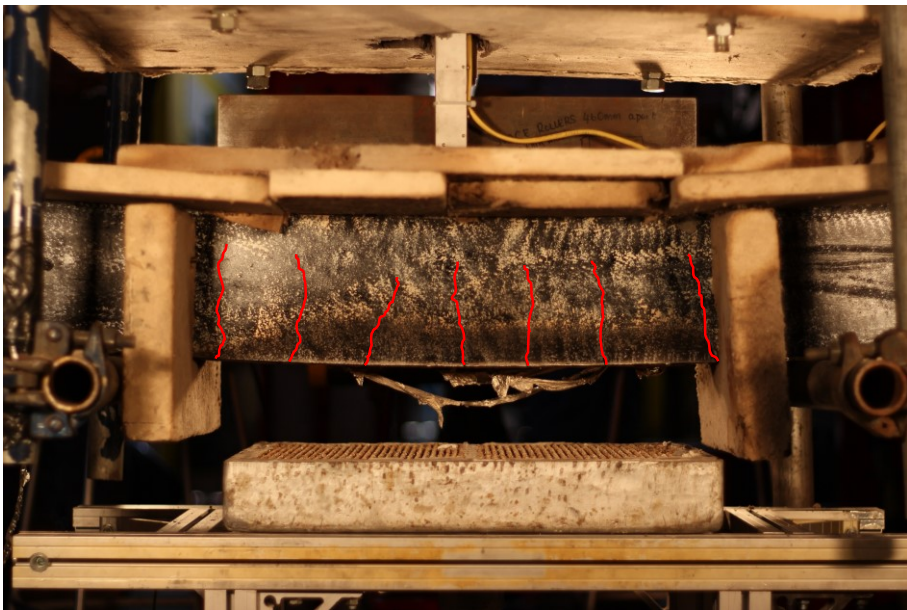
Figure 5. 61 – LocH-HL-1. Slip versus Temperature curves

Figure 5. 62 a depicts the beam (bottom side) immediately after the failure and proves that the resin of the CFRP bar was completely decomposed in the heated zone, since temperature at the failure was significantly higher than the decomposition temperature. Conversely, in the unexposed zone, the CFRP bar was not damaged at all.

Finally, Figure 5. 62 b depicts the beam (front side) after the failure, showing the distribution of the flexural cracks.



a)



b)

Figure 5. 62 – Loch-HL-1 after failure: a) Bottom side of the beam; b) Front side of the beam

Similarly, the Loch-HL-2 test provided a debonding failure mode of the strengthening, which occurred when the temperature in the CFRP bar in the heated zone ranged between  $570\div 630^{\circ}\text{C}$  (higher than that achieved in Loch-HL-1), whereas the temperature near the supports was practically that at ambient.

Actually, the CFRP bar, close to the exposed zone, due to the longitudinal thermal conductivity of the bar, may have achieved the glass transition temperature, leading to a reduction of the effective end-anchorage length, which was not able to sustain the stress transferred from the midspan. As stated above for LocH-SL\_i, the portion of end-anchorage effectively entered in the glass transition stage was evaluated through a thermal numerical analysis (see section 6.1), since no thermocouples were placed on the CFRP bar, in the unexposed zone, close to that exposed.

Figure 5. 63 shows the comparison between LocH-HL-1 and LocH-HL-2, depicting the slip versus the maximum temperature in the bar. Note that the beam LocH-HL-1 behaved worse than LocH-HL-2 already at ambient temperature, during the loading stage, in fact LocH-HL-1 deflected of about 11 mm, when the sustained load was achieved, whereas LocH-HL-2 deflected of about 8.5 mm. It may be related to a manufacturing defect of the strengthening system. Actually, the manufacturing stage needs to be conducted with extreme care, in fact, a certain scatter was, in some cases, observed in the results of bond tests, as well as in flexural tests.

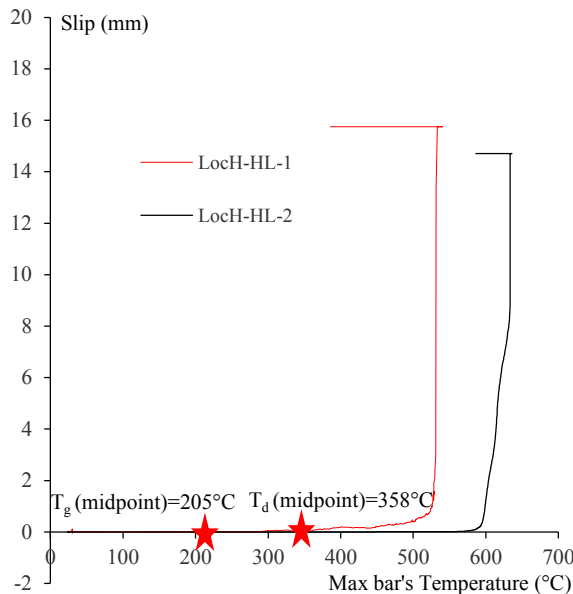


Figure 5. 63 –Slip versus Temperature curves. LocH-HL-1 vs LocH-HL-2

Finally, note that the tensile strength of the CFRP bar was not ever attained, although the significant temperature (more than 600°C) attained in the bar during the heating phase, and the significant stress, due to sustained load.

### 5.3.4 Residual tests

The beam that did not fail during high temperature tests were tested in displacement control until the failure, in order to define their residual strength.

The residual test of UN-S\_GloH-SL provided, as expected, a residual strength equal to about 49 kN, which is roughly its strength at ambient temperature (Figure 5. 64). In fact, during the heated test, the temperature in the reinforcing cage was lower than that able to reduce the steel strength.

Similarly, the residual tests of GloH-SL-1 and GloH-SL-2 provided a residual strength ranging between 49÷51 kN, which is the strength at ambient temperature of the un-strengthened beam (Figure 5. 65). This means that during the heated tests, the beams lost the strengthening system, but they did not fail, since the un-strengthened beams were able to bear the sustained load. Figure 5. 66 shows the beam after the residual test, highlighting that the failure mode was a typical flexural failure mode of an un-strengthened beam, characterized by the concrete crushing.

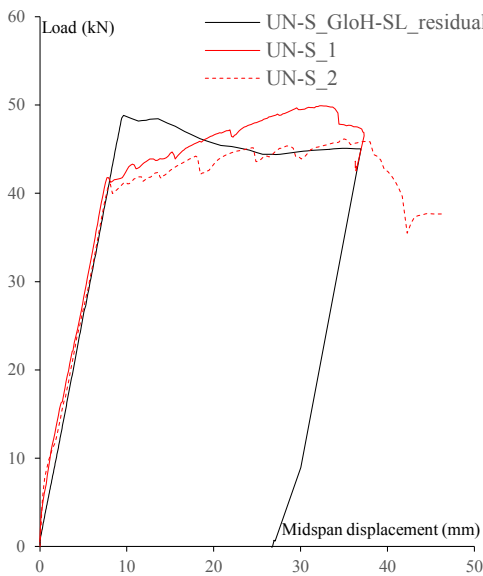


Figure 5. 64 – Load versus Midspan displacement. Comparison between UN-S\_GloH-SL\_residual and UN-S\_i.

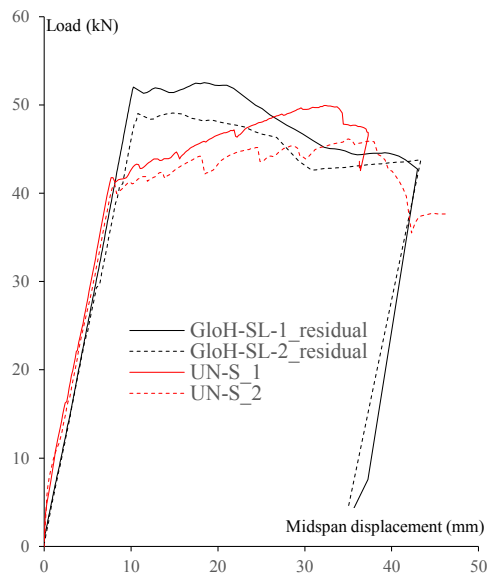
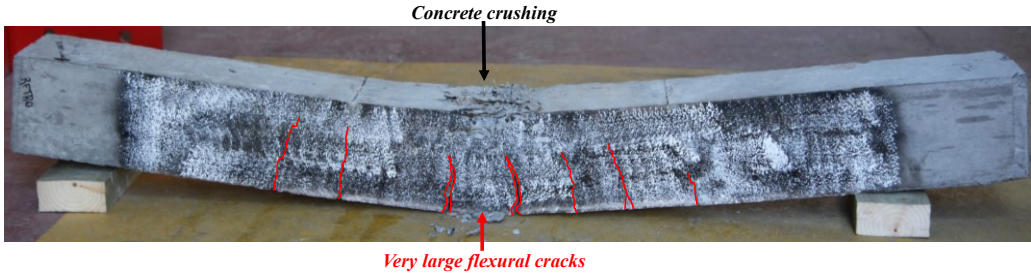


Figure 5. 65 – Load versus Midspan displacement. Comparison between GloH-SL-i\_residual and UN-S\_i.



a)



b)

Figure 5. 66 – GloH-SL-1\_residual after the residual test: a) Front side; b) Bottom side

The residual tests of Loch-SL-1 and Loch-SL-2 provided, as expected, a different residual strength. In fact, as shown in section 5.3.3.2, the CFRP bar slipped significantly during the test of Loch-SL-2, whereas the slip of the bar in Loch-SL-1 was negligible.

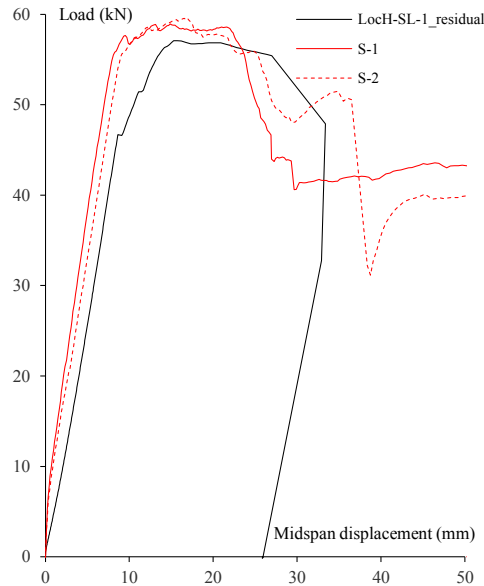


Figure 5. 67 – Load versus Midspan displacement. Comparison between Loch-SL-1\_residual and S-i.

Really, the residual strength of Loch-SL-1 was about 57 kN, which is the 96% of the failure load of the NSM FRP strengthened RC beams at ambient temperature (average between S-1 and S-2, see Figure 5. 67), while the residual strength of Loch-SL-2 was about 50 kN, which is roughly the strength at ambient temperature of the un-strengthened beam.

Figure 5. 68, shows the Loch-SL-1 beam after the residual test, highlighting the position and the width of the largest cracks.

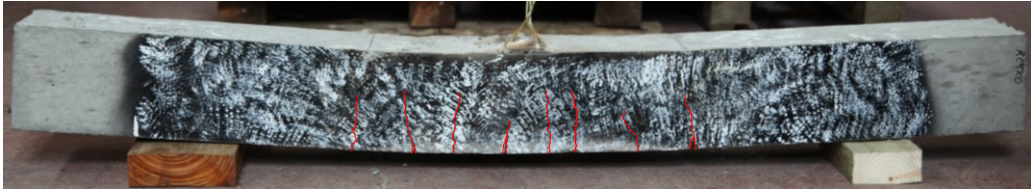


Figure 5. 68 – Loch-SL-1 \_residual after the residual test

#### 5.4 SUMMARY OF THE EXPERIMENTAL RESULTS AND CONCLUSION

The high temperature tests highlighted the efficiency of the strengthening system both in global and in local heating configuration. Obviously, the effectiveness of the strengthening system during the accidental event and its residual strength depends also on the utilization factor of the member in fire,  $\eta_{fi}$ , namely the ratio between the relevant effects of actions in the fire situation at time  $t$ ,  $E_{d,fi,t}$ , and the design value of the resistance of the member in fire situation at beginning of thermal transient,  $R_{d,fi,0}$  (EN1991-1-2). The tests in global heating, conducted on beams with a utilization factor equal to about 0.7 (sustained load: 40 kN), showed that the attainment of  $T_{d,midpoint}$  (360°C) along the overall bonded length of the CFRP bar leads to the debonding, namely to the loss of the effectiveness of the strengthening system. Nevertheless, the beam did not fail after 90 min of heating exposure since the un-strengthened beam, which was not affected by the strength's reduction due to high temperature, bore the load, even though it exhibited very large deflection (Figure 5. 69). The residual tests confirmed that stated above, since the residual failure load was equal to that obtained testing the un-strengthened beams at ambient temperature.

The strengthening system of the tested beams with  $\eta_{fi}$  equal to about 0.7 in local heating configuration, did not fail after 90 min of fire exposure, even if the temperature of the CFRP bar, in the heated zone, was equal to about 600°C. Note that this temperature is significantly higher than the decomposition temperature

of the polymeric matrix of the bar. This means that the CFRP bar in the heated zone, was completely debonded, and it is very likely that, due to the longitudinal thermal conductivity of the CFRP, also the bar, close to the exposed zone, may have achieved the glass transition temperature. Unfortunately, no thermocouples were placed immediately after the exposed zone on the CFRP, therefore this hypothesis could not be experimentally checked, but a thermal-analysis was conducted with this objective and its results are summarized in the next chapter. Anyway, the effective cold-end anchorage was still able to sustain the stress transferred from the midspan. In fact, based on the results of bond tests at ambient temperature and on the measurement of the maximum mechanical strain in the CFRP bar during the tests of LocH-SL\_i, the effective end-anchorage length could have been just 300 mm to avoid the failure. Figure 5. 69 shows deflection versus time, highlighting that, in local heating configuration, the deflection of the beams was significantly lower than that observed in global heating, since the thermal gradient and, therefore, the thermal curvature were lower than that induced by global heating.

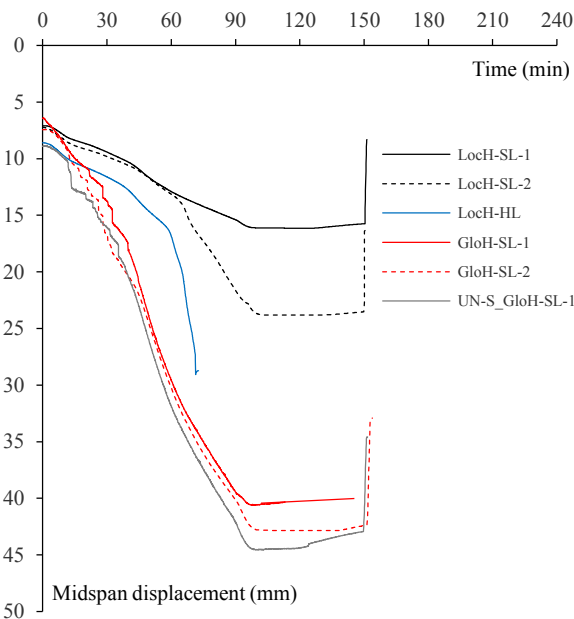


Figure 5. 69 – Midspan displacement versus Time of heating curves. Comparison between high temperature tests.

Finally, the strengthening of the beams tested in local heating configuration with  $\eta_{fi}$  equal to about 0.8 (sustained load: 50 kN), was not able to sustain the stress transferred from the midspan, when the maximum temperature in the CFRP



bar near the midspan achieved about 600°C, even if the temperature at the end-anchorage was practically that at ambient. In fact, as previously observed, it is very likely that the CFRP bar, close to the exposed zone, may have achieved the glass transition temperature, leading to a reduction of the effective end-anchorage length.

The tests showed the importance of the cold end-anchorage length to be provided, in order to maintain the load bearing capacity of the strengthening in case of fire, especially under sustained load, typical of maximum service strain conditions in the FRP.

Finally, note that the tensile strength of the CFRP bar was not ever attained, although the significant temperature (more than 600°C) attained in the bar during the heating phase, and the significant stress, due to sustained load.

## Chapter 6 - Numerical analyses

According to European codes, the fire resistance assessment of a structural member may be performed through experimental tests or applying analytical approaches. In both cases, conventional temperature-time laws of the environment are usually assumed. For instance, for fires characterized mainly on burning of cellulosic substances, the ISO834 standard curve is suggested by EN1991-1-2. Standard fire tests have many inadequacies, such as the absence of a cooling phase. Localised heating may occur in a real structure due to a single bay fire in a continuous multi-bay structure, a travelling fire, a localized ceiling jet fire (Gales et al, 2011).

Therefore, some tests comprising the experimental program presented in the Chapter 5 of this thesis, were executed using propane-fired radiant panels to heat the beams, rather than a standard fire-testing furnace. The radiant panels are very useful to simulate localised fire event, but they are also able to simulate global heating configurations, if an array of radiant panels is used. Currently, few researchers conducted high temperature tests in non-standard localised heating configuration (e.g., Gales et al, 2011; Carvelli et al, 2013) and in global heating configuration (e.g., Smith et al, 2014).

Obviously, the results of non-standard experimental tests cannot be used to define a standard time of fire resistance of the structural members, since the heating history can be significantly different to that provided by standard fire curve in terms of speed of temperature increasing, maximum temperature, duration of the heating stage.

In the previous chapter, it was stated that the tested strengthening system is efficient both in global and in local heating configuration. In fact, the tests in global heating, showed that the attainment of  $T_g$  does not produce any effect on the strengthening system, whereas  $T_{d,midpoint}$  (360°C) is a limiting temperature for its effectiveness. In local heating configuration, the strengthening system

remained effective even when the CFRP bar completely decomposed in the heated zone, due to the attainment of 600°C, which is a temperature significantly higher than the decomposition temperature of the polymeric matrix of the bar. In this condition, the cold end-anchorage sustained the stress transferred from the midspan when  $\eta_{fi}$  of the beam was about 0.7, whereas when  $\eta_{fi}$  was 0.8 the strengthening system failed, since the cold end-anchorage length was not sufficient. In fact, it is very likely that the CFRP bar, close to the exposed zone, due to the longitudinal thermal conductivity of the bar, may have achieved the glass transition temperature, leading to a reduction of the effective end-anchorage length. Unfortunately, no thermocouples were placed immediately after the exposed zone on the CFRP, therefore this hypothesis could not be experimentally checked. In order to check this hypothesis, a thermal analysis was conducted and its results are shown in this chapter. Actually, also the results of bond tests, conducted at ambient temperature, were very useful to determine the minimum needed bonding length to be provided in order to avoid the failure for debonding, when the stress is transferred from the midspan to the end-anchorage, due to the loss of bond in the heated zone. These tests showed that, when  $\eta_{fi}$  on the beam was 0.8, the effective end-anchorage length should have been significantly greater than 400 mm to avoid the failure.

These results highlighted the importance of the cold end-anchorage length to be provided, in order to maintain the load bearing capacity of the strengthening in case of fire, especially under sustained load, typical of maximum service strain conditions in the FRP.

As stated above, these results cannot be completely generalised, providing a time after that the strengthening system might not be effective anymore in case of standard fire.

Therefore, in order to generalize the experimental results, obtained through non-standard fire tests, and provide a reliable time of standard fire exposure that may be critical for the NSM FRP strengthened RC beams, the following numerical analyses were conducted (see section 6.1.3):

- a) thermal numerical analysis of a two-dimensional (2D) cross-sectional finite element model (FEM) of the NSM FRP strengthened RC beam, subjected to the beam's soffit temperature, recorded during the localised heating tests;
- b) thermal numerical analysis of a simplified 2D FEM of the longitudinal section of the NSM FRP strengthened RC beam, subjected to the to the beam's soffit temperature, recorded during the localised heating tests;
- c) thermal numerical analysis of a 2D cross-sectional FEM of the NSM FRP strengthened RC beam, subjected to the standard ISO834 curve.

The results of the numerical analyses a) and b) were compared with the temperature read by the thermocouples during the localised heating tests, in order to assess the reliability of the FEM simulating the experimental results. The results of the numerical model b) enabled also to evaluate the heat transfer from the exposed to the unexposed zone and, therefore, to assess the length of the effective cold end-anchorage.

The results of the numerical analysis c) were used to define a standard time of fire exposure, which may be critical for the effectiveness of the strengthening both in case of local and global heating.

Finally, a thermo-mechanical analysis of a full-scale NSM FRP strengthened RC beam was conducted in order to determine useful fire safety design criteria for this investigated structural typology.

## **6.1 THERMAL ANALYSES OF THE TESTED BEAMS**

The following sections summarizes all the meaningful information about the thermal models implemented in SAFIR 2011, aimed to:

- Assess the reliability of a numerical model to simulate the temperatures recorded during the high temperature tests;
- Predict the thermal behaviour of the beams in case of standard fire, instead of non-standard heating exposure.

Particularly, a short introduction on the SAFIR thermal model is firstly provided; moreover the thermal properties of the materials set in the finite element model are shown. Finally, the analyses results and the comparison with experimental results are also discussed.

### ***6.1.1 The SAFIR thermal model***

The hypothesis of decoupling the thermal behavior of the materials from the mechanical behavior is the basis of the Fourier equation for the study of the heat propagation within solid bodies and may be usually accepted. Due to the variability of the material thermal properties with the temperature (thermal conductivity, specific heat, density), a numerical solution of the heat transfer problem has to be performed. In most practical cases, the thermal field may be considered as uniform along the member axis, therefore, the actual 3D thermal problem can be reduced to more manageable 2D problem.

The FEM thermal analyses were carried out through the software SAFIR 2011 (Franssen, 2005) in which the heat transfer on the boundary may be assumed to

occur through a combination of radiation and convection. The cross-section is divided into a sufficient number of finite elements and in each one the time-dependent temperature is assumed uniform and equal to that of its centroid.

### 6.1.2 Thermal properties of materials

In order to study the thermal behavior NSM FRP strengthened RC beams at high temperature, thermal properties of materials have to be defined.

For concrete and steel bars the properties suggested in EN1992-1-2 were used.

Table 6. 1 – Thermal properties of cementitious mortar

<i>Temperature (°C)</i>	<i>Thermal conductivity (W/mk)</i>	<i>Specific heat (J/kgK)</i>	<i>Specific weight (kg/m<sup>3</sup>)</i>
50	0.560	705	1500
95	0.555		
105	0.660		
110	0.555		
175	0.53		
1200	0.53		

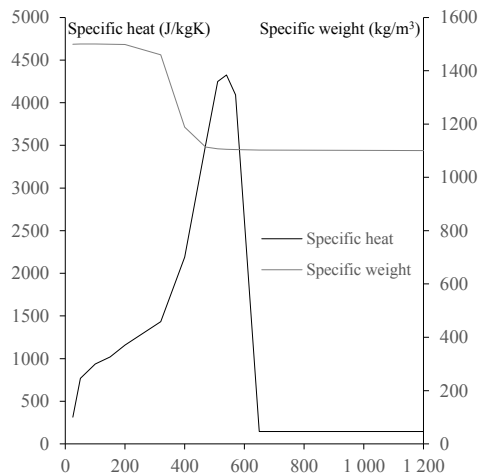


Figure 6. 1 – CFRP's Specific heat and Specific weight versus temperature

The properties of cementitious mortar, such as the thermal conductivity (see also section 3.1.5) and the specific weight, were experimentally measured, whereas for the specific heat was assumed a value provided by Chung (2001). Table 6. 1 summarizes the mortar's thermal properties used in numerical analyses.

As concerns FRP, both the specific weight loss with temperature, the specific heat and the thermal conductivities (Transversal and longitudinal) were

experimentally determined (see also sections 3.1.2.3, 3.1.3.1, 3.1.4.1). Figure 6. 1 shows the specific weight and the specific heat versus temperature, set in numerical analyses. Similarly, Table 6. 2 summarizes the values of thermal conductivities varying with temperature.

Table 6. 2 – Transversal and Longitudinal thermal conductivities of CFRP

<i>Temperature (°C)</i>	<i>Transversal Thermal conductivity (W/mk)</i>	<i>Longitudinal Thermal conductivity (W/mk)</i>
20	0.911	5.431
50	0.99	5.72
100	1.06	6.49
150	1.08	6.92
200	1.29	7.54
1200	1.29	7.54

According to EN1991-1-2, the convection coefficient on hot surfaces was set equal to 35 in case of real fire, and 25 in case of ISO834 standard fire; the convection coefficient on cold surfaces was set equal to 4; the relative emissivity was set equal to 0.7.

### 6.1.3 Finite element thermal models

As stated above, a thermal numerical analysis of a two-dimensional (2D) cross-sectional (CS) finite element model (FEM) of the NSM FRP strengthened RC beam was firstly conducted, in order to assess the reliability of a numerical model to simulate the temperature recorded during the tests. For this aim, the beam's cross-section was discretized in 408 finite elements, as shown in Figure 6. 2 a), and the nodes at beam's soffit were "constrained" to the temperature recorded during the localised heating tests at beam's soffit.

Thereafter, a 2D FEM of the beam's longitudinal section was implemented to simulate the heat transfer from the exposed to the unexposed zone of the beam. For this aim, based on the simmetry, an half of the beam was discretized in 90 finite elements, as shown in Figure 6. 2 a), and the nodes in the heated zone at beam's soffit were "constrained" to the temperature recorded during the localised heating tests at beam's soffit.

Finally, the CS-2D FEM, shown in Figure 6. 3, was exposed to the standard ISO834 curve (Figure 6. 2 b), in order to provide a reliable time of standard fire exposure that may be critical for the NSM FRP strengthened RC beams.

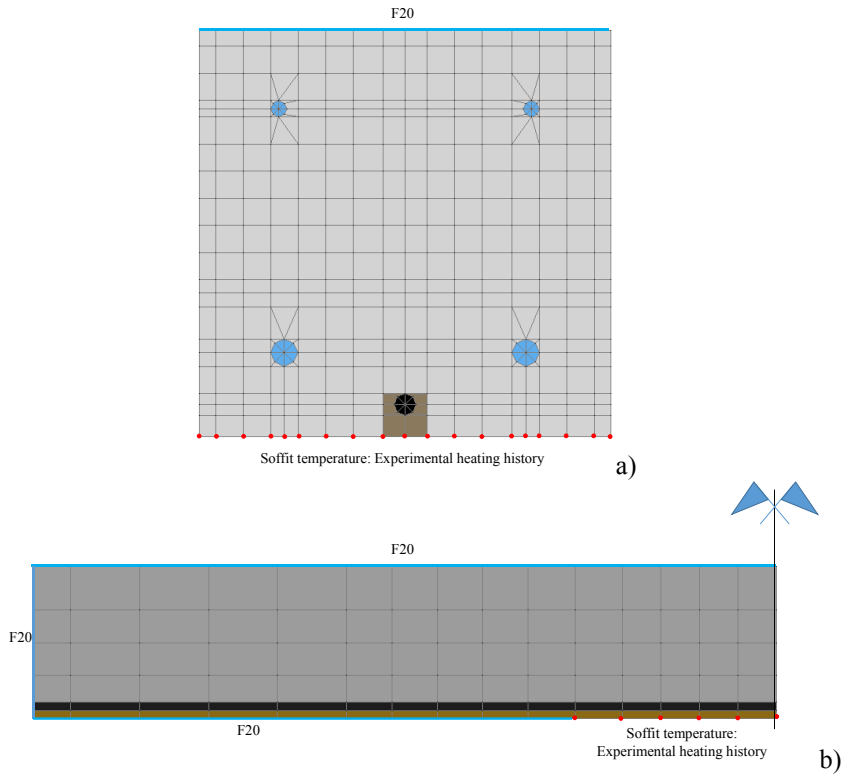


Figure 6. 2 – 2D FEM of NSM FRP strengthened RC beam subjected to the experimental soffit temperature: a) cross-sectional FEM; b) FEM of the longitudinal section

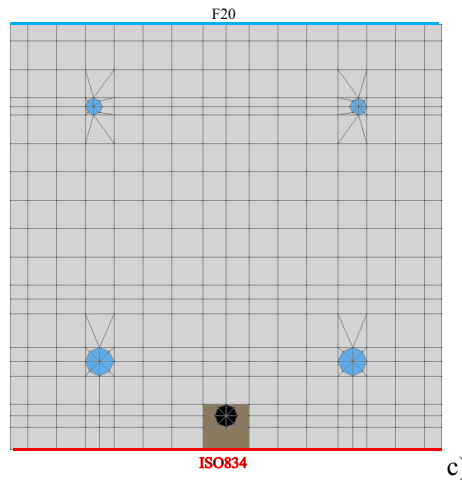


Figure 6. 3 – 2D cross-sectional FEM of NSM FRP strengthened RC beam subjected to ISO834 at beam's soffit

Note that the symbol F20 indicates that the room temperature was considered at the boundary.

### 6.1.4 Analyses results and numerical – experimental comparison

As shown in Figure 6. 4, the cross-section was discretized taking into account the position of the thermocouples in the tested real beams. This figure shows also the nodes of the cross-sectional FEM, which temperatures were compared with those experimental.

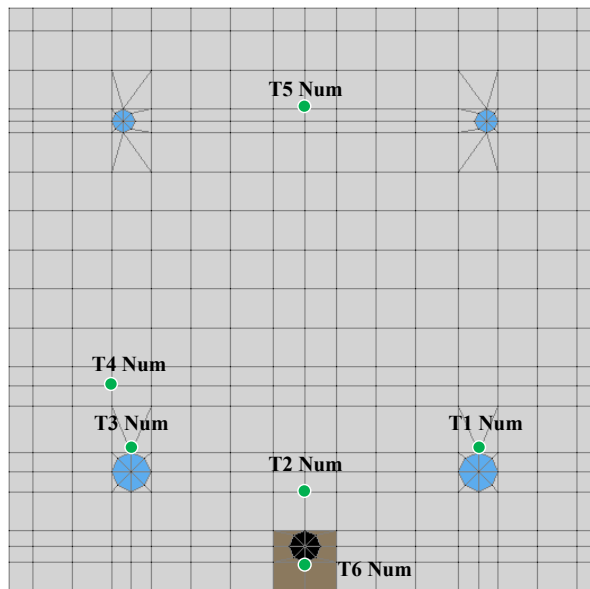


Figure 6. 4 – 2D FEM of NSM FRP strengthened RC beam: location of the monitored nodes

Figure 6. 5 shows the numerical results of the thermal analysis conducted on the FEM, shown in Figure 6. 2 a. Particularly, the dotted curves represent the numerical temperatures of the nodes, shown in Figure 6. 4, plotted versus time and compared with those experimental (continuous curves). In this figure the experimental temperatures provided by the thermocouples T7-T8-T11, placed below the CFRP bar near the midspan in the heated zone (Figure 6. 6), are also shown. The comparison between the temperatures recorded by T6-T7-T8-T11 shows that the temperature in the heated zone was quite uniform, therefore a cross sectional analysis should be sufficient to predict the temperature in the overall heated zone. Figure 6. 5 demonstrates that the numerical model is able to predict the temperature and it is a very reliable model, since a very good agreement was obtained with the experimental temperatures, except for that provided by T5.



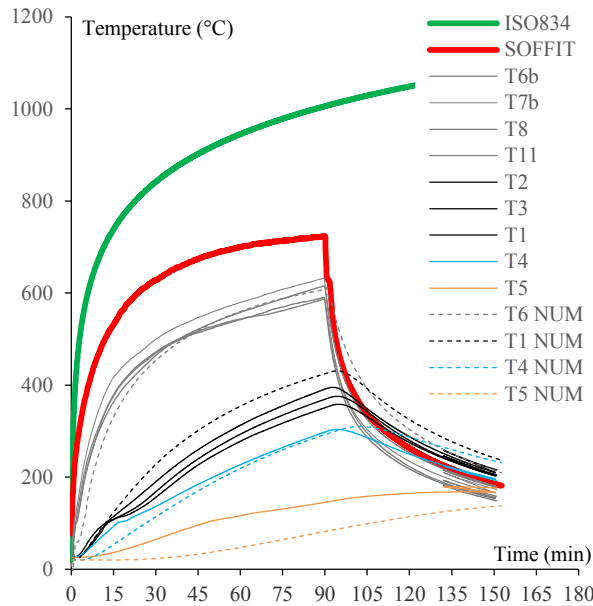


Figure 6. 5 – Temperature vs time curves. Numerical-experimental comparison

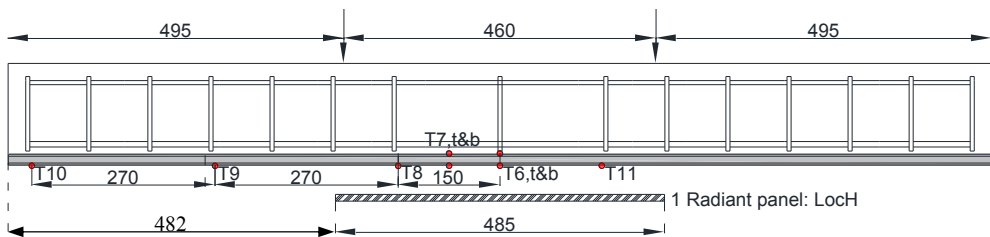


Figure 6. 6 – Thermocouples' position along the CFRP bar

Since only two thermocouples were placed in the unexposed zone during the tests, a simplified 2D FEM of the longitudinal section of the beam was implemented in SAFIR to predict the heat transfer from the exposed to the unexposed zone. Figure 6. 7 shows that the numerical model was also able to simulate the temperatures recorded by the thermocouples T9 and T10, which were almost 50°C and 30°C, respectively. Moreover, due to the longitudinal thermal conductivity of the CFRP, the model provided a temperature in the bar of about 180°C at 45 mm far from the radiant panel, after about 90 min. This means that the bar, in the unexposed zone, but close to that exposed, entered in the glass transition stage.

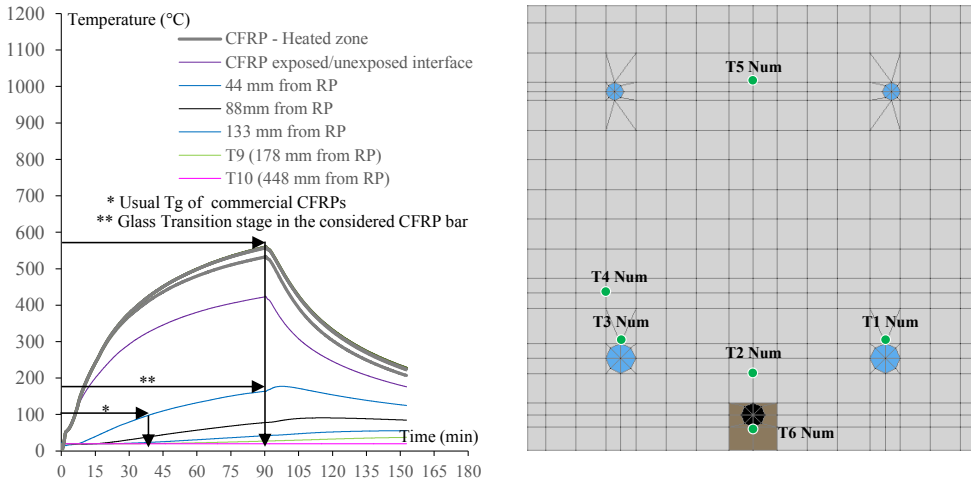


Figure 6. 7 – Temperature vs time curves. Numerical prediction of heat transfer from exposed to unexposed zone

In conclusion, this numerical analysis showed that the effective end-anchorage length, namely the end-anchorage not affected by glass transition, is about 440 mm. Note that the experimental tests in local heating configuration showed that the effective cold end-anchorage was able to sustain the stress transferred from the midspan, when  $\eta_{fi}$  on the beam was about 0.7. Conversely, the strengthening system failed, when  $\eta_{fi}$  on the beam was about 0.8. In fact, as stated in the previous chapter, when  $\eta_{fi}$  on the beam is about 0.7, also an effective end-anchorage of 300 mm should be sufficient, whereas when  $\eta_{fi}$  is 0.8 the effective end-anchorage need to be greater than 400 mm.

Based on that just stated, the behaviour of this strengthening system can be considered very effective, since whatever commercial CFRP bar, with a usual glass transition temperature equal to 100°C, would lose its effectiveness after 45 min corresponding to the attainment of  $T_g$  in the anchorage next to the exposed zone (Figure 6. 7) and  $T_d$  in the exposed zone.

Finally, the thermal analysis of the cross-sectional FEM, shown in Figure 6. 3, provided standard time of ISO834 fire exposure, which may be critical for the effectiveness of the experimentally tested strengthening system. Figure 6. 8 shows that the CFRP bar, after about 15 min of standard fire exposure, achieved 350°C that represents a critical temperature for the effectiveness of the strengthening system in case of global heating, since it leads to the debonding at bar/adhesive interface. Moreover, the numerical thermal model showed that the CFRP bar attained 600°C after about 45 min of standard fire exposure, which

may be critical in case of local heating, in case of  $\eta_{fi}$  on the beam greater than 0.7.

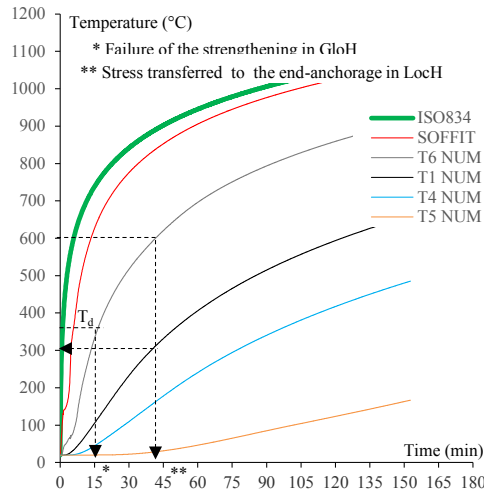


Figure 6. 8 – Temperature vs time curves. Numerical prediction (ISO834) – Experimentally tested strengthening system

Note that, even if the cold end-anchorage should not be able to sustain the stress transferred from the midspan leading to the loss of strengthening system, the un-strengthened RC beam should be able to sustain a load suitable with its strength at ambient temperature. In fact, when the maximum temperature in the CFRP bar is 600°C, the temperature in the steel rebars is about 300°C. Therefore, no strength reduction occurs in RC beam during the fire exposure.

## 6.2 THERMO-MECHANICAL ANALYSIS OF A FULL-SCALE BEAM

The following section summarizes the results of a thermo-mechanical analysis conducted on a full-scale 300 mm x 500 mm NSM FRP strengthened RC beam, aimed to find out useful fire safety design criteria for this investigated structural typology.

The thermo-mechanical properties of the materials set in the analysis are firstly shown. Then, the analyses results are discussed.

### 6.2.1 Description of the case study

The analysed beam is a 300 mm x 500 mm concrete beam. The flexural reinforcement is made of three steel rebars (nominal diameter  $\Phi$  16 mm) on the

tension side and two rebars (nominal diameter 12 mm) in compression. The strengthening system consisted of two CFRP bars (nominal diameter  $\Phi$  8 mm), grouted through a cementitious mortar in a groove 16 mm square in cross-section, cut into the concrete cover of the beam.

The mechanical properties of the materials are shown in Table 6. 3.

Table 6. 3 – Mechanical properties of materials at ambient temperature

Property	Symbol	Value (MPa)
Concrete compression strength	$f_c$	48
Steel yielding strength	$f_y$	525
Cementitious Mortar compression strength	$f_{c,m}$	90
CFRP tensile strength	$f_{ftm}$	1750
CFRP Young modulus	$E_f$	136000

### 6.2.2 Thermo-mechanical properties of materials at high temperature

The thermal properties of the materials set in the numerical model are those shown in section 6.1.2. In order to study the mechanical behaviour, disocoupling the mechanical problem from the thermal one, also mechanical properties have to be defined. Particularly, for concrete and steel bars the properties suggested in EN1992-1-2 were used.

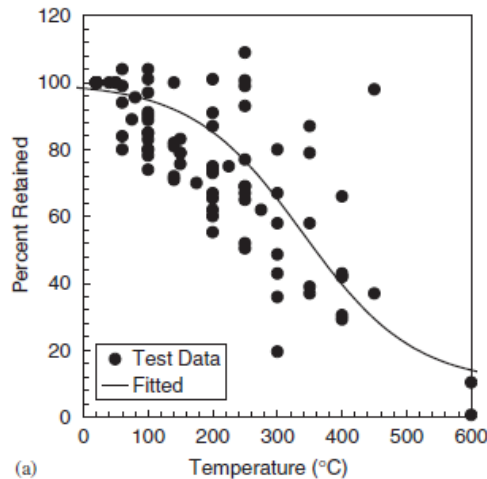


Figure 6. 9 – CFRP tensile strength reduction curve (Bisby et al, 2005)

Regarding the FRP, the CFRP tensile strength reduction curve, shown in Figure 6. 9 was considered. It was determined by Bisby et al (2005), based on the

best fit of experimental data collected in literature. Other tensile strength reduction curves of FRPs are provided in Nigro et al (2008).

Note that the CFRP strength reduction models, provided in literature, are simplified, sometimes, conservative models.

### 6.2.3 The thermal finite element model and analysis results

The beam's cross-section was discretized in 563 finite elements, as shown in Figure 6. 10. The beam was analysed in case of standard ISO834 fire exposure on three side. Note that, in order to consider that the beam is part of a slab, thick 200 mm, the lateral exposed surface was just 300 mm high. Moreover, the ambient temperature was considered above the beam.

Figure 6. 11 shows the temperature in different nodes of the analysed beam, plotted versus time. This figure highlight that the CFRP bar attained the  $T_{g,max\,tan\delta}$  ( $\cong 210\text{-}220^{\circ}\text{C}$ ) after about 10 min of fire exposure and the  $T_{d,midpoint}$  ( $\cong 360^{\circ}\text{C}$ ) after about 15 min. Note that in case of global heating the attainment of the decomposition temperature along the overall bonding length is a limiting factor for the effectiveness of the strengthening system since debonding failure occurs, whereas providing an effective cold end-anchorage length the stress from the debonded length can be transferred to the cold end.

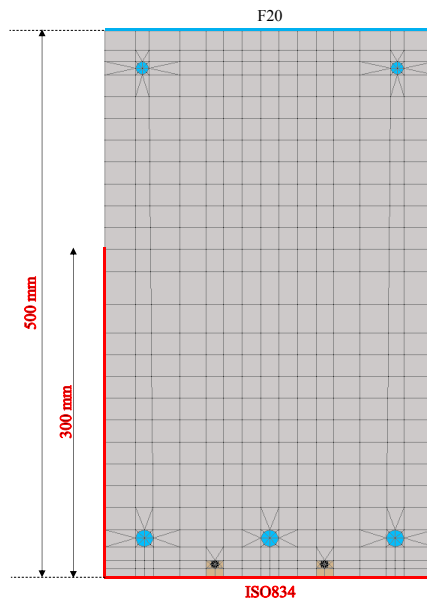


Figure 6. 10 – 2D cross-sectional FEM of NSM FRP strengthened 300x500 RC beam subjected to ISO834

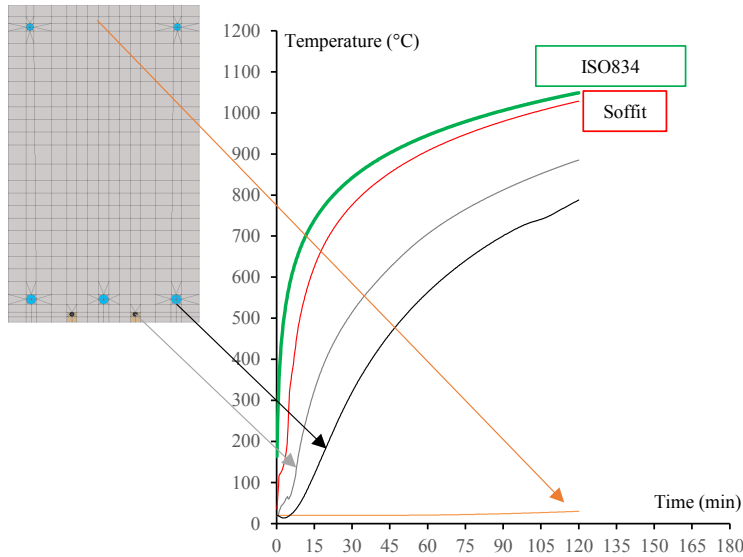


Figure 6. 11 – Temperature vs time curves. Numerical prediction in case of ISO834 standard fire exposure (NSM FRP strengthened 300x500 RC beam)

Therefore, the effectiveness of the strengthening at high temperature is related to the capacity of the cold end-anchorage to support this stress. This means that the strengthened member need to be protected at the end for a length estimated based on the results of bond tests at ambient temperature, which provide the ultimate strength of the strengthening, and on the prediction of the maximum mechanical stress, which can be attained in the CFRP under service load.

#### 6.2.4 Mechanical analysis

The design of NSM FRP strengthened RC members is governed by the serviceability limit state. It is very likely that, in order to satisfy the limit imposed by several codes on the maximum stress in steel rebars, the maximum strain in the FRP in service condition is not greater than 2‰. Based on the bond tests, conducted at ambient temperature, the strengthening systems with a bonding length ( $L_b$ ) equal to 300 mm are characterized by a debonding strain equal to about 3.6‰, therefore this cold end-anchorage length should be sufficient to sustain the mechanical stress transferred by the debonded zone in case of fire.

Based on this hypothesis, a simplified mechanical analysis was conducted considering the beam protected at the end, for a length equal to 300 mm, with a passive protection system, able to keep the temperature in the end-anchorage of the bar very low, in order to avoid the debonding failure and utilize the full strength of the strengthening system.

In practice, based on the thermal field in the cross section, calculated through the thermal analysis, the flexural resistance of the beam for different instant of fire exposure was calculated in a simplified way as in (6. 1)

$$M_{Rd,fi}(t_{ISO834}) = A_s k_{y,\theta} f_y 0.9d + A_f k_{f,\theta} f_f 0.9h \quad (6. 1)$$

where:

$A_s$  is the steel area;

$A_f$  is the FRP area;

$k_{y,\theta}$  is the reduction factor of the steel tensile strength at high temperature;

$k_{f,\theta}$  is the reduction factor of the FRP tensile strength at high temperature;

$h$  is the height of the beam;

$d = h - c$ ;

$c$  is the concrete cover, equal to 35 mm.

Figure 6. 12 shows the bending moment resistance plotted versus time of fire exposure, showing that after about 40 min the load bearing capacity is almost provided by the un-strengthened beam, since the contribution provided by the CFRP bars is very low. In fact, after 40 min of fire exposure the temperature in the CFRP bars is about 600°C (Figure 6. 11), therefore their strength is only the 15-20% of their strength at ambient temperature (see Figure 6. 9). Actually, as previously stated, the used CFRP strength reduction curve may be very conservative for the CFRP bars used in this work. In fact, during high temperature tests, the CFRP bar did not fail, bearing a stress greater than its expected strength at temperature of about 600°C (15-20% of the bar's strength at ambient temperature). Figure 6. 12 provides the resistance of the beam, in the time domain ( $t_R$ ), for the typical values of utilization factor on the beam ( $\eta_{fi} = \frac{M_{Ed,fi,t}}{M_{Rd,fi,0}} = 0.3$ ;  $\eta_{fi} = 0.5$ ;  $\eta_{fi} = 0.7$ ). Particularly, when  $\eta_{fi}$  is 0.7 the beam fails for a time of fire exposure  $t_R$  equal to 38 min; when  $\eta_{fi}$  is 0.5, then  $t_R$  is 55 min; when  $\eta_{fi}$  is 0.3,  $t_R$  is greater than 90 min.

Note that  $\eta_{fi}$  equal to 0.7 is not compatible with the limit imposed on the strain in the FRP equal to 2‰. To satisfy this limit, the effect of the action in case of fire ( $M_{max,FRP=2‰}$ ) should be lower than  $0.6 \cdot M_{Rd,fi,0}$ . Figure 6. 13 shows the bending moment resistance of the un-strengthened beam ( $M_{Rd,fi_{UN-S}}$ ) plotted versus time of fire exposure. The comparison between Figure 6. 12 and Figure 6. 13 shows that the strengthening provides an increase of flexural resistance at ambient temperature of about 59% and enables an increase of the load,

compatibly with the strain limite in the FRP, equal to about 27% ( $M_{max,FRP=2\%}/0.7M_{Rd,fi,0-UN-S}$ ).

Finally, note that the minimum requirements for obtaining satisfactory structural performances in fire, aimed also to warrant safety conditions for human life, are usually greater than 60 minutes of fire exposure. This requirement may be satisfied only for  $\eta_{fi} < 0.5$ , considering 300 mm protection system only at the end of the full scale NSM FRP strengthened RC beam. This protective length was set in order to keep as low as possible the costs for repairing/strengthening. In order to increase the time of fire resistance, an “ad hoc” fire protection system in the anchorage zone may be designed to protect both FRP and steel.

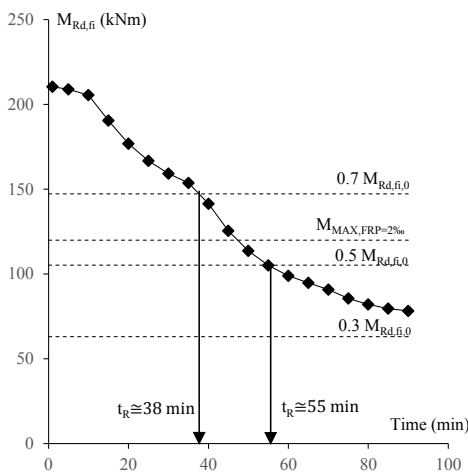


Figure 6. 12 – Bending moment resistance versus time of standard fire exposure (strengthened beam)

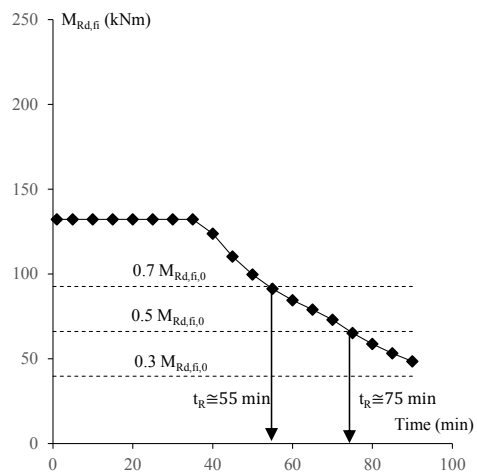


Figure 6. 13 – Bending moment resistance versus time of standard fire exposure (un-strengthened beam)



## **CONCLUSIONS**

### **Primary Conclusions**

The available literature about the behaviour of cementitious-bonded Near Surface Mounted (NSM) FRP strengthening systems both at ambient and elevated temperature is very limited, probably due to a presumption that cementitious adhesives are likely to be less effective at room temperature. Therefore, this thesis has presented the results of an experimental testing and modelling programme to investigate the performance at elevated temperature of a specific novel cementitious-bonded CFRP NSM strengthening system for concrete beams in bending.

Based on the testing and modelling presented in this thesis, the following key conclusions can be drawn for this system.

At ambient temperature, the surface treatment of the CFRP bar is critical for the efficiency of the strengthening system:

- The bond behaviour of this system is worse than resin-bonded NSM, but the performance of the cementitious-bonded NSM CFRP ribbed bar is comparable with common EBR CFRP plates.
- The bonding length and position of the bar inside the groove influence the bond behaviour more than the dimensions of the grooves (2-2.5 times the bar's diameter).

At elevated temperature, the high  $T_g$  and  $T_d$  of the CFRP bar, and the low thermal conductivity and good stability of the cementitious bonding agent, enabled NSM flexurally strengthened RC beams to exploit good performances in fire testing:

- The cementitious-bonded NSM FRP strengthening system is able to sustain loads typical of service conditions, having carbon fibres a significant strength also at elevated temperature.
- The capacity depends on the effective cold-end anchorage length.
- Local insulation systems at the end-anchorage only, instead of insulation along the overall bonded length, noticeably improve the fire resistance.

---

### **Summary of the Thesis and Secondary Conclusions**

The response at ambient and elevated temperature of cementitious-bonded Near Surface Mounted (NSM) Fibre Reinforced Polymer (FRP) strengthened reinforced concrete (RC) members has not yet been significantly studied through research, aside from a limited number of available studies. NSM FRP strengthening is potentially less prone to damage due to fire exposure than Externally Bonded FRP reinforcement (EBR), also possibly without needing costly insulation systems, provided that: (a) an FRP strengthening material with high glass transition temperature ( $T_g$ ) and decomposition temperature ( $T_d$ ); and (b) a bonding agent with low thermal conductivity and good thermal stability, are used. NSM FRP systems with cementitious adhesives may perform better at elevated temperatures because: (a) cementitious grout is not as severely affected as typical epoxies by elevated temperature; (b) the cementitious grout can provide additional thermal protection to the FRP bars; and (c) the resin of the FRP bar, when the bar is manufactured by pultrusion, typically has a  $T_g$  higher than common in-situ cured epoxy resins used in wet lay-up FRP strengthening applications.

This thesis has presented a research project undertaken on a commercially available high  $T_g$  CFRP bar bonded within a cementitious matrix through the NSM technique, and used to strengthen RC members in bending.

Dynamic Mechanic Analysis (DMA) and Thermogravimetric Analysis (TGA) on the novel, high  $T_g$  commercial CFRP bars was conducted, to define the  $T_g$  and the  $T_d$ , respectively, of this particular FRP product. The results of DMA and TGA were processed using several techniques, proposed in literature. The available techniques provided a range of  $T_g$  applicable values, which can be used to define the temperature region where the material changes from a glassy phase to a rubbery phase upon heating, rather than an on/off temperature where all properties are lost. The obtained  $T_g$  values ranged between 160°C ( $T_{g,offset}$ ) and 220°C ( $T_{g,max(tan\delta)}$ ). Similarly, the processing of TGA results provided decomposition temperatures ranging between 315°C ( $T_{d,offset}$ ) and 360°C ( $T_{g,midpoint}$ ).

Differential Scanning Calorimetry (DSC) was also performed to define the specific heat capacity ( $c_p$ ) of the CFRP bar and its variance with the temperature; this can be very useful for simulating the thermal behaviour of the strengthening system through numerical modelling. Thermal conductivity tests were also performed on the CFRP bar and on the cementitious grout used, to verify their respective thermal conductivities ( $\lambda$ ). The thermal conductivity of the

FRPs, when used as NSM FRP strengthening, does not significantly affect the heat transfer within the structural member due to its small cross-sectional area, relative to concrete section. However FRPs are thermally anisotropic materials, characterized by different thermal conductivity values in various directions; in unidirectional composites, the longitudinal thermal conductivity ( $\lambda_l$ ) is fibre controlled while the transverse thermal conductivity ( $\lambda_t$ ) is matrix controlled. For this reason, CFRPs are characterized by high longitudinal thermal conductivity, due to the high thermal conductivity of individual carbon fibres. As expected, the longitudinal thermal conductivity was significantly higher than the transverse one (about six times higher). Moreover, the thermal conductivities varied almost linearly over the analysed temperature range: the longitudinal varied from 5.72 W/m°C to 7.54 W/m°C between the temperatures 50°C and 200°C, whereas the the transverse thermal conductivity varied from 0.99 W/m°C to 1.29 W/m°C in the same temperature range. The tests conducted on the cementitious grout adhesive provided thermal conductivity values almost constant in the temperature range 50-175°C and equal to 0.55 W/mK; a slightly higher value (0.66 W/mK) was obtained at about 100°C due to the evaporation of water, which led to a greater energy absorption than that needed to maintain a certain gradient of temperature in the sample, at other testing temperatures.

In order to characterize the mechanical properties of the materials, several ancillary tests were conducted, such as tensile tests of CFRP and steel bars, and compression tests of cementitious mortar and concrete. The tests were conducted with traditional techniques and according to the suggestion provided by several available codes. A novel technique was used to evaluate strain. Digital Image Correlation was used in addition to traditional contact measurement, i.e., strain gauges.

The efficiency of any NSM FRP system depends on several parameters, namely: the materials' mechanical properties, the dimensions and surface treatment of the grooves, the geometry of the FRP product, the position of the FRP reinforcement in the groove, and the type of bonding agent amongst others. Several prior studies on NSM FRP strengthening have presented experimental bond tests and have shown that the bond between concrete and NSM FRP is particularly efficient if epoxy adhesive is used, whereas relatively few tests are available in literature using cementitious adhesive, probably due to a presumption that cementitious adhesives are likely to be less effective at room temperature. However, as stated above, NSM FRP systems with cementitious adhesives may perform better at elevated temperatures. Therefore, a series of bond pull-out tests were performed on concrete specimens strengthened with the novel cementitious-

bonded CFRP NSM system; this specific system has been developed specifically to address the performance of FRP strengthening systems at elevated temperatures, to investigate the bond between FRP and concrete. The tests were conducted by varying the bonding agent (cementitious mortar or epoxy resin), the position of the bar in the groove (Top surface of the groove; Centre of the groove), the bonding length ( $L_b=300$  mm and  $L_b=400$  mm), the dimension of the groove ( $16\times 16$  mm and  $20\times 20$  mm). The experimental program demonstrated that the maximum load recorded during the tests for resin-bonded NSM CFRP strengthening systems was about 50 kN, when the bonding length ( $L_b$ ) was 300 mm and the bar was placed at the top surface of the groove. After the achievement of this peak load the strengthening recovered a residual strength (65-80% of maximum load), based on the interlocking mechanism between the adhesive resin and the ribbed surface of the bars. The tests of cementitious-bonded NSM CFRP strengthening systems showed that the maximum load was about 25 kN, when  $L_b$  was 300 mm and the bar was placed at the top surface of the groove. In these cases, the specimens did not recover any significant residual strength, since this was about 25% of the maximum load. The failure occurred always by debonding at the bar/adhesive interface (B/A). The test results showed also that the dimension of the groove did not significantly affect the maximum load or the stiffness of the strengthening. Conversely, the type of bonding agent affected the stiffness. The resin-bonded CFRP strengthened specimens were stiffer than those that were cementitious-bonded. The tests conducted considering the bar bonded in cementitious mortar, and with  $L_b$  equal to 400 mm instead of 300 mm, demonstrated an increase of the maximum load equal to about 12%. Conversely, for the tests conducted with the bar placed at the centre of the groove and bonded in mortar, a maximum load 16% lower than that obtained when the bar was at the top surface of the groove was observed. Similarly, when the bar was placed at the centre of the groove and bonded in resin, the maximum load was 27% lower than that obtained when the bar was placed at the top surface of the groove.

From these results, it can be concluded that at ambient temperature, the bond behaviour of this system is worse than resin-bonded NSM, but the performance of the cementitious-bonded NSM CFRP ribbed bar is comparable with common EBR CFRP plates. Therefore, the surface treatment of the CFRP bar is critical for the efficiency of the strengthening system. Moreover, the bonding length and position of the bar inside the groove influences the bond behaviour more than the dimensions of the grooves (2-2.5 times the bar's diameter).

To evaluate the response at both ambient and elevated temperature of NSM FRP strengthened reinforced concrete beams, a series of four-point flexural tests

on beams were performed. The tested specimens were 1450 mm long and 150 mm square in cross-section, and were strengthened with a NSM CFRP bar of 8 mm diameter. The tests at high temperature were executed using propane-fired radiant panels to heat the beams, rather than a standard fire-testing furnace. Two heating configurations were used, namely: (1) localised heating near midspan only (485 mm heated zone over 1450 mm total strengthened length); and (2) global heating over the entire bonded length of the FRP system. The thermo-structural response was investigated under sustained loads typical of maximum permissible service strain conditions in the FRP. Internal temperatures, beam displacements and slip of the FRP strengthening were measured, and strain gauges were applied for measuring the FRP bar strains; Digital Image Correlation (DIC) was also used to study strain distributions and beam displacements. All of the results obtained were correlated with DMA and TGA tests results in order to better explain the failure modes of the strengthened beams.

The tests at ambient temperature of the reference un-strengthened specimens showed that flexural failure occurred under an average load of about 48 kN, with concrete crushing, steel compressive reinforcement buckling and wide flexural cracks on the tension side. During the tests, the beams' displacements were using a traditional Linear Potentiometer (LP), and high resolution cameras were also set to take pictures every 5 seconds. The latter were processed with the software GeoPIV8, which provided the deflection of the tested beams through the DIC technique. Both the LP and DIC yielded the same midspan deflection, which was equal to about 8 mm, in the yielding stage, and about 35 mm in the failure stage. DIC was also used to calculate the strains along the beams, enabling the localization of the neutral axis and the definition of the curvature for different values of the load. These results were compared with those numerically obtained through a Cross Sectional Analysis (CSA), conducted using an iterative-incremental procedure that provided the Moment-Curvature diagrams of the beams. The comparison showed that the CSA was able to predict the failure load with reasonable accuracy.

The flexural test of strengthened beams at ambient temperature highlighted that the strengthening provided a considerable increase of the load bearing capacity, with a gain in yielding load ranging between 32-36% and a gain in failure load ranging between 17-25%. After the steel yielding stage, the overloading of the CFRP bar led to slippage between the FRP and the cementitious bonding agent, with a consequent increase of the midspan deflection until complete debonding of the CFRP bar occurred within the cementitious grout. After FRP debonding occurred at a strain in the CFRP equal to 5.8%, the beams

behaved as un-strengthened members and eventually failed due to concrete crushing in the same manner as the unstrengthened beams.

The high temperature tests on NSM CFRP strengthened concrete beams highlighted the efficiency of the strengthening system both in global and in local heating configuration. Obviously, the effectiveness of the strengthening system during the accidental event and its residual strength depends also on the utilization factor of the member in fire,  $\eta_{fi}$ , namely the ratio between the relevant effects of actions in the fire situation at time  $t$ ,  $E_{d,fi,t}$ , and the design value of the resistance of the member in fire situation at beginning of thermally transient regime,  $R_{d,fi,0}$ . The tests in global heating, conducted with a  $\eta_{fi}$  equal to about 0.7 (sustained load: 40 kN), showed that the attainment of  $T_{d,midpoint}$  (360°C) along the overall bonded length of the CFRP bar leads to the debonding, namely to the loss of the effectiveness of the strengthening system, due to slippage at B/A interface. Nevertheless, the beam did not fail after 90 min of heating exposure since the un-strengthened beam, which was not affected by the strength's reduction due to high temperature, bore the load, even though it exhibited very large deflection. The DIC was revealed to be a very useful technique, especially at high temperature, since the contact measurement did not work properly when high temperatures were attained. The residual tests confirmed the observation stated above: the residual failure load of the strengthened beams tested in global heating, was equal to the failure load of un-strengthened beams at ambient temperature.

The strengthening system of the beams tested with  $\eta_{fi}$  equal to about 0.7 in a local heating configuration, did not fail after 90 min of fire exposure, even when the temperature of the CFRP bar, in the heated zone, was equal to about 600°C. Note that this temperature is significantly higher than the decomposition temperature of the polymeric matrix of the bar. This means that the CFRP bar in the heated zone, was completely debonded, and it is very likely that, due to the longitudinal thermal conductivity of the CFRP, also the bar, close to the exposed zone, may have achieved the glass transition temperature. Unfortunately, no thermocouples were placed immediately after the exposed zone on the CFRP, therefore this hypothesis could not be experimentally checked, but a thermal-analysis was conducted with this objective. In any case, the effective cold-end anchorage achieved in these beams was still able to sustain the stress transferred from the midspan region. Based on the results of bond tests at ambient temperature and on the measurement of the maximum mechanical strains in the CFRP bars during the flexural tests at high temperature, the effective end-anchorage length could have been just 300 mm to avoid failure. As expected, in

the local heating configuration, the deflection of the beams was significantly lower than that observed in global heating, since the thermal gradients and therefore the thermal curvature were lower than those induced by a global heating scenario. The residual tests showed that the strengthening system preserved a residual strength, after the heating exposure, equal to 57 kN, which is about the 96% of the failure load of the NSM FRP strengthened RC beams at ambient temperature.

Finally, the strengthening of the beams tested in a local heating configuration with  $\eta_{fi}$  equal to about 0.8 (sustained load: 50 kN), was not able to sustain the stress transferred from the midspan at elevated temperature, when the maximum temperature in the CFRP bar near the midspan achieved about 600°C even if the temperature at the end-anchorage was practically that at ambient. As previously discussed, it is likely that the CFRP bar, close to the exposed zone, may have achieved the glass transition temperature, leading to an increase of the required end-anchorage length. Based on the results of bond tests at ambient temperature and on the measurement of the maximum mechanical strain in the CFRP bar during the flexural tests at high temperature, the effective end-anchorage length should probably have been greater than 400 mm to avoid failure under this condition.

The beam tests therefore have confirmed the importance of assuring that a cold end-anchorage length is provided to maintain the load bearing capacity of the strengthening in case of fire especially under sustained loads sufficient to cause, typical maximum service strain conditions in the FRP.

According to European codes, the fire resistance assessment of a structural member may be performed through experimental tests or by applying analytical approaches. In both cases conventional temperature-time relationships of the fire environment are usually assumed. For instance, for fires characterized mainly on burning of cellulosic substances, the ISO834 standard curve is suggested by EN1991-1-2. Standard fire tests has many inadequacies, such as the absence of a cooling phase. Moreover, they do not enable simulation of localised fire event that may occur in real structures.

The results of non-standard experimental tests, such as those presented herein, cannot easily be used to define a standard time of fire resistance for structural members, since the heating history may be significantly different to that provided by standard fire curve in terms of speed of temperature increasing, maximum temperature, and duration of the heating stage.

Thus, to generalize the experimental results obtained through the non-standard fire tests discussed in this thesis, and to provide a reliable time of standard fire

exposure that may be critical for the NSM FRP strengthened RC beams, the following numerical analyses were conducted:

- 1) thermal numerical analysis of a two-dimensional (2D) cross-sectional finite element model (FEM) of the NSM FRP strengthened RC beam, subjected to the beam's soffit temperature, as recorded during the localised heating tests;
- 2) thermal numerical analysis of a simplified 2D FEM of the longitudinal section of the NSM FRP strengthened RC beam, subjected to the to the beam's soffit temperature, as recorded during the localised heating tests;
- 3) thermal numerical analysis of a 2D cross-sectional FEM of the NSM FRP strengthened RC beam, and subjected to the standard ISO834 curve.

The results of the numerical analyses (1) and (2) were compared with the temperatures recorded by the thermocouples during the localised heating tests to assess the reliability of the FEM simulating the experimental results. The results of the numerical model (2) also enabled evaluation of the heat transfer from the exposed to the unexposed zones in the concrete, and therefore to assess the length of the effective cold end-anchorage that was likely achieved during the tests.

The results of the numerical analysis (3) were used to define a standard time of fire exposure, which may be critical for the effectiveness of the strengthening both in case of local and global heating.

Finally, a thermo-mechanical analysis of a full-scale NSM FRP strengthened RC beam was conducted to determine useful fire safety design criteria for the investigated structural typology.

The numerical thermal analyses were conducted using the software SAFIR 2011. The results of the analyses (1) and (2) showed that the implemented model was very reliable since good agreement was obtained between the numerical and the experimental temperatures. Moreover, the analysis of the model (2) showed that the effective end-anchorage length, namely the end-anchorage not affected by glass transition of the FRP bars, is about 440 mm over the total unexposed zone equal to about 483 mm. This justifies the observation that the failure did not occur in case of local heating, when  $\eta_{fi}$  was 0.7, since the minimum effective end-anchorage length, sufficient to sustain the stress transferred from the midspan in case of debonding of the bar in the exposed zone, could have been only 300 mm. Conversely, 440 mm of effective end-anchorage length was not sufficient in the case of local heating whilst  $\eta_{fi}$  on the beam was equal to 0.8.



The thermal analysis of the model (3) simulated standard times of ISO834 fire exposure, which may be critical for the effectiveness of the strengthening system. Particularly, the CFRP bar, after about 15 min of standard fire exposure, achieved 350°C, which represents a critical temperature for the effectiveness of the strengthening system in the case of global heating, since it leads to the debonding at bar/adhesive interface. Moreover, the numerical thermal model showed that the CFRP bar attained 600°C after about 45 min of standard fire exposure, which may be critical in case of local heating, when  $\eta_{fi}$  of the beam is greater than 0.7, since the cold end-anchorage may be not sufficient to sustain the stress transferred from the heated midspan.

Finally, a computational thermo-mechanical analysis was conducted on a full-scale reinforced concrete beam, 300 mm x 500 mm in cross section, strengthened with two CFRP bars of 8 mm diameter, and subjected to the ISO834 standard fire. The objective was to determine useful fire safety design criteria for this investigated structural typology. The thermal analysis highlighted that the CFRP bar attained the  $T_{g,max\ tan\delta}$  ( $\cong 210\text{-}220^\circ\text{C}$ ) after about 10 min of fire exposure and the  $T_{d,midpoint}$  ( $\cong 360^\circ\text{C}$ ) after about 15 min. This means that in case of global heating, 15 min of fire exposure may lead to the debonding of the strengthening system, whereas providing an effective cold end-anchorage length the stress from the debonded zone can be transferred to the cold end. Therefore, the effectiveness of the strengthening at high temperature is related to the capacity of the cold end-anchorage to support this stress. This means that the strengthened member needs an ends' protection length estimated on the basis of the results of the bond tests performed at ambient temperature, which provide the ultimate debonding strength of this NSM strengthening system, and of the prediction of the maximum mechanical stress, which can be attained in the CFRP under service load.

Note that the design of NSM FRP strengthened RC members is governed by the serviceability limit state and it is very likely that, in order to satisfy the limit imposed by several codes on the maximum stress in steel rebars, the maximum strain in the FRP in service condition is not greater than 2‰. Therefore, mechanical analyses were conducted considering the beam insulated for 300 mm at its end, since the bond tests showed that strengthening systems with 300 mm bonding length were characterized by a debonding strain equal to about 3.6‰. If debonding failure was avoided, the full strength of the strengthening system could be exploited. The mechanical analysis results showed that after about 40 min of standard fire exposure, the load bearing capacity was almost provided by the un-strengthened beam, since the contribution provided by the CFRP bars was very low. In fact, the temperature in the CFRP bars was about 600°C, therefore

their strength was only 15-20% of that at ambient temperature, based on a simplified CFRP strength reduction model. Actually, the latter may be very conservative for the CFRP bars used in this work: during high temperature tests, the CFRP bar did not fail, bearing a stress greater than its expected strength at 600°C (15-20% of the bar's strength at ambient temperature). Finally, the resistance of the beam, in the time domain ( $t_R$ ) was also calculated for the typical values of utilization factor of the beam ( $\eta_{fi} = \frac{M_{Ed,fi,t}}{M_{Rd,fi,0}} = 0.3$ ;  $\eta_{fi} = 0.5$ ;  $\eta_{fi} = 0.7$ ): when  $\eta_{fi}$  was 0.7 the beam failed for a time of fire exposure  $t_R$  equal to 38 min; when  $\eta_{fi}$  was 0.5, then  $t_R$  was 55 min; when  $\eta_{fi}$  was 0.3,  $t_R$  was greater than 90 min.

Note that  $\eta_{fi}$  equal to 0.7 is not compatible with the limit imposed on the strain in the FRP equal to 2‰. To satisfy this limit, the effect of the action in case of fire ( $M_{max,FRP=2‰}$ ) should be lower than  $0.6 \cdot M_{Rd,fi,0}$ .

The strengthening provides an increase of flexural resistance at ambient temperature of about 60% and enables an increase of the load, compatibly with the strain limit in the FRP, equal to about 30%.

A requirement of 60 minutes of fire exposure, aimed to obtain satisfactory structural performances in fire and to warrant safety conditions for human life, may be satisfied only for  $\eta_{fi} < 0.5$ , with protection system only at the end of the full scale NSM FRP strengthened RC beam. In order to increase the time of fire resistance, an "ad hoc" fire protection system in the anchorage zone may be designed.

Moreover, the obtained fire resistance is certainly greater than that provided by an EBR FRP strengthening system, based on the tests results shown in literature. NSM is also less costly than EBR, which generally requires a fire protection along the overall length of the beam.

In summary, the NSM FRP strengthening technique is a valid, attractive and efficient alternative to the EBR FRP strengthening system, especially for its better performance in fire compared to that provided by EBR.

---

**REFERENCES**

Aiello M.A., Leone M., (2008). “Interface analysis between FRP EBR system and concrete”, *Composites: Part B* 39 (2008) 618–626

Asplund SO, (1949). “Strengthening bridge slabs with grouted reinforcement”, *J Am Concrete Inst*, 20(6):397–406.

Bewerse C., Gall K. R., McFarland G. J., Zhu P., Brinson L. C., (2013). “Local and global strains ratios in shape memory alloys using digital image correlation”, *Material Science & Engineering A* 568 (2013) 134-142)

Beyler C.L., Hirschler M. M. (2001). "Thermal Decomposition of Polymers", Chapter in *SFPE Handbook of Fire Protection Engineering (3rd Edn)*", Editor-in-chief: P.J. DiNenno, pp., NFPA, Quincy, MA

Bilotta A., Ceroni F., Di Ludovico M., Nigro E., Pecce M., (2011). “Bond Efficiency of EBR and NSM FRP Systems for Strengthening Concrete Members”, *J. Compos. Constr.* 2011.15:757-772

Bilotta A., Faella C., Martinelli E., Nigro E. (2012). “Indirect Identification Method of Bilinear Interface Laws for FRP Bonded on a Concrete Substrate” *Journal Of Composites For Construction*, vol. 16, p. 171-184, ISSN:1090-0268, doi: 10.1061/(ASCE)CC.1943-5614.0000253

Bilotta A., Ceroni F., Nigro E., Pecce M., (2014). “Strain assessment for the design of NSM FRP systems for the strengthening of RC members”, *Construction and Building Materials* 69 (2014) 143–158

Bilotta A., Ceroni F., Barros J.A.O., Costa I., Palmieri A., Szabo K.Z., Nigro E., Matthys S., Balazs G.L., Pecce M., (2015). “Bond of NSM FRP strengthened concrete: round robin test initiative”, *Journal of Composite for Construction (ASCE)*

Bisby L.A., Green M.F., Kodur V.K.R (2005a). “Response to fire of concrete structures that incorporate FRP”, *Prog. Struct. Engng. Mater.*, 7:136-149

Bisby L.A., Williams V.R.K.; Kodur V.R.K.; Green M.F.; Chowdhury E., (2005b). “Fire Performance of FRP Systems for Infrastructure: A State-of-the-Art Report”, *NRC Publications Archive (NPArc) Research Report 179, Canada*

Bisby L.A., Take W.A., (2008). “Strain Localizations in FRP Confined Concrete: New Insights”, *Structures and Buildings*, 162(SB1): 9pp (2008).

Bisby L.A., Stratford T., Hart C., Farren S., (2013). “Fire Performance of Well-Anchored TRM, FRCM and FRP Flexural Strengthening Systems”, *Advanced Composites in Construction 2013*, Publisher: Network Group for Composites in Construction

Blaschko M., (2003). “Bond behaviour of CFRP strips glued into slits”, *Proceedings of the 6th International Symposium on FRPRCS (Tan KH, ed.)*, Singapore, 2003, 205–214

Blontrock H., Taerwe L., Vandeveld, P. (2001) “Fire Testing of Concrete Slabs Strengthened with Fibre Composite Laminates”, *The Fifth Annual Symposium on Fibre-Reinforced-Plastic Reinforcement for Concrete Structures (FRPRCS-5)*. Edited by C. Burgoyne, Thomas Telford, London, 547-556

Blontrock, H. (2003). “Analysis and modeling of the fire resistance of concrete elements with externally bonded FRP reinforcement”, Ph.D. Thesis, Ghent Univ., Ghent, Belgium.

Burke P.J., (2008). “Low and High Temperature Performance of Near Surface Mounted FRP Strengthened Concrete Slabs”, Master thesis, Queen’s University, Kingston, Ontario, Canada

Burke P.J., Bisby L. A., Green M., (2013). “Effects of elevated temperature on near surface mounted and externally bonded FRP strengthening systems for concrete”, *Cement & Concrete Composites* 35 (2013) 190–199

Buyukozturk O., Gunes O., Karaca E., (2004). “Progress on understanding debonding problems in reinforced concrete and steel members strengthened using FRP composites”, *Construction and Building Materials* 18 (2004) 9–19

Cai, Z. H. (2008). “Research on bond property of FRP-to-concrete interface under elevated temperatures.” M.S. thesis, Tongji University, Shanghai, China

Carvelli V., Pisani M. A., Poggi C., (2013). “High temperature effects on concrete members reinforced with GFRP rebars”, *Composites: Part B* 54 (2013) 125–132, <http://dx.doi.org/10.1016/j.compositesb.2013.05.013>

Castro E. K., Melo G. S., Nagato Y., (2007). “Flexural strengthening of RC “T” beams with Near Surface Mounted (NSM) FRP reinforcements”, *FRPRCS-8*, University of Patras, Patras, Greece, July 16-18, 2007

Ceroni F., Pecce M., Bilotta A., Nigro A (2012). “Bond behavior of FRP NSM systems in concrete elements”, *Composites: Part B* 43, 99–109

Ceroni F., Barros J.A.O.; Pecce M., Ianniciello M., (2013). “Assessment of nonlinear bond laws for near-surface-mounted system in concrete elements”, *Composites: Part B* 45 , 666-681

Chen JF, Yang ZJ, Holt GD, (2001). “FRP or steel plate-to-concrete bonded joints: effect of test methods on experimental bond strength”. *Steel Compos Struct* 2001; 1(2):231–44

Chen J. F., Teng J. G. (2001). “Anchorage strength models for FRP and steel plates bonded to concrete”, *J. Struct. Eng.* 2001.127:784-791.

Chikh N., Merdas A., Laraba A., Benzaid R., (2013). “Study of the Bond Behavior of Concrete Beam Strengthened with NSM-CFRP”, *Proceedings of the World Congress on Engineering 2013 Vol III, WCE 2013, July 3 - 5, 2013, London, U.K. ISBN: 978-988-19252-9-9, ISSN: 2078-0958 (Print); ISSN: 2078-0966 (Online)*

Chung D.D.L., (2001). “Cement-matrix composites for thermal engineering”, *Applied Thermal Engineering* 21 (2001) 1607-1619

Costa I., Barros J., (2011). “Assessment of the bond behaviour of NSM FRP materials by pullout tests”, *First Middle East Conference on Smart Monitoring, Assessment and Rehabilitation of Civil Structures, 2-9, 8-10 February 2011, Dubai*

Dai J., Ueda T., Sato Y. (2005). “Development of the nonlinear bond stress-slip model of fiber reinforced plastics sheet—Concrete interfaces with a simple method.” *J. Compos. Constr.*, 9(1), 52–62.

Dai J.G., Gao W.Y., Teng J.G., (2013). “Bond-Slip Model for FRP Laminates Externally Bonded to Concrete at Elevated Temperature”, *Journal of Composites for Construction*, Vol. 17, No. 2, April 1, 2013. © ASCE, ISSN 1090-0268/2013/2-217-228

Del Prete I., Bilotta A., Nigro E., (2015). “Performancs at high temperature of RC bridge decks strengthened with EBR-FRP”, *Composites: Part B* 68 (2015) 27-37

Deuring M. (1994). Brandversuche an Nachtraglich Verstärkten Tragern aus Beton, “Research Report EMPA No. 148’795”, Dubendorf, Swiss Federal Laboratories for Materials Testing and Research, 1994.

De Lorenzis L., Nanni A., La Tegola A., (2000). “Strengthening of Reinforced Concrete Structures with Near Surface Mounted FRP Rods” , bibl. International Meeting on Composite Materials, PLAST 2000, Milan, Italy, May 9-11, 1-9.

De Lorenzis L., Rizzo A., La Tegola A., (2002). “A modified pull-out test for bond of near-surface mounted FRP rods in concrete”, *Composites: Part B* 33 (2002) 589–603

De Lorenzis L., Teng JG., (2007). “Near-surface mounted FRP reinforcement: an emerging technique for structural strengthening”. *Compos Part B: Eng* 2007;38:119–43

Dutton, (2012). “Digital Image Correlation for evaluating structural engineering materials”, Master Thesis submitted to the Department of Civil Engineering, Queen’s University Kingston, Ontario, Canada

Ehrenstein, G. V., Riedel G., Trawiel P., (2004). “Thermal analysis of plastics – Theory and practice”, Carl Hanser Verlag GmbH & Co. KG, ISBN: 978-3-446-22673-9

El-Gamal S., Al-Salloum Y., Alsayed S., Aqel M., (2012). “Performance of near surface mounted glass fiber reinforced polymer bars in concrete”, *Journal of Reinforced Plastics and Composites*, 31 (22) 1501–1515 DOI: 10.1177/073168441246408

El-Hacha R., Rizkalla S: H., (2004). “Near-Surface-Mounted Fiber-Reinforced Polymer Reinforcements for Flexural Strengthening of Concrete Structures”, *ACI Structural Journal*, September-October 2004, 717-726

Enochsson O., Lundqvist J., Täljsten B., Rusinowski P., Olofsson T., (2007). “CFRP strengthened openings in two-way concrete slabs - An experimental and numerical study”, *Construction and Building Materials* Volume 21, Issue 4, 810-826

Ferracuti B., Mazzotti C., and Savoia M. (2008). “A new single-shear set-up for stable delamination tests on FRP-concrete joints”, *Constr. Build. Mater.*, 23(4), 1529–1537.

Franssen J. M., (2005). “SAFIR: A thermal/structural program for modeling structures under fire”, *Engineering Journal-American Institute of Steel Construction Inc*, 42(3), 143-158

Firmo J. P., Correia J. R., França P., (2012). “Fire behaviour of reinforced concrete beams strengthened with CFRP laminates: Protection systems with insulation of the anchorage zones”, *Composites: Part B* 43 (2012) 1545–1556

Foret G., Limam O., (2008). “Experimental and Numerical analysis of RC two-way slabs strengthened with NSM CFRP rods”, *Construction and Building Materials* 22 (2008) 2025-2030

Foster, S. and Bisby, L. (2008). “Fire Survivability of Externally Bonded FRP Strengthening Systems”, *J. Compos. Constr.*, 12(5), 553–561

Gabbott P. (2008). “Principles and Applications of Thermal Analysis”, Blackwell Publishing

Gales J., Bisby L., Gillie M., (2011). “Unbonded Post Tensioned Concrete Slabs in Fire - Part I: Experimental Response of Unbonded Tendons under Transient Localized Heating”, *Journal of Structural Fire Engineering*. 2(3):139-153

Gales J.A., Bisby L., Stratford T., (2012) “New parameters to describe high-temperature deformation of prestressing steel determined using digital image correlation”. *Structural Engineering International*, 22(4), 476–486

GangaRao H. V. S., Vijay P. V., (1998). “Bending behavior of concrete beams wrapped with carbon fabric”, *J. Struct. Eng.* 1998.124:3-10

Haines P. (2002). “Principles of Thermal Analysis and Calorimetry”, Royal Society of Chemistry

Jia J., Boothby T.E., Bakis C.E., Brown T.L. (2005), “Durability Evaluation of Glass Fiber Reinforced-Polymer-Concrete Bonded Interfaces”, *Journal of Composites for Construction*, Vol. 9, No. 4, August 1, 2005. ©ASCE, ISSN 1090-0268/2005/4-348–359

Klamer, E. (2009). “Influence of temperature on concrete beams strengthened in flexure with CFRP.” Ph.D. Thesis, Eindhoven University of Technology, Eindhoven, Netherlands

Kodur V.K.R., Baingo D., (1998). “Fire Resistance of FRP Reinforced Concrete Slabs”, National Research Council Canada, Internal Report No. 758

Kodur V. R., Bisby L. A., Williams B. K., Green M. F., (2005). “Fire Performance of FRP Systems for Infrastructure: A State-of-the-Art Report”, Chowdhury E.NRC Publications Archive (NPARC) Archives des publications du CNRC (NPARC)

Kodur V. K. R., Yu B., (2013). “Evaluating the Fire Response of Concrete Beams Strengthened with Near-Surface-Mounted FRP Reinforcement”, *J. Compos. Constr.* 2013.17:517-529

Lamond J.F., Pielert H., (2006). “Significance of Tests and Properties of Concrete & Concrete-making materials”, ASTM International, STP 169D

Leone M., Matthys S., Aiello M.A. (2009). “Effect of elevated service temperature on bond between FRP EBR systems and concrete”. *Composites Part B - Engineering.* 40(1). p.85-93

Menczel J. D., Prime R. B. (2008). “Thermal Analysis of Polymers – Fundamentals and Applications”, Wiley

Martinelli E., Bilotta A., Faella C., Nigro E., (2011). “On the Behavior of FRP-to-concrete Adhesive Interface: Theoretical Models and Experimental Results”, *Advances in Composite Materials - Ecodesign and Analysis*, Edited by Dr. Brahim Attaf, 517-546, ISBN 978-953-307-150-3

Mander, J. B., Priestley, M. J. N., and Park, R. (1988). “Theoretical Stress-Strain Model for Confined Concrete.” *J. Struct. Eng., ASCE*, 114(8), 1804-1826.

McIntyre E., Bilotta A., Bisby L. A., Nigro E., (2014). “Mechanical properties of fibre reinforced polymer reinforcement for concrete at high temperature”, 8th International Conference on Structures in Fire (SIF), 1227-1234, Edited by Li G.Q., Kodur V. K. R., Jiang S.C., Jiang J., Chen S.W., Lou G.B., Shanghai, China, June 11-13, 2014

Mindess S., Young JF (1981). “Concrete”. Prentice-Hall, Englewood Cliffs, NJ

Netsch Instruments, Inc. “Operation & maintenance manual Holometrix model TCHM-LT C-MATIC - Guarded Heat Flow Meter - Thermal conductivity instrument”

Nigro E., Manfredi G., Cosenza E., Cefarelli G., (2008). “High-temperature behaviour of concrete slabs reinforced with FRP bars”, Fourth International



---

Conference on FRP Composites in Civil Engineering (CICE2008), 22-24 July 2008, Zurich, Switzerland

Nigro, E., Cefarelli, G., Bilotta, A., Manfredi, G. and Cosenza, E. (2011a). “Fire resistance of concrete slabs reinforced with FRP bars. Part I: experimental investigations on the mechanical behavior”. *Composites: Part B*, 42 (2011), 1739–1750

Nigro, E., Cefarelli, G., Bilotta, A., Manfredi, G. and Cosenza, E. (2011b). “Fire resistance of concrete slabs reinforced with FRP bars. Part II: experimental results and numerical simulations on the thermal field”. *Composites: Part B*, 42 (2011), 1751–1763

Nigro E., Di Ludovico M., Bilotta A. (2011c). “Experimental Investigation of FRP-Concrete Debonding under Cyclic Actions”, *Journal of Materials in Civil Engineering*, vol. 23, p. 360-371, ISSN: 0899-1561, doi: 10.1061/(ASCE)MT.1943-5533.0000173

Nigro E., Bilotta A., Cefarelli G., Manfredi G., Cosenza E., (2012). “Performance under fire situations of concrete members reinforced with FRP rods: bond models and design nomograms”, *Journal of Composites for Construction*. *Journal of Composites for Construction*, Vol. 16, No. 4, August 1, 2012

Nigro, E., Cefarelli, G., Bilotta, A., Manfredi, G. and Cosenza, E. (2013). “Adhesion at high temperature of FRP bars straight or bent at the end of concrete slabs”, *Journal of Structural Fire Engineering*, vol. 4, p. 71-86, ISSN: 2040-2317, doi: 10.1260/2040-2317.4.2.71

Novidis, D. G., and Pantazopoulou, S. J. (2008). “Beam pull out tests of NSM—FRP and steel bars in concrete”, *Proc., CICE 2008*, Zurich, Switzerland

Palmieri, A., Matthys S., Taerwe L., (2010). “Experimental Investigation on bond of NSM strengthened RC structures”, *proceeding CICE 2010*, September 27-29, 2010 Beijing, China

Palmieri A., Matthys S., Taerwe L. (2010). “Strengthening with Near Surface Mounted Reinforcement: Structural and Fire behavior”, *3rd fib 2010 Washington DC, USA*

Palmieri, A., Matthys S., Taerwe L., (2011a). “Fire testing of RC beams strengthened with NSM reinforcement”, *10th International Symposium Fiber-Reinforced Polymer Reinforcement for Concrete Structures*, Editors: Rajan Sen,

---

Rudolf Seracino, Carol Shield, Will Gold, 51\_1-51\_16, 2-4 April 2011, Tampa, Florida (USA)

Palmieri, A., Matthys S., Taerwe L., (2011b). “Influence of High Temperature on Bond between NSM FRP Bars/Strips and Concrete”, 10th International Symposium Fiber-Reinforced Polymer Reinforcement for Concrete Structures, Editors: Rajan Sen, Rudolf Seracino, Carol Shield, Will Gold, 52\_1-52\_12, 2-4 April 2011, Tampa, Florida (USA)

Palmieri A., Matthys S., Taerwe L., (2012). “Double Bond Shear tests on NSM FRP strengthened members”, Proceedings of CICE 2012, Rome, Italy, June 13-15, 2012, [http://www.iifc-hq.org/proceedings/CICE\\_2012/CICE.html#ID2](http://www.iifc-hq.org/proceedings/CICE_2012/CICE.html#ID2)

Palmieri A., Matthys S., Taerwe L., (2013). “Fire Endurance and Residual Strength of Insulated Concrete Beams Strengthened with Near-Surface Mounted Reinforcement”, *J. Compos. Constr.* 2013.17:454-462

Parretti R., Nanni A., “Strengthening of RC members using near-surface mounted FRP composites: Design overview”, *Advances in Structural Engineering* 7 (2004), no. 5, 1–16

Petri P., Blaszak G., Rizkalla S., (2013). “Structural Fire Endurance of an RC Slab Strengthened with High  $T_g$  Near Surface Mounted CFRP Bars”, Conference Proceedings Advanced Composites in Construction (ACIC) 2013, Edited by Miss Claire. J. Whysall and Prof. Su. E. Taylor, 140-151, Queen's University Belfast on 10 -12 September 2013

Rieger J. (2001), “The glass transition temperature  $T_g$  of polymers - Comparison of the values from differential thermal analysis (DTA, DSC) and dynamic mechanical measurements (torsion pendulum), *Polymer Testing* 20 (2001) 199–204

Savoia M., et al. (2009). “Experimental round robin test on FRP concrete bonding.” Proc., 9th Int. Symp. on Fiber Reinforced Polymer Reinforcement for Reinforced Concrete Structures, American Concrete Institute, Farmington Hills, MI

Sauerbrunn S. R., Crowe B. S. and Reading M. (1992). *NATAS Proc.*, 21, pp 137-144

Seracino R, Jones NM, Page MW, Ali MSS, Oehlers DJ, (2007). “Bond strength of near surface mounted FRP-to-concrete joints”, *ASCE J Compos Constr.*11(4):401–9

---

Seo S-Y., Feo L., Hui D., (2013). “Bond strength of near surface-mounted FRP plate for retrofit of concrete structures”, *Composite Structures* 95 (2013) 719–727

Shui Z., Zhang R., Chen W., Xuan D, (2010). “Effects of mineral admixtures on the thermal expansion properties of hardened cement paste”, *Construction and Building Materials* 24 (2010) 1761–1767

Smith H. K.M., Stratford T. J., Bisby L. A:, (2014). “Punching shear of restrained reinforced concrete slabs under fire conditions”, 8th International Conference on Structures in Fire (SIF), 443-450, Edited by Li G.Q., Kodur V. K. R., Jiang S.C., Jiang J., Chen S.W., Lou G.B., Shanghai, China, June 11-13, 2014

Spadea G.; Bencardino F., Swamy R. N., (1998). “Structural behavior of composite RC beams with externally bonded CFRP”, *J. Compos. Constr.* 1998.2:132-137

Springer GS, Tsai SW. Thermal conductivities of unidirectional materials. *J Compos Mater* 1967; 1:166±73

Sweeting R.D., Liu X.L., (2004). “Measurement of thermal conductivity for fibre-reinforced composites”, *Composites: Part A* 35 (2004) 933–938, Elsevier Ltd. doi:10.1016/j.compositesa.2004.01.008, 2004

Szabó Z. K., Balázs G. L. (2007). “Near surface mounted FRP reinforcement for strengthening of concrete structures” *Periodica Polytechnica* 2007, *Civil Engineering* 51/1 33–38 doi: 10.3311/pp.ci.2007-1.05

Teng J.G., de Lorenzis L., Wang B., Li R., Wong T.N., Lam L., (2006). “Debonding failures of RC beams strengthened with near surface mounted CFRP Strips”, *Journal of composites for construction* 10 (2006), no. 2, 92–105, DOI 10.1061/(ASCE)1090-0268(2006)10:2(92)

White D. J., Take W. A., Bolton M. D., (2003). “Soil Deformation measurement using particle image velocimetry (PIV) and photogrammetry”, *Géotechnique*, 53(7), 619-631 (2003)

Williams B., Kodur V., Green M., Bisby L., (2008). “Fire endurance of Fiber-Reinforced Polymer Strengthened Concrete T-Beams” *ACI Structural Journal*, 105(1), 60-67

Wu G.; Dong Z. Q., Wu Z. S., Zhang L. W., (2013). “Performance and Parametric Analysis of Flexural Strengthening for RC Beams with NSM-CFRP

Bars”, *J. Compos. Constr.* DOI: 10.1061/(ASCE)CC.1943-5614.0000451. © 2013 American Society of Civil Engineers

Wu Z. S., Yuan H., Yoshizawa H., and Kanakubo T., (2001). “Experimental/analytical study on interfacial fracture energy and fracture propagation along FRP-concrete interface.” SP-201-8, American Concrete Institute, Farmington Hills, MI, 133–52

Yao, J., Teng, J. G., and Chen, J. F. (2005). “Experimental study on FRP-to-concrete bonded joints.” *Compos., Part B*, 36(2), 99–113

Yu B., Kodur V.K.R., (2014). “Effect of high temperature on bond strength of near-surface mounted FRP reinforcement”, *Composite Structures* 110 (2014) 88–97

Zeiler B. (2013). “FireStrong: Installation Guide & Contractor Training Manual”

## **CITED CODES**

ACI 224.1R-07 (2007) . “Causes, Evaluation, and Repair of Cracks in Concrete Structures”, ACI Committee 224, American Concrete Institute

ACI 318-08 (2009) . “Building Code Requirements for Structural Concrete”, ACI Committee 318, American Concrete Institute

ACI 440.2R-08 (2008) . “Guide for the Design and Construction of Externally Bonded FRP Systems for Strengthening Concrete Structures”, ACI Committee 440, American Concrete Institute

ACI 440.3R-04. “Guide Test Methods for Fiber-Reinforced Polymers (FRPs) for Reinforcing or Strengthening Concrete Structures”, ACI Committee 440, American Concrete Institute

ASTM C39. “Standard Test Method for Compressive Strength of Cylindrical Concrete Specimens”

ASTM D 3039/D 3039M, “Standard Test Method for Tensile Properties of Polymer Matrix Composite Materials”

ASTM D 3418. “Standard Test Method for Transition Temperatures and Enthalpies of Fusion and Crystallization of Polymers by Differential Scanning Calorimetry”

ASTM E 176. “Standard Terminology of Fire Standards”, Annual Book of ASTM Standards, Vol. 4.07, American Society for Testing and Materials, West Conshohocken, PA

ASTM D 4092 – 07 (2013). “Standard Terminology for Plastics: Dynamic Mechanical Properties”

BS EN 10002-1:2001. “Tensile testing of metallic materials. Method of test at ambient temperature”

CAN/CSA-S806-02 (2004). “Design and Construction of Building Components with Fibre-Reinforced Polymers”

CNR DT-200 R1/2013, “Guide for the Design and Construction of Externally Bonded FRP Systems for Strengthening Existing Structures: Materials, RC and PC structures, masonry structures”, CNR – Advisory Committee on Technical Recommendations for Construction

DIN 65 583 (1999). “Aerospace - Fibre reinforced materials - Determination of glass transition of fibre composites under dynamic load”

EN1991-1-2, (2002). European committee for standardization, “Eurocode 1, Actions on structures Part 1-2: General actions - Actions on structures exposed to fire”, November 2002

EN1992-1-1 (2004). “Eurocode 2: Design of concrete structures - Part 1-1: General rules and rules for buildings”

EN1992-1-2 (2004). “Eurocode 2: Design of concrete structures - Part 1-2: General rules - Structural fire design”

fib Bulletin n°14 (2001). “Externally Bonded FRP Reinforcement for RC structures”, Technical Report, ISBN: 978-2-88394-054-3

IS 5816-1970 (1999) Indian Standard. “Splitting tensile strength of concrete - Method of test”

ISO 6721-1:2011. “Plastics - Determination of dynamic mechanical properties - Part 1: General principles”

ISO/CD 6721 - 11:2008. “Plastics - Determination of Dynamic Mechanical Properties: Determination of glass transition temperature”

JCI TC952 (1998). “Technical Report on Continuous Fiber Reinforced Concrete”, Japan Concrete Institution, Sept.,1998

Model Code 2010, fib-CEB-FIP, bulletin 65

NTC2008 Ministry of Infrastructure and Transport (Italian Government)  
2008, “Technical Code for the Constructions”, G.U. n. 29 of 14/02/2008

UNI EN 12390-3 (2003). “Testing hardened concrete - Compressive strength  
of test specimens”

## ANNEX I – PROCESSING OF DMA AND TGA DATA

This annex shows the results of the processing of the data, collected during Dynamic Mechanic Analysis (DMA) and Thermogravimetric Analysis (TGA), conducted on specimens, extracted by the novel CFRP bar, used for strengthen reinforced beams (RC), object of this thesis. The value of glass transition temperature ( $T_g$ ) and decomposition temperature ( $T_d$ ) of the CFRP bar were calculated averaging the values obtained testing the overall set of specimens. Both  $T_g$  and  $T_d$  were evaluated by means of several techniques proposed in literature.

### Evaluation of the peak of the loss factor $\tan \delta$

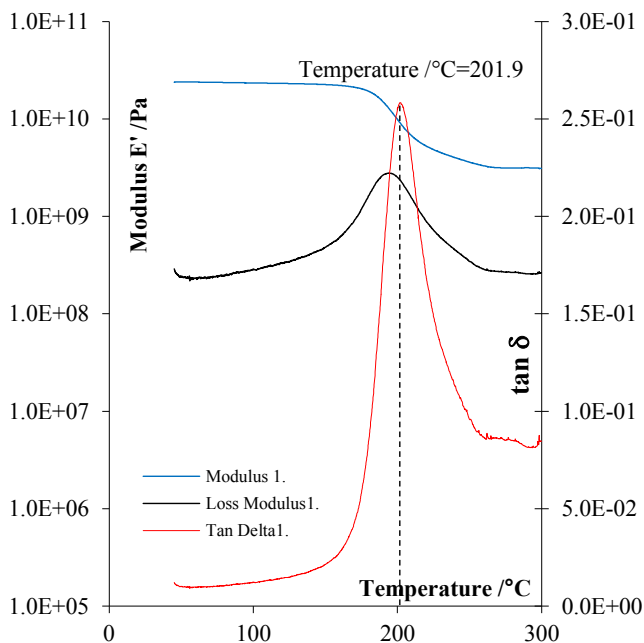


Figure I. 1 - SC CFRP-1-15: storage modulus  $E'$ , loss modulus  $E''$  loss factor  $\tan \delta$  vs temperature

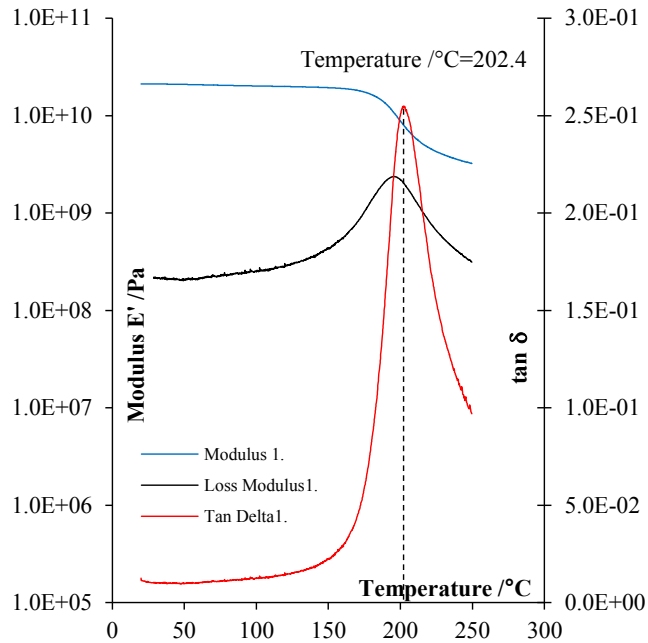


Figure I. 2 - SC CFRP-2-15: storage modulus  $E'$ , loss modulus  $E''$ , loss factor  $\tan \delta$  vs temperature

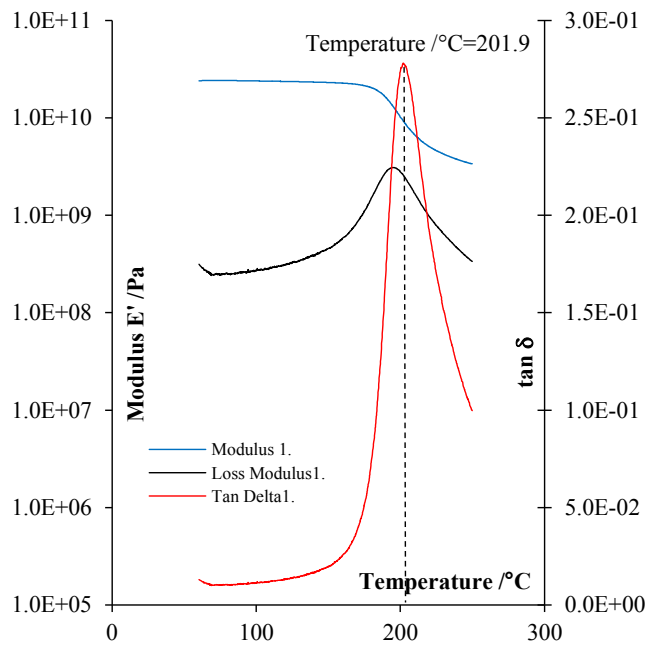


Figure I. 3 - SC CFRP-3-15: storage modulus  $E'$ , loss modulus  $E''$ , loss factor  $\tan \delta$  vs temperature



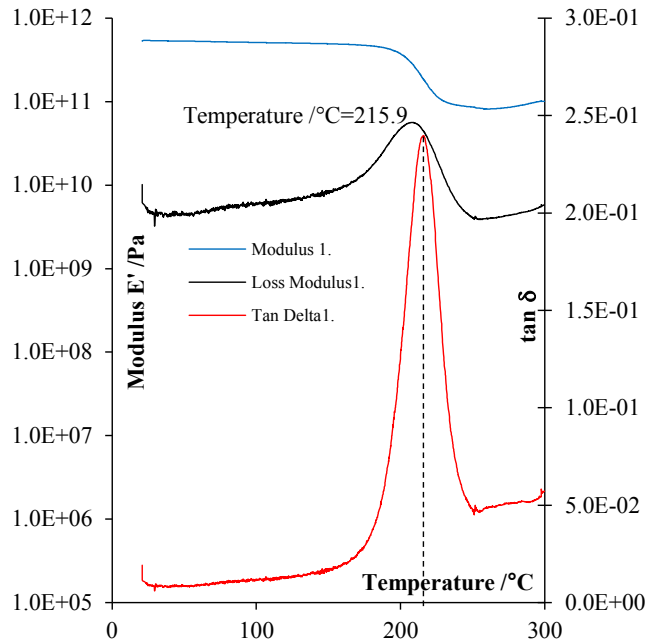


Figure I. 4 - TPB CFRP-1-40: storage modulus  $E'$ , loss modulus  $E''$  loss factor  $\tan \delta$  vs temperature

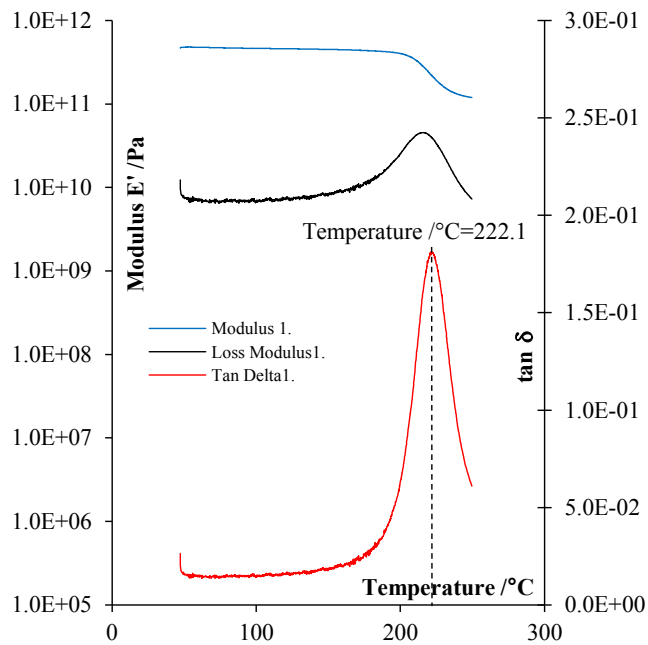


Figure I. 5 - TPB CFRP-2-40: storage modulus  $E'$ , loss modulus  $E''$  loss factor  $\tan \delta$  vs temperature

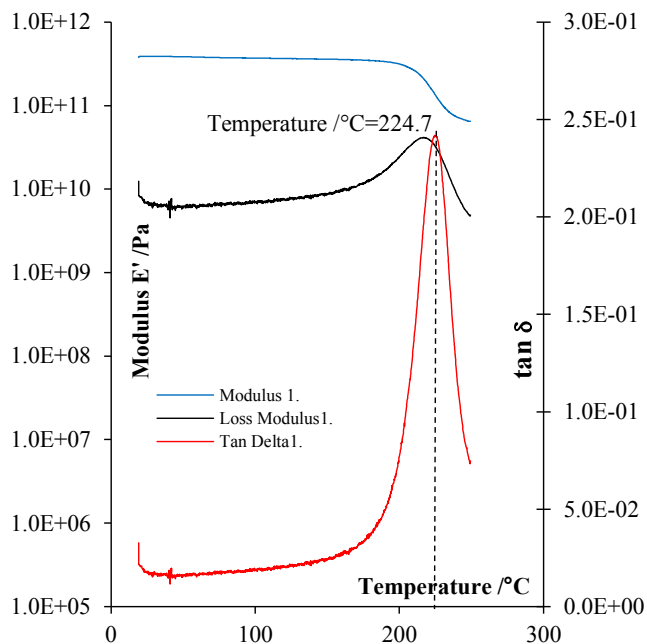


Figure I. 6 - TPB CFRP-3-40: storage modulus  $E'$ , loss modulus  $E''$ , loss factor  $\tan \delta$  vs temperature

Table I. 1 -  $T_g$  (max  $\tan \delta$ ). Average ( $\mu$ ) and standard deviation ( $\sigma$ ) of test results

Analyzer arrangement	Label	$T_g$ (°C)	$\mu$	$\sigma$	$\mu$	$\sigma$
SC	CFRP-1-15	201.9	202.7	0.29	211.48	10.71
	CFRP-2-15	202.4				
	CFRP-3-15	201.9				
TPB	CFRP-1-40	215.9	220.9	4.52		
	CFRP-2-40	222.0				
	CFRP-3-40	224.7				

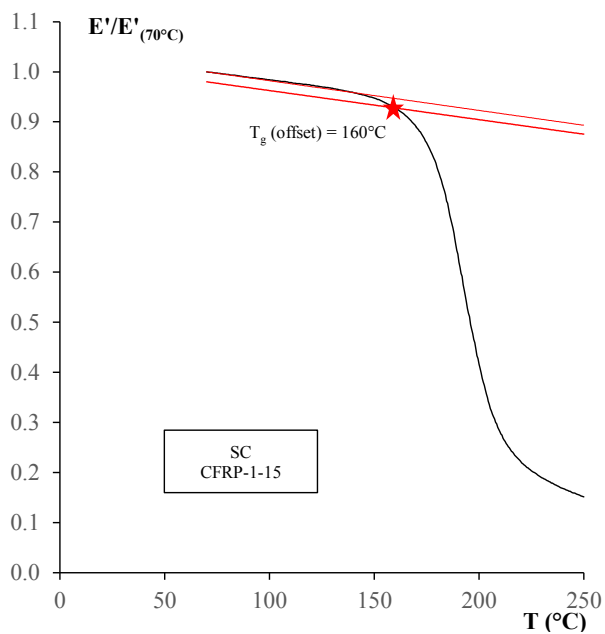
Evaluation of  $T_g$  offset

Figure I. 7 - SC CFRP-1-15: Normalized storage modulus vs Temperature. Definition of  $T_g$  offset

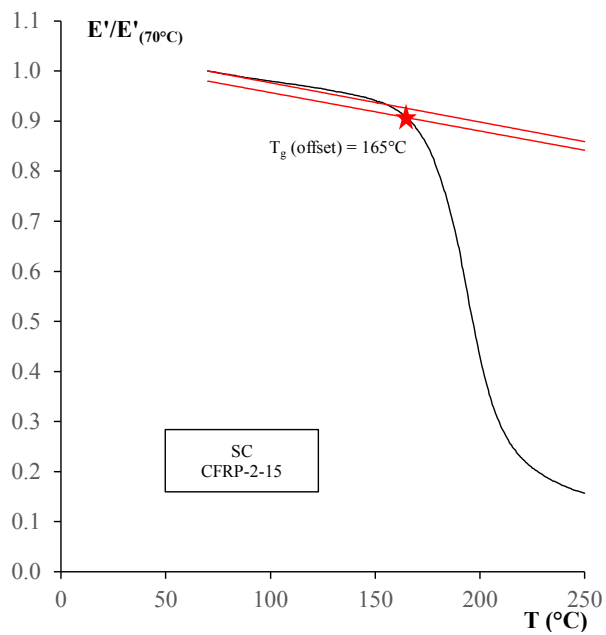


Figure I. 8 - SC CFRP-2-15: Normalized storage modulus vs Temperature. Definition of  $T_g$  offset

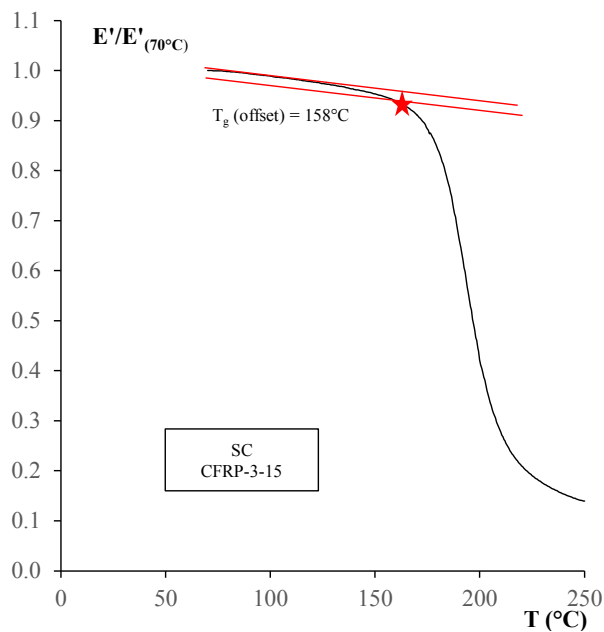


Figure I. 9 - SC CFRP-3-15: Normalized storage modulus vs Temperature. Definition of  $T_g$  offset

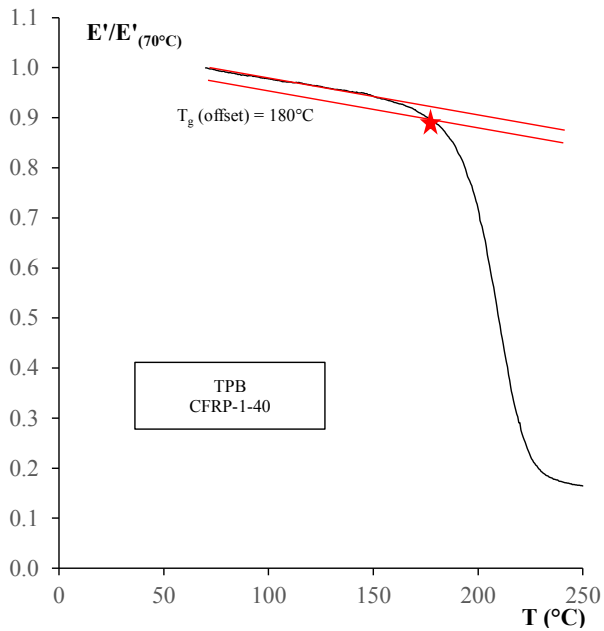


Figure I. 10 - TPB CFRP-1-40: Normalized storage modulus vs Temperature. Definition of  $T_g$  offset

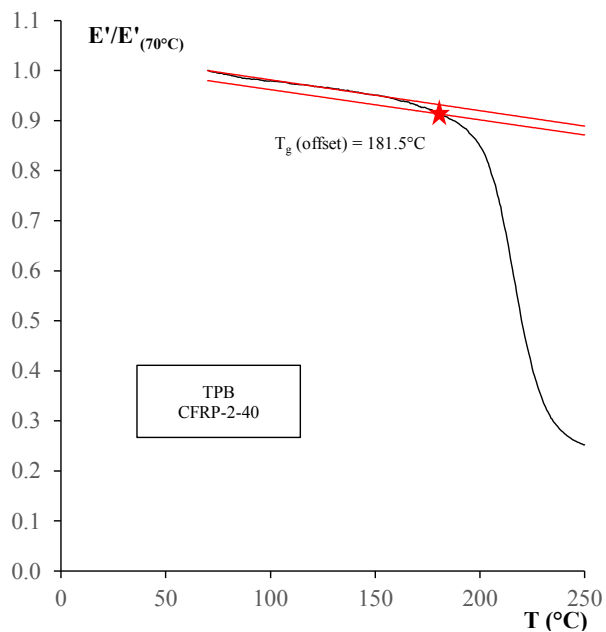


Figure I. 11 - TPB CFRP-2-40: Normalized storage modulus vs Temperature. Definition of  $T_g$  offset

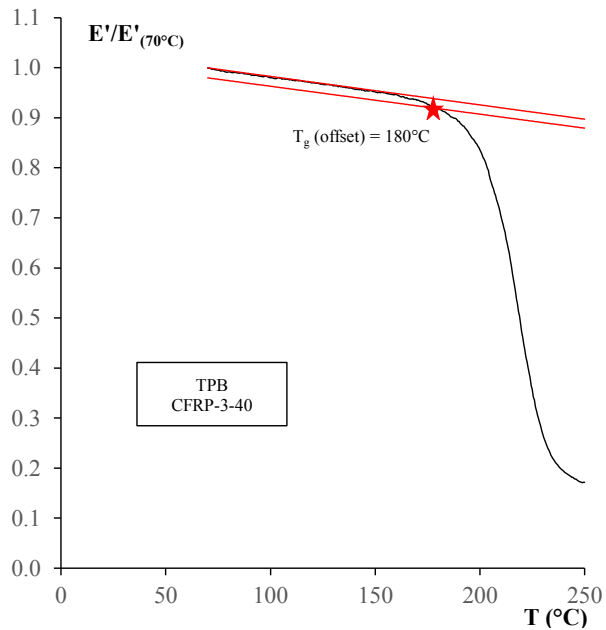


Figure I. 12 - TPB CFRP-3-40: Normalized storage modulus vs Temperature. Definition of  $T_g$  offset

Table I. 2 -  $T_g$  offset. Average ( $\mu$ ) and standard deviation ( $\sigma$ ) of test results

<b>Analyzer arrangement</b>	<b>Label</b>	<b><math>T_g</math> (°C)</b>	<b><math>\mu</math></b>	<b><math>\sigma</math></b>	<b><math>\mu</math></b>	<b><math>\sigma</math></b>
SC	CFRP-1-15	160.0	161.0	3.61	170.75	10.94
	CFRP-2-15	165.0				
	CFRP-3-15	158.0				
TPB	CFRP-1-40	180.0	180.5	0.87		
	CFRP-2-40	181.5				
	CFRP-3-40	180.0				

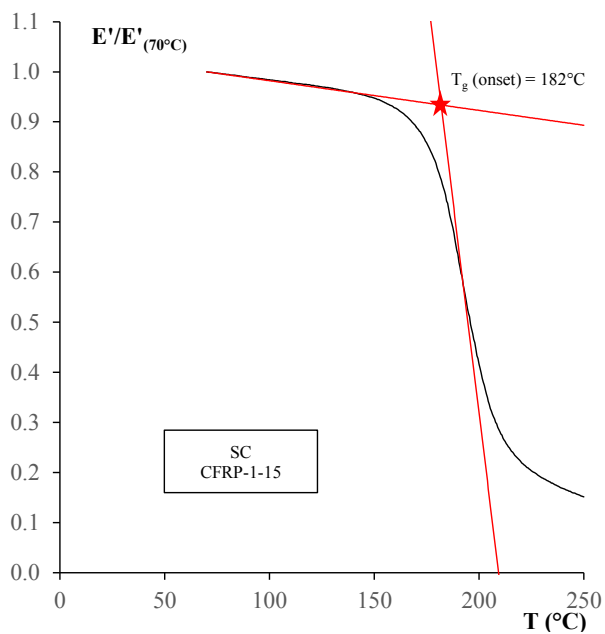
Evaluation of  $T_g$  onset

Figure I. 13 - SC CFRP-1-15: Normalized storage modulus vs Temperature. Definition of  $T_g$  onset

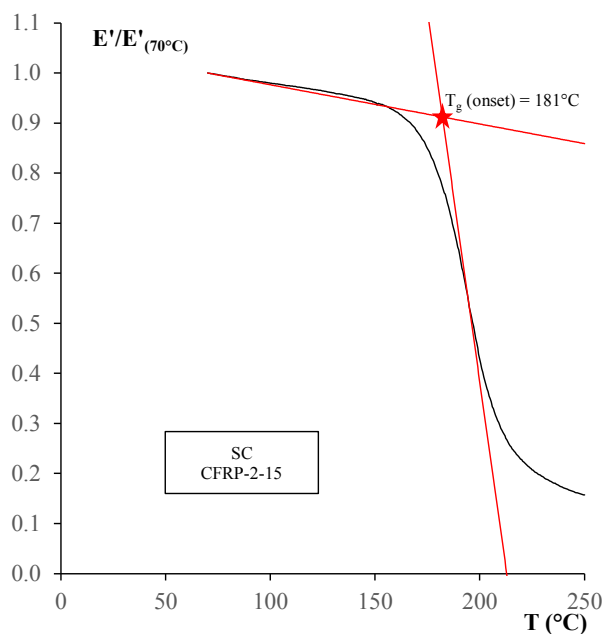


Figure I. 14 - SC CFRP-2-15: Normalized storage modulus vs Temperature. Definition of  $T_g$  onset

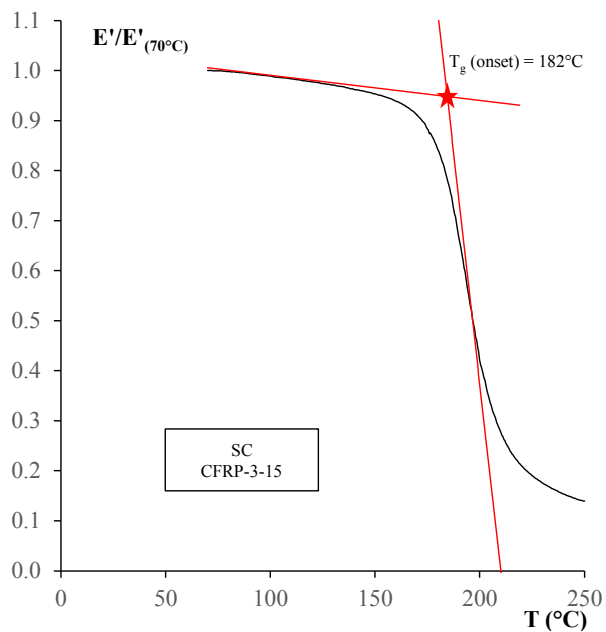


Figure I. 15 - SC CFRP-3-15: Normalized storage modulus vs Temperature. Definition of  $T_g$  onset

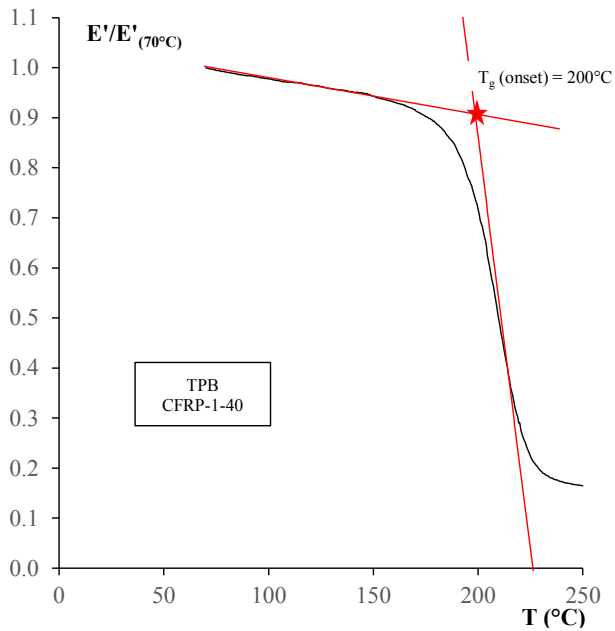


Figure I. 16 - TPB CFRP-1-40: Normalized storage modulus vs Temperature. Definition of  $T_g$  onset



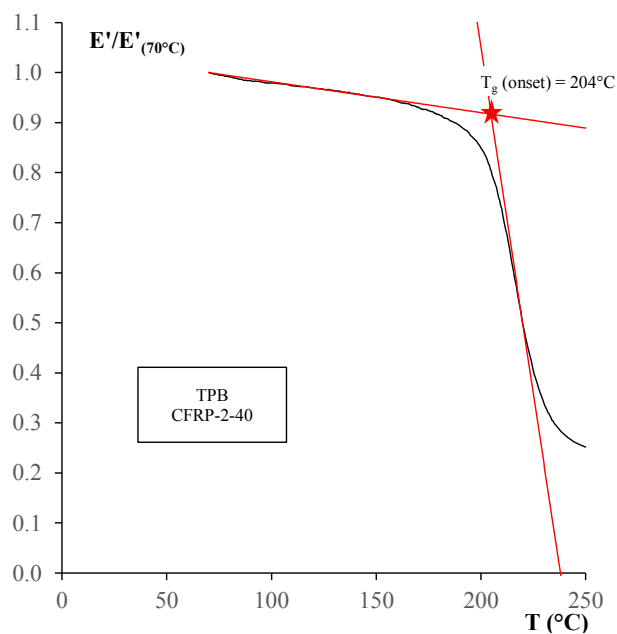


Figure I. 17 - TPB CFRP-2-40: Normalized storage modulus vs Temperature. Definition of  $T_g$  onset

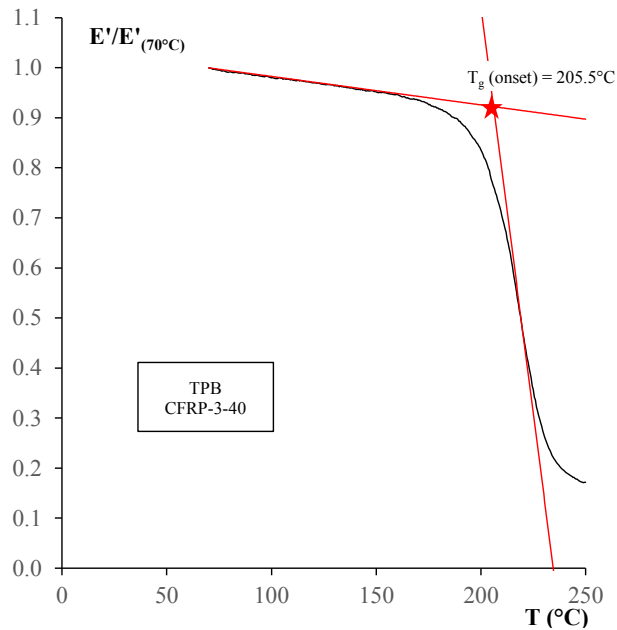


Figure I. 18 - TPB CFRP-3-40: Normalized storage modulus vs Temperature. Definition of  $T_g$  onset

Table I. 3 -  $T_g$  onset. Average ( $\mu$ ) and standard deviation ( $\sigma$ ) of test results

<b>Analyzer arrangement</b>	<b>Label</b>	<b><math>T_g</math> (°C)</b>	<b><math>\mu</math></b>	<b><math>\sigma</math></b>	<b><math>\mu</math></b>	<b><math>\sigma</math></b>
SC	CFRP-1-15	182.0	181.67	0.58	192.42	11.92
	CFRP-2-15	181.0				
	CFRP-3-15	182.0				
TPB	CFRP-1-40	200.0	203.17	2.84		
	CFRP-2-40	204.0				
	CFRP-3-40	205.5				

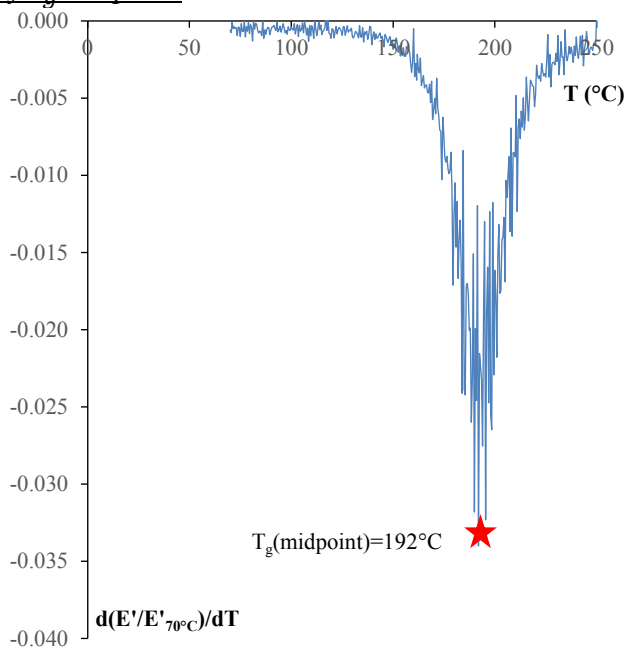
Evaluation of  $T_g$  midpoint

Figure I. 19 - SC CFRP-1-15: First derivative of  $E/E_{(70^\circ\text{C})}$  vs Temperature. Definition of  $T_g$  midpoint

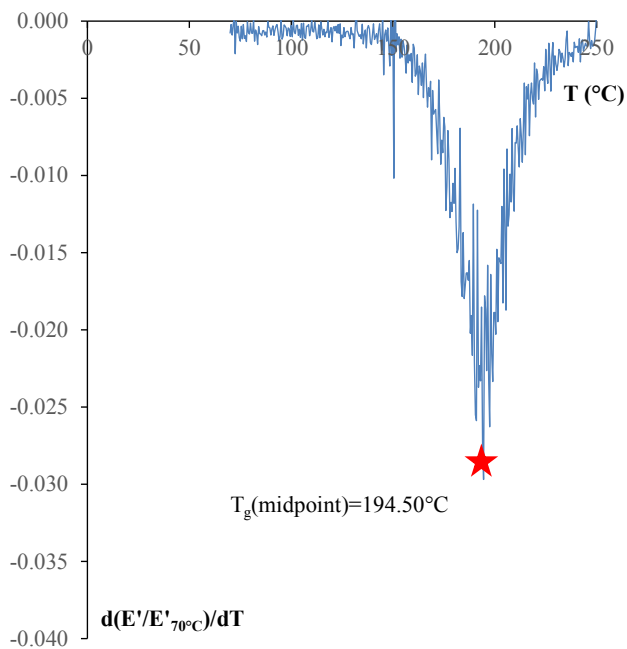


Figure I. 20 - SC CFRP-2-15: First derivative of  $E/E_{(70^\circ\text{C})}$  vs Temperature. Definition of  $T_g$  midpoint

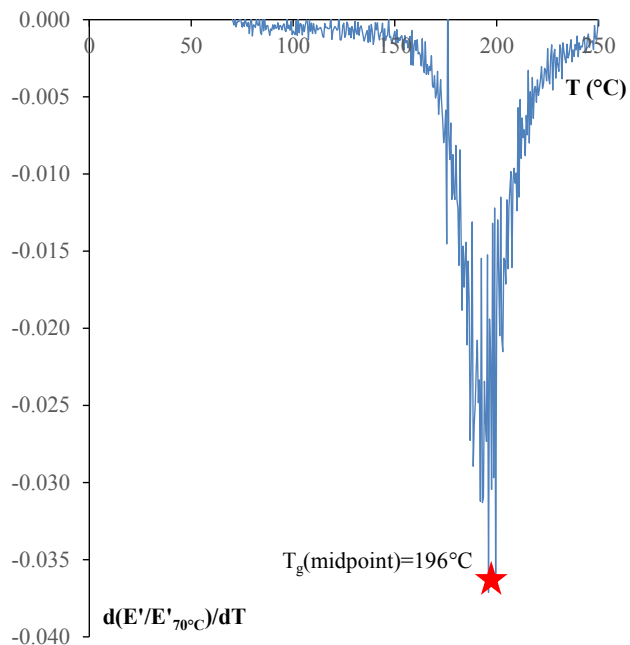


Figure I. 21 - SC CFRP-3-15: First derivative of  $E/E_{(70^\circ\text{C})}$  vs Temperature. Definition of  $T_g$  midpoint

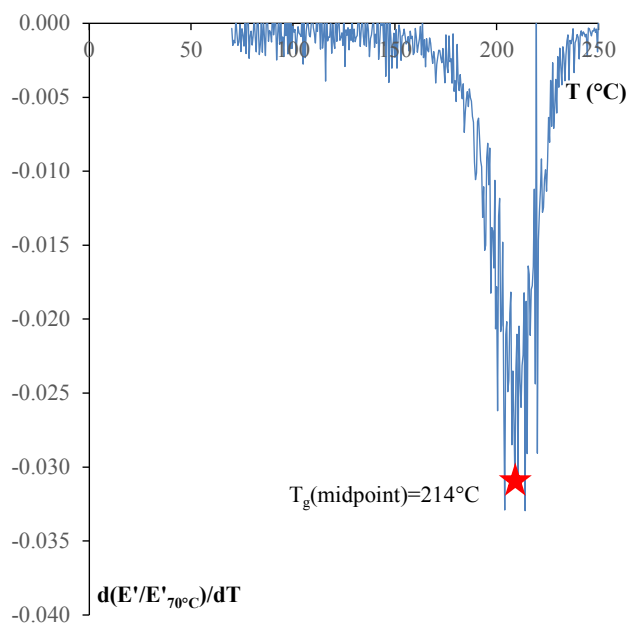


Figure I. 22 - TPB CFRP-1-40: First derivative of  $E/E_{(70^\circ\text{C})}$  vs Temperature. Definition of  $T_g$  midpoint

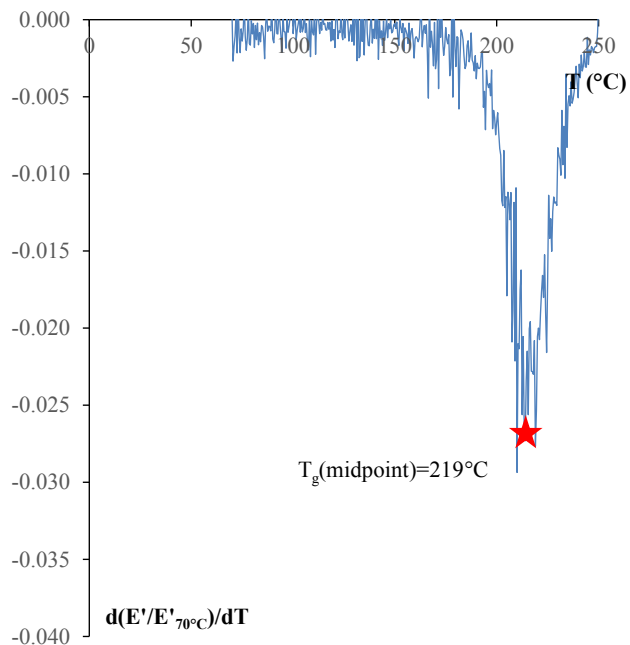


Figure I. 23 - TPB CFRP-2-40: First derivative of  $E/E_{(70^\circ\text{C})}$  vs Temperature. Definition of  $T_g$  midpoint

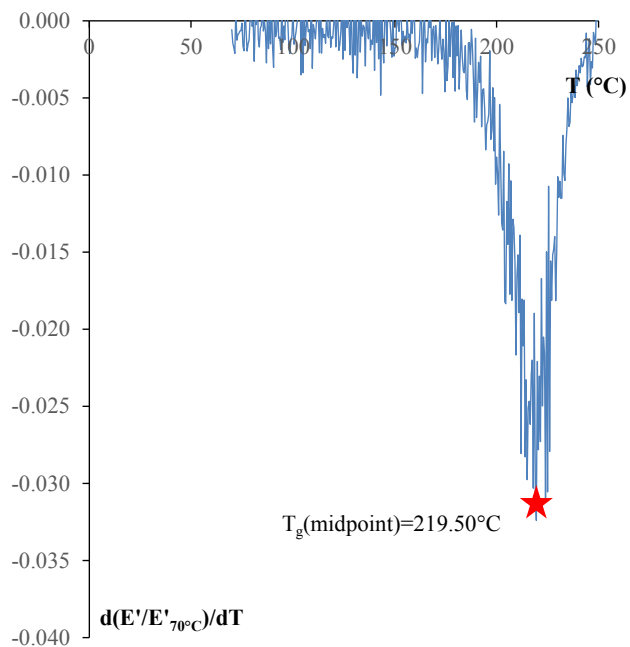
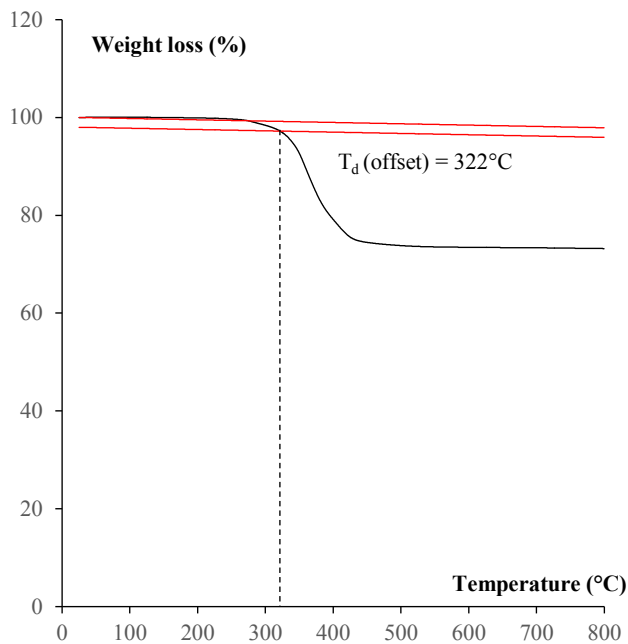
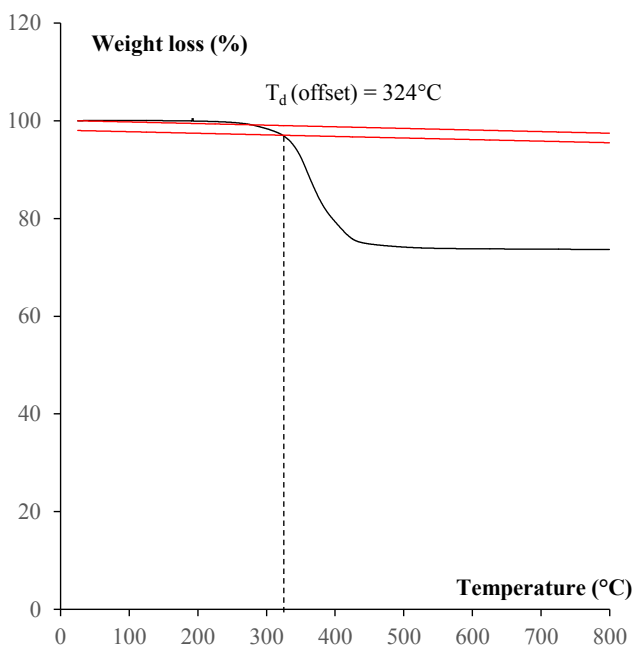


Figure I. 24 - TPB CFRP-3-40: First derivative of  $E/E_{(70^\circ\text{C})}$  vs Temperature. Definition of  $T_g$  midpoint

Table I. 4 -  $T_g$  midpoint. Average ( $\mu$ ) and standard deviation ( $\sigma$ ) of test results

<b>Analyzer arrangement</b>	<b>Label</b>	<b><math>T_g</math> (°C)</b>	<b><math>\mu</math></b>	<b><math>\sigma</math></b>	<b><math>\mu</math></b>	<b><math>\sigma</math></b>
SC	CFRP-1-15	192.0	194.17	2.02	205.83	12.99
	CFRP-2-15	194.5				
	CFRP-3-15	196.0				
TPB	CFRP-1-40	214.0	217.50	3.04		
	CFRP-2-40	219.0				
	CFRP-3-40	219.5				

Evaluation of  $T_d$  offsetFigure I. 25 - CFRP-N<sub>2</sub>-A: Weight loss vs Temperature. Definition of  $T_d$  offsetFigure I. 26 - CFRP-N<sub>2</sub>-B: Weight loss vs Temperature. Definition of  $T_d$  offset

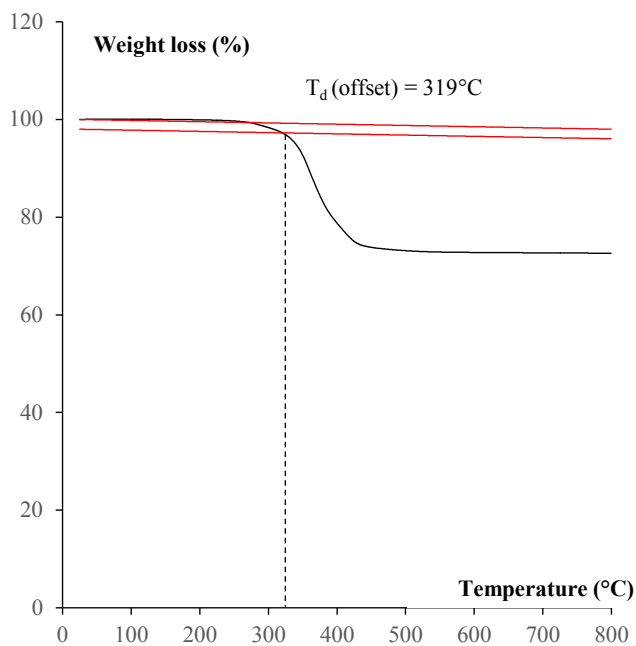


Figure I. 27 - CFRP-N<sub>2</sub>-C: Weight loss vs Temperature. Definition of  $T_d$  offset

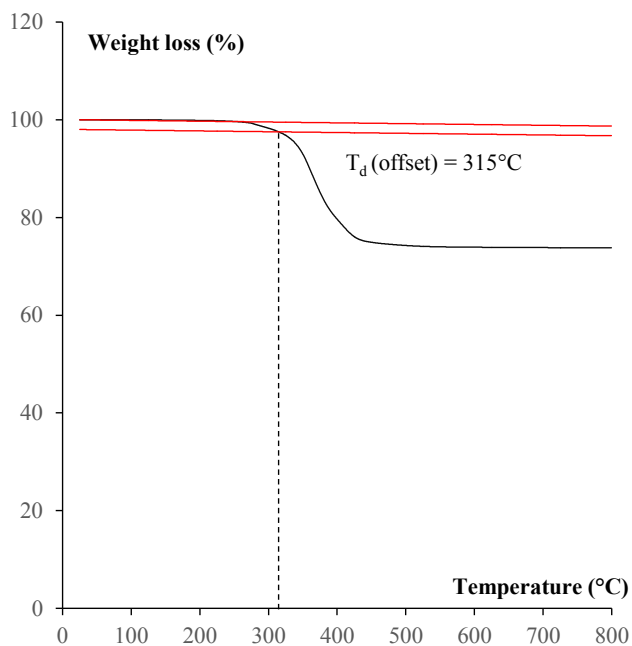


Figure I. 28 - CFRP-Air-A: Weight loss vs Temperature. Definition of  $T_d$  offset



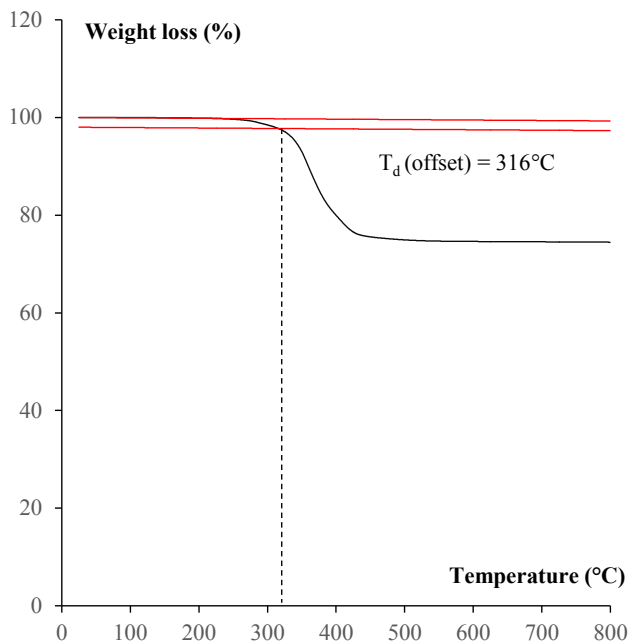
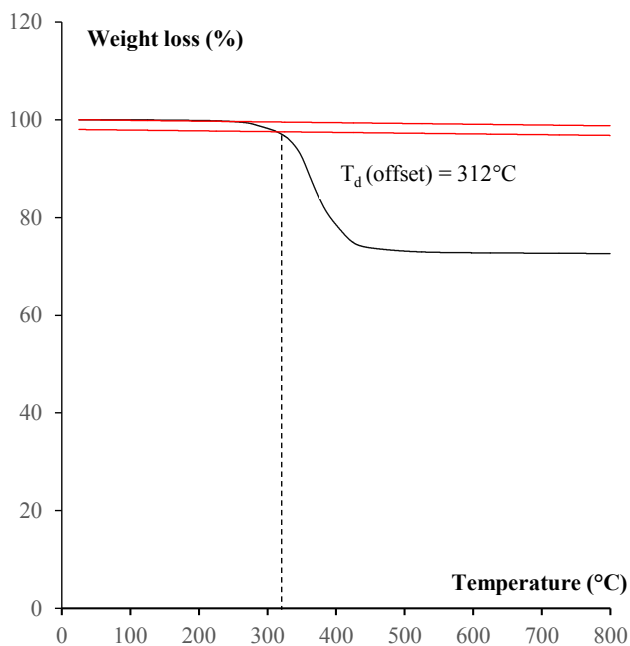
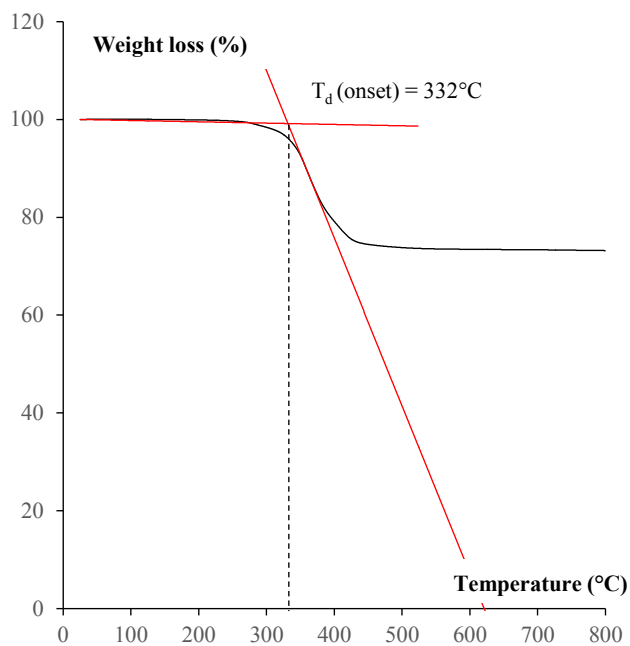
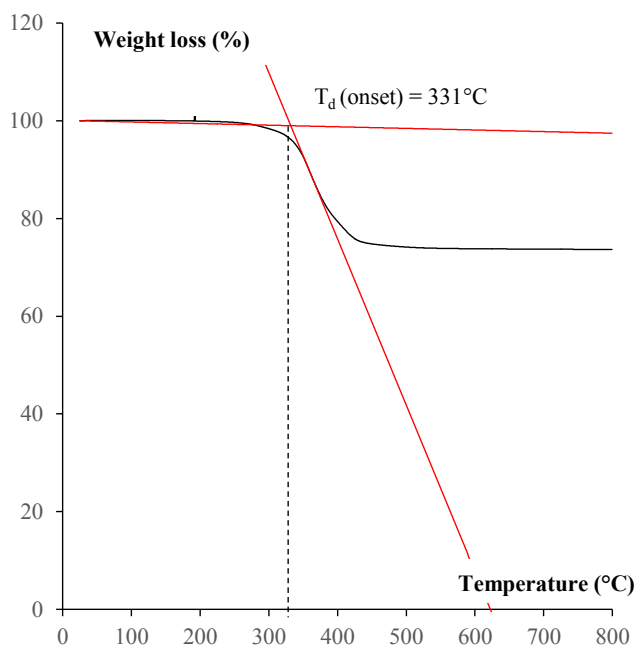
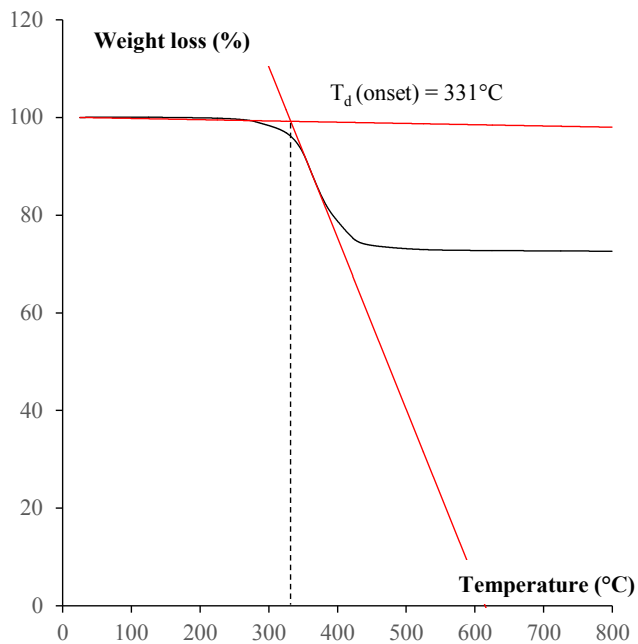
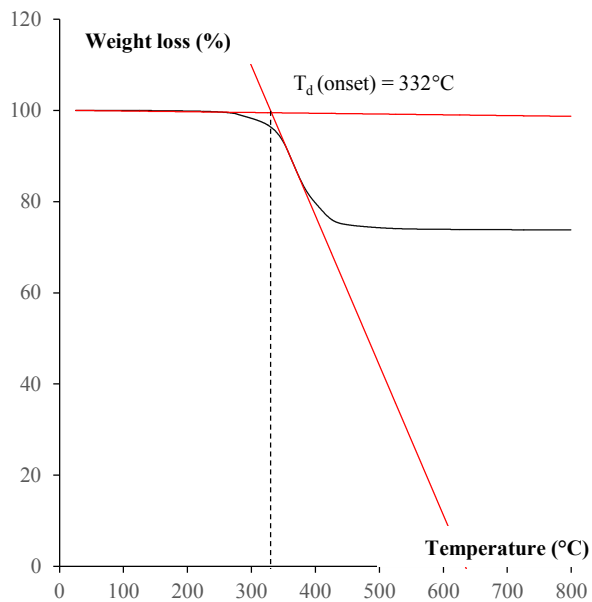
Figure I. 29 - CFRP-Air-B: Weight loss vs Temperature. Definition of  $T_d$  offsetFigure I. 30 - CFRP-Air-C: Weight loss vs Temperature. Definition of  $T_d$  offset

Table I. 5 -  $T_d$  offset. Average ( $\mu$ ) and standard deviation ( $\sigma$ ) of test results

<b>Label</b>	<b><math>T_d</math> (°C)</b>	<b><math>\mu</math></b>	<b><math>\sigma</math></b>	<b><math>\mu</math></b>	<b><math>\sigma</math></b>
CFRP- N <sub>2</sub> -A	322.0	321.50	2.50	317.92	4.43
CFRP- N <sub>2</sub> -B	324.0				
CFRP- N <sub>2</sub> -C	319.0				
CFRP-Air-A	315.0	314.33	2.08		
CFRP- Air -B	316.5				
CFRP- Air -C	312.0				

Evaluation of  $T_d$  onsetFigure I. 31 - CFRP-N<sub>2</sub>-A: Weight loss vs Temperature. Definition of  $T_d$  onsetFigure I. 32 - CFRP-N<sub>2</sub>-B: Weight loss vs Temperature. Definition of  $T_d$  onset

Figure I. 33 - CFRP-N<sub>2</sub>-C: Weight loss vs Temperature. Definition of  $T_d$  onsetFigure I. 34 - CFRP-Air-A: Weight loss vs Temperature. Definition of  $T_d$  onset

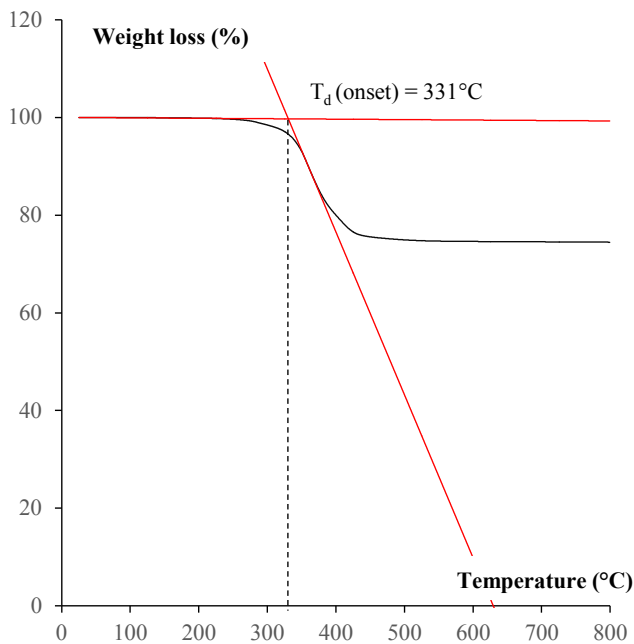


Figure I. 35 - CFRP-Air-B: Weight loss vs Temperature. Definition of  $T_d$  onset

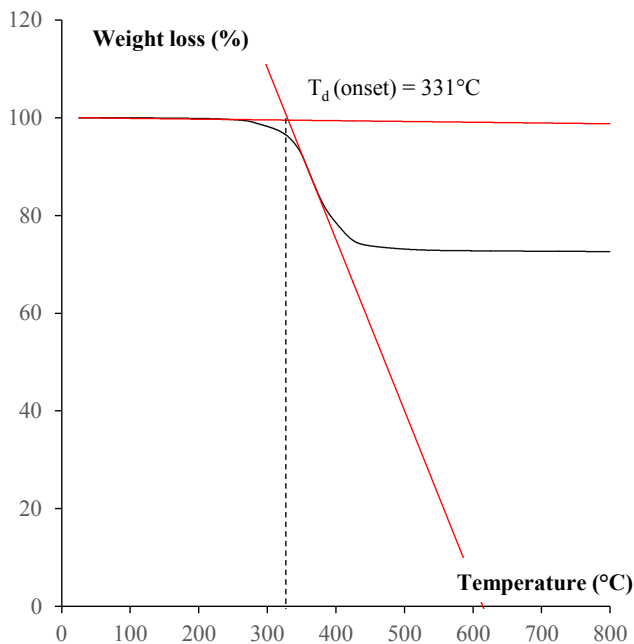
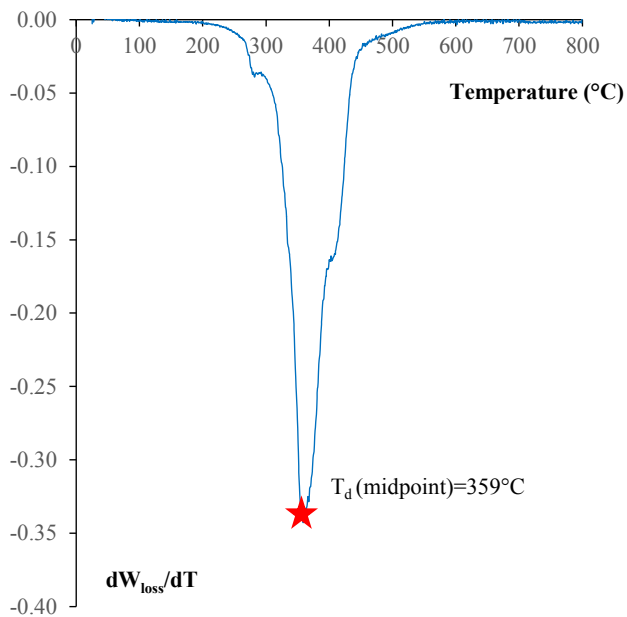
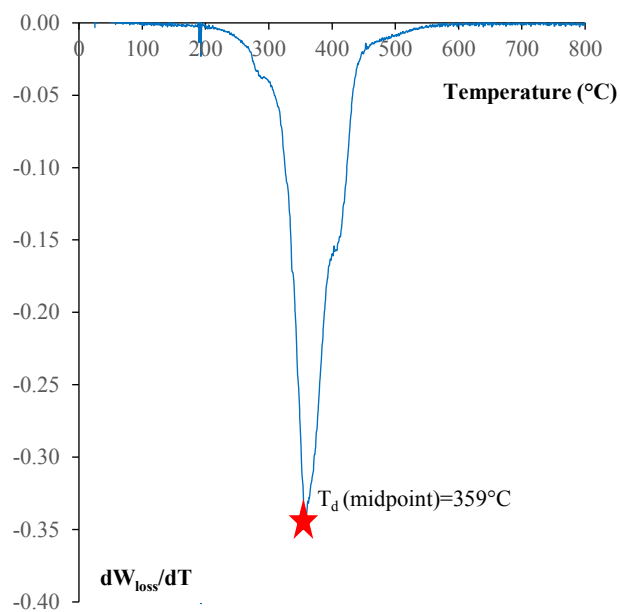
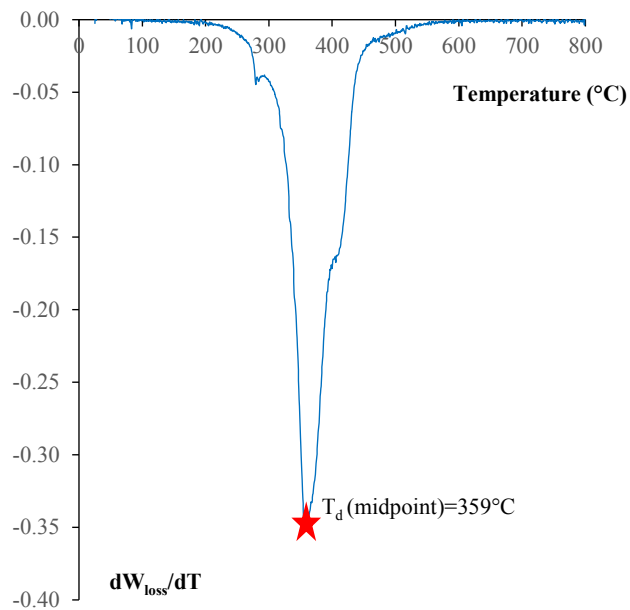
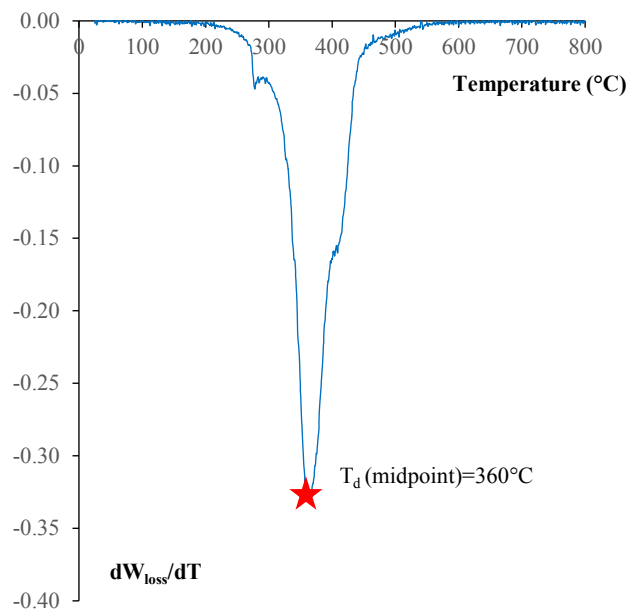


Figure I. 36 - CFRP-Air-C: Weight loss vs Temperature. Definition of  $T_d$  onset

Table I. 6 -  $T_d$  onset. Average ( $\mu$ ) and standard deviation ( $\sigma$ ) of test results

Label	$T_d$ (°C)	$\mu$	$\sigma$	$\mu$	$\sigma$
CFRP- N <sub>2</sub> -A	332.0	331.00	0.50	330.92	0.49
CFRP- N <sub>2</sub> -B	331.0				
CFRP- N <sub>2</sub> -C	331.0				
CFRP-Air-A	332.0	331.00	0.50		
CFRP- Air -B	331.5				
CFRP- Air -C	331.0				

Evaluation of  $T_d$  midpointFigure I. 37 - CFRP-N<sub>2</sub>-A: DTG curve. Definition of  $T_d$  midpointFigure I. 38 - CFRP-N<sub>2</sub>-B: DTG curve. Definition of  $T_d$  midpoint

Figure I. 39 - CFRP-N<sub>2</sub>-C: DTG curve. Definition of  $T_d$  midpointFigure I. 40 - CFRP-Air-A: DTG curve. Definition of  $T_d$  midpoint



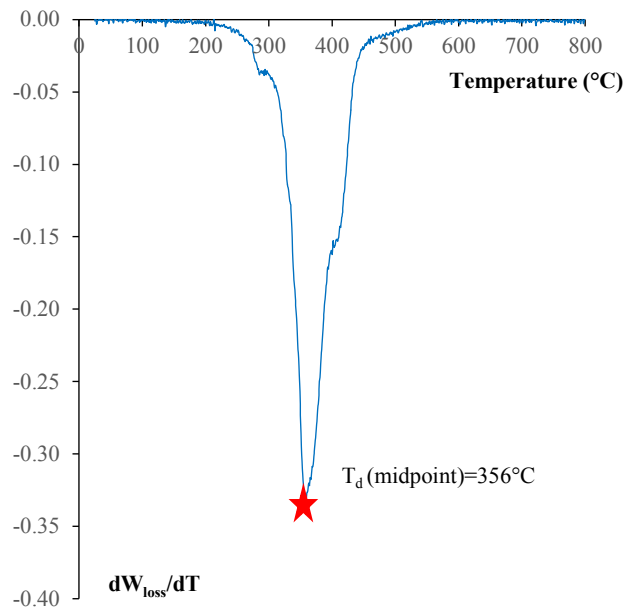
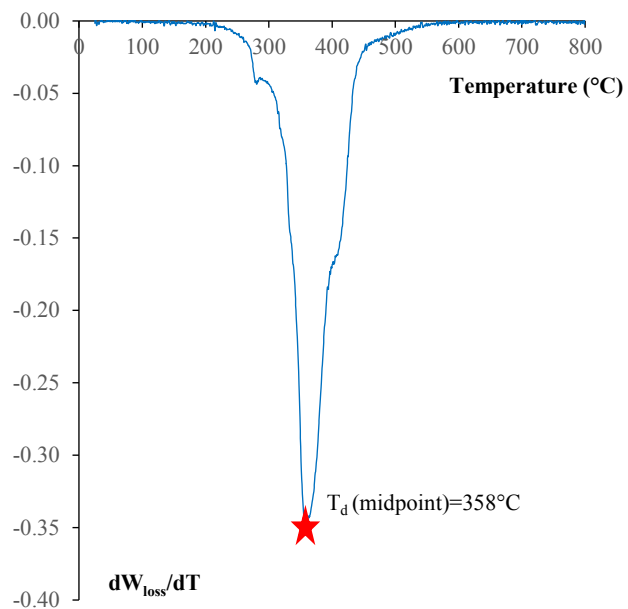
Figure I. 41 - CFRP-Air-B: DTG curve. Definition of  $T_d$  midpointFigure I. 42 - CFRP-Air-C: DTG curve. Definition of  $T_d$  midpoint

Table I. 7 -  $T_d$  midpoint. Average ( $\mu$ ) and standard deviation ( $\sigma$ ) of test results

<b>Label</b>	<b><math>T_d</math> (°C)</b>	<b><math>\mu</math></b>	<b><math>\sigma</math></b>	<b><math>\mu</math></b>	<b><math>\sigma</math></b>
CFRP- N <sub>2</sub> -A	359.0	359.00	0.00	358.33	1.33
CFRP- N <sub>2</sub> -B	359.0				
CFRP- N <sub>2</sub> -C	359.0				
CFRP-Air-A	360.0	357.70	1.76		
CFRP- Air-B	356.5				
CFRP- Air-C	358.0				